UNIVERSITY OF CALIFORNIA, SAN DIEGO

Measurement of the Ratio of the Neutron and Proton Structure Functions F_2 in Inelastic Muon Scattering

A dissertation submitted in partial satisfaction
of the requirements for the degree
Doctor of Philosophy in Physics

by

Robert D. Kennedy

Committee in charge:
- Professor Robert A. Swanson, Chair
- Professor H. Kobrak, Co-Chair
- Professor J. Branson
- Professor W. Coles
- Professor J. Hildebrand
- Professor J. Kuti

1992

The dissertation of Robert D. Kennedy is approved, and it is acceptable in quality and form for publication on microfilm:

Chair

University of California, San Diego
1992

Dedication

This thesis is dedicated to my wife Liz and daughter Kathleen.

這份論文同時獻給在1989年6月4日中國北京
天安門事件中喪生的學生們

(This thesis is also dedicated to the students murdered in Tiananmen Square, Beijing, China on the fourth of June, 1989.)

Epigraph

Para mí solo recorrer los caminos que tienen corazón, cualquier camino que tenga corazón. Por ahí yo recorro, y la única prueba que vale es atrevesar todo su largo. Y por ahí yo recorro mirando, mirando, sin aliento.

(For me there is only the traveling on paths that have heart, on any path that may have heart. There I travel, and the only worthwhile challenge is to traverse its full length. And there I travel looking, looking, breathlessly.)

— Don Juan Matus

Carlos Castañeda, *The Teachings of Don Juan: A Yaqui Way of Knowledge* (1968)

Table of Contents

List of Symbols

Symbol	Description
η	Radiative corrections weight
μ	True beam phase space
μ^*	Measured beam phase space
ξ	True (x_{bj}, Q^2)
ξ^*	Measured (x_{bj}, Q^2)
ϕ	Azimuthal orientation of scattering plane
ρ	Mass density
σ	Cross section
θ_{scat}	Polar scattering angle
A	Experiment acceptance
A_N	Atomic number
A_W	Atomic weight
B	Normalized beam phase space density
E	Experiment efficiency
F_2	Structure function
I	Iterative extraction correction
I_G	Gottfried Integral
L	Integrated luminosity
l_f	Fiducial target length
M	Molar density
N	Number of inelastic muon scattering events
N_A	Avogadro's Number
N_μ	Number of acceptable beam muons entering experiment
R	Ratio of photon absorption cross sections
S	Experiment smearing function
S_G	Gottfried Sum Rule
W	Weighted number of inelastic muon scattering events

List of Figures

List of Tables

Acknowledgements

I wish to thank Liz for patience and understanding during this long and frustrating ordeal.

I am indebted to the many people at Fermilab, too numerous to mention individually, who were involved with the construction and operation of the Tevatron, New Muon Beamline, and the New Muon Lab. In particular I wish to thank Harry Melanson, Richard Nickerson, Vassili Papavassiliou, Heidi Schellman, Steve Wolbers, and Dave Jaffe for their many contributions and advice. Silhacène Aïd and Anwar Bhatti were helpful in discussing the details of their earlier structure function ratio analyses. I thank for friendship and a ready helping hand when needed fellow students Mark Baker, Tim Carroll, Janet Conrad, Pat Madden, Eric Ramberg, John Ryan, Alex Salvarani, Mike Schmitt, and Mathias Wilhelm. I thank Helmut Braun, Don Geesaman, Andreas Manz, and Jorge Morfín for suggestions and for always having a hearty hello ready. I wish to thank Guang Fang, Rurng-Sheng Guo, Ashutosh Kotwal, Bogdan Pawlik, and Panagiotis Spentzouris for help in documenting elements and properties of the apparatus not already documented. Finally, I thank Hans Kobrak and Bob Swanson for their support and advice over the years.

Curriculum Vitae

Biography

Robert Daniel Kennedy

23 March 1962	Born, Fresno, California, USA
1984	B.S. with High Honors in Physics, University of Florida (Gainesville, Florida)
1984	Teaching Assistant, Department of Physics, University of Florida (Gainesville, Florida)
1984 - 1985	Teaching Assistant, Department of Physics, University of California, San Diego (La Jolla, California)
1984 - 1985	U. C. Regents Fellowship, Department of Physics, University of California, San Diego (La Jolla, California)
1985 - 1992	Research Assistant, Department of Physics, University of California, San Diego (La Jolla, California)
1986	M.S. in Physics, University of California, San Diego (La Jolla, California)
1992	Ph.D. in Physics, University of California, San Diego (La Jolla, California)

Publications

M. R. Adams *et al.* (E665 Collaboration), "A Spectrometer for Muon Scattering at the Tevatron", *Nucl. Instrum. Meth.* **A291**, 533 (1990).

M. R. Adams *et al.* (E665 Collaboration), "Distributions of Charged Hadrons Observed in Deep-Inelastic Muon-Deuterium Scattering at 490 GeV", *Phys. Lett.* **B272**, 163 (1991).

M. R. Adams *et al.* (E665 Collaboration), "Saturation of Shadowing at Very Low Bjorken x", *Phys. Rev. Lett.* **68**, 3266 (1992).

M. R. Adams *et al.* (E665 Collaboration), "First Measurements of Jet Production Rates in Deep-Inelastic Lepton-Proton Scattering", *Phys. Rev. Lett.* **69**, 1026 (1992).

M. R. Adams *et al.* (E665 Collaboration), "Shadowing in the Muon-Xenon Inelastic Scattering Cross Section at 490 GeV/c", *Phys. Lett.* **B287**, 375 (1992).

Conference Presentations

R. D. Kennedy, for the E665 Collaboration, "*Measurement of the Ratio of the Neutron and Proton Cross Sections to Very Low X_{Bj} in Inelastic Muon Scattering*", presented at the Seventh Meeting of the Division of Particles and Fields, November 10–14, 1992, Fermi National Accelerator Laboratory, Batavia, Illinois (USA).

Abstract

Measurement of the Ratio of
the Neutron and Proton Structure Functions F_2
in Inelastic Muon Scattering

by

Robert D. Kennedy

Doctor of Philosophy in Physics
University of California, San Diego, 1992
Professor Robert A. Swanson, Chair

The ratio of the neutron and proton structure functions F_2 has been measured to very low x_{bj} using inelastic muon scattering. Data were taken in 1990 using 475 GeV muons incident on hydrogen and deuterium targets. Electromagnetic calorimetry has been used to remove radiative backgrounds and muon-electron elastic scattering. Results of the measurement are presented which cover the kinematic region $0.0001 \leq x_{bj} \leq 0.4$ and $0.1 \text{ GeV}^2/c^2 \leq Q^2 \leq 100.0 \text{ GeV}^2/c^2$.

Chapter 1

Introduction

> *But the reason I call myself by my childhood name is to remind myself that a scientist must be absolutely like a child. If he sees a thing, he must say that he sees it, whether it was what he thought he was going to see or not. See first, think later, then test. But always see first. Otherwise you will only see what you were expecting. Most scientists forget that.... So, the other reason I call myself Wonko the Sane is so that people will think I am a fool. That allows me to say what I see when I see it. You can't possibly be a scientist if you mind people thinking you're a fool.*
>
> — Wonko the Sane

Douglas Adams, *So Long, and Thanks for All the Fish* (1984)

1.1 Opening

This thesis reports the measurement of the ratio of the neutron and proton structure functions F_2 in Inelastic Muon Scattering. The data used in this work were collected during the 1990 running of the Fermilab Experiment E665. The results reported here, as well as those from an analysis of an earlier E665 data set [170], extend the world data set to lower values of x_{bj} than previously seen.

In this region of very small x_{bj}, obstacles not encountered in analyses reported by other experiments have been overcome in the extraction of the inelastic cross section ratio from the relatively large radiative and muon-electron elastic scattering backgrounds. Information from the E665 electromagnetic calorimeter is used to identify and eliminate these large backgrounds from the data sample.

The reported ratio F_2^n/F_2^p is expected to approach unity as $x_{bj} \rightarrow 0$, but the manner in which it approaches unity affects the outcome of a number of physics results, such as the calculation of the Gottfried Integral. Various effects, such as shadowing in the deuteron or flavor asymmetry in the quark sea, may lower the ratio, in other words slow the approach to unity. Phenomenological estimates of the size of these effects exist. While these estimates appear to explain the violation of the Gottfried Sum Rule seen by the NMC experiment, they have not been explicitly confirmed by experiment. This measurement seeks to determine the behavior of the ratio, especially at small x_{bj}. This might be used as a check of the $x_{bj} \rightarrow 0$ extrapolations of the ratio used to arrive at Gottfried Integral results.

1.2 Thesis Structure and Conventions

This thesis is divided into 5 chapters and several appendices. This first chapter gives a brief introduction to the current experimental and theoretical understanding of the structure of the proton and the neutron. Chapter Two describes the apparatus that gathered the data. In Chapter Three, the procedure used to convert the raw data into events with understood kinematics is outlined. The method by which these events are used to measure the ratio of the neutron and proton structure functions F_2 is documented in Chapter Four. The results of this measurement are given in Chapter Five, along with a comparison to other measurements. Discussions of several topics related to this thesis, including elements of the experiment to which I contributed directly, are in the appendices.

Note that in this thesis I use MKS units and the Heaviside-Lorentz system of electromagnetic units.

1.3 Historical Background

Particle scattering experiments have been used throughout the twentieth century to probe the structure of matter. In the early 1900's, the atom was thought to be composed of a diffuse positively-charged substance with negatively-charged electrons imbedded in its exterior, the Thomson model of the atom. In 1909 Ernest Rutherford performed experiments with an alpha particle beam impinging on a gold foil target to test this. The Thomson model predicted that the alpha particles would scatter only at small angles. The polar angular distribution of the scattered alpha particles, however, extended all the way from 0° to 180°. To explain this, Rutherford proposed in 1911 that the atom consists of a small, dense, positively-charged nucleus which is surrounded by a negatively-charged cloud of electrons. While an atom is approximately 10^{-10} m in radius, the nucleus is less than 10^{-14} m in radius and contains most of the atomic mass. In 1919, Rutherford demonstrated that a single particle, which he called the proton, makes up the hydrogen nucleus. By 1920, Rutherford had extended his model of nuclei by demonstrating that they are all composed of positively-charged protons. In addition, he proposed that they also generally contain electrically neutral neutrons. The existence of the neutron was later established by James Chadwick in 1932. Since the proton and the neutron are the primary constituents of nuclei, they are collectively referred to as nucleons.

In the 1950's and 1960's, many experiments measured the cross section for the scattering of electron beams off of various target nuclei in order to measure the spatial distribution of charge in the nucleon. The radius of the nucleon was found to be poorly defined and on the order of 10^{-15} m. These electron beam experiments did not reveal any nucleon sub-structure at the distance scales probed. The probe used was a virtual photon exchanged between the beam electron and the target nucleon. In hindsight, the beams were insufficiently energetic to resolve the quark structure of the nucleon. Greater beam energies permit higher energy virtual photons to be exchanged. The higher energy photons have a shorter wavelength, enabling smaller structures to be resolved.

1.4 Nucleon Structure

The 20 GeV electron beam at SLAC, brought on-line in 1968, was the first to be able to resolve distinct components inside the nucleon [51, 55]. The nucleon structure appeared to be independent of the energy scale of the probe once the distinct components were resolved, as was previously predicted by Bjorken [50]. These nucleon constituents were interpreted to be the quarks in the Gell-Mann model [95] and the Zweig model [210, 211] of hadronic structure and the partons in the Feynman model

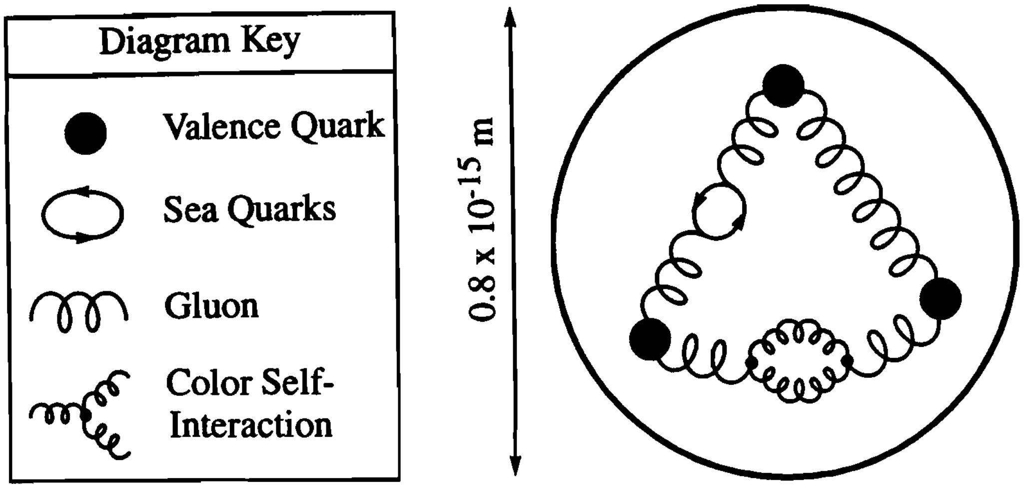

Figure 1.1: The QCD-enhanced Quark-Parton Model of the nucleon

of the nucleon [88, 89]. These models were subsequently fused into the original Quark-Parton Model by Kuti and Weisskopf in 1971 [139]. A review of this model of nucleon structure and its successors can be found in Appendix B.

In the Quark-Parton Model, the nucleon consists of electrically-charged quarks and neutral gluons. There are three quarks, called valence quarks, in the nucleon and an indefinite number of virtual quark-anti-quark pairs, called sea quarks. The quarks are now believed to exist in six "flavors", labelled down, up, strange, charm, bottom (or beauty), and the as-yet unobserved top (or truth). The nucleon also contains an indefinite number of electrically neutral gluons, the quanta of the quark-quark interactions. The exact form of the interactions mediated by the gluons is not specified in the original Quark-Parton Model.

Quark-quark interactions are now generally believed to be described by the relativistic field theory Quantum Chromodynamics based on the SU_3^{color} local gauge symmetry group. The current model of the structure of the nucleon is a combination of the Quark-Parton Model and Quantum Chromodynamics, referred to here as the the QCD-enhanced Quark-Parton Model. This model of the nucleon is illustrated in Figure 1.1 on page 4. In the QCD-enhanced Quark-Parton Model, the gluons are interpreted to be the vector gauge bosons in the SU_3^{color} theory. Inelastic Muon Scattering is viewed as the elastic scattering of a muon off a quark. A kinematic variable, x_{bj}, describes the fraction of the nucleon momentum carried by the quark involved.

Scattering at high x_{bj} generally involves valence quarks. At low x_{bj}, scattering usually involves the sea quarks and, indirectly, the gluons.

While Quantum Chromodynamics has been quite successful at predicting the quark-quark interactions at short distance scales, it is very difficult to use to calculate quantities that involve distance scales on the order of the nucleon radius. The QCD perturbative expansions used in calculations involving short distance scales are divergent at distance scales on the order of the nucleon size or larger. Because of this, our working model of the nucleon is actually based on the fusion of the Quark-Parton Model, Quantum Chromodynamics, and some phenomenological enhancements. This model is still evolving, in large part because of the results of inelastic scattering experiments. In 1983, the European Muon Collaboration (EMC-NA2) at CERN[1] demonstrated that the inelastic scattering cross section of a nucleus is affected by the number of nucleons in the nucleus, the EMC effect [27]. This can be said to imply that the structure of a bound nucleon depends on its nuclear environment, and therefore that the structure of a bound nucleon differs from that of a free nucleon [162, 43]. In 1991, the New Muon Collaboration (NMC-NA37) at CERN reported that their measurement of the Gottfried Integral appears to disagree with the Gottfried Sum Rule prediction obtained in the Quark-Parton Model under the assumption that the quark sea is flavor symmetric [18, 20]. This can be taken to imply that the proton and the neutron differ not only in the flavor of their valence quarks, but also in the flavor content of their quark seas [77]. Various efforts to extend the QCD-enhanced Quark-Parton model of the nucleon with new phenomenological models to account for these measurements, which involve "non-perturbative" QCD effects, have achieved some success [32, 77, 31]. Nevertheless, none has yet proven to be convincingly predictive.

1.5 Inelastic Muon Scattering

Inelastic Muon Scattering is used to study the momentum distributions of the constituent particles of the nucleon. Beam particles with a measured phase space (position, track slopes, and energy) are generated and directed towards a target. The angular distribution and energies of the scattered beam particles is then measured. The inelastic scatter of an incoming beam muon μ with a target nucleon N yielding the scattered muon μ' and a hadronic final state X is shown in Figure 1.2 on page 6 in the laboratory frame, much as an experimenter might view it.

Given the interaction energy scale at E665 (50 GeV to 500 GeV) and the small size of the electromagnetic coupling constant, the dominant process involved in this

---

[1] **CERN: Conseil Européen pour la Recherche Nucléaire (European Organization for Nuclear Research), a high energy physics laboratory in Geneva, Switzerland**

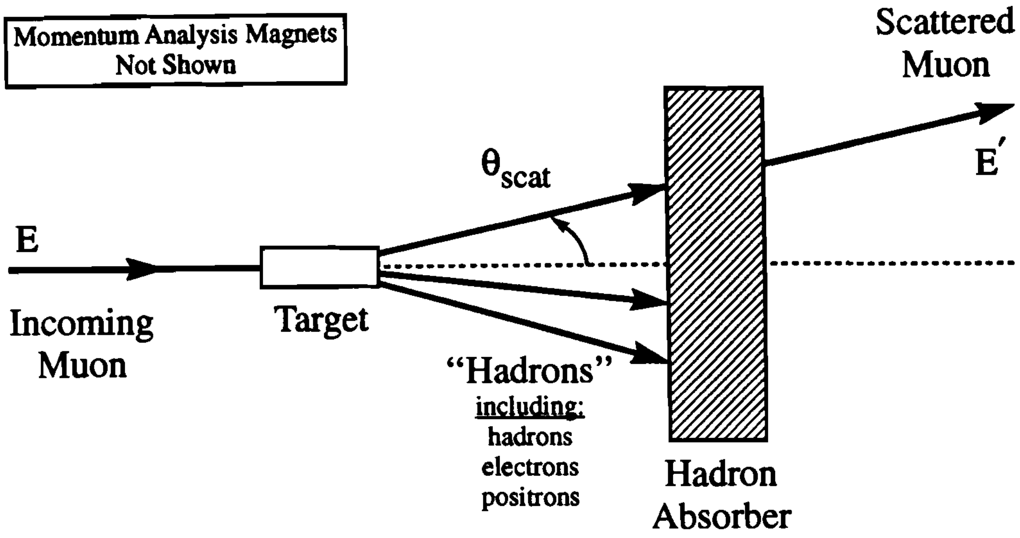

Figure 1.2: Simplified view of an inelastic muon scattering event

scattering is the simple electromagnetic interaction of one-photon-exchange as shown in Figure 1.3 on page 7. In the one-photon-exchange process, the incoming muon of four-momentum k exchanges a virtual photon of four-momentum q with a nucleon of four-momentum P. The scattered muon is left with four-momentum k'. The number of particles in the hadronic final state and the fraction of the available energy each carries are not measured in general. The hadronic final state is usually characterized by its invariant mass-squared W^2.

The Lorentz scalars most often used to describe an inelastic muon scatter are listed in Table 1.1 on page 8 and are defined in the following equations.

$$Q^2 \equiv -q^2 = -(k-k')^2 \tag{1.1}$$

$$\nu \equiv \frac{P \cdot q}{M} \tag{1.2}$$

$$x_{bj} \equiv \frac{-q \cdot q}{2P \cdot q} = \frac{Q^2}{2M\nu} \tag{1.3}$$

$$y_{bj} \equiv \frac{P \cdot q}{P \cdot k} = \frac{\nu}{E} \tag{1.4}$$

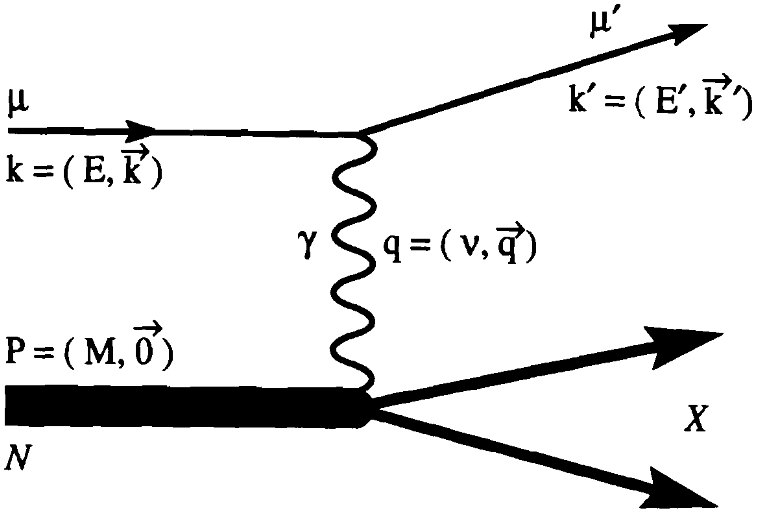

Figure 1.3: One-photon-exchange interaction

$$W^2 \equiv (P+q)^2 = M^2 + 2M\nu - Q^2 \tag{1.5}$$

$$\sqrt{s} \equiv \sqrt{(P+k)^2} \tag{1.6}$$

Some of the expressions for the kinematic variables can be simplified by assuming that the target nucleon is at rest, that the muon mass squared is much smaller than Q^2. These approximations hold well in the laboratory reference frame in much of the E665 accepted kinematic range[2].

$$Q^2 \approx 4EE'sin^2(\theta_{scat}/2) \tag{1.7}$$

$$\nu = E - E' \tag{1.8}$$

The inelastic scattering cross section for the one-photon-exchange process is

---

[2] Muon mass terms are not negligible at small Q^2, however, and are included in event reconstruction calculations.

Table 1.1: Kinematic variables

Symbol	Description
	Momenta
k	Incoming muon 4-momentum
E	Incoming muon energy
q	Virtual photon 4-momentum
P	Nucleon 4-momentum
M	Nucleon mass
k'	Scattered muon 4-momentum
E'	Scattered muon energy
	Angles Describing Scatter
θ_{scat}	Polar scattering angle
ϕ	Azimuthal orientation of scattering plane
	Lorentz Scalars
Q^2	Negative 4-momentum-squared of virtual photon
ν	Energy transfer in lab frame
x_{bj}	Bjorken-x, also written simply as x
y_{bj}	Bjorken-y, also written simply as y
W^2	Invariant mass-squared of hadronic final state
$\sqrt{s}$	Center-of-mass energy

parameterized by two functions, F_2 and R, each of which are dependent on two kinematic variables. The form of the cross section is:

$$\frac{d\sigma^{1\gamma}}{dxdQ^2}(x,Q^2) = \frac{4\pi(\alpha\hbar c)^2}{Q^4}\left\{1 - y - \frac{Q^2}{4E^2} - \frac{y^2 + Q^2/E^2}{2(1+R(x,Q^2))}\right\}\frac{F_2(x,Q^2)}{x} \quad (1.9)$$

where y_{bj} is treated as a function of x_{bj} and Q^2 via Equations 1.3 and 1.4. A detailed review of the physical model behind this cross section is given in Appendix B.

The measured differential cross section is used to calculate the functions F_2 and R, which are then compared to the predictions of the QCD-enhanced Quark-Parton Model. In order to calculate both functions from the cross section measurement, however, the same kinematic region must be sampled with different beam energies. Since E665 has insufficient event statistics to do this, I extract only the F_2 ratio for deuterium and hydrogen by relying upon the experimental result that R is essentially identical for deuterium and hydrogen, even where the value of R is noticeably greater than zero and comparable to one [202].

1.6 Comparing the Neutron to the Proton

In the thesis, the ratio of the neutron and proton structure functions F_2 is extracted from the the ratio of the inelastic cross sections for deuterium and hydrogen. This measurement involves a number of important experimental issues.

The incoming muons can scatter off nucleons by any number of higher order electroweak processes. The QCD-enhanced Quark-Parton Model predictions, however, are stated in terms of the one-photon-exchange process. This can generally be handled in one of two ways. In order to isolate the one-photon-exchange contribution, corrections can be calculated and applied to the measured cross section for all muon-nucleon interactions. This method is difficult to apply in the new, very low x_{bj} kinematic region since a corrections program has not yet been verified to work in this region for both hydrogen and deuterium. As an alternative, explicit event cuts can be applied to remove nearly all events involving observable higher-order processes, such as bremsstrahlung, from the data sample used to measure the cross section ratio.

In addition to the incoming muons scattering off nucleons in the target, they can also scatter elastically off atomic electrons in the target. These events occur in the region of $x_{bj} = m_e/M \approx 1/1836$ called the "mu-e peak". This region in x_{bj}

has not been explored by other experiments with Inelastic Muon Scattering. Events containing muon-electron elastic scattering are identified and cut from the data set.

Ideally, one would use absolute structure functions to compare the neutron to the proton. Precise measurements of absolute structure functions, however, are plagued by relatively large systematic errors from the measurement of the beam flux, the detector acceptance, and the detector efficiency. Relative structure function measurements in which identical targets containing different materials are frequently interchanged are relatively much less affected by such systematics.

Since free neutrons are not stable particles, the neutron cross section cannot easily be measured directly. The assumption is made that since the proton and neutron in the deuteron are very weakly bound, the neutron cross section is given by the difference of the deuteron cross section and the proton cross section.

1.7 Contemporary Experiments

Figure 1.4 on page 11 shows the kinematic coverage of contemporary inelastic scattering experiments that have measured $F_2^{\mathrm{n}}/F_2^{\mathrm{p}}$. SLAC experiments use an electron beam and cover a region of small Q^2, large x_{bj} with high statistics [204]. NMC, BCDMS, and E665 use a muon beam. BCDMS covers a region of large Q^2, large x_{bj} with high statistics [40]. NMC covers a region of lower x_{bj} than BCDMS with high statistics and does not extend to as large a value of Q^2 [13]. E665 covers a region of much lower x_{bj} and somewhat lower Q^2 in the 1990 data set upon which this thesis is based. E665 has relatively lower event statistics than the other experiments. In the 1987-88 data set, E665 covered even lower values of x_{bj} and Q^2 because the target was in a different location, but the event statistics in that data set were limited compared to the 1990 and 1991 data sets [170].

It is this region of very low x_{bj} which this thesis treats that is of particular interest. While the $F_2^{\mathrm{n}}/F_2^{\mathrm{p}}$ ratio has been well measured in the region $x_{bj} > 0.002$ by NMC, BCDMS, and SLAC experiments, the region $x_{bj} < 0.002$ has not been explored with inelastic scattering before. Yet in a number of contemporary results, the behavior of the $F_2^{\mathrm{n}}/F_2^{\mathrm{p}}$ ratio as $x_{bj} \to 0$ is crucial. The surprising results from the measurement of the Gottfried Integral by NMC [18, 20], for instance, depend explicitly on the evaluation of an integral similar in form to:

$$I_{\mathrm{G}}(x_0) \approx 2\int_{x_0}^{1} \frac{dx}{x}\left(\left(1-\frac{F_2^{\mathrm{n}}(x)}{F_2^{\mathrm{p}}(x)}\right) f(x)\right) \tag{1.10}$$

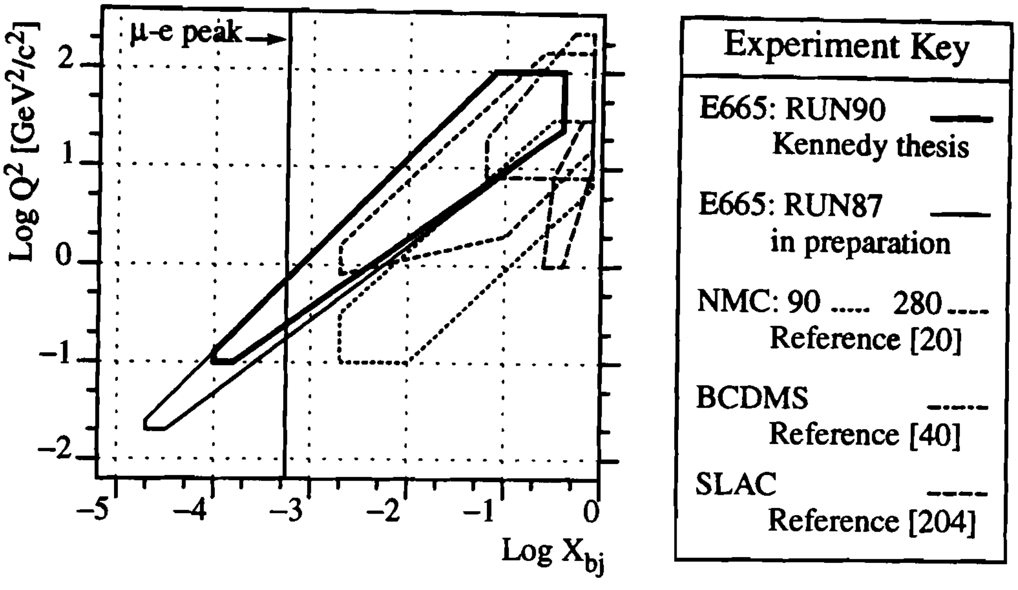

Figure 1.4: Kinematic regions covered by recent inelastic scattering experiments

where $f(x)$ is a structure function. The measure of the integral, dx/x, makes the result generally very sensitive to the behavior of the F_2^n/F_2^p ratio in the very small x_{bj} region. While E665 does not have the event statistics that these other experiments have, it can explore a region of x_{bj} to which some physics calculations are quite sensitive.

1.8 Summary

This thesis describes a measurement of the inelastic cross section of the deuteron relative to that of the proton. This measurement is then used to compare the structure of the neutron to that of the proton by extracting the ratio of the structure function F_2 for the neutron to that for the proton. The measurement extends the respective world data set to lower values of the kinematic variable x_{bj} and low values of Q^2 where the QCD-enhanced Quark-Parton model predicts that nucleon structure is dominated by the interactions of virtual quark-anti-quark pairs and gluons. This region is especially interesting since it involves some of the long-range dynamics that are not yet calculable from the fundamental theory of quark-quark interactions, Quantum Chromodynamics.

Chapter 2

Apparatus

> *Detection is, or ought to be, an exact science, and should be treated in the same cold and unemotional manner. You have attempted to tinge it with romanticism, which produces much the same effect as if you worked a love-story or an elopement into the fifth proposition of Euclid.*
>
> — Sherlock Holmes

Sir Arthur Conan Doyle, *The Sign of Four* (1890)

2.1 General Overview of the Experiment

This chapter describes the apparatus that gathered the data used in this study. Although the E665 apparatus has been described in detail in Reference [3], significant changes have been made to some parts of the apparatus since the publication of that article. For example, the targets used are now changed on a spill-by-spill basis to reduce the effect of time-dependent systematics. The streamer chamber used in the past has been removed. Drift chambers have been installed in the target region to greatly improve vertex resolution. Several new scattered muon triggers have been implemented. A new wall of scintillator has been installed upstream of the hadron absorber to improve the rates and time resolutions of several of the scattered muon triggers. In this chapter, emphasis is placed on the description of the new pieces of apparatus that are relevant to this analysis. For other items, the reader is referred to the appropriate documentation for details.

2.1.1 Introduction to E665

The Fermilab Experiment E665 collaboration consists of over 95 professors, research scientists, and graduate students from 18 institutions in the United States, Germany, and Poland[1]. The goals of E665 are to study hadron production and to measure nucleon structure functions with Inelastic Muon Scattering using a variety of targets. Formally proposed [90] in 1983, E665 first received muon beam in 1985, and first took publishable data in 1987.

The data sets recorded at E665 are labelled according to the year in which the data-taking began. The data set gathered from June 1987 to February 1988 is referred to as the RUN87 data set. The data set acquired from February 1990 to August 1990 is the RUN90 data set. The data set taken from June 1991 to January 1992 is called the RUN91 data set. This thesis uses two samples of the RUN90 data listed in Table 2.1 on page 14.

2.1.2 E665 Coordinate System

Global Cartesian Coordinates

The global coordinate system used by E665 is a right-handed cartesian system with the X-axis defined along the nominal beam path. In reference to the outside

---

[1] **Appendix A contains a complete author list for E665.**

Table 2.1: RUN90 data runs

Description of Period	Begin of Period Run	Tape	Date	End of Period Run	Tape	Date
RUN90	12071	WD6199	11-Jun-90	13267	WD6675	27-Aug-90
Sample I	12884	WD6514	08-Aug-90	12981	WD6563	13-Aug-90
Sample II	13195	WD6633	22-Aug-90	13267	WD6675	27-Aug-90

world, the X-axis runs close to Fermilab site north-south with X increasing towards north. The Y-axis is defined to run parallel to the experiment floor with Y increasing towards Fermilab site west. The Z-axis corresponds to altitude with Z increasing with increasing altitude. The center of this coordinate system is nominally defined to be the center of the Chicago Cyclotron Magnet.

In the context of particle track reconstruction, the X-Y plane is referred to as the bend view since nearly all bending of tracks due to magnetic fields used in E665 is in this plane. The X-Z plane is referred to as the non-bend view. This usage is approximate, however, since inhomogeneities in the magnetic fields do lead to some bending of tracks in the non-bend view [33].

Scattering Angles

Two angles are defined to describe a scattering event. The polar angle θ_{scat} measures the deflection of a scattered muon relative to the incoming muon. The range of θ_{scat} is $[0, \pi)$. The azimuthal angle ϕ describes the orientation of the event plane defined by the incoming and scattered muon. The orientation is given by the component of the scattered muon momentum three-vector normal to the incoming muon momentum three-vector. The origin of ϕ is the Y-axis, and ϕ increases toward the Z-axis. The range of ϕ is $[0, 2\pi)$.

Local Detector Coordinates

Local coordinate systems are frequently used to describe the orientation of elements in a detector package. The local coordinate system of each detector in E665 is defined in reference to a spatial vector $\vec{\Theta}$ which lies in the plane of the wire chamber or scintillator array and is perpendicular to the direction of the measuring elements. The vector $\vec{\Theta}$ describes the spatial coordinate that the detector measures. The orientation of $\vec{\Theta}$ is described, in radians, by the rotation angles (α, β, γ) about the X axis and two other axes defined differently for each detector package, respectively.

Detectors are also described, in degree units, by the rotation angle θ about their normal. For detectors normal to the beam path this angle is given by $\theta = 90° - \alpha$. The angle θ increases with clockwise rotations, as seen when viewed looking downstream. Chambers measuring the Y coordinate are called Y chambers and have $\theta = 0°$. Those measuring Z are called Z chambers and have $\theta = 90°$. Those with $-90° < \theta < 0°$ are called V chambers. Those with $0° < \theta < 90°$ are called U chambers.

2.2 The Muon Beam

2.2.1 The Tevatron

The Tevatron is located at Fermi National Accelerator Laboratory in Batavia, Illinois. It is a dual purpose synchrotron measuring 2.0 km in diameter [140]. The Tevatron is operated as either a 900 GeV/c proton on 900 GeV/c anti-proton collider or as an 800 GeV/c proton accelerator for fixed target experiments. The two modes are mutually exclusive. In fixed target mode, the Tevatron provides protons to experiments in 20 second long spills occurring every 59 seconds. The 53 MHz radio frequency signal used to accelerate the protons in the Tevatron forces a discrete time structure on the proton beam. A separate signal having the same frequency as the accelerator "RF", also colloquially called "RF", is made available to experiments for precision timing.

2.2.2 The Muon Beamline

The muon beam used by E665 was a tertiary beam generated from the 800 GeV/c proton beam delivered by the Tevatron [143]. This proton beam was extracted from the Tevatron and steered into the New Muon (NM) beamline, shown in Figure 2.1 on page 16, during a beam spill. In a typical spill, about 4×10^{12} protons were directed into the NM beamline. The protons were focussed on a 48.5 cm long beryllium target. Collisions between the protons and this target produced a number of secondary particles, most of which were pions and kaons carrying a fraction of the original proton momentum. The protons that did not interact were steered into beam dumps. The secondaries were momentum selected and steered into the 1.1 km long Decay FODO beamline[2] in which a small fraction (for example, roughly

---

[2] FODO is an acronym referring to a collection of magnets containing a (F)ocussing quadrapole, a zero-gradient(O) space or magnet, a (D)efocussing quadrupole magnet, and a zero-gradient(O) space or magnet.

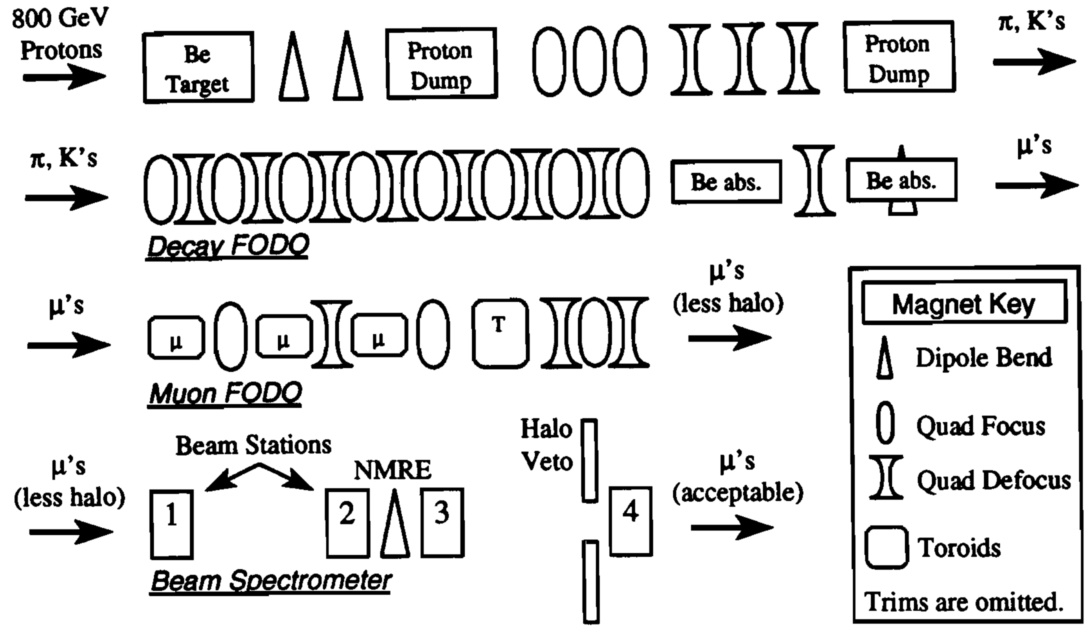

Figure 2.1: The NM Muon Beamline

5% of 800 GeV pions) decayed into muons and neutrinos. At the end of the Decay FODO, 11 m of beryllium was used to degrade any undecayed mesons which were then steered out of the beamline. This left a nearly pure muon beam (ignoring the remaining neutrinos). The fraction[3] of protons entering the muon beamline that were converted into usable muons entering the experiment hall ranged from 5×10^{-6} to 10×10^{-6}, depending on the tuning of the muon beamline.

The muons were steered into the 366 m long Muon FODO to improve the spatial distribution of the muon beam. Throughout RUN90, E665 used a relatively higher momentum tune, with mean momentum close to 475 GeV/c after cuts imposed by trigger logic, and positively charged muons. The spatial distribution of the muons was improved by pushing muons which were not going to hit the experiment target, called "halo" muons, further away from the nominal beam path. The halo muons could have been mistaken by the experiment for deep-inelastically scattered muons. While these undesirable muons could be rejected by detectors near the beam, the high rate of "halo" lying very close to the acceptable beam overwhelmed the abilities of the trigger electronics. Inefficiency in these counters to even a small fraction of halo could cause the recording of many useless events, many more than those involving deep-inelastic scattering. To help reduce this effect, toroidal magnets were used to deflect the halo radially away from the beam. The net effect of the toroids was that

---

[3] This was given by the beamline scaler ratio NMSBM/NM2SEM.

the ratio of the number of halo muons within a 3 m × 7 m area about the beam to the number of beam muons dropped from 1:1 to 1:2 [3]. About half of the remaining halo was located within 20 cm of the beam axis, and the other half was spread out across the 3 m × 7 m area over which halo is detected.

The muon beam inherited the time structure of the proton beam imposed by the accelerator RF. The frequency of the accelerator RF signal during a spill was about 53.1 MHz. Thus, the separation between muons was an integral multiple of the 18.8 ns cycle with an uncertainty of less than 1 ns per cycle [3]. The fact that muons were localized around a certain phase of an RF cycle was often represented by saying that the muons were in temporal features called "buckets" whose width was less than 1 ns. Provided that the number of muons generated in a spill was small compared to the number of buckets in a spill and that the buckets had an equal probability of containing a muon, the distribution of muons in buckets was well described by a Poisson distribution [45]. Generally, few buckets contained a muon, and very few contained more than one muon. At the highest beam intensities, however, the number of buckets that contained two or more muons could reach 20%. The design of the beamline and related electronics took this into account.

The purity of the muon beam was checked during a special run at the end of RUN87 [59]. The interaction rate was measured as a function of the length of the beryllium absorber at the end of the Decay FODO section of the NM beamline. The hadron contamination of the muon beam was determined to be at the level of $(0.9 \pm 0.1) \times 10^{-6}$ hadrons per muon for the standard length 11 m beryllium absorber.

The state of the muon beam was monitored in a number of ways. Segmented wire ionization chambers, SWICs, along the beamline provided a particle density profile integrated over time increments throughout a beam spill. The EPICURE system gave information on magnet settings, beamstop status, and beamline scaler counts [158]. It also provided a facility to record this information to tape for later use. During the data-taking, some events were sent to a beam reconstruction program in order to check the momentum profile of the accepted beam. Various ratios, such as the muon-to-proton transmission ratio and the ratio of the total muon beam count to the acceptable muon beam count, were tracked continuously to check for beamline tuning problems.

2.2.3 The Beam Spectrometer

Before entering the experiment hall, the muon beam traversed the 55.4 m long Beam Spectrometer, show in Figure 2.1 on page 16. Here, the location of the beam muon was measured by four stations of multi-wire proportional chambers (MWPCs)

Table 2.2: Beam Spectrometer

Magnets

Name	Type	Aperture $Z \times Y$ [m]	P_t kick [GeV/c]	Max B_z [kGauss]	Superconducting?
NMRE	Dipole	0.10×0.10	-1.541	-8.243	No

Wire Chambers

Name	Type	Aperture $Z \times Y$ [m]	Number of Planes and Orientation	Wire Spacing	Gas Used
PBT	MWPC	0.06×0.06	$4(U, Z, Y; V, Z', Y')$	1 mm	Ar-Ethane

Scintillation Counters

Name	Thickness	Aperture $Z \times Y$ [m]	Number of Planes and Orientation	Counters per Plane	Material Used
SBT	0.3 cm	0.18×0.14	$3(Z, Y)$, $1Y$	13	NE110
SVJ	1.0 cm	0.5×0.5	3 [hole]	2	NE110
SVW	2.5 cm	3.0×7.0	$1Y$ in 2 banks [hole]	14	NE110

and scintillators, two stations upstream of a momentum analysis magnet and two downstream [155]. The use of the Beam Spectometer in the measurement of the incoming muon momentum is described in Section 3.3.4. The Beam Spectrometer also provided a signal for the scattered muon trigger logic indicating that a beam muon has entered the experiment. The use of the Beam Spectrometer in the scattered muon triggers is discussed in Section 2.6. Table 2.2 on page 18 summarizes the characteristics of the equipment in the Beam Spectrometer.

NMRE

NMRE was a Fermilab model WGNT-4 warm dipole magnet [208], used by the Beam Spectrometer to bend the positively-charged muon beam to the east. The effective P_t kick of NMRE was measured[4] to be 1.541 GeV/c when the magnet was operated at the nominal current setting of 3350 amps [194]. The angle of deflection for a 475 GeV/c beam muon was about 3 mrad.

---

[4] See Section 3.3.4 for a discussion of this measurement.

PBT

The Beam Spectrometer wire chambers, referred to as the PBT detector, were constructed according to a standard Fermilab design for beamline wire chambers [87]. The detector consisted of 4 packages, one at each beam station. The wire spacing was 1 mm. Each package was made up of 6 detector planes that were organized into two packets, each with a Y, a Z, and a tilted plane. The second set of Y and Z planes in each package were nominally offset from the first by half their wirespacing to improve the effective spatial resolution. The sensitive area of the Y and Z planes was 12.8 cm × 12.8 cm and that of the U and V planes was 6.4 cm × 6.4 cm.

SBT

The SBT detector was a set of scintillator hodoscopes which provided better temporal resolution, but poorer spatial resolution, on the measurement of the incoming muon position than the PBT detector. Each beam station consisted of a Y and a Z plane, except for station 2 which had only a Y plane. Each plane had thirteen counters. All but one plane contained counters that were graded in width to evenly distribute the nominal incident beam rate per counter. Plane $1Z$ had counters of equal size to improve the SAT trigger acceptance. In order to improve the understanding of the beam timing for RUN90, signals from plane $4Y$ were sent to LeCroy[5] 2228 and 2226A TDC modules.

SVJ

Beam stations 2, 3, and 4 contained a set of scintillators, SVJ, to detect halo very close to the beam where the halo rate was highest. Each SVJ plane consisted of 2 counters. Notches were cut out of each counter to form an aperture through which beam passed.

SVW

A wall of 28 large scintillators, called SVW, was used to detect halo over a wider area [156]. The counters were mounted in an upper and lower bank of 14 counters each to form a 3 m by 7 m detector wall. This wall had a 25 cm by 25 cm central aperture through which beam passed. The SVJ and SVW counters were located sufficiently far away from the experiment target that photons from an interaction in the target could not veto the generating event [164].

---

[5] LeCroy: LeCroy Research Systems Corp.

The SVW counter at the lower east edge of the beam aperture became completely inefficient shortly after data-taking began in RUN90 [142]. This was discovered, unfortunately, well into RUN90. The dead SVW counter affected the WAM trigger in particular since a halo muon passing through the dead SVW counter, in coincidence with an acceptable unscattered beam muon, would appear to be an acceptable scattered muon event to the trigger. Other triggers were not so affected since they contained veto elements that explicitly rejected events with unscattered beam muons.

2.2.4 The Beam Profile

Figure 2.2 on page 21 demonstrates the spatial distribution of the beam measured in the middle of the liquid targets used in this analysis. The beam distribution shown is a random sampling of all beam entering the experiment, limited by the acceptance of the beam tracking chambers. It was approximately 12 cm wide in Y and 5 cm wide in Z. Figure 2.3 on page 22 shows the energy distribution in the beam. The incoming muons varied widely in energy with a mean beam energy of about 450 GeV.

2.3 Experiment Targets

A new target system, installed after the RUN87 data-taking, was used for RUN90 [157, 133]. The system, as is shown in Figure 2.4 on page 22, consisted of a motorized stand capable of holding three identical cryogenic liquid targets and a number of solid disc targets. The changing of targets once every spill and the equivalence of the cryogenic target vessels are crucial points in this analysis since the effect of time-dependent systematic errors is greatly reduced in the measurement of the cross section ratio.

The target system was controlled by a software program running on a DEC[6] Vax 11-780 [132]. Though manual control was possible, throughout all of the physics data-taking the program automatically changed the targets according to the content of a particular text file, called the target cycle list [123]. The automatic target changing process itself is referred to as target cycling. The system included a means of recording in the data record for each event which target was in the beam. Infrequently, the target system did not have a target positioned correctly during an event[123]. This condition was signalled by the target readout system by a distinct error code, allowing events occurring on the undefined target to be eliminated from analysis. Also, a video

---

[6] DEC: Digital Equipment Corporation

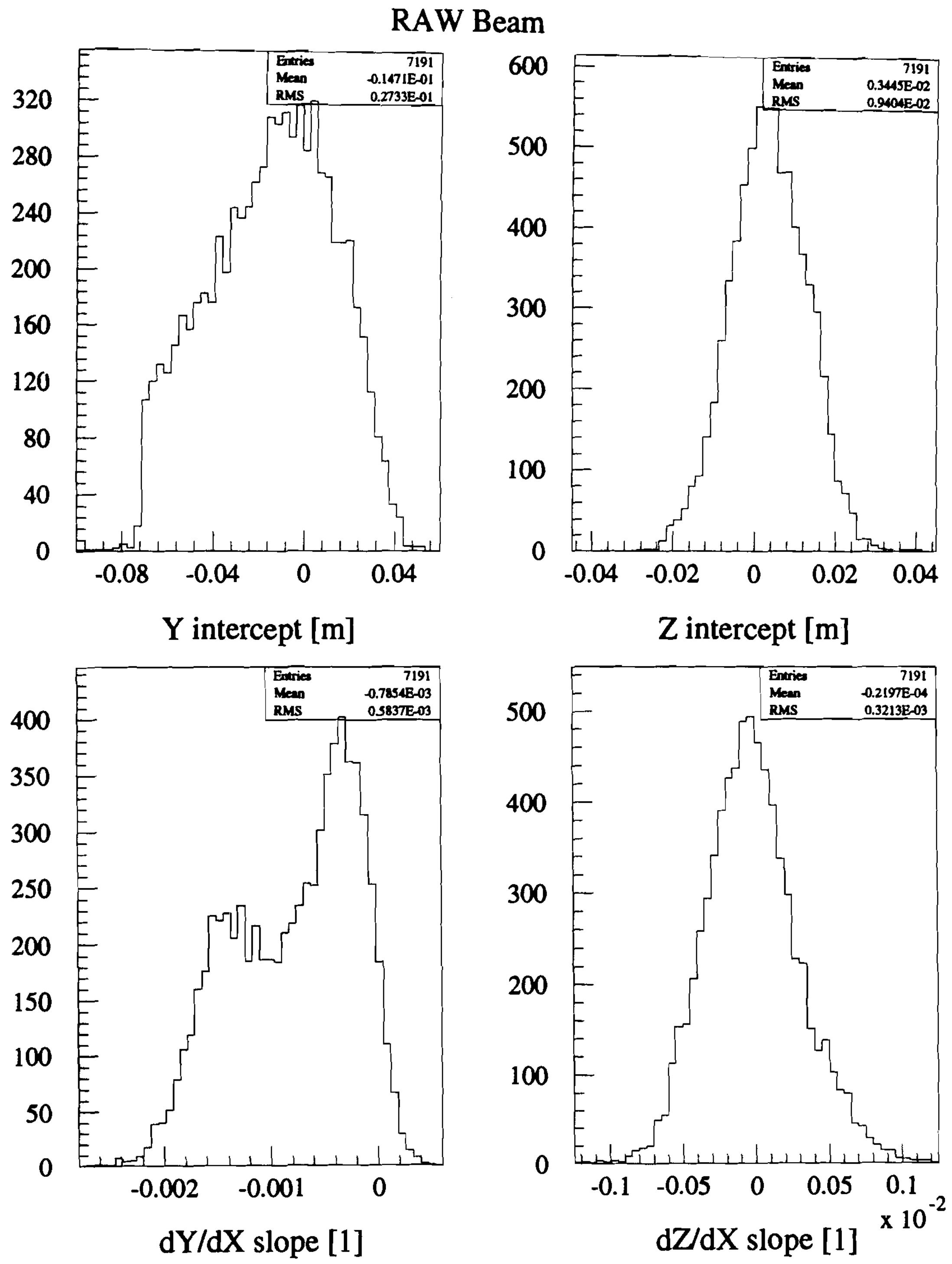

Figure 2.2: Spatial distribution of raw beam at mid-target

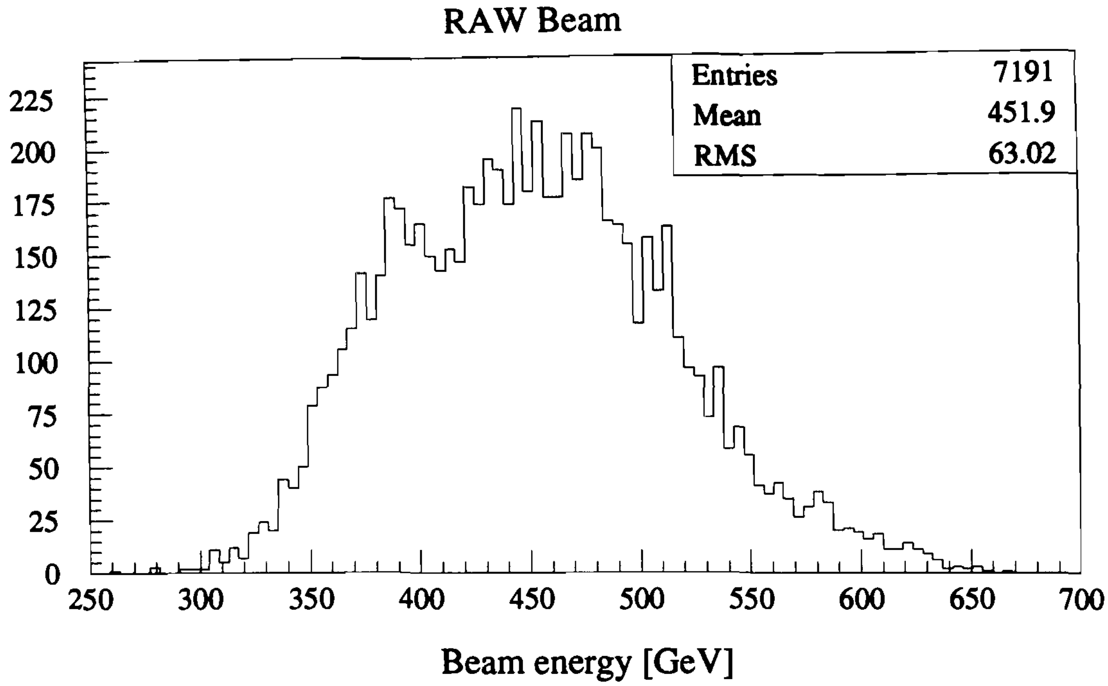

Figure 2.3: Energy distribution of raw beam

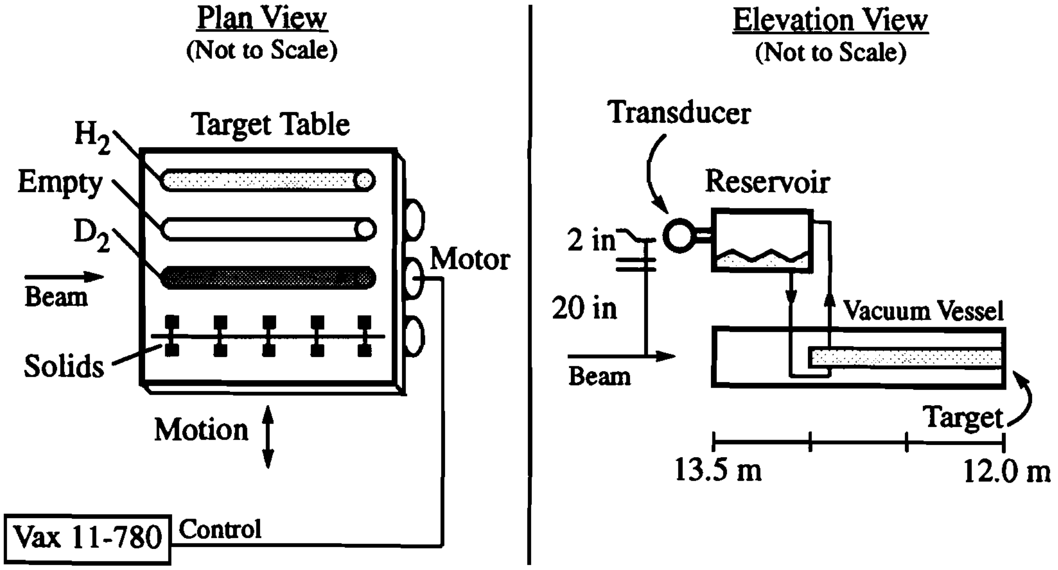

Figure 2.4: The E665 target stand and liquid target detail

camera was trained on the apparatus allowing the E665 shift crew to view the target stand operation.

2.3.1 Liquid Targets

Three, essentially identical, cryogenic targets were used. One contained liquid hydrogen, one liquid deuterium, and the last was left evacuated. Each target was a cylinder 1.00 m long and 0.100 m in diameter. During the data sample used in this analysis, all liquid targets were operational and automatic cycling of the targets was enabled. The saturated vapor pressure in each of the liquid reservoirs was monitored 2 inches above the liquid surface by a pressure-to-voltage transducer, and was recorded once an hour throughout RUN90 by the Fermilab Cryogenics Group monitoring system.

2.3.2 Solid Targets

Solid targets were mounted in disc holders. Seven groups of five holders each were mounted radially about a rotating axle. Any one group of holders could be rotated into the beam at a time. A set of lead targets, one set each of carbon targets at two thicknesses, a set of copper and carbon targets, a set of calcium targets, and an empty target holder set were used. Each calcium target was sealed in a stainless steel can to prevent interaction of the calcium with water in the atmosphere. In addition to a set of empty disk holders, a single empty stainless steel can was used as a target to determine the interaction rate on the stainless steel can. This thesis does not use data taken on any of these solid targets.

2.4 Charged Particle Tracking

E665 used an open geometry, double magnet spectrometer to detect particles over a broad range of momentum. The CERN Vertex Magnet, CVM, was a superconducting dipole magnet located immediately downstream of the target assembly. It and some associated detectors called the Vertex Spectrometer were used to analyze lower momentum particles. The Chicago Cyclotron Magnet, CCM, was also a superconducting magnet. It and some associated detectors called the Forward Spectrometer were used to analyze higher momentum particles. The CVM and CCM field integrals were arranged in a focussing condition, so that unscattered particles were focussed on the same spot on the Scattered Muon Detector, independent of their momentum over a broad range of momenta, as unscattered beam with the magnets turned off. Drift chambers and multi-wire proportional chambers were located along the beam axis from the CVM, through the CCM, and beyond to detect charged particles. A 3 m thick wall of steel and lead shot-filled shielding block, called the hadron absorber, was used to absorb all particles of interest except muons. Behind and immediately in front of the absorber was the Scattered Muon Detector which consisted of four stations of proportional tube planes and a number of scintillator planes. Between stations of the Scattered Muon Detector behind the absorber were concrete shielding walls to reduce the effects of electromagnetic interactions generated by a muon traversing the material upstream of a station.

2.4.1 Vertex Spectrometer

The Vertex Spectrometer detected particles as they traverse and emerge from the CVM magnet aperture. Its importance to this analysis is that it largely determined the resolution of the vertex position, especially along the beam axis. This directly influenced the measurement of the scattering angle and, therefore, of Q^2. It also was used to measure the momentum of low momentum particles that were swept out of the experiment before reaching the next analysis magnet.

CVM

The CERN Vertex Magnet, CVM, was originally used in the NA9 experiment at CERN in Geneva, Switzerland. Its nominal operating current was 5000.0 Amps. The current was monitored visually by the Cryogenics shift crew and, via a video camera, by the experiment shift crew. The field map used to represent the CVM magnetic field in the RUN90 analysis was the original field map from NA9 [138]. Although a fairly substantial amount of ferromagnetic material had been removed from the vicinity of the CVM, such as the streamer chamber used in RUN87, it has been shown that the changes to the CVM magnetic field were small enough not to affect the event reconstruction process [172].

VDC

In order to improve the vertex resolution, the Vertex Drift Chambers were installed for RUN90 [180, 184] in the CVM aperture immediately downstream of the target. For RUN90, the detector consisted of 13 planes[7] which were made in several

---

[7] Three additional planes were installed after RUN90 between the target and the thirteen planes described here.

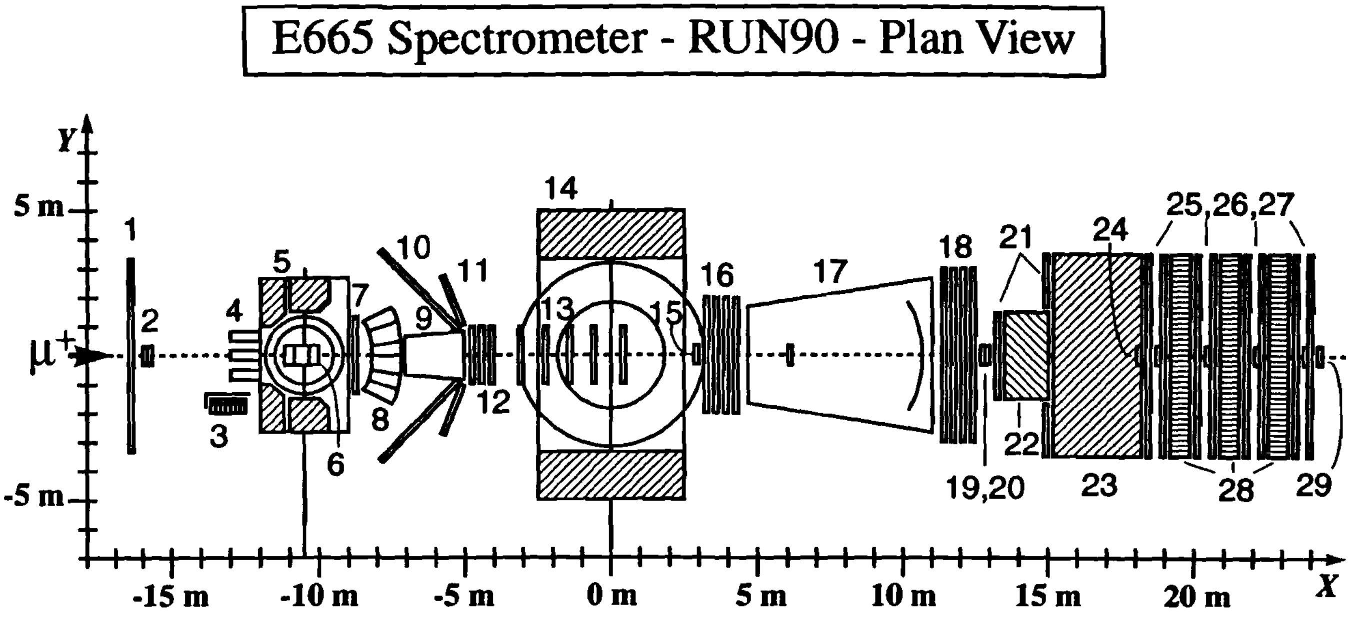

1) SVW: Veto Wall
2) Beam Station 4: PBT4, SBT4, SVJ3
3) SNC: Slow Neutron Detector
4) Liquid Targets (Solids not shown)
5) CERN Vertex Magnet
6) VDC: Vertex Drift Chambers
7) PCV: 3m x 1m MWPC
8) C0: Threshold Cerenkov Counter
9) C1: Threshold Cerenkov Counter
10) TOF: Time-of-Flight Arrays
11) PTA: Proportional Tubes
12) PC: 2m x 2m MWPC
13) PCF: 2m x 1m MWPC
14) Chicago Cyclotron Magnet
15) PSC: 0.1m x 0.1m MWPC
16) DC1-4: 4m x 2m Drift Chambers
17) Ring Imaging Cerenkov Counter
18) DC5-8: 6m x 2m Drift Chambers
19) SSA: Scintillator Hodoscope
20) PSA: 0.1m x 0.1m MWPC
21) SUM: Upstream Trigger Wall
22) CAL: Electromagnetic Calorimeter
23) Hadron Absorber
24) SVS: Scintillator Hodoscope
25) PTM: Proportional Tubes
26) SMS: Scintillator Hodoscope
27) SPM: Scattered Muon Wall
28) Shielding Block Wall
29) PHI: RF Sync Hodoscope

Figure 2.5: Plan view of the E665 Spectrometer

Table 2.3: Vertex Spectrometer

Magnets					
Name	Type	Aperture $Z \times Y$ [m]	P_t kick [GeV/c]	Max B_z [kGauss]	Superconducting?
CVM	Dipole	1.0×1.4	+2.60	+15.0	Yes

Wire Chambers					
Name	Type	Aperture $Z \times Y$ [m]	Number of Planes and Orientation	Wire Spacing	Gas Used
VDC	drift	0.7×1.2	13 [various]	1.0 cm	Ar-Ethane
PCV	MWPC	1.0×2.8	$Y, 2U; 2V, Z$	2.0 mm	Ar-Isobutane
PTA	prop tube	2.0×2.0	(Y, Z, V, U) in 2 wings	1.27 cm	Ar-Ethane
PC	MWPC	2.0×2.0	$3(Y, Z, V, U)$	3.0 mm	Ar-Isobutane

different designs, labelled A (wide angle), B (beam), and Z (multi-section Z view). The planes were arranged as follows, in order of increasing X-coordinate: a B-U, B-V, Z-Z, A-V, A-U, Z-Z, B-U, Z-Z, A-V, A-U, Z-Z, B-U, and a B-V view.

The type A design contained 14 cells each 7.4 cm in width, and had an 18 cm dead spot through which the unscattered muons pass. Type B planes contained 16 cells each 1.3 inches in width and had no dead spot. The type B planes covered the dead spots in type A planes. Type Z planes in the central (beam) region contained 8 cells each 1.3 cm in width. In the wide angle region they contained 8 cells each 7.0 cm in width. Including cell edge effects, the coverage of the entire package was about 65 cm × 100 cm. The coverage of the B type planes was 21 cm in the Y and tilt views, 10.5 cm in the Z view. The VDC detector was digitized by LeCroy 1879 FASTBUS multi-hit TDCs. The TDCs were situated in a FASTBUS sub-system that was practically identical to, but separate from, that which was used by the electromagnetic calorimeter detector [183].

Calibration of the Vertex Drift Chambers was performed [172], resulting in a spatial resolution of the chambers that varies from 150 μm to 250 μm according to the drift cell size and other factors.

PCV

The PCV detector [93, 12] consisted of six MWPC planes including a Y, a U (+45°), a U' (+18.5°), a V (−45°), a V' (−18.5°), and a second Y view. The PCV detector had a sensitive area of 2.8 m × 1.0 m. The wire separation was 2 mm.

PC

The PC detector [144, 169] consisted of three packages of four MWPC planes each. Each package contained a Y, a Z, a U (+28.07°), and a V (−28.07°) view. The sensitive area of the chambers was 2 m × 2 m. The anode wire spacing was 3 mm. Note that in some E665 literature the PC detector is called the PCN detector.

PTA

The PTA detector consisted of two wings, one on each side of the nominal beam path [22, 176, 24]. Each wing was made up of four proportional tube planes including a Y, a Z, a U (+45°), and a V (−45°) view. The planes were made of the same material as that used in the PTM detector described in Section 2.4.3.

2.4.2 Forward Spectrometer

The Forward Spectrometer detected particles as they travel through and beyond the CCM magnet. Its importance to this analysis is that it largely determined the resolution of the scattered muon energy. This directly influenced the error in the measurement of ν.

CCM

The Chicago Cyclotron Magnet, CCM, was originally used as a cyclotron magnet at the University of Chicago, Chicago, Illinois. Its nominal operating current was 750.0 Amps. The current was monitored visually by the Cryogenics shift crew and, via a video camera, by the experiment shift crew. The field map used to represent the CCM magnetic field was derived from measurements made before the magnet was installed in the New Muon Lab building [135]. Since then several partial remeasurements have been made and have shown the original measurement to be acceptable [136].

PCF

The PCF detector was a set of five packages of three MWPC planes each [47, 46], including a Z, a U (+15°) and a V (−15°) view. The total sensitive area of the detector was 1 m × 2 m. The wire spacing was 2 mm. The size of the PCF

Table 2.4: Forward Spectrometer

Magnets					
Name	Type	Aperture $Z \times Y$ [m]	P_t kick [GeV/c]	Max B_z [kGauss]	Superconducting?
CCM	Dipole	1.2 × 3.0	−4.06	−13.2	Yes

Wire Chambers					
Name	Type	Aperture $Z \times Y$ [m]	Number of Planes and Orientation	Wire Spacing	Gas Used
PCF	MWPC	1.0 × 2.0	$5(U, V, Z)$	2.0 mm	Ar-CO_2-Freon
PSC	MWPC	0.15 × 0.15	$2Z, 2Y; 2U, 2V$	1.0 mm	Ar-CO_2-Freon
DC1-4	Drift	2.0 × 4.0	$4Z, 2U, 2V$ [hole]	2.0 in	Ar-Ethane
DC5-8	Drift	2.0 × 6.0	$4Z, 2U, 2V$ [hole]	2.0 in	Ar-Ethane
PSA	MWPC	0.13 × 0.13	$2Z, 2Y; 2U, 2V$	1.0 mm	Ar-Ethane

detector, limited by the CCM aperture, was one of the major limitations on the geometric acceptance of the experiment.

PSC

The PSC detector was installed for RUN90. It consisted of a single package of a newly developed low mass design [53]. The package consisted of a Y, a half cell staggered Y', a Z, a half cell staggered Z', a U (+45°), a half cell staggered U' (+45°), a V (−45°), and a half cell staggered V' (−45°) view. The detector covered 15.3 cm × 15.3 cm and had a 1 mm wire spacing. Signals from the detector were amplified and discriminated by Nanometrics[8] N277 modules. The resulting digital signals were delayed in LeCroy 2731A modules and read out with a PCOS III MWPC Readout System. The PSC improved small angle tracking by providing a space-point near the maximum lateral displacement of charged tracks in the CCM. It was also intended to cover the deadened beam region in the DC1-4 detector.

DC

The DC detector consisted of eight packages of large aperture drift chambers [150]. The detector was divided into two distinct parts labelled DC1-4 and DC5-8. DC1-4 had a sensitive area of 2 m × 4 m, while DC5-8 had a sensitive area of 2 m × 6 m. Each part consisted of a Z, a half cell staggered Z', a U (+5.76°), a

---

[8] Nanometrics: Nanometrics Systems, Inc.

half cell staggered U' (+5.76°), a V (−5.76°), a half cell staggered V' (−5.76°) a second Z, a second half cell staggered Z' view. The drift cells were 2.0 inches wide, though the effective width was halved by the staggering of the planes. Since the DC could not handle the signal rate that unscattered muons generated, all planes had a deadened region through which the unscattered beam passed. This dead region, measuring about 10 cm × 5 cm, was covered by the PSC and PSA detectors. The DC information was read out by a multi-hit time encoder system, or MUTES for short [134]. The long horizontal wires in the Z and Z' views were cut in half and read out separately.

Calibration of the Drift Chambers has been performed [149]. The calibration method has been described elsewhere [146, 147]. The spatial resolution of the DC for the data used in this thesis was less than 400 μm. With improved calibration and alignment specific to RUN90, the detector is expected to reach the design goal resolution of about 250 μm that was achieved in RUN87.

PSA

The PSA detector [1] was used for small angle tracking in the dead region of the DC5-8. It consisted of a single package of the same standard Fermilab beamline MWPC as the PBT beam chambers [87], although the individual planes in a package were arranged differently. The package consisted of a Y, a half cell staggered Y', a Z, a half cell staggered Z', a U (+45°), a half cell staggered U' (+45°), a V (−45°), and a half cell staggered V' (−45°) view. The wire spacing was 1 mm.

The PSA detector suffered a number of partial or complete failures during RUN90 [102, 103]. These were linked to the higher HV setting used compared to the other chambers of similar design. Runs in which the PSA produced no data have been removed from the analysis.

2.4.3 Scattered Muon Detector

A major ingredient in Inelastic Muon Scattering is the unambiguous identification of the scattered muon. While the Forward Spectrometer was used to measure the momentum of charged-particle tracks, the Scattered Muon Detector was used to identify which of these tracks was a muon. Information from it was used by the scattered muon triggers to detect the passage of a scattered muon candidate through the experiment. It accomplished this by absorbing all hadrons, electrons, and photons in the hadron absorber. A number of detectors were then used for tracking and/or triggering on charged-particle tracks penetrating the absorber.

Table 2.5: Scattered Muon Detector

Wire Chambers					
Name	Type	Aperture $Z \times Y$ [m]	Number of Planes and Orientation	Wire Spacing	Gas Used
PTM	prop tube	3.6×7.2	$2(Y, Z)$ [hole]	12.7 mm	Ar-Ethane

Scintillation Counters					
Name	Thickness	Aperture $Z \times Y$ [m]	Number of Planes and Orientation	Counters per Plane	Material Used
SSA	1.27 cm	0.13×0.13	$1Z$	12	Bi404
SUM	2.54 cm	3.0×6.0	$2Y$ in 6 banks [hole]	5, 13	Pilot Y
SVS	2.54 cm	0.20×0.25	1 [various]	24	Pilot U
SMS	1.3 cm	0.2×0.2	$4(Y, Z)$	16	NE110
SPM	2.5 cm	3.0×7.0	$4Y$ in 2 banks [hole]	15	GS2030
PHI	1.27 cm	0.5×0.5	1 [various]	4	NE110

SSA

The SSA detector was installed for RUN90. This detector consisted of a single Z-view hodoscope of twelve scintillation counters [111]. The counters were coplanar with overlapping edges to eliminate cracks. The phototubes used were Hamamatsu[9] R1398. The signals were taken to LeCroy 4413 discriminators and LeCroy 2249 ADCs. The discriminated output went to the SAT trigger electronics and to LeCroy 1879 FASTBUS TDCs in the VDC read-out system. The SSA detector was used to add a veto element located upstream of the hadron absorber to the scattered muon definition in the SAT trigger.

SUM

The SUM detector was installed for RUN90 [166]. It consisted of a total of 96 counters arranged in two layers. Each layer consisted of an upper and lower bank. Each counter was 1.5 m tall, 31.8 cm wide, and overlapped its neighbors to each side by approximately 2.5 cm. The SUM detector was installed in three separate sections. The two outer wings consisted of five upper and five lower counters in each layer and were located on the east and west side of the electromagnetic calorimeter. The central section consisted of 13 upper and 13 lower counters in each layer and was located just upstream of the electromagnetic calorimeter. The central counters in the central wall section were drawn away from each other in the Z-coordinate to

---

[9] Hamamatsu: Hamamatsu Photonics K. K.

provide an aperture through which the unscattered beam passes. In addition, there were two counters in each layer in the central section that lay horizontally along the experiment zero-altitude line to define the sides of the SUM wall beam aperture.

The SUM counters were made of Pilot Y scintillator material [85]. Light was collected in Amperex[10] XP2020 (12 stage) photomultiplier tubes. The phototube signals were passively split, with one set going to LeCroy 1885 FASTBUS ADCs for digitization and one set going to LeCroy 4413 discriminators. The discriminated output was then sent to LeCroy 4448 latches and LeCroy 2228A TDCs, as well as to various scattered muon trigger processors.

The SUM wall was installed primarily to aid in the rejection of false triggers due to electromagnetic showers originating in the hadron absorber. A description of how the SUM wall was implemented in the trigger logic is given in Section 2.6.3.

SVS

The SVS detector was installed for RUN90 [165, 83]. It consisted of 24 coplanar counters with overlapping edges to eliminate cracks. The orientation of the counters varied, as is shown in Figure 2.6 on page 32. A 12 inch deep hole was drilled into the downstream face of the hadron absorber, and the hodoscope was placed in the hole flush against the absorber. The detector was approximately centered on the nominal position of unscattered beam at this X-position. The SVS hodoscope was used as a segmented fixed beam veto hodoscope. A description of how the SVS wall was implemented in the trigger logic is given in Section 2.6.3. The unusual orientation of the counters allowed different rectangular shapes to be used for the beam veto in the triggers by disabling various counters on the periphery of the hodoscope.

The SVS counters were made of Pilot U scintillator material [85]. Light was collected in Amperex XP2982 (11 stage) photomultiplier tubes. The phototube signals were passively split, with one set going to LeCroy 1885 FASTBUS ADCs for digitization and one set going to custom-built deadtime-less discriminators. The discriminated output was then sent to LeCroy 4448 latches and LeCroy 2228A TDCs, as well as to various scattered muon trigger processors.

A trade-off made in the design of the custom-built SVS discriminators to achieve deadtime-less operation led to the SVS counters producing variable width output signals. This resulted in the false vetoing of about 3% of the buckets trailing properly vetoed buckets [84]. The effect was independent of the target, and thus does not affect relative normalization.

---

[10] Amperex: Amperex Electronic Corp.

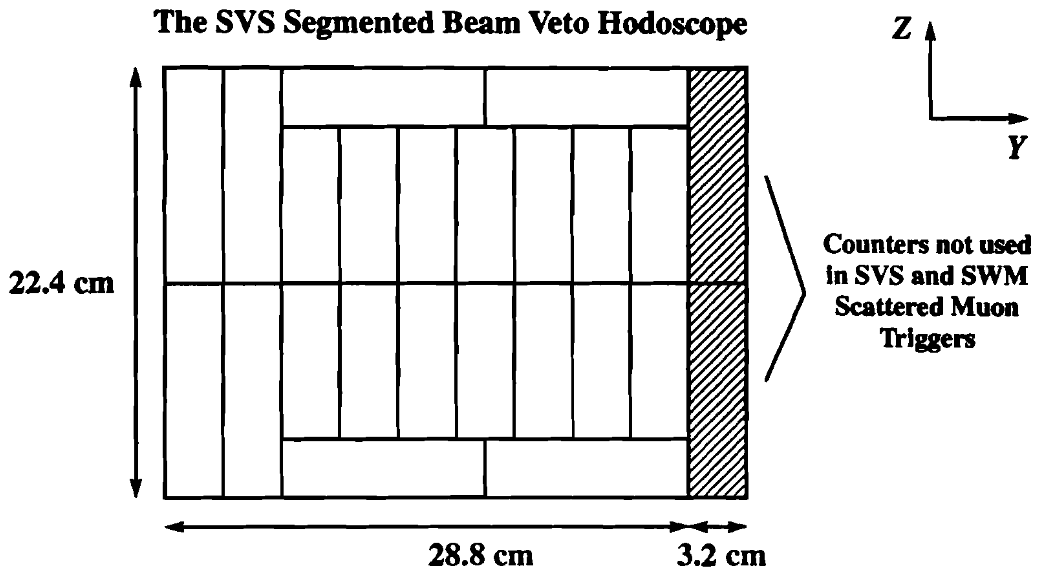

Figure 2.6: Downstream face of the SVS segmented beam veto hodoscope

PTM

The PTM detector provided the spatial measurement of the scattered muon track over most of the aperture of the Scattered Muon Detector. It was used in both event reconstruction and triggering. The PTM detector consisted of four stations of proportional tube planes [176, 24] made of extruded aluminum tube modules in a staggered cell array. Each station contained a Y view with 38 modules and a Z view with 19 modules. Each module contained a group of 15 cells divided into two rows offset by a half cell width, yielding an effective wire spacing is 12.7 mm. The active area of each plane was 3.6 m × 7.2 m. Each plane contained a deadened region since the detector cannot handle the high rate of unscattered beam muons.

SMS

The SMS detector provided fine spatial and time resolution measurement of the scattered muon in the deadened region of the PTM and the beam hole in the SPM. It, too, was used in both event reconstruction and triggering. Each detector package consisted of 16 scintillators in the Y view and 16 scintillators in the Z view. The inner 14 scintillators in a view were 1.32 cm wide by 21.6 cm long. The outer one scintillator on each side in a view was 1.96 cm wide by 21.6 cm long.

The SMS detector was one of several detectors I have directly supported in my role as a UCSD graduate student. Details on the implementation and support for the detector are in Appendix C.

SPM

The SPM detector provided the poorest spatial resolution measurement of the scattered muon track in the Scattered Muon Detector. It was primarily used in fast triggering since its time resolution of 30 ns was far better than that of the PTM detector. The SUM detector was used in coincidence with the SPM detector to form a combined detector capable of one bucket time resolution.

The SPM counters have been described in great detail elsewhere [179]. The detector was arranged in four walls of 30 counters. Each wall consisted of an upper and a lower bank of 15 counters each. There were several different size counters used, though most were 1.5 m tall and 0.5 m wide. The counters closest to the unscattered beam were shaped to provide an aperture through which the unscattered beam passed. The active area of each plane was 3.0 m × 7.0 m.

The SPM detector was one of several detectors I have directly supported in my role as a UCSD graduate student. A description of the use of the SPM in the Large Angle Triggers is given in Section 2.6.3. Details on the implementation and support for the detector, as well as the improvements to the detector made since the publication of the last description of the detector, are in Appendix C.

PHI

The PHI detector was used to provide a precision timing standard for the experiment. The timing of the passage of muons through the PHI detector was used to alter by fractions of a cycle the phase of the local RF oscillator used in triggering and detector gating. This is described in greater detail in Section 2.6.1. The PHI detector consisted of four 5.08 cm by 5.08 cm counters made of 1.27 cm thick NE110. Two RCA[11] 8575 and two Hamamatsu R329 phototubes were used to collect the light. The signals were discriminated and sent to the RF phase-locking electronics. Note that in some E665 literature the PHI detector is called the PLRF detector.

---

[11] RCA: RCA Tube Corporation

2.5 Particle Identification

One of the primary goals of the E665 experiment is to study the production of hadrons by deep-inelastic collisions between muons and target nuclei. Much of the hadron analysis depends on knowing the type of hadron produced. For the most part, this is irrelevant to the measurement of Inelastic Muon Scattering cross sections. Information from the electromagnetic calorimeter, however, proved to be crucial in identifying radiative background and muon-electron elastic scattering events in order to eliminate them from the analysis.

2.5.1 Electromagnetic Calorimeter

The E665 Electromagnetic Calorimeter (CAL) has been described in great detail elsewhere [152, 163, 175, 189]. The CAL had a 3 m × 3 m active area and was composed of twenty 5 mm thick lead planes (one radiation length each) interspersed with Iarocci proportional tube planes [108]. The twenty proportional tube planes were arranged in alternate Y and Z views. These planes consisted of modules, each containing eight wires at 1 cm spacing. The tubes were read out in pairs, leading to the term "bitubes" that is common in the CAL documentation. The cathode planes were split into 1188 pads whose individual size varies from 4 cm × 4 cm in the central region to 16 cm × 16 cm in the outer regions. The bi-tube and pad read-out was performed by a FASTBUS sub-system using LeCroy 1885 ADCs. In order to accommodate the SUM detector, the CAL detector was moved 20 cm downstream from its RUN87 location. The calibration of the electromagnetic calorimeter has been described in detail elsewhere [175, 189].

2.5.2 Other Detectors

The remaining E665 particle identification detectors were not used in this analysis. They have been described elsewhere. This includes the C0 Cerenkov detector [54], the C1 Cerenkov detector [199], the RICH Cerenkov detector [70], the Time-of-Flight detector [82, 76], and the SNC liquid scintillator neutron detector [106].

2.6 Triggering

E665 used two levels of trigger logic, differentiated by their timing with respect to the passage of the scattered muon. The Level One Trigger was produced as soon after the scattered muon passage as possible. This trigger was used to generate the gates and strobes for the detector readout electronics. Since it must be generated so quickly, it used information from scintillators to form a relatively broad definition, in terms of angular acceptance, of an acceptable muon scattering event. The Level One Trigger was expected to accept $< 1 \times 10^{-2}$ of all incoming muons. The Level Two Trigger, if one was generated, occurred some 200 ns after the Level One Trigger. This allowed the Level Two Trigger electronics time to gather and process hundreds of MWPC or proportional tube signals. The Level Two Trigger used a much stricter definition of an acceptable muon scatter. The Level Two Trigger initiated data acquisition; the lack of it initiated equipment reset. The Level Two Trigger was expected to accept $< 1 \times 10^{-5}$ of all incoming muons. A more detailed description of the trigger gating and timing is given in Appendix D.

2.6.1 Phase-Locked RF

All the E665 scattered muon triggers contained the Phase-Locked RF as a timing standard relative to the passage of a muon through the experiment. This timing standard simplified the proper relative timing of signals generated in the experiment and brought together to form triggers for the experiment or coincidences in latches for a detector. The Phase-Locked RF signal was generated by a phase-locking circuit using the four-fold coincidence of the PHI counters to vary the phase of the distributed accelerator RF. The PHI counter coincidence had a time jitter of less than 1 ns relative to the passage of a muon and about 1.1 ns relative to accelerator RF [3]. The phase-locking circuitry could track time shifts at a rate of 300 ps per arriving muon. The circuitry also maintained a back-up local oscillator in case the accelerator RF failed to reach it.

2.6.2 The Small Angle Trigger

The Small Angle Trigger (SAT) fired if a muon failed to reach its predicted unscattered intercept with the SSA and SMS detectors [110]. The location of this intercept was evaluated for each beam muon individually. Since RUN87, the fraction of the beam accepted by the SAT trigger processor was substantially increased [2]. Most of the data used in this thesis, and all of the data in the region $x_{bj} < 0.001$, were generated by the SAT trigger.

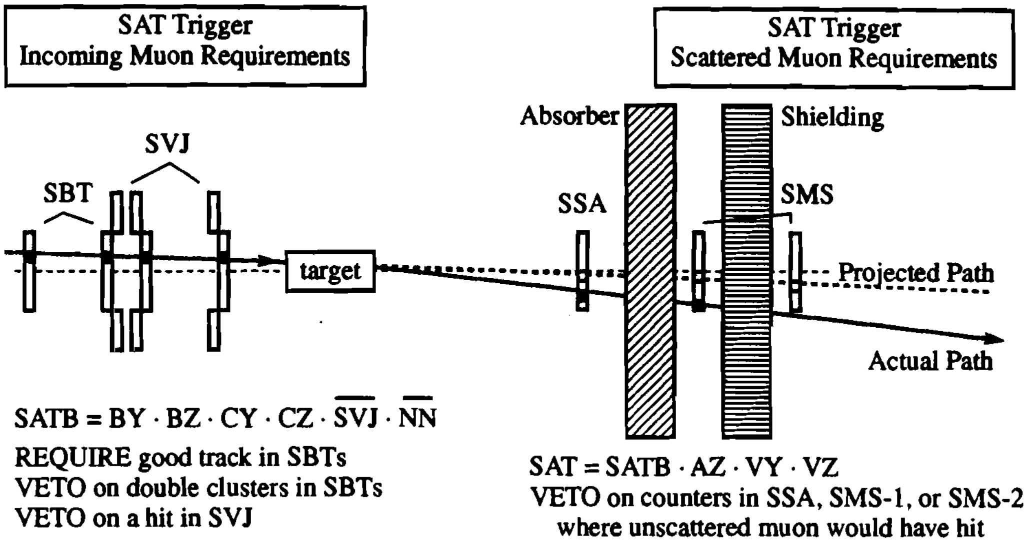

Figure 2.7: The SAT Small Angle Trigger

SAT Beam

Trigger matrix BY defined acceptable trajectories through SBT $2Y$, $3Y$, and $4Y$. Trigger matrix BZ defined acceptable trajectories through SBT $1Z$, $3Z$, and $4Z$. Cluster module CY required single clusters[12] in SBT $3Y$ and $4Y$, while CZ required the same in SBT $1Z$ and $4Z$. Clusters were defined as consisting of a single SBT counter or two adjacent SBT counters. To help eliminate events with halo close to the beam axis, the SAT beam also required that there be no hit in any of the SVJ counters. Such close halo sometimes hit the counters in the SAT scattered muon definition, thus forcing the trigger condition to fail even on an otherwise acceptable scattering event.

$$\text{SATB} = \text{BY} \cdot \text{BZ} \cdot \text{CY} \cdot \text{CZ} \cdot \overline{\sum(\text{SVJ})} \cdot \overline{\text{NN}} \tag{2.1}$$

where the SVJ sum was over all the SVJ counters. The nearest neighbor requirement "NN" was defined by:

---

[12] A wire cluster is a group of adjacent hit wires.

Table 2.6: SBT counters used in the SAT beam logic

Plane	Counters
SBT 1Y	none
SBT 2Y	3 - 10
SBT 3Y	2 - 9
SBT 4Y	2 - 8
SBT 1Z	0 - 12
SBT 3Z	2 - 10
SBT 4Z	2 - 9

$$\mathrm{NN} = \sum(\mathrm{SBT}Z)\cdot\sum(\mathrm{SBT12}Y)\cdot\sum(\mathrm{SBT34}Y) \tag{2.2}$$

where the SBTZ sum was over all SBT Z counters and the SBTlmY sums were over all Y counters in planes l and m. The NN signal was delayed so that it would veto any muons in the bucket preceding the potential trigger. Not all SBT counters, however, were included in their respective plane sums. Table 2.6 on page 37 lists those counters that were included in the sums [2].

Figure 2.8 on page 38 shows the spatial distribution of SAT beam in the middle of the liquid targets. The SAT beam was about 5 cm wide in Y and 4.5 cm wide in Z. Figure 2.9 on page 39 shows the energy distribution in the SAT beam.

SAT Scattered Muon

The trigger matrices projected the observed SBT track into the SSA and the SMS. A veto region was defined where the track projection intercepted these detectors. The veto region was one counter wide in the SSA (AZ), four counters wide in the SMS Y view (VY), and four counters wide in the SMS Z view (VZ). If conditions for more than one SBT track were met, then the the total veto region in the SSA and SMS detectors was the union of the veto regions corresponding to each SBT track. A hit in any of these veto regions killed the scattered muon trigger.

$$\mathrm{SAT} = \mathrm{SATB}\cdot\overline{\mathrm{AZ}}\cdot\overline{\mathrm{VY}}\cdot\overline{\mathrm{VZ}} \tag{2.3}$$

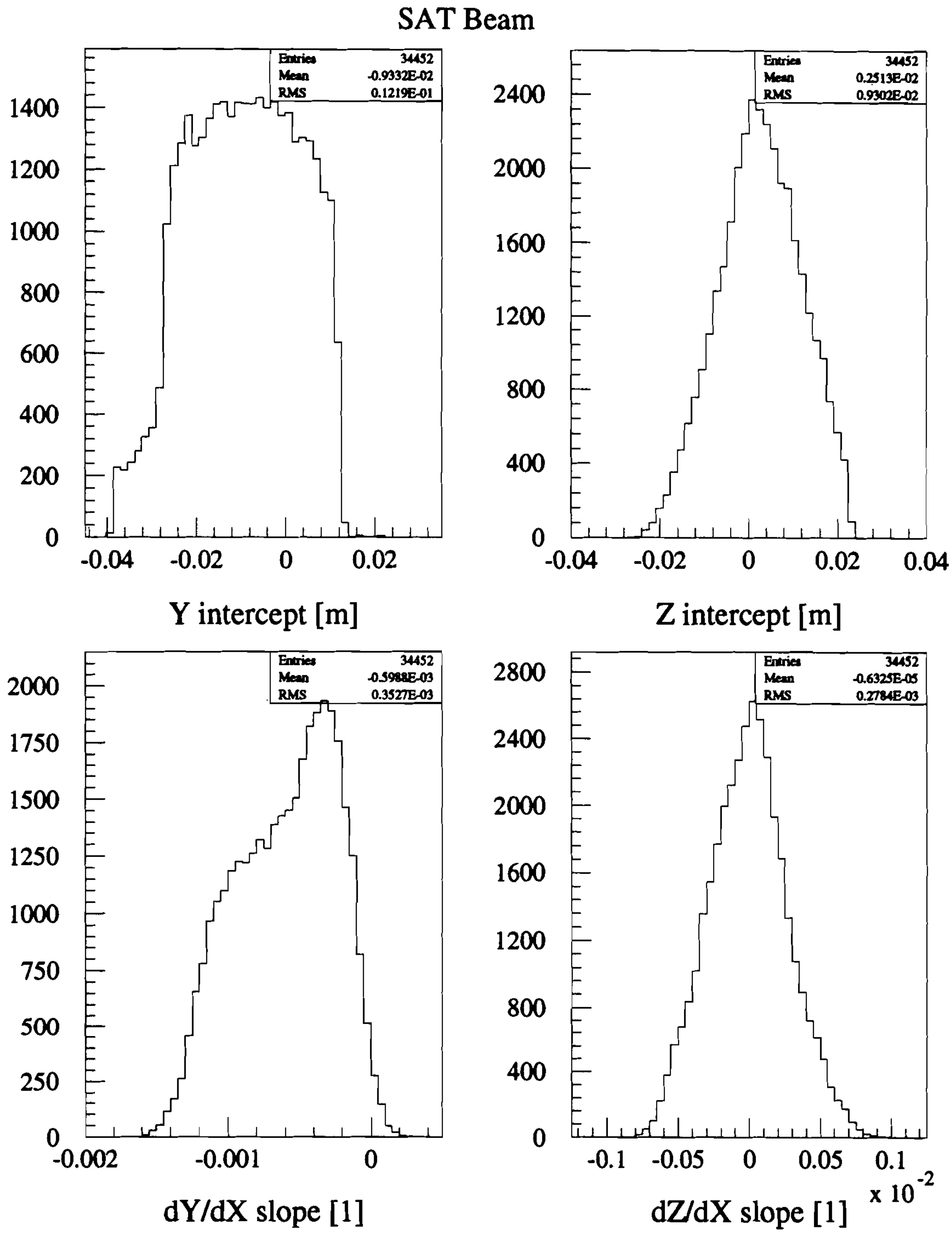

Figure 2.8: Spatial distribution of SAT beam at mid-target

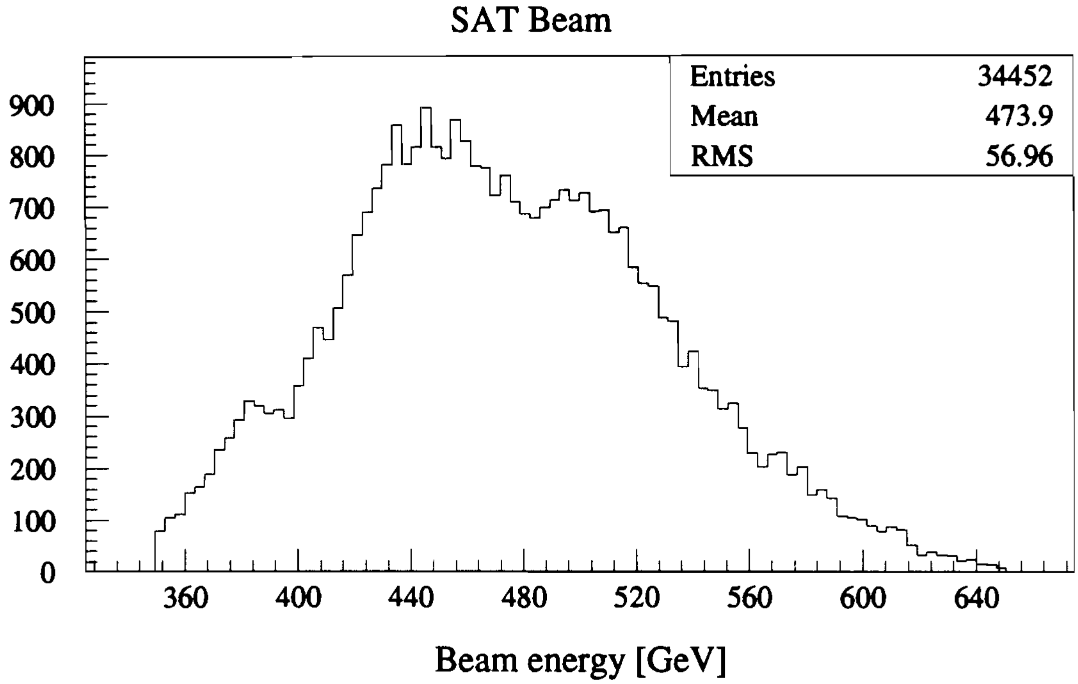

Figure 2.9: Energy distribution of SAT beam

The average minimum scattering angle for the SAT trigger, as determined by the beam distribution and the size of the scattered muon veto region, was about 0.8 mrad.

2.6.3 The Large Angle Triggers

A substantial effort was made between RUN87 and RUN90 to upgrade the large angle triggers [66]. The veto-less Wide Angle Muon Level One Trigger of RUN87 was redesigned to reduce its trigger rate. Its Level Two Trigger component was installed. The SUM detector was installed upstream of the hadron absorber to improve the trigger timing resolution and to reduce sensitivity to electromagnetic showers generated in the hadron absorber. A new trigger, called CVT or Constrained Veto Trigger, was developed and implemented that used a minimal size veto using the SMS detector. The CVT trigger definition was balanced to insure acceptable trigger rates while minimizing the extent of the veto elements. A segmented veto hodoscope (SVS) imbedded in the downstream face of the hadron absorber was used to reduce the rate of accidental vetoing of events by stray electromagnetic activity. Two new triggers, the SVS and the SWM, were developed that used the SVS hodoscope as a veto. The SVS trigger used the SUM and SPM scintillators to confirm the presence of the scattered muon, while the SWM trigger used the PTM proportional tubes.

Table 2.7: SBT counters used in the LAT beam logic

Plane	Counters
SBT 1Y	3 - 9
SBT 2Y	0 - 12
SBT 3Y	2 - 12
SBT 4Y	2 - 10
SBT 1Z	0 - 12
SBT 3Z	0 - 12
SBT 4Z	4 - 10

LAT Beam

All the Large Angle Triggers used the LAT beam definition. The LAT beam logic required that at least one hit occur in each of the seven SBT planes (SBT7/7) and that no hits occur in the SVJ or SVW counters. The NN requirement was in the LATB definition for the data used in this thesis, but not for all of the RUN90 data.

$$\mathrm{LATB} = \mathrm{SBT7/7} \cdot \overline{\sum(\mathrm{SVJ})} \cdot \overline{\sum(\mathrm{SVW})} \cdot \overline{\mathrm{NN}} \tag{2.4}$$

$$\begin{aligned}\mathrm{SBT7/7} \equiv\ & \sum(\mathrm{SBT1}Z) \cdot \sum(\mathrm{SBT3}Z) \cdot \sum(\mathrm{SBT4}Z) \cdot \\ & \sum(\mathrm{SBT1}Y) \cdot \sum(\mathrm{SBT2}Y) \cdot \sum(\mathrm{SBT3}Y) \cdot \sum(\mathrm{SBT4}Y)\end{aligned} \tag{2.5}$$

and the SVJ and SVW sums were over all the SVJ and SVW counters, respectively. The NN requirement was defined in Equation 2.2. As with the SAT beam, not all SBT counters were included in their respective plane sums. Table 2.7 on page 40 lists those counters that were included in the sums. SBT fingers were removed from the LATB definition to improve the fraction of the accepted beam that actually hit the target.

Figure 2.10 on page 41 shows the spatial distribution of LAT beam in the middle of the liquid targets. The LAT beam was about 6.5 cm wide in Y and 3.5 cm wide in Z. Figure 2.11 on page 42 shows the energy distribution in the LAT beam.

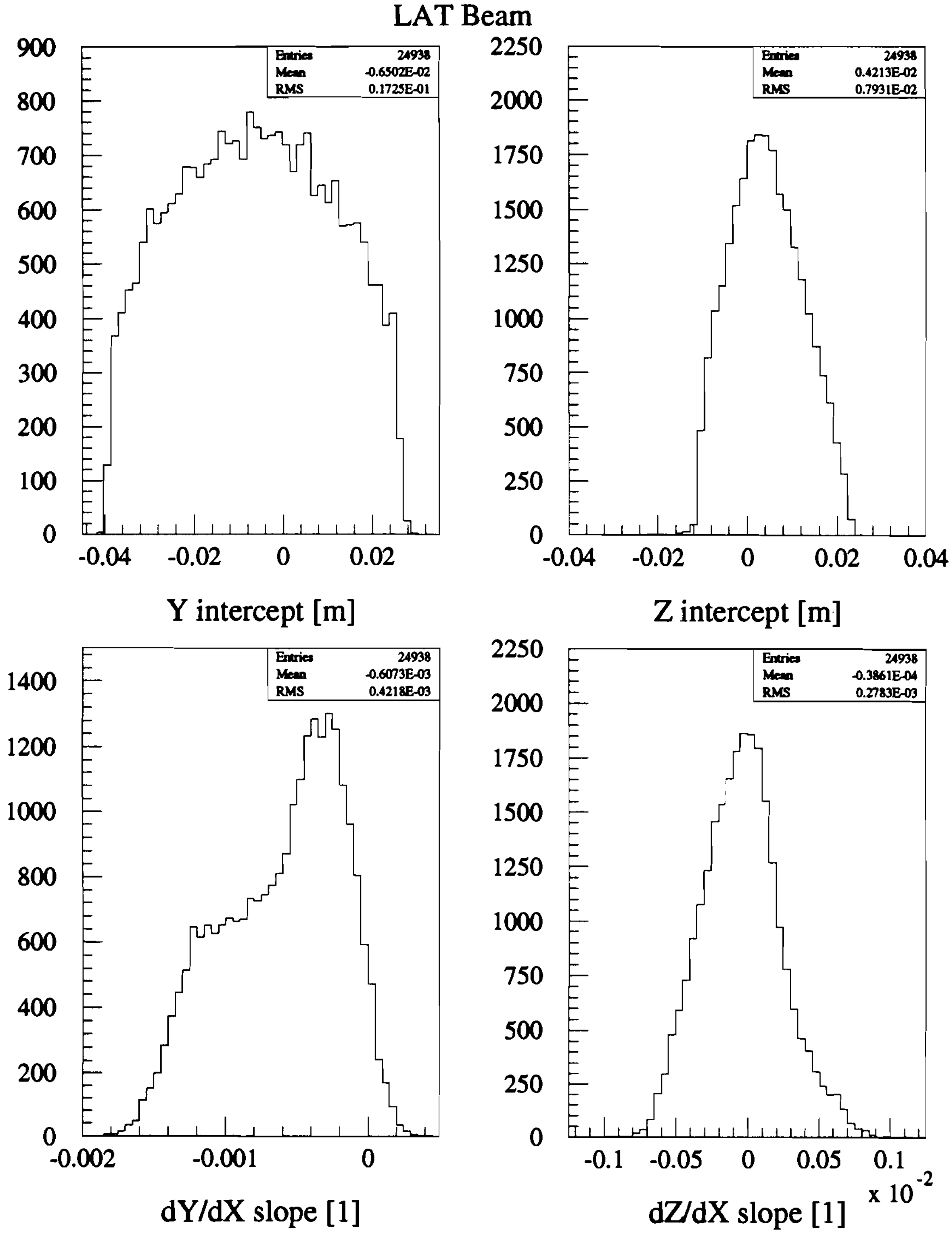

Figure 2.10: Spatial distribution of LAT beam at mid-target

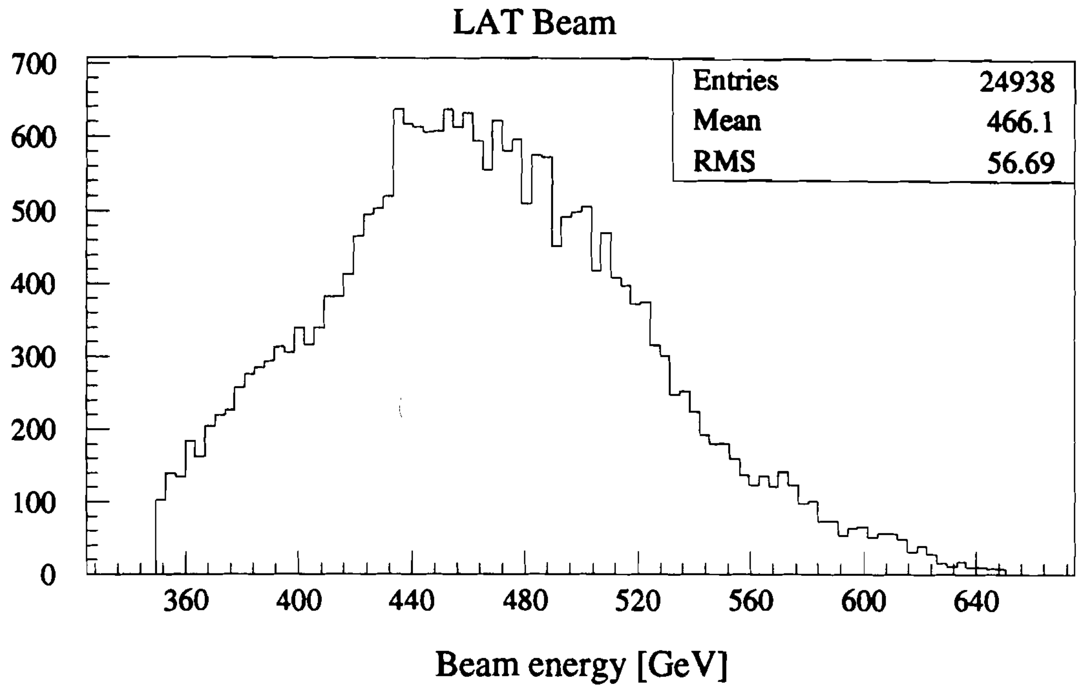

Figure 2.11: Energy distribution of LAT beam

WAM-L1 Scattered Muon

Since the Level One and Level Two components of the WAM trigger were used separately in other triggers, each is described separately here. The complete WAM trigger itself was not used in this analysis.

The Level One component of the WAM trigger (WAM-L1) is described in Appendix D and elsewhere [115]. The development and implementation of the WAM-L1 trigger and related components was one of my responsibilities as a UCSD graduate student. The WAM-L1 trigger used information from the SUM and SPM detectors to detect the scattered muon. All the top and corresponding bottom SPM and SUM counter pairs were summed to form towers in the trigger logic. These towers were combined to form roads, counter combinations which, when present, indicated the passage of a muon. The roads were two or more towers across in the SUM layers, one tower across in the first SPM plane (where the muon beam is focussed), and three towers across in the remaining SPM planes. Within a road, if one of two SUM layers detected a muon and three of four SPM planes detect a muon, then the WAM-L1 trigger fired.

WAM-L2 Scattered Muon

The Level Two component of the WAM trigger is also described elsewhere [69, 64]. Whereas the WAM-L1 provided a faster, but not very restrictive (in angular acceptance), scattered muon definition, the WAM-L2 definition was slower, but highly restrictive in angular acceptance. It used information from the PTM detector to reject all tracks which did not appear to originate in the target. The PTM wires were shifted into the WAM-L2 trigger processor after a Level One trigger occurred. Wires from the Y and Z views were treated separately. The wire hits were checked with a programmable look-up table for patterns that satisfied any of the acceptable target-pointing track definitions. Like the WAM-L1, the WAM-L2 track definitions were in the form of roads. The road width varied by plane and view. In the Y view, the roads were, from plane 1 to plane 4, 1-4-6-8 wires wide. In the Z view, the roads were 1-3-3-5 wires wide. A hit in plane 1 and at least two of three of the remaining planes were required to satisfy a road. At least one acceptable road in the Y view and one in the Z were required for the trigger to fire.

In the WAM trigger, the WAM-L2 scattered muon signal was used in coincidence with the NHB (No Halo Beam) requirement. NHB vetoed on SVJ halo arriving within 5 buckets of the trigger bucket. In order to optimize the rejection of halo, the width of this veto was extended up to 20 buckets before and after the trigger bucket during RUN90. Because of the unacceptably high trigger rate from the WAM trigger, the trigger was prescaled before being used in the data acquisition system. The WAM trigger itself is not used in this analysis, but the Level Two component is used via the SWM trigger.

CVT Scattered Muon

The CVT scattered muon definition was the same as the WAM scattered muon definition with the additional requirement that there be no SMS tracks found by the CVT processor, as is described in detail elsewhere [65]. Like the WAM trigger, the CVT trigger included the NHB requirement at Level Two trigger time. CVT trigger information is not used in this analysis due to the number of problems the trigger suffered during RUN90. For instance, the CVT trigger was essentially dead in the lower west quadrant of the Scattered Muon Detector. The cause of this is under investigation.

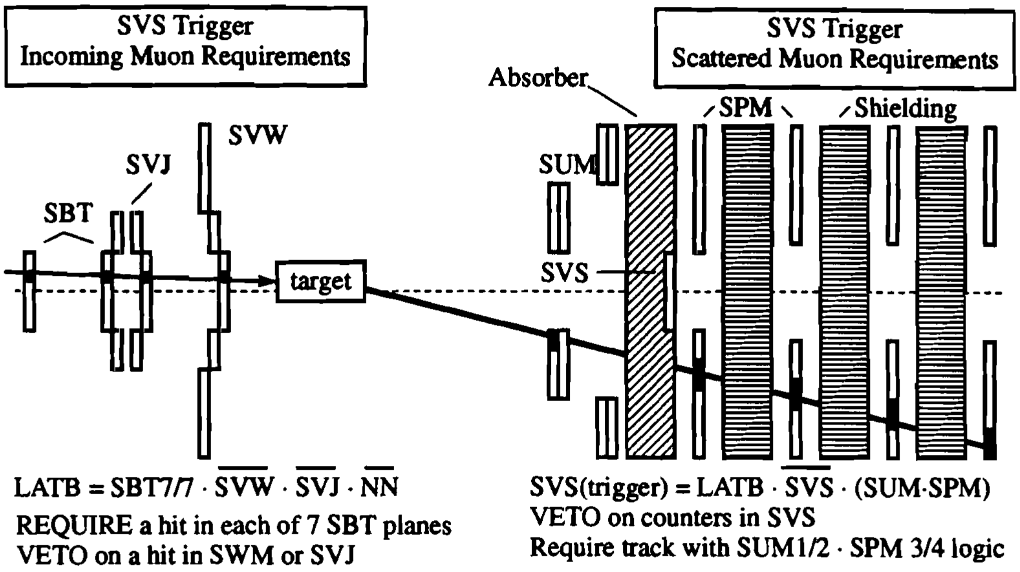

Figure 2.12: The SVS Large Angle Trigger

SVS Scattered Muon

The SVS trigger used the sum of all SVS counters, except two on the west edge of the detector, as a fixed beam veto. Information from the SUM and SPM detectors was then used to confirm the presence of a scattered muon. The top and bottom SUM counters at the same Y location were combined to form towers. From three to five SUM towers were combined with each SPM counter in SPM planes 1 and 2. The SUM and SPM counter combinations were then summed and combined in three out of four majority logic. The SPM top and bottom banks were treated separately. Thus, the SVS trigger required that there be at least one hit anywhere in one of two SUM layers and one hit anywhere nearby (in the Y-coordinate) in three out of four of either the top SPM banks or the bottom SPM banks.

SWM Scattered Muon

Like the SVS trigger, the SWM trigger used the sum of all SVS counters, except numbers 15 and 16, as a fixed beam veto. Information from the PTM detector, by way of the WAM-L2 trigger signal, was then used to confirm the presence of a scattered muon. Note that in some E665 literature the SWM trigger is called the SVSWAM2 trigger.

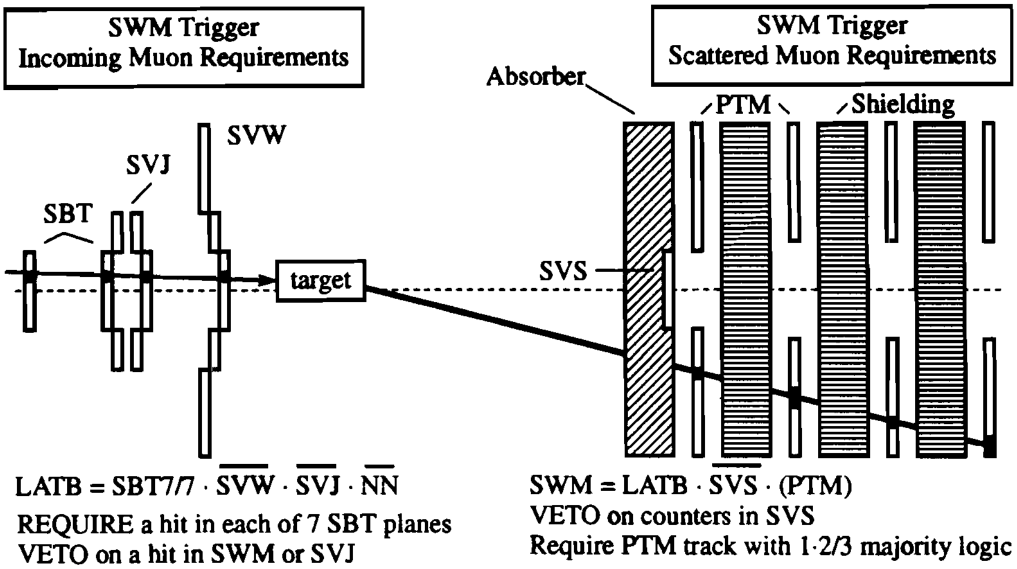

Figure 2.13: The SWM Large Angle Trigger

There were some timing problems with the SWM trigger during the first part of the RUN90 data-taking. The mis-timing allowed a number of SWM triggers to occur at a slightly different time relative to the passage of the scattered muon than other triggers. The data set used in this analysis is restricted to the time period after the SWM trigger timing was fixed.

LAT Scattered Muon

This analysis defines the sum of the SVS and SWM triggers to be the LAT trigger. The average minimum scattering angle for the LAT trigger, as determined by the beam distribution and the size of the SVS veto region, was about 3.0 mrad.

2.6.4 Normalization Triggers

Several triggers, generically referred to as "Rbeam" triggers, were dedicated to the normalization of the physics data set by randomly sampling the beam. This enabled the measurement of the fraction of all beam muons that pass the analysis requirements imposed on the reconstructed beam. In addition to being used to calculate the relative normalization of the different data sets, the Rbeam events were used to evaluate corrections to other methods of normalization due to incoming muon acceptance, track reconstruction inefficiencies in the Beam Spectrometer, and other effects. The Rbeam events were also used to evaluate detector efficiencies in the beam region.

RSATB Trigger

The RSATB trigger was formed by a coincidence between the SAT beam signal and randomly prescaled RF. The randomly prescaled RF was generated by the E665-designed "Argonne random prescaler" modules which incorporate the "feedback shift register" method [107] to produce a pseudo-randomly prescaled output. The prescale factors applied by the modules were downloaded in software.

RLATB Trigger

Similarly, The RLATB trigger was formed by a coincidence between the LAT beam signal and randomly prescaled RF. The randomly prescaled RF used is generated in the same manner as thay used by the RSATB trigger. The prescaled factors applied to the Rbeam triggers are independent of one another.

2.6.5 Monitoring Triggers

Several triggers were used simply to provide a means to monitor the performance of event reconstruction or of the detectors. The PSRF trigger was a randomly (and greatly) prescaled RF signal, without any beam requirements. This was used as an unbiased event sample, for instance to test detector efficiency and response [186]. Several so-called "Halo" triggers were used to gather a sample of halo events that are used to measure detector efficiencies away from the beam region. Since the halo rate was so strongly peaked near the beam region, two halo triggers were used in RUN90, the prescaled close halo (CHALO) and the wide halo (WHALO) triggers.

2.7 Data Acquisition System

2.7.1 Collection and Storage

The data acquisition system used at E665 has been described elsewhere [94, 151]. Since the publication of these articles, a few central pieces of the E665 data acquisition system system have been altered. The software control and monitoring of the data acquisition system was still implemented primarily through the FNAL VAXONLINE [44] and RSX-DA packages [42]. A new FASTBUS sub-system was added to collect data from the VDC detector. This sub-system used a DEC MicroVax II for detector monitoring. The concatenation machine was upgraded from a DEC microVax II to a DEC VaxStation 3200. The DEC microVax II used as an off-line monitoring machine was replaced by a DEC VaxStation 3200 and SGI[13] Personal IRISes. The off-line storage medium was changed from 6250 BPI nine-track open-reel tape to 8 mm video tape.

Detector interfaces were located in CAMAC and FASTBUS electronics crates. The CAMAC type A-1 and A-2 crate controllers were linked by six parallel CAMAC branches to three front-end DEC PDP 11/34s. In addition to this, a serial branch was used for monitoring and command services. Two FASTBUS systems, one for the CAL detector and one for the VDC detector, also acted as front-ends. The front-end machines read out in parallel, with data stored in PDP bulk memory and in LeCroy 1892 FASTBUS memory modules. Asynchronously, a VaxStation read out the buffered information, concatenated the pieces of single events from different buffers, and wrote the information to 8 mm video tape. Two Exabyte[14] EXP-8200 8 mm cartridge tape drives were used to minimize the downtime while changing tapes. One tape drive was used to write to tape while the other was held in reserve until the first tape filled. The tape files were limited in size to the equivalent a nine-track tape used in RUN87. The concatenation VaxStation also sent a sample of events for monitoring and reconstruction to a data pool available to the E665 Vax cluster.

2.7.2 Special Runs

In addition to runs dedicated to gathering physics data, a number of runs were set aside to measure the relative location of the E665 detectors. These alignment runs required unusual conditions, such as having the momentum analysis magnets turned off, or using only a beam-sampling or halo-sampling trigger. A series of runs were

---

[13] SGI: Silicon Graphics Inc.

[14] Exabyte: Exabyte Corp.

set aside to calibrate various particle identification detectors using a electron beam generated in place of the muon beam. Special runs were also set aside for detector and trigger studies.

2.7.3 Scalers

In order to monitor the experiment, counts of various signal transitions were maintained in scalers. These have been described elsewhere [123, 60]. The spill scalers count transitions over a beam spill period. They were read out and reset every spill at the end of the spill. The event scalers were read out with each event, but not reset. Higher rate inputs to both sets of scalers were prescaled down to rates acceptable to the scaler modules. The two sets of scalers were intended to be used in separate, complementary, measurements of the beam flux for normalization, as well as in the general monitoring of rates.

Spill Scalers

The spill scalers suffered from a systematic counting error during certain spills [123]. Whenever an tape file was closed and the next one opened, the data acquisition system suffered a pause in which data taking was suspended. Event buffers filled and subsequent events were lost. The counting of the accepted beam by the spill scalers, however, continued. This effect, called the interfile event loss, occurred in one way or another in about 5-8% of the spills in RUN90. In addition to the spill scalers overcounting, occasionally undercounts occurred when the events lost were those containing spill scaler information. The estimated loss in the spill scaler count after cuts and corrections was about 3%. This loss appeared to be independent of the target in place at the time, so the ratio of beams between targets was affected by relatively much less than this.

Event Scalers

The event scalers for the LAT triggers were not properly installed, yielding no useful information in RUN90. The event scalers for the SAT trigger, on the other hand, were properly installed during the data samples used in this analysis [58, 57]. Nevertheless, the event scalers suffered from overflows, stuck bits, and a variable width counting gate. Corrections for most of these effects were implemented, but occasional glitches in the corrected event scaler counts still appeared. Because of this, information from the event scalers was not used to normalize the data in this analysis.

2.7.4 Monitoring

A monitoring task on the E665 Vax Cluster maintained a visual and printed record of important scaler values and ratios. Two VaxStations in the local cluster were largely dedicated to reading events over the network and feeding them to an event display program, a beam reconstruction program, and a general detector monitoring program, all operated by the E665 shift crew. Raw data tapes were occasionally partially reconstructed to check for gross detector failures. Every eight hours a shift crew volunteer performed a series of equipment checks. Various monitoring processes ran on the PDPs and local Vax cluster, checking for unreasonable equipment behavior. Local data acquisition systems monitored high and low voltage settings and detector response.

2.8 Summary

Since the last published description of the E665 apparatus, significant improvements to the target, particle tracking, and scattered muon triggering systems have been implemented. Identical liquid targets containing H_2, D_2, and vacuum were frequently interchanged to reduce the effect of systematics on cross section ratios. The VDC drift chambers were implemented close to the target to improve vertex resolution. General improvements to other elements of small angle particle tracking, including the installation of the PSC detector, have been made. The Small Angle Trigger has been improved to accept a much larger fraction of the muon beam. Several new detectors and triggers have been installed to improve the Large Angle Trigger performance.

Chapter 3

Event Reconstruction

> *The symptoms of the software crisis "appear in the form of software that is nonresponsive to user needs, unreliable, excessively expensive, untimely, inflexible, difficult to maintain, and not re-usable"*† *.... FORTRAN and COBOL were created early in the history of computer science, long before the problems of massive software-intensive system development were understood. As a result, such languages do not reflect modern software engineering principles, and we have had to compromise them with preprocessors, extensions, and management controls to force them to fit more recent methods. In a sense, these languages constrain our way of thinking about a problem....*

Grady Booch, *Software Engineering with Ada* (1987)

† E. W. Dijkstra, "The Humble Programmer" (Turing Award Lecture), *Comm. ACM* **15**, 862 (1972).

3.1 Overview

This chapter describes the process by which raw data was converted into events with understood kinematics. This process involved several large software programs most of which had not changed substantially since they were last documented. The event reconstruction program PTMV [176, 179] was altered slightly since RUN87 to accommodate new detectors. The event simulation program MC12 was adapted to handle the new detectors and triggers installed for RUN90. The radiative corrections program FERRAD [191] was a slightly improved version of the same program used by NMC and has been documented elsewhere [25, 49, 201].

3.2 Apparatus Constants

Event reconstruction is, in a broad sense, an iterative process. Before event reconstruction can be carried out, studies must be performed to generate a set of consistent apparatus position and calibration constants[1]. These studies, in turn, require some level of event reconstruction to be done. This process is seeded by using surveyor measurements or educated guesses for the apparatus constants. The reconstruction of special data sets is then used to refine the detector position and calibration constants. Once the apparatus constants are established, the quality of the event reconstruction process itself can be tested. Various parameters, such as minimum χ^2 probabilities for acceptable track reconstruction, are tuned to improve the fraction of true particle tracks reconstructed and reduce the fraction of false particle tracks reported. The tuned reconstruction program is then used to further refine the apparatus constants, and so on. The RUN90 analysis benefited tremendously from the many rounds of this iterative process performed in the analysis of RUN87 data. Nevertheless, several more were required to analyze RUN90 data given the movement of old detectors and the introduction of new detectors used in tracking.

All tracking detectors were aligned using the E665 Alignment program [46, 178, 67]. The quality of the RUN90 alignment has been studied [68]. Given the position of detectors along the beam axis measured from surveys, the Alignment program calculated the relative lateral positions (translation and rotation coordinates) of the detector elements. The results of the Alignment program were often enhanced by studies specific to a detector. This was crucial in order to understand the position of those detectors that were found to have move appreciably when the CVM and CCM magnetic fields were turned on, such as the PCV detector, since the normal alignment procedure involved data taken with these magnets off.

---

[1] The term "constants" is actually a misnomer since these constants are generally time-dependent, with time parameterized by the run number.

Apparatus which was not used in tracking, however, was not aligned with the E665 Alignment program. Each non-tracking detector was aligned by its own dedicated program. The non-tracking apparatus includes the SBT beam hodoscopes, the experiment targets, the SSA, SUM, SVS, and SPM scattered muon detectors, and the CAL electromagnetic calorimeter. For instance, given the surveyed X-coordinates of the SPM planes described in Reference [21], the program SPMEFF3 which I developed was used to determine the location of the Y and Z edges of the SPM counters [116].

3.3 PTMV

Event reconstruction was performed by the computer program PTMV. This program used either raw data or Monte Carlo-generated data as input. The PTMV program could be broken down into several distinct phases: decoding and translation, pattern recognition, track fitting, muon match, vertex fitting, and calorimetry. Several phases, such as wide angle pattern recognition and particle identification, were not used in this analysis and are not described here. Since RUN87, PTMV has been adapted to run under the UNIX operating system as implemented by Silicon Graphics (IRIX) [117, 121, 120, 119, 206] and IBM (AIX) [122]. In order to increase the event processing rate of the program, it was further adapted to run under the Fermilab CPS multi-process computing environment [114, 48, 86]. Basic calorimetry was performed in the PTMV program itself.

3.3.1 Decoding and Translation

Decoding is the process by which the raw data stored by the data acquisition system is converted to a standard abstract representation. Each detector had its own set of decoder modules, one for each detector interface type, which hid the details of the detector interfaces from the main event reconstruction program. Each decoder module found the raw information from its detector interface in the variable length raw data block representing an event. The module checked for obvious detector failures and interface error conditions which, if found, were reported to the main program in a standardized fashion. It then transformed the data into a standard representation format for that type of detector and interface.

Translation is the process by which detector hits are transformed from a detector element representation to a spatial coordinate representation. This was performed for those detectors that were involved in particle track detection. The detector constants stored enough position information to allow a quick calculation of the position of any single detector element involved in particle tracking.

3.3.2 Pattern Recognition

Pattern recognition (PR) is the first of two stages of track reconstruction. PR is performed by many modules called processors, each of which attempts to find track segments or track projections using information from a particular set of detector planes [176, 46]. The details of the processors vary according to the number of detector views available and the specific niche the processor is intended to fill in the overall event reconstruction. Descriptions of the elements in track reconstruction introduced since RUN87 are given in Section 3.3.4.

In general, a PR processor takes a set of hits in specific detectors and determines if any subset belongs to a realistic particle trajectory. In regions with a constant magnetic field, the hypothetical trajectory (for charged particles) is a helical path; in field-free regions, it is a straight-line path. The hypothetical paths are required to be consistent with those of a particle coming from the target region, the "target-pointing" constraint. Since the particle momentum is not determined, the effects of multiple Coulomb scattering are not explicitly taken into account at this point in track reconstruction. Instead the target-pointing constraint is loosened to insure that the tracks of particles in a reasonable range of momenta undergoing reasonable amounts of deflection by multiple scattering are pattern recognized.

Two different algorithms are used in the grouping of hits to identify a valid path. In regions with a magnetic field, the space-point method is used. In this method, the overlaps of wires in three or more views in a detector closely spaced in the X-coordinate are checked for consistency with a space-point, a 3-dimensional intersection of a particle trajectory with the detector. Space-points found using different views are checked against each other to determine if they are consistent with a single track intersection. If so, then the similar space-points are merged into a single space-point. The final set of space-points are then tested for combinations that are consistent with a particle trajectory.

In magnetic field-free regions, the simpler projection method is used. In this method, a straight line is fitted to a set of hits in a single view. A χ^2 is defined from the separation of the hypothetical line and the hits included in a fit. Only combinations of hits giving a sufficiently small χ^2 per degree of freedom are accepted. If the contribution to the χ^2 from a single hit is too large, then that hit is dropped from the hypothetical path and the line is refitted. In detectors with three or more views, the projections in different are combined unambiguously to form 3-dimensional track segments. In detectors such as the PTM and SMS, however, the 2-dimensional projections are the final product of PR.

Several new pattern recognition processors have been installed in order to implement the VDC detector in the track reconstruction. These are described in Section 3.3.4.

3.3.3 Track Fitting

Track fitting (TF) is the last stage of track reconstruction and is independently performed in three regions of the apparatus, the Beam Spectrometer, the Forward Spectrometer, and the Wide Angle Spectrometer [179]. TF is performed slightly differently in each region. In general, TF attempts to fit a particle track obeying the Lorentz equation (in the absence of an electric field)

$$\frac{d\vec{p}(x,y,z,t)}{dt} = q\vec{v}(x,y,z,t) \times \vec{B}(x,y,z) \tag{3.1}$$

to the space-points from space-point PR and the hits from projection PR (collectively called generalized hits). At a given X-coordinate, this model track is described by five parameters, three for the momentum 3-vector and two for the track intercept at that X-coordinate. Since there are usually more generalized hits along a track than fit parameters, a constrained fit is performed. Since the momentum of a particle is available at the TF stage, the effects of multiple Coulomb scattering can be explicitly taken into account.

3.3.4 PRTF

The details of Pattern Recognition and Track Fitting (collectively, PRTF) tend to be specific to a region of the apparatus and are described elsewhere [176, 46, 179]. The beam PRTF is described here in order to provide context for a discussion of a momentum miscalibration that is present in the data set used. Also, a new track reconstruction package is described which implements the VDC detector.

Beam PRTF

The first particle track reconstruction performed was in the Beam Spectrometer where only a relatively small number of particle trajectories are found in any

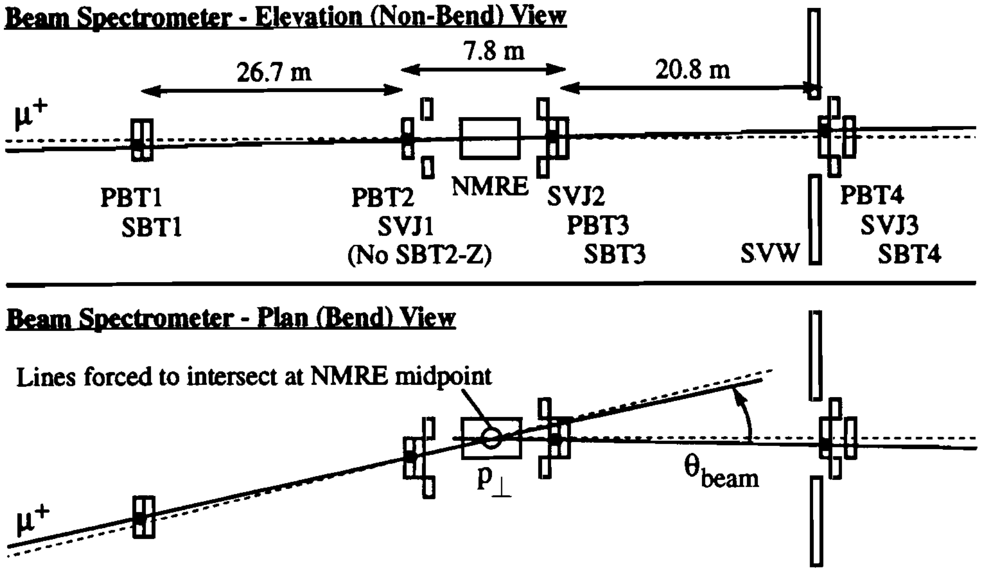

Figure 3.1: Reconstruction of the incoming muon in the Beam Spectrometer

one event. The pattern recognition processor used in the Beam Spectrometer was the PB processor. It used hits in the PBT detector and employed the space-point algorithm. A straight-line was first fitted in the Z (non-bend) view to the space-points. A space-point from each of the four beam stations was required. If the quality of this straight-line fit was acceptable, then the Y (bend) view was considered. Straight-line fits in the Y view were made separately with the space-points in the first two and last two beam stations. These lines must have intersected at the center of the NMRE magnet in order to have been consistent with an acceptable particle trajectory. If they did intersect, then the pair of lines were saved as parts of a valid track.

The track fitting method used in the Beam Spectrometer was quite simple [179]. The magnetic field of the NMRE was described simply by its total momentum kick $p_\perp$, the component momentum perpendicular to the magnetic field picked by a particle when it traverses NMRE. An analytic model of the track was used containing five parameters $(y, z, y', z', 1/p)$ evaluated at the X-coordinate corresponding to the downstream-most PBT4 view. A χ^2 was defined using the separation between the generalized hits and the model track and the uncertainty in the location of the generalized hits. The value of the fit parameters was found by minimizing this χ^2. Since the mean deviation angle due to multiple scattering of such a high momentum particle was practically negligible compared to the NMRE bend angle, multiple scattering was not considered in the track fit in the beam spectrometer.

The NMRE $p_\perp$ was evaluated from a measurement of the current through NMRE and measurements of the NMRE field integral [194, 34]. The value used in the analysis of this data set was not the measured value, but rather the one used in the analysis of RUN87 data, namely[2] 1.52708 GeV/c with a relative error of 0.7%. With both of these values of the $p_\perp$ kick, the values of the momentum measured for unscattered beam muons in the Beam Spectrometer and the Forward Spectrometer differed. This momentum miscalibration is referred to as the "ν offset" since the ν spectrum for unscattered beam is systematically shifted. This is still under investigation. The $p_\perp$ kick value used for the reconstruction was chosen based on its previous use in the RUN87 reconstruction effort. The value of the nu offset in RUN90 data set used in this thesis was about 11 GeV and was approximately linearly dependent on the beam energy. The correction applied to the data set to fix this energy miscalibration is described in Section 3.6.1.

VDC PRTF

Track reconstruction in the VDC detector has been implemented using three new pattern recognition processors. In some cases, however, these processors perform both pattern recognition and track fitting [172]. The VDC processors were executed after all other PRTF processors have been run, but before any muon matching or vertex fitting.

The VA processor tested hits in the VDC to see if any belong to tracks found in the Forward Spectrometer. Each Forward Spectrometer track was extrapolated into the VDC, taking into account the effects of the CVM magnetic field. If at least a minimum number of VDC hits appeared to be consistent with an extrapolated track, then the hits were assigned to the track and removed from any further consideration. The extrapolated track was then extended into the VDC.

The VB processor tested hits in the VDC detector to see if they were consistent with a track inside the VDC. Information about tracks outside the detector was not used. Combinations of hits in the Z (non-bend) views were tested for consistency with a straight-line fit. The consistent Z view lines were called projections and were then used to test combinations of hits in the U and V views for consistency with parabolic paths. This was done iteratively with variations made in the combination of U and V hits under test and in the momentum of the hypothetical path. A minimum number of U and V hits were required to be consistent with a path before the path was considered an acceptable track.

---

[2] The exact value of the NMRE $p_\perp$ used in track reconstruction is shown, including the excess precision used there.

The VD processor tested hits in the Forward and Wide Angle Spectrometers to see if any belonged to the VDC track found by the VB processor. Only hits outside the VDC which were not already used by tracks were considered.

3.3.5 Muon Match

The Muon Match phase of event reconstruction attempts to associate a muon track in the Scattered Muon Detector with a track in the Forward Spectrometer[24, 23]. All possible combinations are tested after projecting the Forward Spectrometer tracks and the Scattered Muon Detector projections to the downstream face of the hadron absorber. The smearing of the extrapolated Forward Spectrometer track intercept by multiple Coulumb scattering in the calorimeter and the hadron absorber is calculated, and the value is added in quadrature to the error on the extrapolated track intercept. A χ^2 characteristic based on the track intercept, slope, and the corresponding errors is then used to decide which of the Y and Z Scattered Muon projections link to which Forward Spectometer track. Each Forward Spectrometer track can be associated with at most one Scattered Muon projection in each view. Each projection, however, can be associated with more than one Forward Spectrometer track. Any resulting ambiguities are resolved at the ensuing Vertex Fitting phase.

The Muon Match is a major source of event reconstruction failures [8, 9]. A difficulty specific to RUN90 event reconstruction was the failure of two of the eight planes in the PSA detector. This prevented the established pattern recognition processor from finding a track segment in the PSA detector. Such a segment in the PSA was required by the Muon Match code for matching scattered muons passing through the PSA. To avoid this problem, hits in the PSA were used directly to constrain tracks found without PSA track segments [61]. While the muon match efficiency was reduced, the quality of the track fits after the additional constraints was acceptable.

3.3.6 Vertex Fitting

The Vertex Fitting procedure is used to determine the point of closest approach between the beam muon track, the scattered muon track, and a set of Forward Spectrometer tracks [46]. This point is defined to be the interaction vertex. Once the location of the vertex is determined, the kinematics and associated errors can be calculated. An important feature of this phase is that, in addition to χ^2 probability cut-offs, absolute distance cut-offs are employed to determine how close tracks must be before being fitted to a common vertex or merely being reported as being close to each other.

The first stage of the Vertex Fitting, the "muon phase", attempts to fit only beam and scattered muons to a vertex. Every combination of beam track and scattered muon candidate track is tried. The beam track is extrapolated from the last Beam Spectrometer station to the proposed vertex. The scattered muon track, however, must be "swum" through the magnetic field of the CVM frm the VDC detector to the proposed vertex location. The center of the target is used as an initial guess at the vertex location. The χ^2 probability that this is an acceptable vertex is calculated based on the separation of the tracks, the track errors, and the hypothesis that the tracks meet at a common point. If it is not acceptable, then a new location is chosen and its associated probability is checked. This is repeated until a vertex is found or the process is delared a failure with these tracks as inputs. If a vertex is found, then the scattered muon candidate track giving the best vertex fit is defined to be the scattered muon. Any remaining ambiguities, which occur quite infrequently, are resolved by defining the highest energy scattered muon track to be the scattered muon. If no muon phase vertex found, then no further processing of the event occurs.

The second stage of the Vertex Fitting, the "hadron phase", attempts to include a set of "hadron tracks"[3] in the set of all tracks fitted to the vertex. Initially all hadron tracks are considered. If the χ^2 probability associated with the vertex fit for this collection of tracks is greater than some cut-off, then the hadron track giving the largest χ^2 contribution is removed and the fit is redone. This process is repeated until the χ^2 probability falls below the cut-off value. The vertex location is also varied as in the muon phase.

In principle, when performing cross section measurements, only the muon phase results should be used to avoid complications like hadron multiplicity-dependent vertex resolution. The resolution in the scattering angle (and therefore Q^2 and x_{bj}) at the smallest scattering angles is greatly improved, however, by the addition of a few more constraints. Since the measurement is of inelastic cross sections, a few hadrons are likely to be produced. This effect is not entirely removed from the analysis. It is not expected to be significant in the ratio of cross sections except as a second order effect due to differences in hadron multiplicity between the targets.

The last stage of the Vertex Fitting is the fitting of secondary vertices. Combinations of the hadron tracks are tested to find a consistent secondary vertex. If such a vertex is found, the tracks involved are removed from the set of tracks associated with the primary (interaction) vertex. The primary vertex is then refitted.

---

[3] Hadron tracks are defined to be all the Forward Spectrometer tracks other than the scattered muon track. This may include electron tracks, muon tracks, or hadron tracks.

3.3.7 Calorimetry

The processing of the CAL data was installed as a standard part of the event reconstruction program. The processing of the CAL data is described in detail elsewhere [187, 175, 189]. The CAL ADC pedestals were determined from data gathered between beam spills. The calorimetry software subtracted these pedestals from the data. The corrected pad information was used to identify clusters of pads which appeared to belong to the same shower in the calorimeter.

Detailed corrections to the calorimeter gas gain were required to account for changes in the atmospheric pressure, temperature, and the high voltage settings used. In addition, an overall energy calibration correction to the calorimeter energy was required. Correction of the gas gains was performed after data reduction, and is described in Section 3.6.2.

3.3.8 CPS

In order to provide optimal computing throughput at a minimal cost for typical High Energy Physics event reconstruction efforts, Fermilab has developed a multiprocessing environment called CPS for UNIX workstation farms [48, 86]. Adapting PTMV to run under CPS involved splitting the program into separate co-operative pieces, each of which is a complete and independent program handling a specific task in the CPS model of event processing [114]. As illustrated in Figure 3.2 on page 60, in any one production job, CPS integrates one class 1 process to handle event input, some number of class 2 processes[4] to perform event reconstruction on different events in parallel, and one class 3 process to handle the output of reconstructed events and related data. The class 1 program, PTMV1, reads an event in from tape or disk and places it in the input event queue. A set of class 2 programs, PTMV2, process events from this input queue. Once a class 2 program finishes with an event, it places the reconstructed event in the output event queue and fetches another raw event from the input queue. The class 3 program, PTMV3, outputs any events found in the output queue to tape or disk.

Since some events may require much more CPU in order to be processed, and since no synchronization on the event processing is made between the class 2 processes, the events are not necessarily output in the same order that they were input. In a sense, the event order is sacrificed to obtain the maximum CPU efficiency from the parallel processing of the events. Tasks that are dependent on the event order must be isolated and placed in the class 1 process, the last place where events are ordered as they were originally written to the raw data tape. Since no event

---

[4] The typical number of class 2 processes used to reconstruct the data in this thesis was eight.

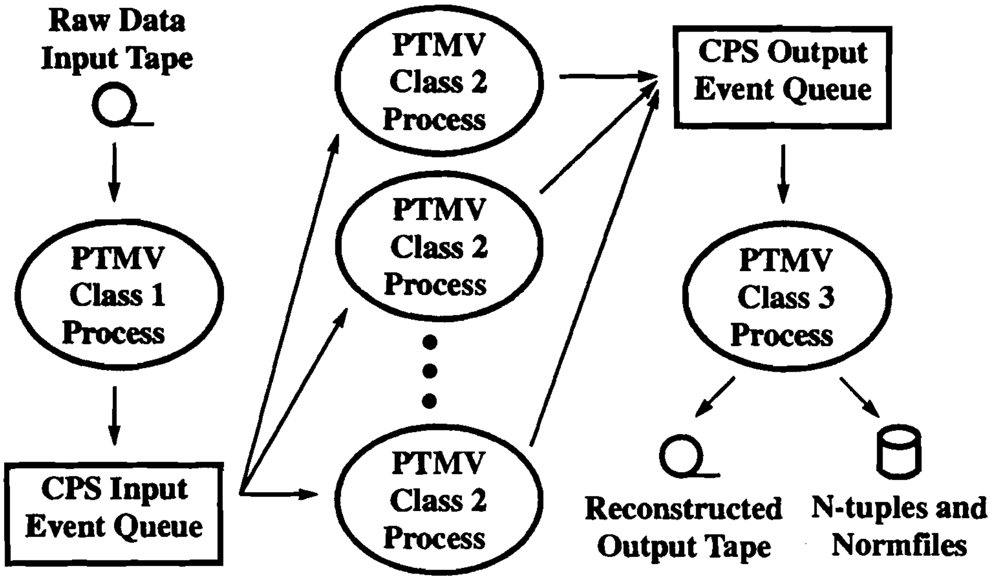

Figure 3.2: Data flow in the E665 use of CPS for event reconstruction

reconstruction is performed by the class 1 process, event reconstruction must be completely independent of event order. Other than code to correct defects in the event scaler readout, the PTMV program was almost completely independent of event order before adaptation to CPS. Several routines to calculate the relative event clock time and spill number, however, did depend on the ordering of events and no longer gave sensible results. This did not affect the analysis since the RSX-DA spill numbers [118] were not affected.

3.3.9 N-tuples and Normfiles

In addition to writing the acceptable reconstructed events to tape, PTMV wrote various results to different disk files. This analysis, in fact, was primarily based on collections of two such files: analysis n-tuples [125] and normalization database input files called normfiles [124]. Other files were also produced, such as the monitor n-tuples [74], but were not used directly in this analysis.

The analysis n-tuple files were essentially a data summary tape on disk and were generated by the PTMV Class 3 process. Each n-tuple contained a fixed number of quantities describing a single event. The n-tuple files were generated with the PAW RZ n-tuple utilities associated with CERNLIB release 92A. Before being written to the n-tuple file, events were required to pass cuts similar to, but slightly looser than, those imposed on events output to tape. Two different n-tuple formats were maintained in the PAW n-tuple file, one for events possibly containing interesting interactions and one for randomly sampled beam events.

The normfiles were plain text files with records summarizing each spill. They were generated by the PTMV class 1 process. Data from the spill scalers, events scalers (summed over a spill), and trigger statistics (summed over a spill) were included. Also, some irretrievable information about the event ordering was included, such as the identification of the first event in a spill, for certain specialized corrections. All normfiles generated were used to create a single plain text file, called the normalization database. This normalization database was used as the source of spill scaler information for normalization. The normalization database had the attractive property of only containing information from spills for which all events that had been reconstructed, leading to improved bookkeeping of beam counts in normalization.

3.4 Simulation

3.4.1 Event Monte Carlo Program

The E665 event Monte Carlo program is divided up into two major stages. The Stage 1 Monte Carlo (MC1) generates ideal, simulated events. The Stage 2 Monte Carlo (MC2) calculates the detector response to these events. The complete Monte Carlo, called MC12, generates "fake events" which can be used to test the efficiency of the reconstruction software and the magnitude of smearing effects in the detectors and software.

MC1

The Stage One Monte Carlo creates ideal inelastic scattering events [7, 189]. A beam muon is generated using a file of track parameters from a random sampling of beam from Rbeam events [109]. An inelastic interaction is forced to occur to this beam muon. The kinematic parameters are selected at random from a user-defined kinematic distribution. The LUND package is used to generate the hadronic system from the struck parton. The GEANT package is used to propagate the particles through the magnetic fields and matter in the experiment. GEANT also models other processes occurring to the particles, such as pair creation, particle decay, hadronic interactions (using the GHEISHA package), certain forms of bremsstrahlung, and energy loss in matter. GAMRAD is used to simulate other forms of bremsstrahlung. The simulated event is then summarized by a list of the intersections of all particle tracks with a standard set of $Y - Z$ planes called keyplanes.

MC2

The Stage 2 Monte Carlo simulates how the apparatus responds to the simulated particles generated by the Stage 1 Monte Carlo [189]. It converts the keyplane hits into detector hits in the same format as the output of the raw data decoders. The detector efficiencies measured with raw data are used to model imperfect detector response assuming that all inefficiencies are uncorrelated from detector plane to detector plane. The effects of noise from delta rays and electronics glitches are also modelled.

Limitations

The MC12 program cannot be used to study all aspects of the experiment. Since Rbeam events are used for input, MC12 cannot be used unambiguously to test track reconstruction in the Beam Spectrometer. Pulse height information, decoder error condition effects, beam intensity and timing effects, and correlated noise and inefficiencies are largely ignored by MC12. Finally, there is, at present, no simulation of the calorimeter installed in MC12.

3.4.2 Radiative Corrections Program

The program used to calculate radiative corrections was version 35 of FERRAD [191, 131], developed by members of the EMC and NMC collaborations. It contains information on many radiative cross sections, such as coherent and quasi-elastic scattering. FERRAD is based on the treatment of radiative corrections to inelastic scattering cross sections by Mo and Tsai [154] and Tsai [200]. An extensive description of the program can be found in Reference [25].

FERRAD calculates the ratio of the one-photon-exchange cross section to the total cross section[5] as a function of the target material, the beam energy, y_{bj}, and x_{bj}. The total cross section calculation includes an exact treatment of coherent scattering and the quasi-elastic tail, an approximate treatment of the inelastic tail, the effects

---

[5] The phrase "total cross section" in the parlance of radiative corrections calculations refers to the sum of the differential cross sections for all electromagnetic processes, not the integral of the differential cross section.

of vacuum polarization loops for leptons and light quarks, a first-order treatment of electroweak interference, and a partial treatment of second-order corrections to the muon-photon vertex. Corrections related to the hadronic vertex have been predicted to be small [37], and are not included. The relative contributions of each of these processes is reported. FERRAD has been checked against a competing program, TERAD86, which is based on calculations by Bardin and colleagues [10, 37, 11]. For reasonable structure function input, the output of version 35 of FERRAD differs by no more than 2% from the output of the recently corrected version of the TERAD86 program [19].

Local changes to FERRAD were made to the program to increase the beam energy used, widen the (y_{bj}, x_{bj}) grid to match E665 acceptance, and fix minor coding flaws that became apparent with the increased beam energy. In order to accommodate the much lower values of x_{bj} and Q^2 to which our data extends, the F_2 model for the proton and the deuteron by Badełek and Kwieciński [31] was used as input to FERRAD. This model fuses QCD-based fits to precise F_2 data [145] with the ideas from Regge Theory and the Generalized Vector Meson Dominance model to produce a model of F_2 valid at all values of x_{bj} and Q^2. Their model actually includes several variations; the version labelled $D^{-}(2\ \text{GeV}^{-1})$ was used in this analysis. Three radiative corrections tables each were generated for H_2 and D_2 targets, at beam energies of 300, 500, and 700 GeV. Linear interpolation between the table values was used by my cross section ratio calculation program to determine the value of the corrections for a given target, beam energy, y_{bj}, and x_{bj} [127].

3.5 RUN90 Production

3.5.1 Interspill Split

Long before event reconstruction was undertaken, events containing target and spill scaler information were copied from the raw data tapes to other tapes [193]. The target and spill scaler data were later re-organized and written to a disk file [123]. This plain text database was used to calculate beam counts, trigger rates, and monitoring ratios for all of RUN90. In particular, the spill database was used in this analysis to identify acceptable data-taking periods and to measure the prescale factors applied to Rbeam triggers, as is discussed in Section 4.4.1. It was not consulted for the spill scaler information used in the final normalization of the data sets used.

Table 3.1: Data Sample I

Tape Label	Files Used	Begin of Tape Run	Hour	Date	End of Tape Run	Hour	Date
WD6514	10	12884	17:30	08-Aug-90	12884	20:45	08-Aug-90
WD6518	10	12889	03:30	09-Aug-90	12889	05:45	09-Aug-90
WD6519	10	12890	06:00	09-Aug-90	12891	08:45	09-Aug-90
WD6536	10	12918	15:50	10-Aug-90	12918	18:15	10-Aug-90
WD6539	6	12925	00:30	11-Aug-90	12925	02:00	11-Aug-90
WD6540	10	12926	02:00	11-Aug-90	12926	04:15	11-Aug-90
WD6543	8	12931	06:00	11-Aug-90	12931	08:00	11-Aug-90
WD6555	10	12969	15:00	12-Aug-90	12969	17:30	12-Aug-90
WD6556	10	12970	17:30	12-Aug-90	12970	20:00	12-Aug-90
WD6557	4	12975	21:00	12-Aug-90	12975	22:00	12-Aug-90
WD6558	10	12976	22:45	12-Aug-90	12976	00:30	13-Aug-90
WD6559	10	12977	00:45	13-Aug-90	12977	03:00	13-Aug-90
WD6562	4	12980	05:45	13-Aug-90	12980	06:15	13-Aug-90
WD6563	4	12981	06:15	13-Aug-90	12981	07:00	13-Aug-90
14	116	12884	17:30	08-Aug-90	12980	07:00	13-Aug-90

3.5.2 Data Sample Definition

A subset of the RUN90 data set was chosen for an initial pass at event reconstruction. The set of runs considered for this analysis were Run 12071 through Run 13267, practically all of the reasonable quality RUN90 data-taking. Runs dedicated to non-physics data-taking or exhibiting poor detector or trigger performance were not considered. Further criteria for data selection are described in Reference [126] and a detailed description of the data sets chosen can be found in [127].

The data sample used in this thesis is divided into two parts labelled Sample I and Sample II, corresponding to the two separate time periods in which the data was taken. Data Sample I is defined in Table 3.1 on page 64. It includes data taken in the time period from the re-timing of the SWM trigger to the beginning of a major calibration study. Data Sample II, defined in Table 3.2 on page 65, includes data from the end of the same calibration study to the end of RUN90. Note that the approximate time spanned by each tape is listed in the table in order to connect the physics data (organized by run number) to the target pressure data (organized by hour and day).

Table 3.2: Data Sample II

Tape	Files	Begin of Tape			End of Tape		
Label	Used	Run	Hour	Date	Run	Hour	Date
WD6633	4	13165	16:30	22-Aug-90	13167	19:00	22-Aug-90
WD6636	10	13172	20:45	22-Aug-90	13174	01:45	23-Aug-90
WD6637	10	13176	01:45	23-Aug-90	13177	06:30	23-Aug-90
WD6638	4	13179	06:30	23-Aug-90	13179	08:00	23-Aug-90
WD6639	7	13180	08:00	23-Aug-90	13180	10:15	23-Aug-90
WD6640	9	13181	10:15	23-Aug-90	13181	13:30	23-Aug-90
WD6641	8	13183	13:30	23-Aug-90	13183	15:30	23-Aug-90
WD6642	10	13183	15:30	23-Aug-90	13186	18:00	23-Aug-90
WD6643	10	13187	18:00	23-Aug-90	13188	21:00	23-Aug-90
WD6644	9	13189	21:00	23-Aug-90	13192	00:30	24-Aug-90
WD6645	10	13195	00:30	24-Aug-90	13197	03:15	24-Aug-90
WD6646	10	13198	03:15	24-Aug-90	13198	06:15	24-Aug-90
WD6647	10	13199	06:15	24-Aug-90	13200	09:45	24-Aug-90
WD6648	10	13201	09:45	24-Aug-90	13201	11:15	24-Aug-90
WD6649	10	13204	15:15	24-Aug-90	13204	18:15	24-Aug-90
WD6651	10	13206	18:45	24-Aug-90	13209	22:30	24-Aug-90
WD6653	9	13210	23:30	24-Aug-90	13214	04:00	25-Aug-90
WD6654	10	13217	05:30	25-Aug-90	13218	08:45	25-Aug-90
WD6655	10	13219	09:00	25-Aug-90	13219	12:15	25-Aug-90
WD6659	4	13223	17:00	25-Aug-90	13223	18:15	25-Aug-90
WD6661	8	13225	19:15	25-Aug-90	13225	20:45	25-Aug-90
WD6663	4	13227	22:00	25-Aug-90	13227	23:15	25-Aug-90
WD6666	11	13234	03:30	26-Aug-90	13239	07:00	26-Aug-90
WD6668	10	13240	07:15	26-Aug-90	13249	10:30	26-Aug-90
WD6669	6	13250	10:30	26-Aug-90	13255	13:00	26-Aug-90
WD6675	5	13266	04:45	27-Aug-90	13267	06:00	27-Aug-90
26	213	13165	16:30	22-Aug-90	13267	06:00	27-Aug-90

Table 3.3: PTMV 16.04 output cuts

Trigger Type	Tape Output Condition	N-tuple Output Condition
Physics	$\nu > 40$ GeV .OR. $\theta_{scat} > 0.3$ mrad	$\nu > 24$ GeV .OR. $\theta_{scat} > 0.2$ mrad
Rbeam	all accepted	all accepted
Halo	all rejected	all rejected
Interspill	all accepted	all rejected

Table 3.4: SAT events reconstructed and output

	Sample I		Sample II	
Cut Level	Events Passing	Fraction Passing	Events Passing	Fraction Passing
PTMV Input	421949	100.0%	737659	100.0%
PTMV N-tuple Output	151779	36.0%	284465	38.6%
Liquid Target	57066	13.5%	112444	15.2%

3.5.3 PTMV

Data Production

The data were analyzed with PTMV version 16.04 on the Fermilab SGI CPS farm. After reconstruction in a Class 2 process, events are written to tape by a Class 3 process. Events intended for physics analysis were required to pass the cuts listed in Table 3.3 on page 66 before being written to tape. Before being output to the analysis n-tuple, physics events were required pass weaker cuts. These output cuts were not intended to define the data set as much as to reduce the sheer volume of the output by eliminating events likely to contain unscattered beam[6]. With these cuts the output of PTMV was limited to less than two 8 mm tapes of output data for every one 8 mm tape of raw data input. The number of events processed are listed by trigger in Tables 3.4, 3.5, and 3.6.

---

[6] In some cases, the size of the analysis n-tuples reached the maximum n-tuple file size limit of about 16 Megabytes imposed by the CERN PAW package for the n-tuple file configuration used. The affected analysis n-tuples were regenerated from the output tape with the NTPMAKE2 program using the same kinematic cuts as PTMV, but restricting the output to liquid targets only.

Table 3.5: SVS events reconstructed and output

	Sample I		Sample II	
Cut Level	Events Passing	Fraction Passing	Events Passing	Fraction Passing
PTMV Input	138552	100.0%	277108	100.0%
PTMV N-tuple Output	60246	43.5%	120680	43.5%
Liquid Target	21285	15.4%	44784	16.2%

Table 3.6: SWM events reconstructed and output

	Sample I		Sample II	
Cut Level	Events Passing	Fraction Passing	Events Passing	Fraction Passing
PTMV Input	206501	100.0%	357773	100.0%
PTMV N-tuple Output	57641	27.9%	112010	31.3%
Liquid Target	21123	10.2%	43229	12.1%

Reconstruction Performance

The reconstruction program quoted errors on the measurement of the vertex location and kinematic variables based on the track fit and vertex fit errors. For instance, Figure 3.3 on page 68 shows the dependence of the error quoted in the X-coordinate of the vertex[7] as a function of Q^2. The concentration of events at low Q^2 and high $\sigma(X_{vtx})$ were predominantly low multiplicity events, such as bremsstrahlung and muon-electron elastic scattering. The concentration of events at lower $\sigma(X_{vtx})$ were predominantly high multiplicity events such as muon-nucleon inelastic scattering.

Figure 3.4 on page 68 shows the dependence on y_{bj} of the relative error in y_{bj}. Several bands were present which were distinguished by the number of constraints (useful hits in tracking chambers) on the scattered muon track fit. The visible bands were due to the presence or absence of the chambers crucial to energy resolution. The faint upper band was dominant in the RUN87 construction [46]. The improvement in small angle scattered muon reconstruction in RUN90 lead to an improvement in the relative error in y_{bj}, as indicated by the dominance of the lower band.

---

[7] Actually, this is $\sqrt{\sigma^2_{xx}(X_{vtx})}$, the dominant term in the total error on the X-coordinate of the vertex.

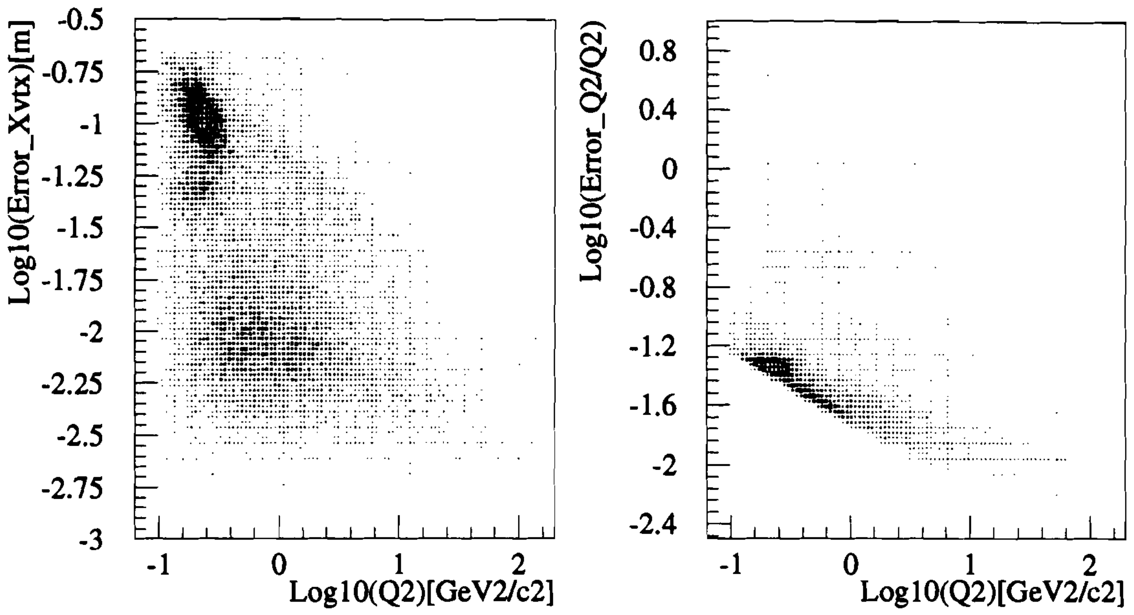

Figure 3.3: Error in X_{vtx} and relative error in Q^2

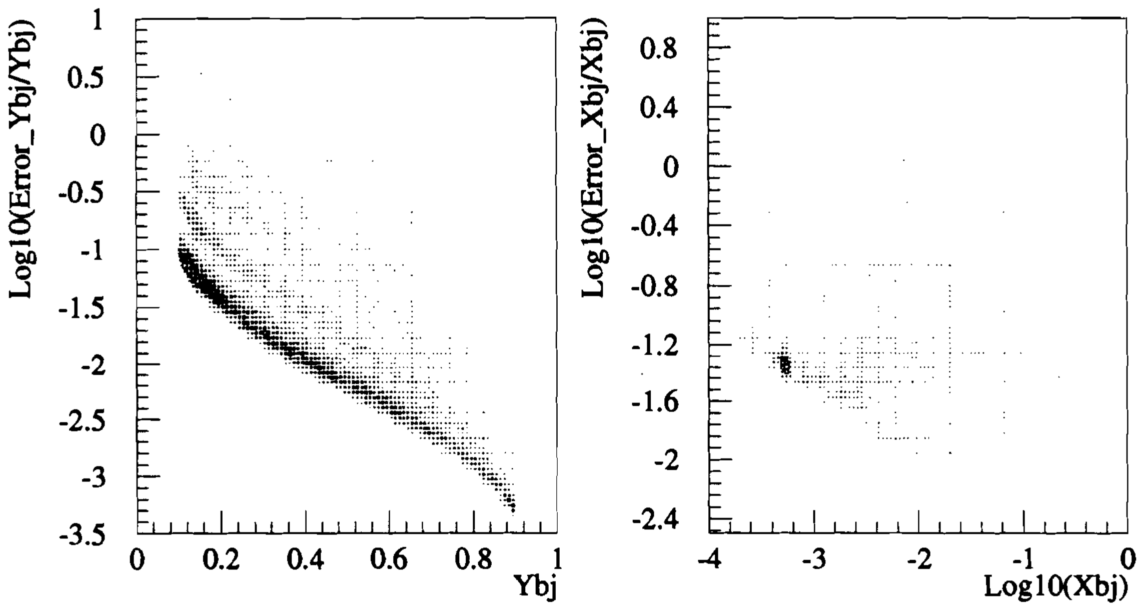

Figure 3.4: Relative error in y_{bj} and x_{bj}

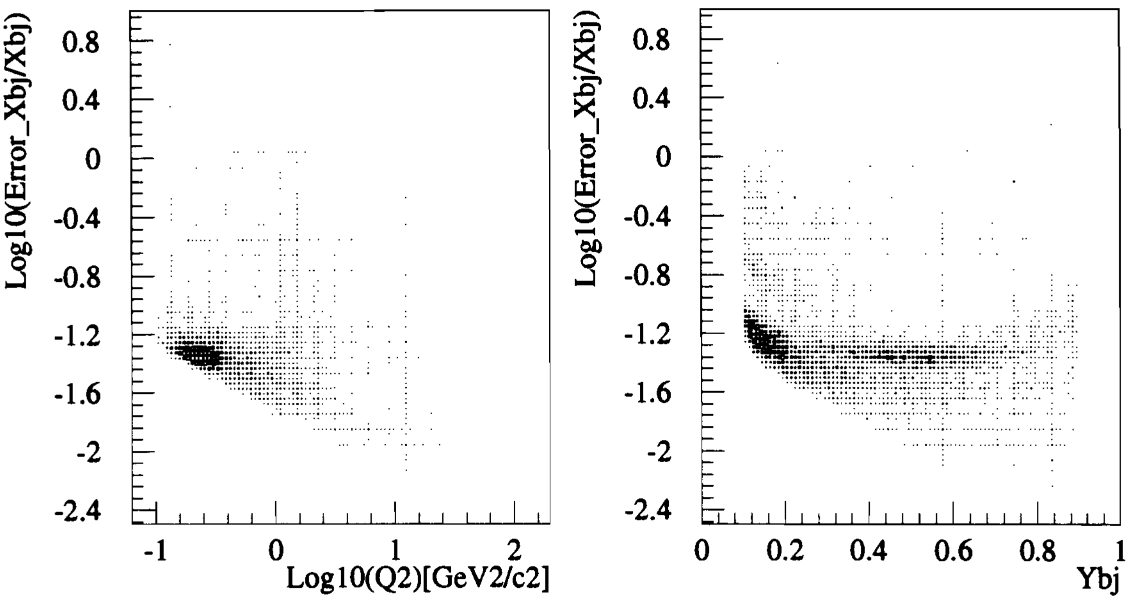

Figure 3.5: Relative error in x_{bj} versus Q^2 and y_{bj}

Also shown in Figure 3.4 is the dependence on x_{bj} of the relative error in x_{bj}. At small x_{bj} the relative error was dominated by the error in Q^2. In this region, the data were at low Q^2, high y_{bj}. The small Q^2 data were affected by poor scattering angle resolution at small angles. At large x_{bj} the relative error was dominated by the error in y_{bj}. Here, the data was at low y_{bj}, where there was very poor resolution in the difference between the large incoming and scattered muon energies. These effects can also be seen in Figure 3.5 on page 69.

3.5.4 MC12

The generation of simulated events was performed by the program MC12TP90. The program used the same detector constants as were used in real data event reconstruction. MC12TP90 was not run under the CPS processing system, but was run as a normal single computer process. MC12TP90 used LUND version 5.2, LEPTO 5.2, JETSET 6.3, ARIADNE 3.0, GEANT 3.12, and an E665-supported radiative calculations program derived from the EMC program GAMRAD [177, 112] which is based on the Mo and Tsai treatment [154, 200]. The implementation of MC12TP90 was geared to study two particular systematic effects that may have affected the measurement of F^n/F^p, namely, smearing of the kinematic variables and differences in the trigger acceptance related to hadron multiplicity or other target-related effects. Three thousand events each for H_2 and D_2 were generated using a cross section based on Morfín and Tung parton distributions [159]. Also, three thousand events each for H_2 and D_2 were generated using a cross section that varied as $1/Q^2$ instead of the physical $1/Q^4$. This was done to enhance the number of events at large x_{bj} where smearing effects were expected to be noticeable. The data was reconstructed by PTMVTP90, a single process program equivalent to the event reconstruction program run under CPS. An n-tuple, extended to hold Monte Carlo information, was generated by PTMVTP90.

3.6 Post-Production Processing

After event reconstruction, a couple of corrections to the data were made to fix shortcomings in the reconstruction program. The momentum miscalibration between the Beam Spectrometer and the Forward Spectrometer requires a transformation of the beam energy in order to avoid a systematic shift of the kinematics from the correct values. Also, variations in the calorimeter response require corrections that were not applied during event reconstruction.

3.6.1 ν Offset

The ν Offset is an energy miscalibration of the Beam Spectrometer and the Forward Spectrometer [130]. It is investigated by measuring the distribution of ν in Rbeam events. The set of Rbeam events used is restricted to exclude scattering events. The effect appears as an offset of the ν distribution from the expected value of 0. The mean offset was about 11 GeV in RUN90. Many attempts to understand the source of this anomaly have been made [148, 188, 190]. The exact cause of this energy miscalibration is still under study. I have developed an *ad hoc* scheme to correct the data set used in this analysis which I estimate very nearly reproduces the properly calibrated data set [182, 196]. A systematic error is added to the reported physics results to account for the expected imperfections in this correction scheme.

The ν Offset correction scheme assumes that the offset in ν comes entirely from systematic errors in the incoming muon energy E. A hypothetical model of the dependence of the ν Offset on the reported (assumed incorrect) E was constructed. The model assumes that there are only two sources of error in the measurement of E, an energy scale error due to using an inappropriate value of the NMRE $p_\perp$ kick and an offset in the measured deflection angle through NMRE. This model leads to the following dependence of the ν Offset ΔE on the reported beam energy E:

$$\Delta E = E\left(1 - \frac{A}{1 - B\frac{E}{E_0}}\right) \tag{3.2}$$

A and B describe the energy scale error and angle offset error, as in

$$A \equiv \frac{p_\perp^*}{p_\perp} \tag{3.3}$$

$$B \equiv \frac{\delta\theta\, E_0}{p_\perp^*} = \frac{\delta\theta}{\sin\theta_0} \tag{3.4}$$

where $p_\perp^*$ represents the correct NMRE $p_\perp$ kick value and $\delta\theta$ is the value of the angle offset. The constant E_0 is arbitrarily set to 500 GeV. The constant $\sin\theta_0$ is then about 3 mrad. The measured and hypothetical dependences of the ν Offset on the beam energy are shown in Figure 3.6 on page 72. The parameters A and B were determined by a least χ^2 fit of the function in Equation 3.2 to the mean offset and energy in 7 energy bins requiring that the mean ν Offset for the data sets be approximately zero. In the fit, the value of A was forced to remain close to the value measured independently with a special test run in which protons of known momentum where sent directly through the experiment [182, 196]. The values arrived at are:

$$A = 0.99214 \tag{3.5}$$

$$B = -0.0174 \tag{3.6}$$

The beam energy for all events was then transformed by

$$\begin{aligned} E^* &= E - \Delta E \\ E^* &= E\left(\frac{A}{1 - B\frac{E}{E_0}}\right) \end{aligned} \tag{3.7}$$

and the event kinematics were recalculated using the corrected beam energy E^*, the reported scattered muon energy, and the reported scattering angle.

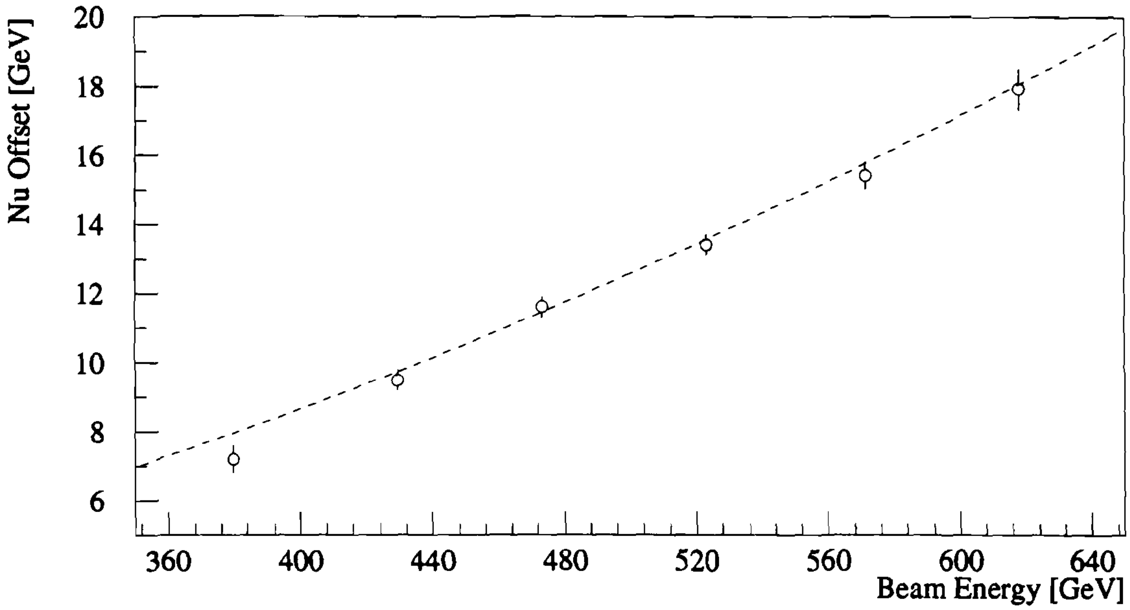

Figure 3.6: Measured (points) and hypothetical (curve) beam energy dependence of the ν Offset

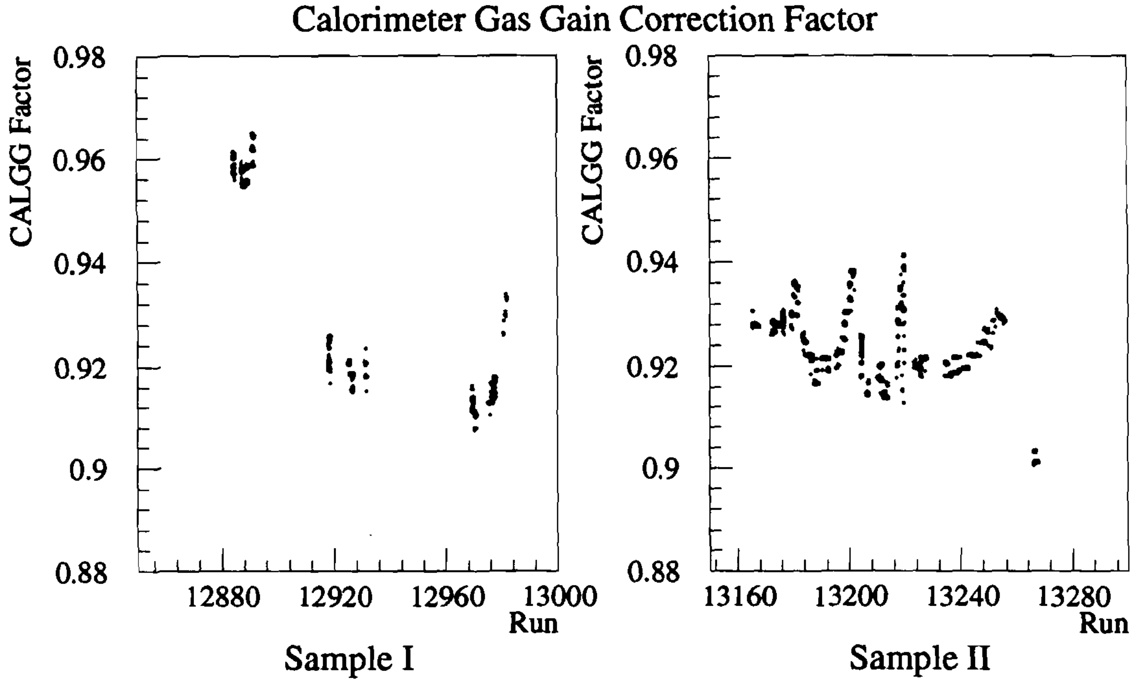

Figure 3.7: Calorimeter gas gain corrections in Sample I (left) and II (right)

3.6.2 CAL Gas Gain

Final calibration of the CAL data was not performed in the event reconstruction program PTMV. The gas gain corrections applied were based on out-of-date calibration data [137]. In addition to the gas gain-related corrections, there is a -16% calibration adjustment to the calorimeter energy.

Two correction factors are applied to all energies reported by the calorimeter software [127]. A run-dependent correction is applied to treat variations due to atmospheric pressure, temperature, and high voltage using current data. The value of this correction is shown in Figure 3.7 on page 72. An overall rescaling of the calorimeter response is also applied. The mean effect of these corrections is to lower the calorimeter energy by 20%. The errors in these corrections do not affect the analysis since the cut values associated with the calorimeter energy are determined from the observed corrected calorimeter energy distributions.

Chapter 4

Physics Analysis

The first precept of the rule is that everything that surrounds us is an unfathomable mystery.

The second precept of the rule is that we must try to unravel these mysteries, but without ever hoping to accomplish this.

The third, that a warrior, aware of the unfathomable mystery that surrounds him and aware of his duty to try to unravel it, takes his rightful place among the mysteries and regards himself as one. Consequently, for a warrior there is no end to the mystery of being, whether that means being a pebble, or an ant, or oneself. That is a warrior's humbleness. One is equal to everything.

— Florinda

Carlos Castañeda, *The Eagle's Gift* (1981)

4.1 Analysis Procedure

This chapter describes the extraction of the ratio of the structure function F_2 for deuterium to that for hydrogen using the data sample described in Chapter 3. The ratio of neutron and proton structure functions F_2 is then extracted from the cross section ratio. A brief outline of this process is given here to demonstrate the relationship between the various studies that constitute this analysis. A detailed description of the extraction method is given in Appendix E.

The structure function ratio is extracted from the cross section ratio through Equation 4.1 and the assumption that the function R is identically the same for H_2 and D_2.

$$\frac{d\sigma^{1\gamma}}{dxdQ^2}(x,Q^2) = \frac{4\pi(\alpha\hbar c)^2}{Q^4}\left\{1 - y - \frac{Q^2}{4E^2} - \frac{y^2 + Q^2/E^2}{2(1+R(x,Q^2))}\right\}\frac{F_2(x,Q^2)}{x} \tag{4.1}$$

The extraction of the cross section ratio from the data is based on the relation between the differential number of scatters and the differential cross section for all scattering processes.

$$\frac{dN}{d\xi}(\xi) = \int_{all\ \xi^*} d\xi^* \int_{accepted\ \mu^*} d\mu^* \, \frac{dL}{d\mu^*}(\mu^*)\, A(\xi^*,\mu^*)\, E(\xi^*,\mu^*)\, S(\xi^*,\mu^*;\xi)\, \frac{d\sigma^{total}}{d\xi^*}(\xi^*) \tag{4.2}$$

where ξ represents the set of true kinematic variables (x_{bj}, Q^2) describing the event and ξ^* represents the measured (x^*_{bj}, Q^{2*}) associated with the event. L is the integrated luminosity, A is the experiment acceptance, E is the experiment efficiency, S is the experiment smearing function, and $\frac{d\sigma^{total}}{d\xi^*}$ is the differential cross section for scattering by all processes. This relation also addresses the dependence of these quantities on the measured beam phase space, using μ^* to represent the measured phase space of the accepted beam muon. The ratio of cross sections for different nuclear targets is extracted from ratios of this relation for different targets. Of the quantities involved, the luminosity (by design) and the number of scatters are expected to differ for different nuclear targets.

4.1.1 Integrated Luminosity

The integrated luminosity is measured using:

$$\frac{dL}{d\mu^*}(\mu^*) = N_A M\, l_f N_\mu B(\mu^*) \tag{4.3}$$

where N_A is Avogadro's number, M is the molar density of nuclei in the target material, l_f is the defined fiducial length of the target, N_μ is the total number of accepted beam muons in the study, and $B(\mu^*)$ is the normalized beam phase space density. $B(\mu^*)$ is used to take into account effects that are strongly dependent on the beam energy (for example, ν resolution) and beam position (for example, detector efficiencies).

The molar density of nuclei M is calculated from the measured liquid target pressure. This is converted to a temperature, which is in turn converted to a mass density. Knowing the isotopic composition of the target material, the molar density can then be found using:

$$M = \frac{\rho}{A_W} \tag{4.4}$$

where A_W is the atomic weight of the target material and ρ is the mass density of target material. The material used in the experiment targets, however, is not pure. Approximately 4.4% of the deuterium target volume was occupied by HD molecules. This impurity affects the target molar density, as well as the number of target nucleons and the extracted cross section. The molar density must be calculated by an iterative process since both the density of the D_2 and HD molecules must be determined assuming that all molecules are at the same temperature.

The fiducial length l_f is defined to be slightly smaller than the physical target length to avoid including in the data sample scatters that occur in the target vessel material.

The counting of the number of beam muons entering the experiment N_μ is called normalization. This is done by a number of independent methods. The results of each method are used to check for systematic errors in the other methods.

The beam phase distribution $B(\mu^*)$ is determined from a study of a randomly selected sample of beam events. This is used in the calculation of the luminosity and as an input to the Monte Carlo simulation of events.

4.1.2 Event Distribution Corrections

To insure that the data sample is not contaminated by events occurring in the target vessel that are mistakenly reported as having occurred in the target material, an "empty target subtraction" is performed. The number of events gathered on an empty target vessel N^{empty}, weighted by the ratio of the empty target and full target beam flux, is subtracted off the accepted number of events bin by bin. The size of this correction is quite small because of the conservative definition of the fiducial target and the quality of the event reconstruction at small angles.

Events that appear to be muon-electron elastic scatters are cut from the data sample. The number of these events is signified by $N^{\mu-e}$. The events are easy to identify by their topology and energy deposition in the calorimeter. The cuts required to eliminate these events from the data sample are quite efficient, and do not eliminate many interesting events.

Radiative events, specifically bremsstrahlung events, can be identified and cut from the data set. The number of these events is signified by N^{brems}. The events are not as obvious as muon-electron elastic scatters. The cuts used are less efficient at removing bremsstrahlung from the data set without also removing a significant number of interesting events from the data set.

These adjustments lead to a corrected raw event count N calculated from the actual raw event count N^{actual}.

$$N = N^{actual} - N^{\mu-e} - N^{brems} - N^{empty}\frac{N_\mu}{N_\mu^{empty}} \tag{4.5}$$

In a different approach, radiative events are not explicitly cut from the data, but are corrected for by weighting each event by a calculated radiative corrections weight:

$$\eta(\xi) \equiv \frac{\frac{d\sigma^{1\gamma}}{d\xi}(\xi)}{\frac{d\sigma^{total}}{d\xi}(\xi)} \tag{4.6}$$

The weighted event count is defined as:

$$W(\xi) \equiv \eta(\xi)N(\xi) \tag{4.7}$$

4.1.3 Cross Section Ratio Extraction

To measure the differential cross section using Equation 4.2, one must solve a complicated integral equation. This is done by using a iterative procedure with an iterative correction defined by:

$$I(\Delta\xi) \equiv \frac{\int\limits_{\Delta\xi} d\xi\,\eta \int\limits_{all\ \xi^*} d\xi^*\,B\,A\,E\,S\,\frac{d\sigma^{total}}{d\xi^*}}{\Delta\xi\,\frac{d\sigma^{1\gamma}}{d\xi}(\xi = \bar{\xi})} \tag{4.8}$$

where the term $\Delta\xi$ represents the area of a measurement bin and $\bar{\xi}$ is the mean value of the kinematic variables of the events falling into that bin. This uses the shorthand expression:

$$f(\Delta\xi) \equiv \int\limits_{\Delta\xi} d\xi\,\frac{df}{d\xi}(\xi) \tag{4.9}$$

The result of this iterative solution is given by:

$$\frac{\frac{d\sigma^{1\gamma}}{d\xi}(\xi = \bar{\xi}; D_2)}{\frac{d\sigma^{1\gamma}}{d\xi}(\xi = \bar{\xi}; H_2)} = \frac{M^{H_2}}{M^{D_2}}\,\frac{N_\mu^{H_2}}{N_\mu^{D_2}}\,\frac{I^{H_2}(\Delta\xi)}{I^{D_2}(\Delta\xi)}\,\frac{W^{D_2}(\Delta\xi)}{W^{H_2}(\Delta\xi)} \tag{4.10}$$

Ideally the procedure would involve using an initial guess of the I ratio in order to evaluate an approximation of Equation 4.8. This result would then used to recalculate Equation 4.10, and so on until convergence is achieved. Due to the relatively large statistical errors involved in the structure function ratio measurement, however, I choose to estimate the size of the iterative correction and assign it as a systematic error to the final results reported.

4.2 Beam Definition

4.2.1 Beam Cuts

Reconstructed Beam

The requirement made of any event used in this analysis is that it contain an acceptable beam. Obviously, a beam muon track must be reconstructed in the beam spectrometer for any analysis to proceed.

Beam Timing

The incoming muon is required to be the only incoming muon in the same RF bucket as the scattered muon. This requirement helps insure that the incoming and scattered muons are in fact the same particle. The SBT detector is used to indicate the timing of the incoming muon. The requirement made is that the all SBT counters intersected by the beam track found in the PBT detector have fired. At least six of the SBT planes must be intersected, and all intersected planes must have a fired counter along the PBT track for the timing of the track to be declared acceptable. The assumption is made that SBT latches in these six or seven planes, taken as a set, have a time resolution of better than one RF period. No requirements are made on the number of out-of-time muons.

Beam Energy

Next, the muon beam is required to be in an acceptable energy range. There is some concern that events with beam detected beyond either end of the energy range may contain unusual and undesirable characteristics. Given that the muon beamline was designed to accept muons over a restricted momentum range for any single tuning of the beamline magnets, both the low and high end of the momentum spectrum include muons that probably scraped beamline magnets. At sufficiently low momentum, for instance, some of the assumptions made in the beam momentum calculation, such as the neglect of multiple Coulomb scattering in the beam spectrometer, begin to fail. Acceptable incoming muons have energy in the range of 350 GeV to 650 GeV inclusive.

Table 4.1: Fraction of RSATB events passing beam cuts

	Sample I		Sample II	
Cut Level	Events Passing	Fraction Passing	Events Passing	Fraction Passing
All RSATB events	31992	—	57990	—
Liquid Target	12791	100.0%	24169	100.0%
Beam Reconstruction	12625	98.7%	23942	99.1%
Beam Timing	12130	94.8%	23538	97.4%
Beam Energy	11991	93.7%	23062	95.4%
Beam Track Fit Quality	11758	91.9%	22698	93.9%
Beam through Target	11758	91.9%	22694	93.9%
Output from Beam Cuts	11758	91.9%	22694	93.9%

Beam Track Fit Quality

The beam track fitting is required to report a χ^2 probability ≥ 0.001 for the beam track under consideration to avoid using poorly reconstructed beam tracks.

Beam Penetration of Target

Finally the acceptable beam muon must fully penetrate the experiment target. This insures that all events have the same fiducial target definition. This cut is implemented by projecting the beam muon track upstream of the target with a straight line extrapolation into the target. Since the target is in an essentially magnetic field-free region, the straight line extrapolation is adequate to find where the track intercepts the target faces. The projected track must intercept both the upstream and downstream target faces. The track must intersect the target faces at least 0.5 cm inside of the radial edge of each face in order to be accepted. This removes any sensitivity to errors in the target constants in use. Since the beam profile is smaller than the target cross section and approximately centered on the targets, this cut does not have a strong effect on the fraction of events passing the beam cuts.

4.2.2 Effect of the Beam Cuts

Table 4.1 on page 80 lists the number and fraction of RSATB events passing the beam cuts. Table 4.2 on page 81 lists the number and fraction of RLATB events passing the beam cuts. Only 10% of the luminosity is lost due to the beam cuts.

Table 4.2: Fraction of RLATB events passing beam cuts

	Sample I		Sample II	
Cut Level	Events Passing	Fraction Passing	Events Passing	Fraction Passing
All RLATB events	23181	—	43986	—
Liquid Target	9329	100.0%	18380	100.0%
Beam Reconstruction	9194	98.6%	18187	98.9%
Beam Timing	8620	92.4%	17496	95.2%
Beam Energy	8457	90.7%	16951	92.2%
Beam Track Fit Quality	8285	88.8%	16657	90.6%
Beam through Target	8285	88.8%	16653	90.6%
Output from Beam Cuts	8285	88.8%	16653	90.6%

Table 4.3 on page 82 lists the number and fraction of SAT events passing the beam cuts. Table 4.4 on page 82 lists the number and fraction of LAT events passing the beam cuts. Since the initial output cuts made by the event reconstruction program require that a beam be reconstructed and that a vertex be found, the statistics presented here are somewhat distorted.

4.3 Target Definition

4.3.1 Fiducial Target Extent

The fiducial extent of the experiment target is defined after considering two opposing points. Maximizing the accepted volume of the target, up to its physical extent, increases the number of scatters in the data sample. Some scatters in nearby material, however, are misidentified as having occurred in the target material. While the empty target subtraction can correct for some of these events, it is undesirable to rely heavily on the empty target subtraction due to the large relative error involved. The fiducial target is defined to be as close to the physical target in size as possible while keeping the number of interactions occurring in the target vessel material, as seen in the empty target data set, to a minimum. The fiducial target is defined by the cuts applied to the interaction vertex location, described in Section 4.6.1. Since the same cuts are applied to each target, and since the cuts were designed to eliminate any sensitivity to errors in the target constants, the ratio of l_f for the targets is exactly one by construction.

Table 4.3: Fraction of SAT events passing beam cuts after initial output cuts

	Sample I		Sample II	
Cut Level	Events Passing	Fraction Passing	Events Passing	Fraction Passing
Output from PTMV	151779	—	284465	—
Liquid Target	57066	100.0%	112444	100.0%
Beam Reconstruction	57066	100.0%	112444	100.0%
Beam Timing	54742	95.9%	110583	98.3%
Beam Energy	53222	93.3%	106160	94.4%
Beam Track Fit Quality	52078	91.3%	104451	92.9%
Beam through Target	50513	88.5%	102851	91.5%
Output from Beam Cuts	50513	88.5%	102851	91.5%

Table 4.4: Fraction of LAT events passing beam cuts after initial output cuts

	Sample I		Sample II	
Cut Level	Events Passing	Fraction Passing	Events Passing	Fraction Passing
Output from PTMV	67056	—	131323	—
Liquid Target	23626	100.0%	48672	100.0%
Beam Reconstruction	23626	100.0%	48672	100.0%
Beam Timing	22955	97.2%	47624	97.8%
Beam Energy	22153	93.8%	45263	93.0%
Beam Track Fit Quality	21644	91.6%	44465	91.4%
Beam through Target	21294	90.1%	44024	90.5%
Output from Beam Cuts	21294	90.1%	44024	90.5%

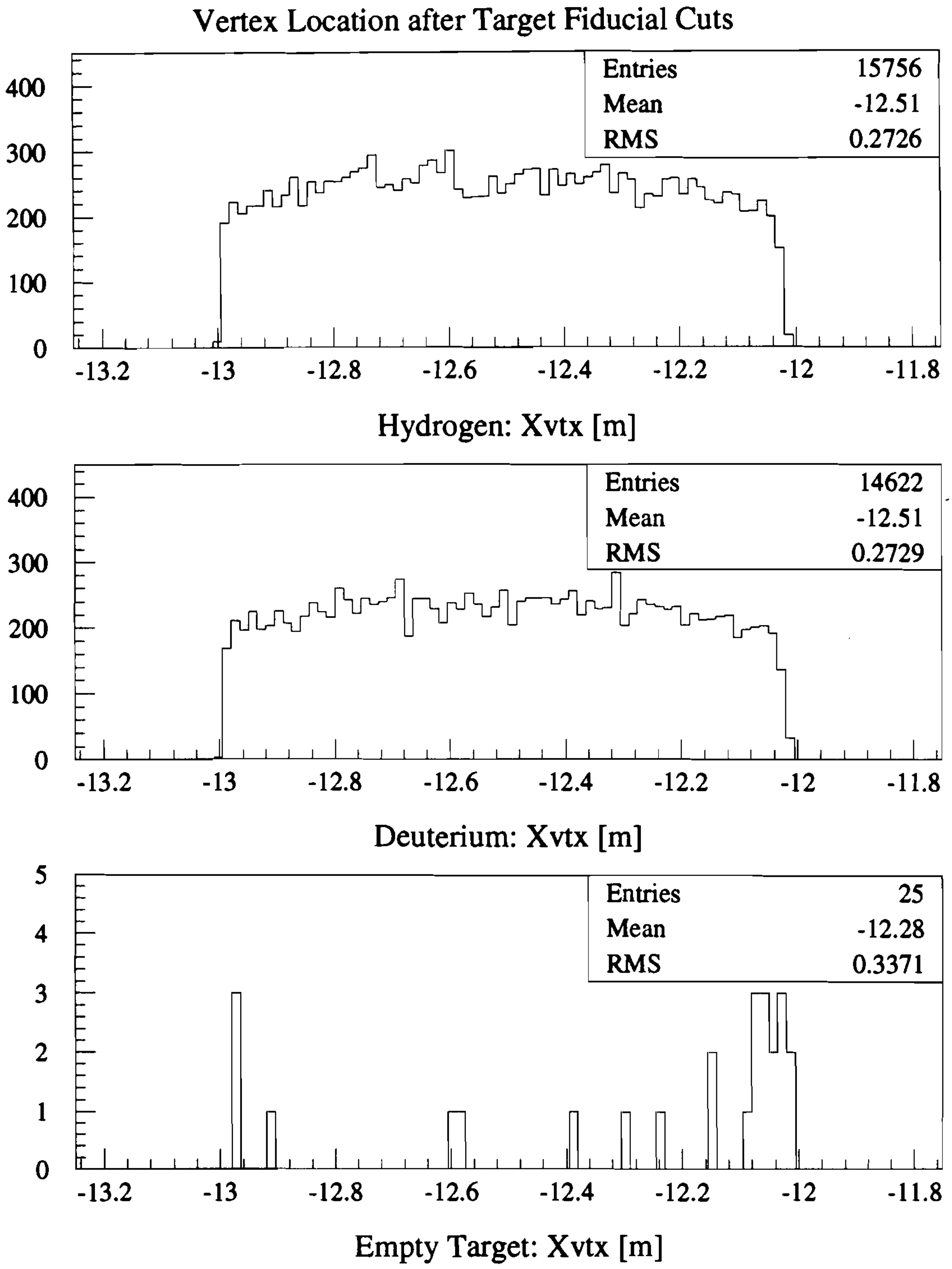

Figure 4.1: X-coordinate of accepted interaction vertices

Table 4.5: Deuterium target chemical assay

Compound	% Volume Fraction
D_2	95.5 ± 0.3
HD	4.4 ± 0.2
N_2	0.07 ± 0.03
H_2	0.06 ± 0.02
O_2	0.014 ± 0.004
H_2O, HDO, D_2O	< 0.05
CO_2	< 0.005
Ar	< 0.004
All other	*not measured*

4.3.2 Target Composition

The chemical content of the deuterium target was analyzed using a boil-off test [81]. The results are shown in Table 4.5 on page 84. Hydrogen deuteride (HD) is the only impurity causing concern. The cross section analysis takes this into account when considering the target molar density and the extraction of the cross section from the inelastic scattering event distribution. The chemical content of the hydrogen target is assumed to be the natural isotopic mix, which is essentially pure hydrogen.

4.3.3 Target Density

The target densities are derived from the measurement of the saturated vapor pressure in the cryogenic liquid reservoir [128]. The mean raw saturated vapor pressures reported for the two data samples are treated separately. The raw pressure is adjusted according to the calibration data for the pressure transducer [14]. The adjusted target pressure for the hydrogen target in the two data samples used is shown in Figure 4.2 on page 85, while that for deuterium is shown in Figure 4.3 on page 85.

For a particular molecular spin distribution in the liquid, the temperature of the liquid is uniquely related to its saturated vapor pressure. The temperature in turn is uniquely related to its density. The data used assumed that H_2 is in the "para" spin state [192, 141] which is a good approximation to the actual "equilibrium" spin state reached some time after liquefaction. The data used assumed D_2 is in the "normal" spin state mixture, however, not the equilibrium spin state [207, 63, 113]. The time constant for D_2 to convert to the equilibrium configuration is 200 times larger than that for H_2 [207], making it unlikely that a significant fraction of the liquid reached

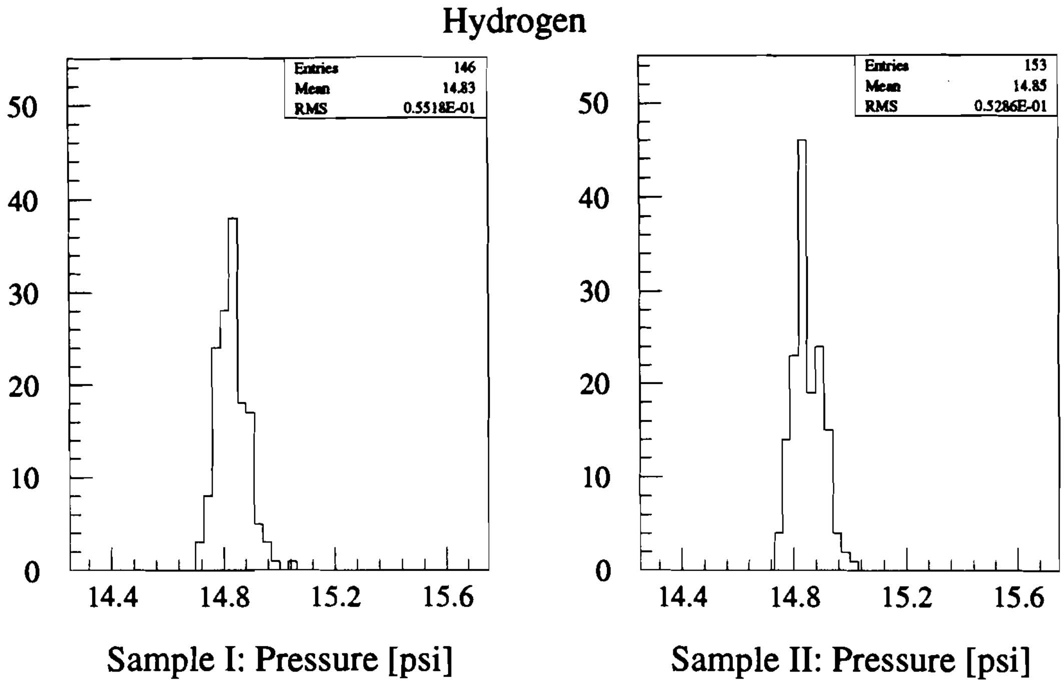

Figure 4.2: Adjusted H_2 pressure in Samples I (left) and II (right)

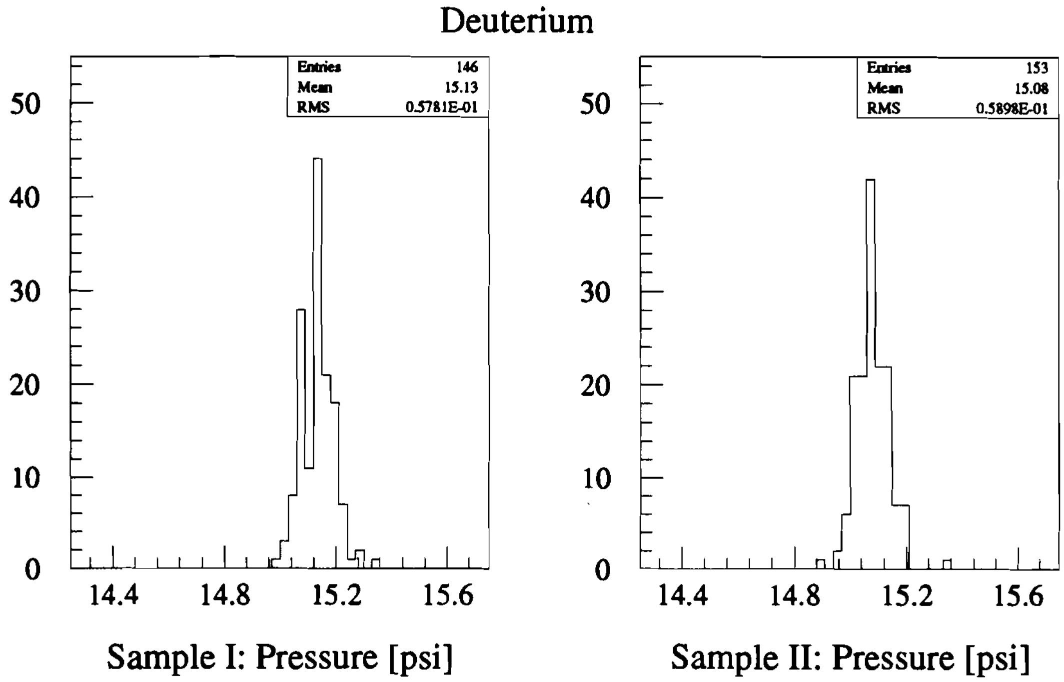

Figure 4.3: Adjusted D_2 pressure in Samples I (left) and II (right)

Table 4.6: Liquid target densities for H_2, D_2, and D_2 corrected for HD contamination (labelled D_2^*)

	Sample I	Sample II
H_2 Raw Pressure [psi]	14.35 ± 0.08	14.36 ± 0.07
H_2 Adjusted Pressure [psi]	14.84 ± 0.11	14.85 ± 0.10
H_2 Temperature [K]	20.304 ± 0.033	20.306 ± 0.032
H_2 Mass Density [mg/cm^3]	70.734 ± 0.044	70.730 ± 0.043
H_2 Molar Density [mol/m^3]	35090 ± 22	35088 ± 22
D_2 Raw Pressure [psi]	16.28 ± 0.08	16.23 ± 0.08
D_2 Adjusted Pressure [psi]	15.13 ± 0.11	15.08 ± 0.11
D_2 Temperature [K]	23.765 ± 0.035	23.753 ± 0.035
D_2 Mass Density [mg/cm^3]	162.37 ± 0.10	162.40 ± 0.11
D_2 Molar Density [mol/m^3]	40309 ± 26	40317 ± 27
D_2^* Adjusted Pressure [psi]	14.45 ± 0.11	14.40 ± 0.11
D_2^* Temperature [K]	23.605 ± 0.036	23.594 ± 0.036
D_2^* Mass Density [mg/cm^3]	162.95 ± 0.13	162.90 ± 0.14
D_2^* Molar Density [mol/m^3]	40410 ± 32	40418 ± 33

this state.

The calculation of the density of D_2 is complicated by the presence of HD molecules in the D_2 target [181, 128]. This requires that the temperature and pressure of the D_2 and HD components be calculated in an iterative procedure, using the original "pure" D_2 values as a starting point and requiring that the temperatures of the two molecular species be the same. The behavior of HD is described in References [207, 63]. Correction for the contamination causes an approximately 0.25% increase in the value of the D_2 molar density.

4.4 Normalization

Measurement of the integrated luminosity requires measurement of the number of acceptable beam muons entering the experiment which could have generated a deep-inelastic scatter. This counting of the number of acceptable beams entering the experiment is called normalization, and is a leading source of experimental error in past Inelastic Scattering experiments. Fortunately, to measure the cross section ratio, one need only measure the relative, not the absolute, number of beam muons accepted on each target. This simplification permits several different means of normalization to be used to verify the beam count ratio [129].

4.4.1 Rbeam Normalization

Rbeam events are a random sampling of the beam used in the physics triggers. The RSATB trigger sampled the beam used in the SAT trigger, and the RLATB sampled the beam used in the SVS, SWM, CVT, and WAM triggers. Combined with the measured prescale factor applied to the appropriate beam signal (as opposed to the nominal prescale factor set in hardware), the number of beam muons in the Rbeam events that pass the cuts applied to beams in physics trigger events gives the number of acceptable beam muons that entered the experiment. Rbeam events are a very powerful tool for normalization since they permit the study of acceptance effects due to the beam cuts applied. Also, since the events are embedded in the physics event data set, there are no "bookkeeping" errors involved as there can be with scaler measurements.

$$N_\mu = N_{Rbeam} \, F_{prescale} \tag{4.11}$$

where N_{Rbeam} is the number of Rbeam events passing the beam cuts and $F_{prescale}$ is the actual Rbeam prescale factor.

Prescale Factor Measurement

The prescale factor used in the definition of the Rbeam triggers has been measured. The measurements currently available use the spill database and are calculated with the program TRIGRAT4. The quantity actually measured was the Prescale Ratio which is defined as the ratio of the measured prescale factor (LiveBeam/Rbeam) and the documented hardware prescale factor.

$$R_{prescale} \equiv \frac{F_{prescale}}{F_{setting}} \tag{4.12}$$

where $F_{setting}$ is the setting on the prescaler hardware. The prescale ratio distribution, measured spill by spill, does not necessarily have to peak at unity [197, 129], but did during the time period in which the data in this analysis was gathered. The prescale

Table 4.7: Prescale factor ratios

Targets	SAT	LAT
H_2/D_2	0.9976 ± 0.0038	1.0043 ± 0.0079
$H_2/Empty$	1.0071 ± 0.0053	0.9958 ± 0.0097
$D_2/Empty$	1.0094 ± 0.0057	0.9916 ± 0.0101

ratios for periods of different prescale settings were originally measured separately since it was suspected that the prescale factor ratio may have been dependent on the prescaler setting. For all normal periods of data-taking, however, the prescale factor ratios were approximately 1. Figure 4.4 on page 89 shows the prescale factor ratios for the period covered by this thesis. No time dependence could be found to the ratios, so all measurements of the ratios for RUN90 were combined. The results are summarized in Table 4.7 on page 88.

Note that the interfile event loss described in Section 2.7.3 does not affect the results of this prescale factor measurement, even though the spill scalers were used to measure the prescale factor ratios. The only spills used were those in which both the gated beam and the gated Rbeam totals were reported by the spill scalers. Thus, if one number was lost, the other was lost as well, and only the total statistics involved in the measure of the ratio, hence the quality of the statistical precision, was reduced. The measured ratio itself was unaffected.

No count was kept of the gated LATB*NN signal which was, for most of RUN90, the actual beam for the LAT triggers. The NN or "nearest neighbor" requirement vetoed beam that had a beam muon in a time-adjacent RF bucket. The RLATB prescale factors measured from periods with and without the "nearest neighbor" agree within error. In the RSATB prescale factor measurement, the same type of comparison shows that the "NN" requirement reduces the beam count by about 3% at the mean beam rate. The beam rate dependences introduced by not having the "nearest neighbor" requirement in the scaled signal cancel in the relative RLATB prescale factor measurement between targets provided the two target see the same beam rate. This problem did not affect the RSATB prescale factor measurement.

Rbeam Ratio

In terms of the prescale ratio defined in Equation 4.12, the Rbeam relative normalization ratio is

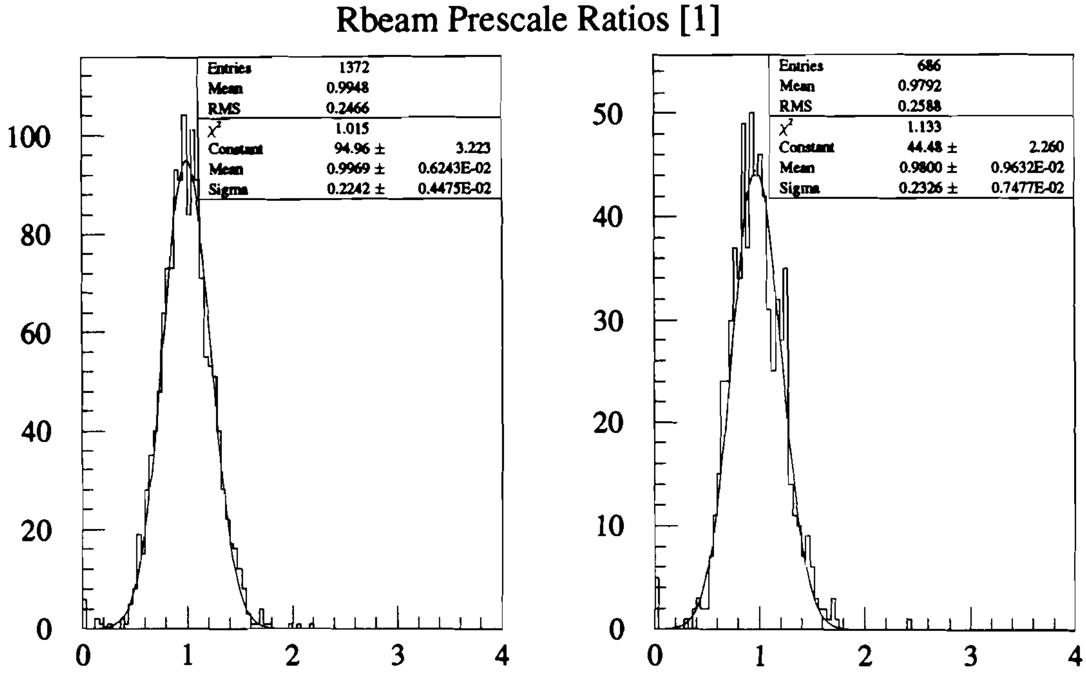

RSATB: Hydrogen

RSATB: Deuterium

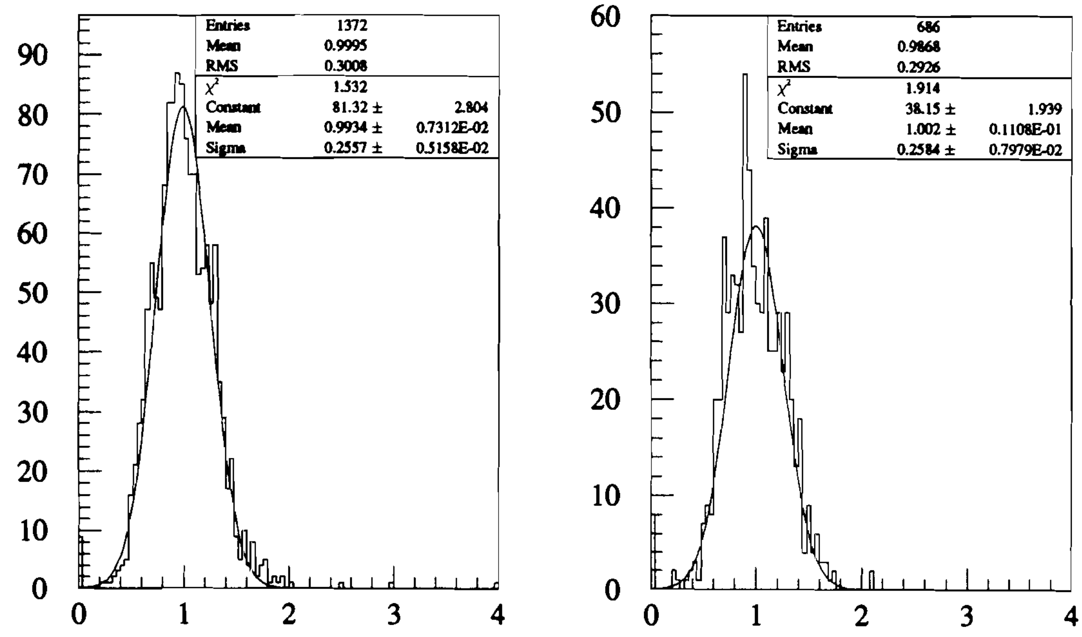

RLATB: Hydrogen

RLATB: Deuterium

Figure 4.4: Example of the RSATB and RLATB prescale ratio distributions for Samples I and II

Table 4.8: Acceptable SAT beam ratios

Target Ratios	Sample I	Sample II
H_2/D_2	1.005 ± 0.029	0.989 ± 0.020
$H_2/Empty$	1.003 ± 0.050	0.996 ± 0.034
$D_2/Empty$	0.998 ± 0.052	1.007 ± 0.036

$$\frac{N_\mu^{H_2}}{N_\mu^{D_2}} = \frac{N_{Rbeam}^{H_2}}{N_{Rbeam}^{D_2}} \frac{R_{prescale}^{H_2}}{R_{prescale}^{D_2}} \tag{4.13}$$

The standard beam cuts are applied to the Rbeam events, and only those passing are considered in the count used for normalization. The primary source of error in these results is the statistical error on the Rbeam event counts.

4.4.2 Spill Scaler Normalization

The spill scalers provide a direct count of the number of muons entering the experiment during the live time of the experiment. They do not measure exactly the quantity of interest, however, which is the number of *acceptable* live beams that entered the experiment. Rbeam data is used to calculate the ratio of the acceptable beam fraction on hydrogen to that on deuterium. This ratio is applied as a correction to the SCL normalization ratio. Most of the error on the measurement made with the spill scalers comes from the statistical error in the measurement of this accepted beam ratio.

$$\frac{N_\mu^{H_2}}{N_\mu^{D_2}} = \frac{N_{SCL}^{H_2}}{N_{SCL}^{D_2}} \frac{R_{\mu accepted}^{H_2}}{R_{\mu accepted}^{D_2}} \tag{4.14}$$

Although the absolute normalization of the data set with the spill scalers is hampered by the interfile event loss described in Section 2.7.3, the relative normalization is largely unaffected by this since the effect occurs at random, without any correlation to the identity of the target in place [123, 129].

The error in the relative Spill Scaler count due to the interfile event loss, lost scaler records at end of runs, and related effects is estimated to be negligible since such problems are independent of the target in place.

Table 4.9: Acceptable LAT beam ratios

Target Ratios	Sample I	Sample II
H_2/D_2	1.080 ± 0.034	0.984 ± 0.023
$H_2/Empty$	1.001 ± 0.058	1.003 ± 0.041
$D_2/Empty$	0.993 ± 0.061	1.050 ± 0.044

4.4.3 External-to-Target Normalization

Since only knowledge of the relative number of beam muons is required in the measurement, any process that is assured of being independent of the differences in the nuclear content of the targets can be used to determine this relative number. Deep inelastic scattering well outside of the target vessel, for instance, should provide a direct measurement of the relative beam flux since the scattering rate remains the same away from the target as targets are changed. This method is referred to as the "external-to-target" normalization method.

In the external-to-target method, the relative beam flux is simply given by the relative number of events observed scattering outside of the target. The cuts applied to the sample were identical to those applied to the inelastic scatters inside the target, except that the X-coordinate of the interaction vertex is required to be at least 1 m outside of the target. To provide some control over this event sample, events were further required to originate from one of four scattering regions containing somewhat dense material. These subsamples were the SBT station 4 region upstream of target and the VDC, PCV, and C1 regions downstream of the target.

$$\frac{N_\mu^{H_2}}{N_\mu^{D_2}} = \frac{N_{External}^{H_2}}{N_{External}^{D_2}} \tag{4.15}$$

4.4.4 Normalization Results

The results from the Rbeam, Spill Scaler, and External-to-Target methods are considered sufficently well understood to be used in this analysis. The results from these methods were combined in a weighted average. Some care was taken with the error on the results since the errors in the Rbeam method and Spill Scaler are not entirely independent. The error in the Rbeam measurement is dominated by the statistical error due to the number of Rbeam events considered. The error in the Spill Scaler measurement, however, is also dominated by the number of Rbeam events, in

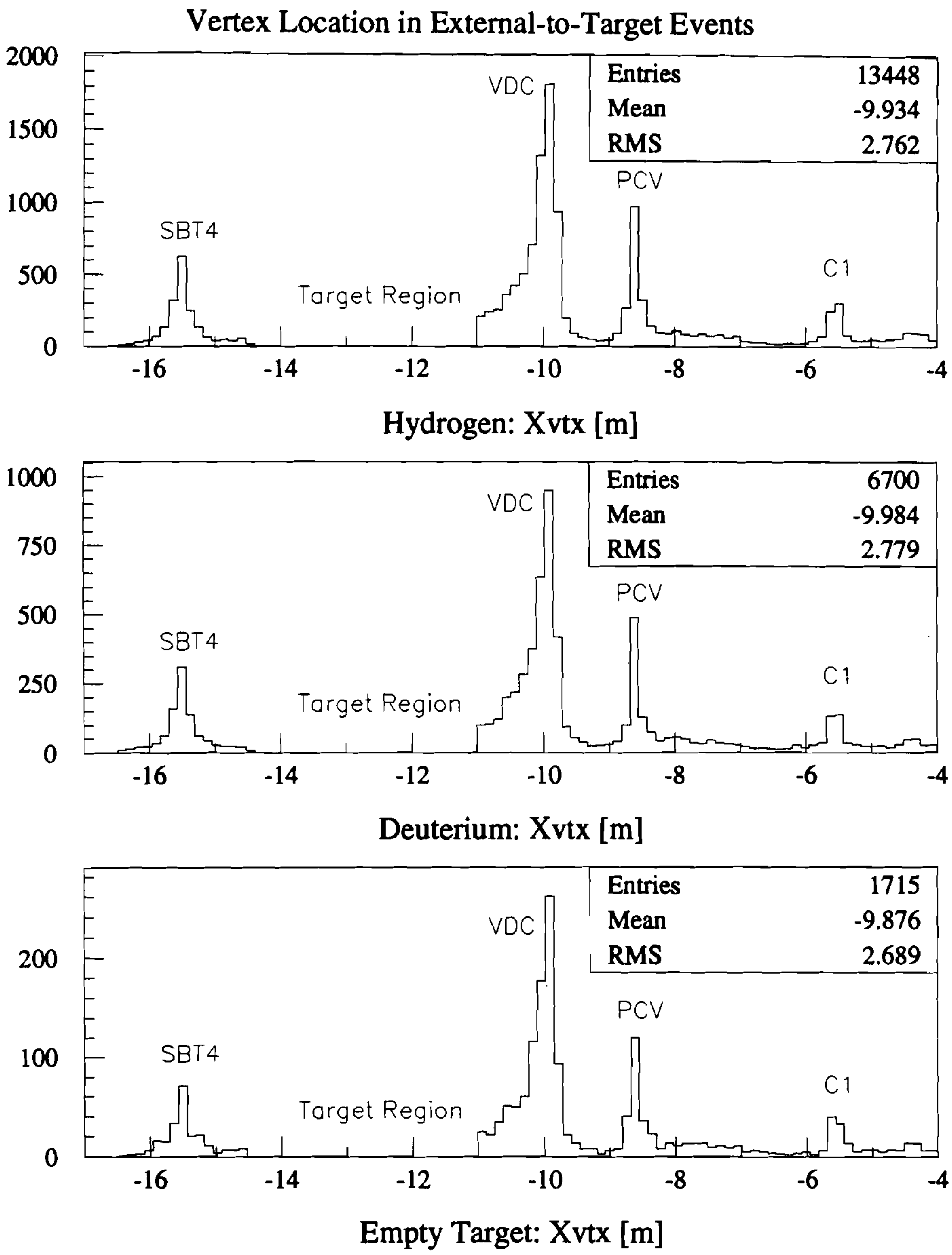

Figure 4.5: Longitudinal distribution of vertices outside the target

Table 4.10: SAT H_2/D_2 normalization results

Method	Sample I	Sample II
Rbeam	2.202 ± 0.046	1.996 ± 0.030
Spill Scaler	2.177 ± 0.062	1.984 ± 0.041
External	2.089 ± 0.069	1.988 ± 0.044
Combined	2.169 ± 0.033	1.990 ± 0.021

Table 4.11: LAT H_2/D_2 normalization results

Method	Sample I	Sample II
Rbeam	2.123 ± 0.055	1.997 ± 0.038
Spill Scaler	2.183 ± 0.073	1.975 ± 0.047
External	2.15 ± 0.22	2.01 ± 0.13
Combined	2.145 ± 0.043	1.990 ± 0.029

this case, used to measure the fraction of beam passing the beam cuts. The error in the External-to-Target method is dominated by the number of scattering events counted outside of the target, and is not related to the other errors. The value of resulting combination, taking this error correlation between the methods into account, was essentially the same as that of a weighted average of all used results.

Table 4.10 on page 93 gives the SAT normalization results for the beam flux ratio for H_2 and D_2. Table 4.11 on page 93 gives the LAT normalization results.

4.5 Processes in the Data Set

Several kinds of backgrounds exist in the data sample. The data set contains, for instance, muon-electron elastic scattering events involving atomic electrons in the target. Bremsstrahlung events occur in which the muon radiates much of its energy as a real photon. Electroweak radiative processes beyond the one-photon-exchange process can occur between the muon and nucleon. A small number of interactions in the target vessel are misindentified as having occurred in the target material. In order to justify how these events are removed, a description of each kind of event is given and compared to inelastic muon-nucleon scattering events of interest. Figure 4.6 on page 94 illustrates these processes which survive the initial events cuts.

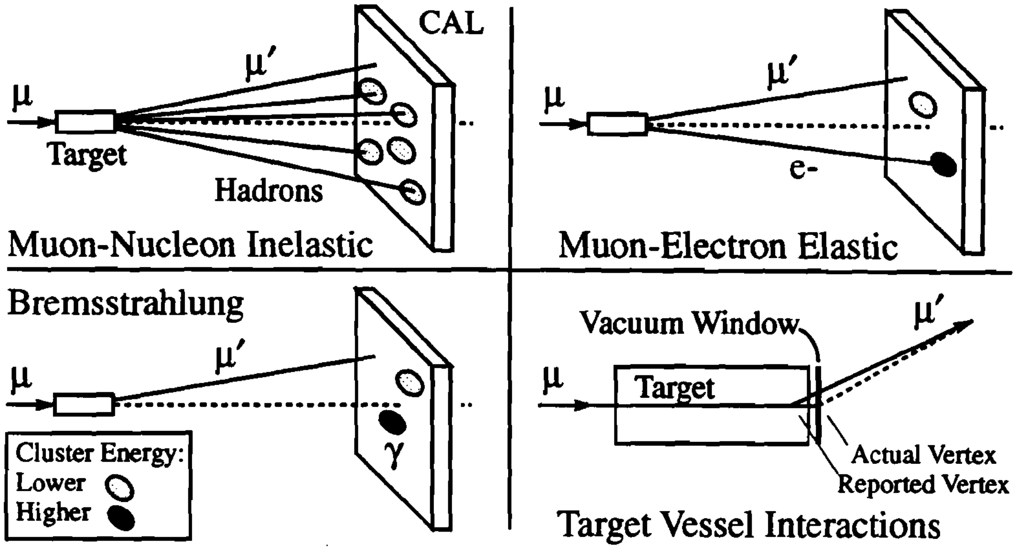

Figure 4.6: Examples of processes surviving initial events cuts

4.5.1 Characteristics of Electromagnetic Background

Certain electromagnetic backgrounds can be identified using information from the electromagnetic calorimeter [185, 4, 5]. Three characteristics, *Ecal*/ν, *Ecal*/(ν *Nclus*), and the *coplanarity*, are used to test whether an event was a bremsstrahlung or muon-electron scatter event. If so, the event is cut from the data sample used to measure the muon-nucleon inelastic cross section ratio.

Ecal/ν

The ratio *Ecal*/ν describes the fraction of the virtual photon energy in the lab frame that is transferred to and absorbed by the electromagnetic calorimeter. The energy transferred is generally carried by electrons from muon-electron elastic scattering, photons from bremsstrahlung, and the decay products of hadrons generated by muon-nucleon inelastic scattering. Generally, however, only muon-electron scattering and bremsstrahlung tend to involve the deposition of nearly all of the energy transfer ν into the calorimeter. The calorimeter response to such large, concentrated energy deposition tends to saturate. The ideal *Ecal*/ν distribution for these backgrounds would peak near 1. Due to saturation effects, the *Ecal*/ν distribution peaks below 1 for events in which there is 250 GeV or more deposited into the calorimeter in one cluster.

Ecal/(ν Nclus)

The characteristic $Ecal/(\nu\ Nclus)$ is similar to $Ecal/\nu$, but it uses the number of energy clusters in the electromagnetic calorimeter to improve the differentiation between the muon-nucleon inelastic scattering events and background. This characteristic can be thought of as the mean cluster energy scaled by the energy transfer. Since the background cuts all include a requirement that there be some energy in the calorimeter, the number of clusters in events is forced to be at least one. Small background interactions in the detector often lead to at least one small energy cluster.

Coplanarity

Another characteristic used is the *coplanarity* of the event. This is defined, as shown in Figure 4.7 on page 96 by:

$$coplanarity = -\log\left(\mathrm{abs}\left(\frac{(\vec{k}\times\vec{k}')\cdot\vec{x}_\gamma}{|\vec{k}||\vec{k}'||\vec{x}_\gamma|}\right)\right) \tag{4.16}$$

where $\vec{k}$ is the incoming muon 3-momentum, $\vec{k}'$ is the scattered muon 3-momentum, and $\vec{x}_\gamma$ is the displacement from the interaction vertex to the most energetic cluster in the calorimeter. In the case of a clean bremsstrahlung event, the normalized $\vec{x}_\gamma$ gives the direction of the bremsstrahlung photon momentum. The energy deposition by the photon in the calorimeter is coplanar with the incoming and scattered muon, leading to an event with very large *coplanarity*. Muon-electron elastic scattering events can also be treated this way with the electron substituted for the photon, the trajectories of lower energy electrons are noticeably bent by the CVM. Note that events with relatively large *coplanarity* are relatively coplanar events.

4.5.2 Inelastic Muon-Nucleon Scattering

The events of interest contain inelastic muon-nucleon scattering. An event sub-sample is used to illustrate the characteristics of these events. The sub-sample is defined by requiring an event have at least 3 "hadron" tracks fitted to the vertex (in addition to the incoming and scattered muon) in order to isolate inelastic processes, has a moderate value of y_{bj} to avoid radiative events, and has a value of x_{bj} that is inconsistent with muon-electron elastic scattering. The $Ecal > 0$ requirement avoids infrequent events with calorimeter readout errors.

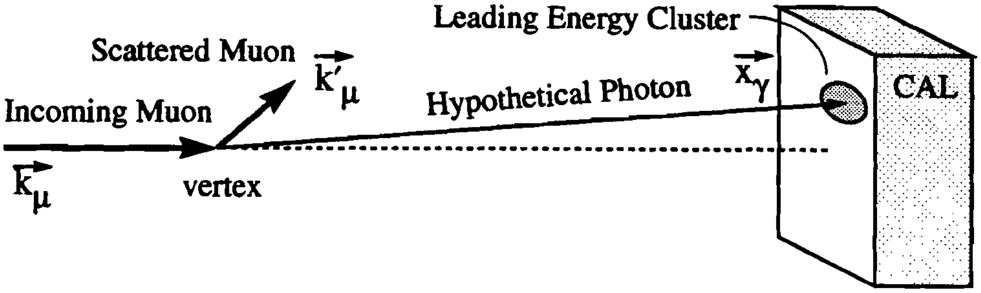

$$\vec{x}_\gamma \equiv \vec{x}\,(\text{leading energy cluster}) - \vec{x}\,(\text{vertex})$$

$$\boxed{\text{Coplanarity} \equiv -\log 10\left(\text{abs}\left(\frac{(\vec{k}_\mu \times \vec{k}'_\mu)\cdot \vec{x}_\gamma}{|\vec{k}_\mu|\;|\vec{k}'_\mu|\;|\vec{x}_\gamma|}\right)\right)}$$

Figure 4.7: Definition of *Coplanarity*

Figure 4.8 on page 97 illustrates the properties of this sub-sample. Muon-nucleon inelastic scattering events tend not to be coplanar, to have little of the energy transfer ν deposited in the electromagnetic calorimeter, and to have very low mean cluster energy scaled by the energy transfer. Much of the energy transfer in these events goes to several hadrons resulting from the interaction. Since hadrons tend to be much less efficient at transfering energy into the electromagnetic calorimeter, relatively little of ν is deposited. Each of the hadrons, however, is likely to deposit some small, but recognizable, amount of energy leading to the reporting of an energy cluster.

4.5.3 Bremsstrahlung

Bremsstrahlung involves the incoming muon giving up a fraction of its energy to a real photon [127]. Since the distribution of radiated photons is peaked along the incident muon momentum vector and along the scattered muon momentum vector, the radiated photon tends to hit the electromagnetic calorimeter and deposit all of its energy. Bremsstrahlung events are represented by a sub-sample defined by requiring that no "hadron" tracks be fitted or close to the vertex, that $y_{bj} \geq 0.7$, and that the value of x_{bj} be inconsistent with muon-electron elastic scattering. Also, the *Ecal* > 0 requirement avoids infrequent events with calorimeter readout errors.

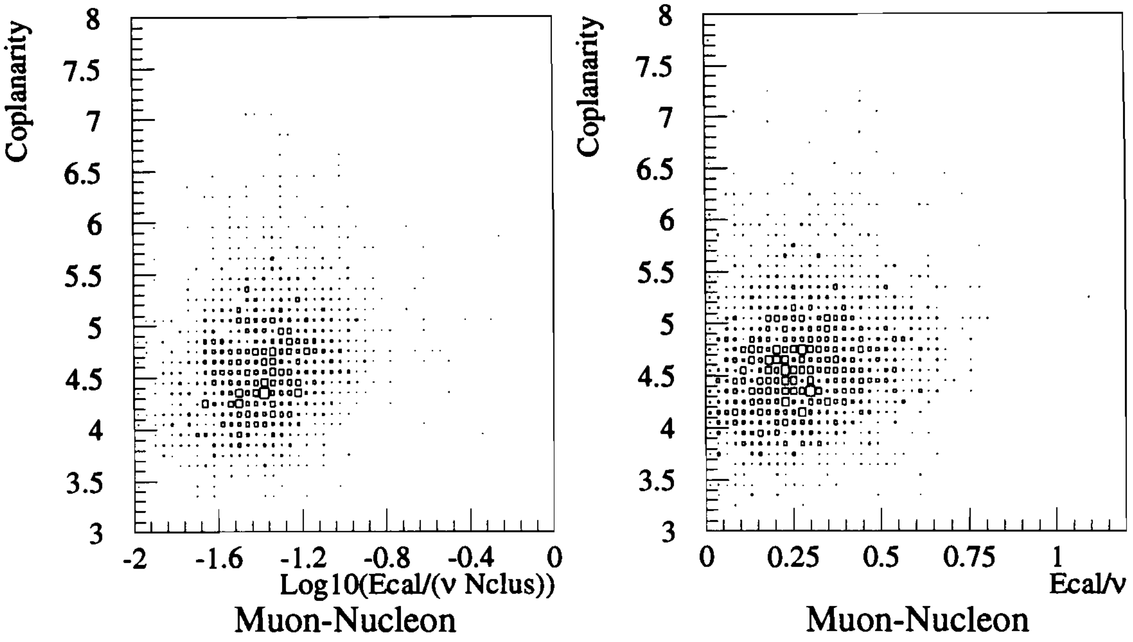

Figure 4.8: Characteristics of inelastic muon-nucleon scattering

Ideally, bremsstrahlung events would have an $Ecal/\nu$ and an $Ecal/(\nu\ Nclus)$ of one. Given the high energy of the bremsstrahlung photons (50 GeV to 500 GeV), however, the calorimeter response saturates for the more energetic photons. Since there is often an extraneous low energy cluster, the number of clusters in these events is more often 2 than 1, leading to a second peak in the $Ecal/(\nu\ Nclus)$ distribution. The actual distributions are shown in Figure 4.9 on page 98.

4.5.4 Muon-Electron Elastic Scattering

Muon-electron scattering events [127], called mu-e events for short, involve the muon giving up a fraction of its energy to an atomic electron. The electron usually strikes the electromagnetic calorimeter, giving up all its energy. The mu-e event subsample requires events to have $4.0 \times 10^{-4} \geq x_{bj} \geq 6.5 \times 10^{-4}$. Further, the events must have exactly one negatively-charged and zero positively-charged "hadron" track fit or close to the interaction vertex. Finally, the $Ecal > 0$ requirement avoids infrequent events with calorimeter readout errors.

As with bremsstrahlung, the actual $Ecal/\nu$ and $Ecal/(\nu\ Nclus)$ distributions observed, shown in Figure 4.10 on page 99, are not peaked at 1 due to calorimeter response saturation and an extraneous low energy cluster. There are a significant

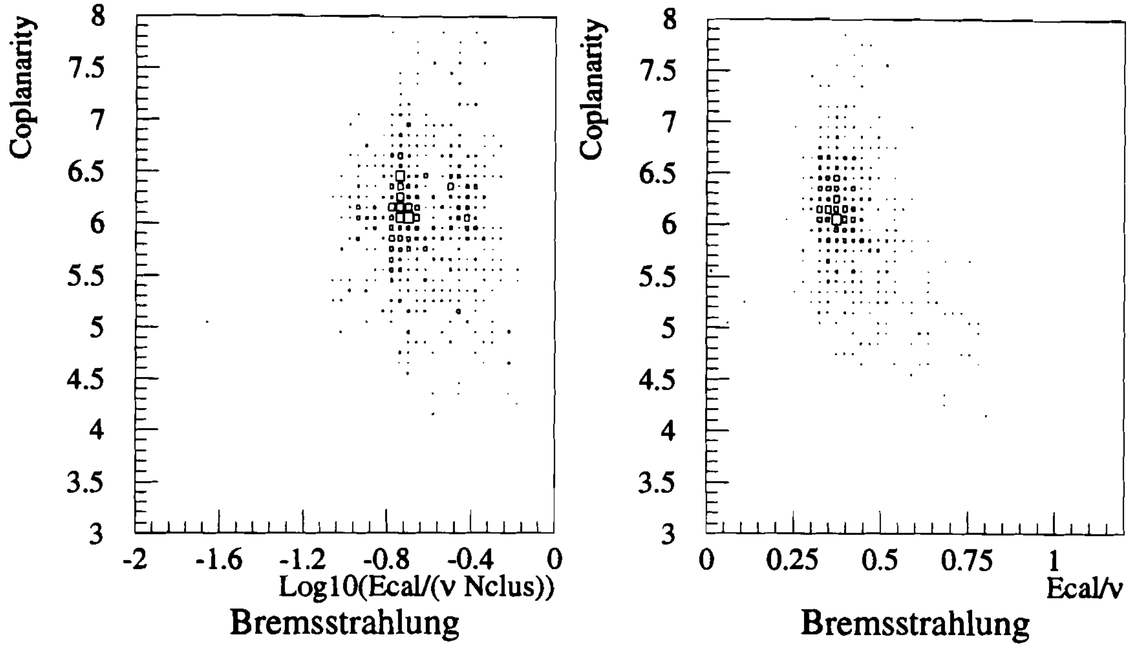

Figure 4.9: Characteristics of bremsstrahlung

number of mu-e events, however, in which the electron radiates a real photon which also strikes the calorimeter. This can split the original electron energy between two calorimeter clusters, greatly reducing the effects of saturation, but also increasing the number of energy clusters. The $Ecal/\nu$ distribution for these electron bremsstrahlung events is peaked closer to 1, but the $Ecal/(\nu\ Nclus)$ distribution is, on balance, unchanged. As with bremsstahlung, the *coplanarity* can be defined using location of the leading (most energetic) calorimeter cluster. Muon-electron elastic scattering events without electron radiation, as demonstrated by a saturation-reduced $Ecal/\nu$, show a very high *coplanarity*. Mu-e events with radiation by the electron show a degraded, but still quite high *coplanarity*. Note that no distinction is made between the electron cluster and the electron-radiated photon cluster in the calorimeter when the *coplanarity* is calculated.

4.5.5 Separating the Processes

Figure 4.11 on page 100 shows the distribution of events in the *coplanarity* versus $Ecal/(\nu\ Nclus)$ plane and the *coplanarity* versus $Ecal/\nu$ plane for all SAT events and for SAT events at very small x_{bj}, where the electromagnetic background dominates the inelastic muon-nucleon event sample. As with the small sub-samples shown, the muon-nucleon inelastic scattering events in the complete data sample

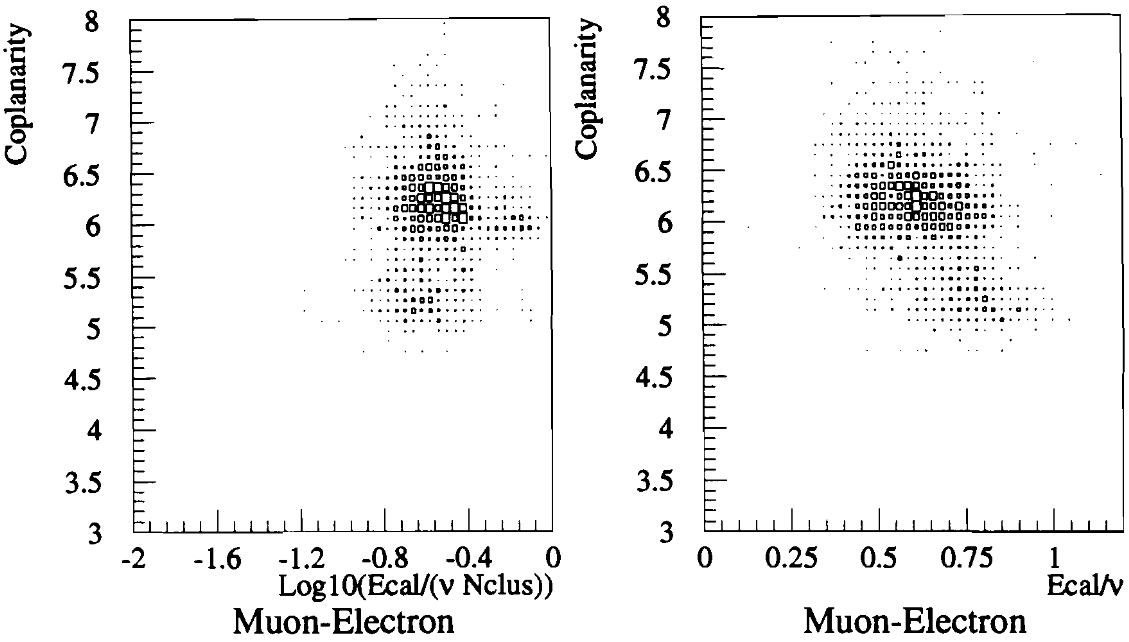

Figure 4.10: Characteristics of mu-e scattering

appear to be differentiable from the bremsstrahlung and muon-electron elastic scatter events using these characteristics described.

4.5.6 Radiative Processes

Bremsstrahlung is not the only radiative process represented in the data set. The traditional manner of correcting for these other processes is to apply calculated radiative corrections in order to extract the one-photon-exchange process, as described in Section 3.4.2 and Appendix E. Such a calculation program has not yet been verified to work for both D_2 and H_2 in the region $x_{bj} < 1.0 \times 10^{-3}$ and $Q^2 < 1.0$ GeV$^2/c^2$. While a model of the one-photon-exchange cross section exists, complete treatments of processes such as bremsstrahlung which, given the E665 acceptance, dominate the observed total cross section at very low x_{bj} are not available. For $x_{bj} \geq 1.0 \times 10^{-3}$, I measure the cross section ratio using each calorimetry cut and a simple application of radiative corrections separately. The latter is intended to verify that the calorimetry cuts indeed work reasonably well at eliminating backgrounds, and provides some confidence in the results obtained with the calorimetry cuts used for $x_{bj} < 1.0 \times 10^{-3}$.

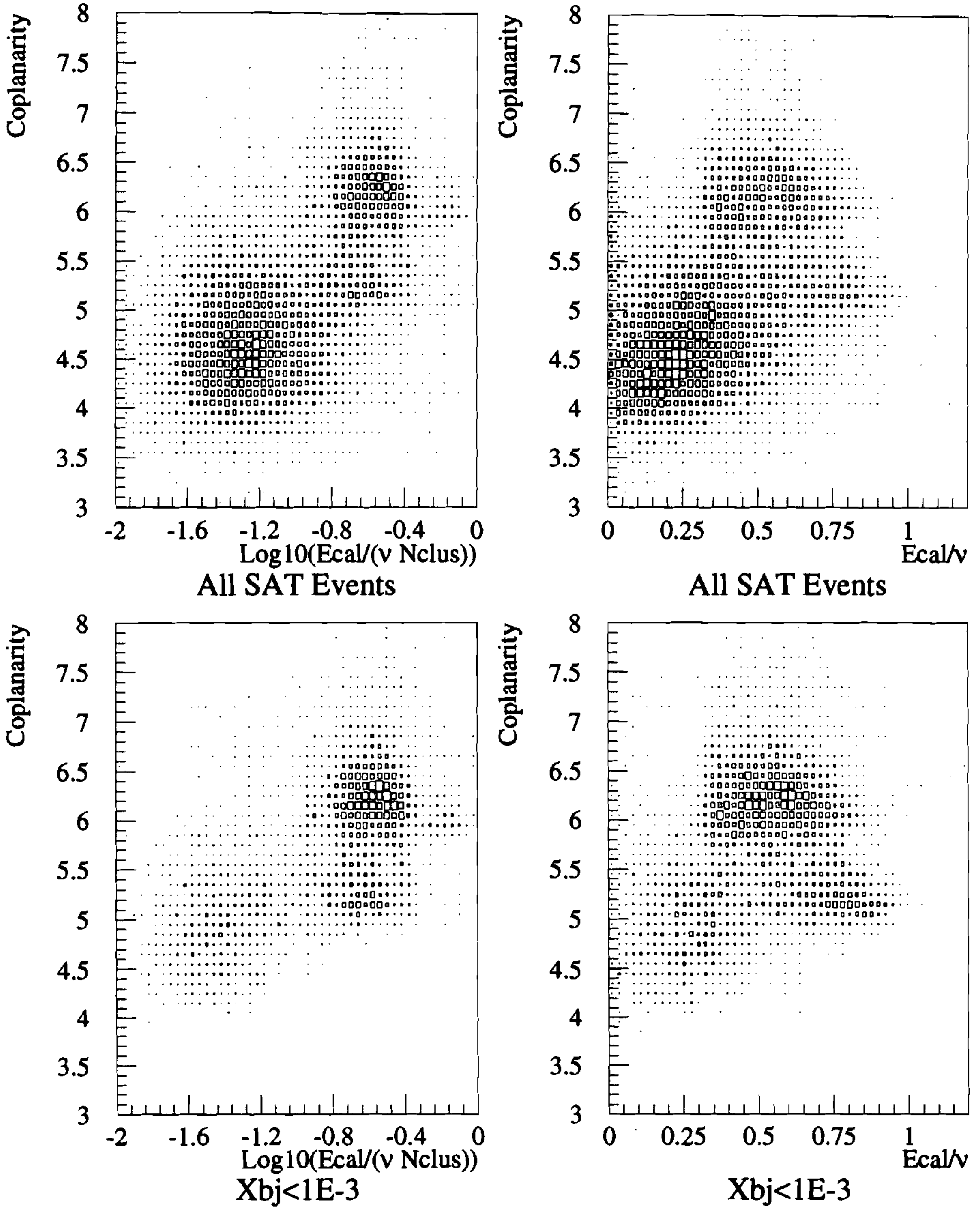

Figure 4.11: Calorimetry distributions for all SAT events (top) and for SAT events with $x_{bj} < 1 \times 10^{-3}$ (bottom)

Table 4.12: Interaction vertex cuts

Property	Cut
Longitudinal Location	$X_{vtx} \geq 1.0$ cm inside upstream target face
Longitudinal Location	$X_{vtx} \geq 1.0$ cm inside downstream target face
Radial Location	$R_{vtx} \geq 0.5$ cm inside target radial wall
Error in Long. Location	$\sigma^2_{xx}(X_{vtx}) \leq 0.05$ m^2
Vertex Fit Quality	$\chi^2 probability \geq 0.001$

4.5.7 Target Vessel Interactions

Despite the careful definition of the fiducial target volume, a few events containing interactions in the target vessel and not the target material are present in the data set. These events are misidentified as occurring in the target material because of the error in the X-coordinate assigned to the vertex due to finite detector resolution. The correction for these target vessel interactions is called the the empty target subtraction. The target vessel events are eliminated by subtracting off the scaled number of events observed on an empty target vessel after kinematic and vertex location cuts are applied. The number of "empty target" events subtracted off bin-by-bin is scaled by the full target to empty target beam flux ratio. As is shown in Figure 4.1 on page 83 (though unscaled in the figure), the scaled number of empty target events is quite small compared to the number of full target events, roughly 1 to 200 for *empty* to D_2. The effect of the empty target subtraction is negligible; the target fiducial cuts worked well.

4.6 Cross Section Ratio Extraction

4.6.1 Vertex Cuts

The cuts applied to the vertex define the extent of the fiducial target and reject events with very poor vertex resolution. The vertex location cuts are made relative to the target position constants in use. The cut on the error in the X-coordinate assigned to the vertex and the cut on the χ^2 probability assigned to the vertex fit eliminates events in which the vertex location was so poorly resolved or the vertex fit so poor that the kinematics assigned to the interaction are likely to be useless.

Table 4.13: Kinematic cuts

SAT	LAT
350.0 GeV $\leq E \leq$ 650.0 GeV	350.0 GeV $\leq E \leq$ 650.0 GeV
$\theta \geq$ 0.8 mrad	$\theta \geq$ 3.0 mrad
$Q^2 \geq 0.10$ GeV$^2/c^2$	$Q^2 \geq 1.00$ GeV$^2/c^2$
$\nu \geq$ 50.0 GeV	$\nu \geq$ 50.0 GeV
$1.0 \times 10^{-4} \leq x_{bj} \leq 0.9$	$1.0 \times 10^{-3} \leq x_{bj} \leq 0.9$
$0.1 \leq y_{bj} \leq 0.9$	$0.1 \leq y_{bj} \leq 0.9$

Table 4.14: LAT scattered muon cuts

Property	Cut
SVS Veto Hodoscope Extent	-0.170 m $\leq Y_{PTM1} \leq +0.130$ m
SVS Veto Hodoscope Extent	-0.125 m $\leq Z_{PTM1} \leq +0.100$ m

4.6.2 Kinematic Cuts

A number of kinematic cuts were applied to the data set. The cut on beam energy has been explained already. The minimum scattering angles are related to the size of the veto elements used for the scattered muon definition in the triggers. The minimum energy transfer ν and minimum y_{bj} cuts eliminate regions of large relative errors in the kinematics. The minimum energy transfer cut also eliminates quasi-elastic events. The maximum y_{bj} cut eliminates a region of very large radiative corrections and bremsstrahlung. The remaining cuts are simply used to better define the sample in the kinematic plane.

4.6.3 Scattered Muon Cuts

For LAT events to be accepted, the scattered muon track was required not to intercept any of the SVS counters used in the SVS veto. Since the position of the scattered muon is reported (in the analysis n-tuples) at plane 1 of the PTM detector, the cut uses the coordinates of the shadow of the SVS detector on PTM plane 1.

Table 4.15: $Ecal/(\nu\ Nclus)$ calorimetry cut

Description	Condition
Calorimeter Decoder	$A = (Ecal > 0)$
Energy Transfer	$B = (Ecal/(\nu\ Nclus) < 0.075)$
Energy Flow Topology	$C = (Coplanarity < 4.5)$
Final Requirement	A .AND. (B .OR. C)

4.6.4 Empty Target Subtraction

The empty target events were scaled by the relative beam flux and subtracted from the full target events on a bin-by-bin basis. There were very few empty target events observed, with most coming from the downstream vacuum vessel window. Compared to the previous analysis of RUN87 data at E665 [46], there are two orders of magnitude fewer empty target events. This is due to the greatly improved resolution of the longitudinal position of the vertices, which in turn comes from the improvement in the tracking of small scattering angle scattered muons over E665 RUN87.

4.6.5 Removal of Electromagnetic Backgrounds

The approach made in this analysis is to apply an event cut based on calorimetry to eliminate practically all of the bremsstrahlung and mu-e events. The results of this method are then checked by a simple application of radiative corrections. The event characteristics described are those related to the isolating cuts applied.

$Ecal/(\nu\ Nclus)$ Cut

Both calorimetry cuts first require events to have non-zero calorimeter energy. This avoids events in which the calorimetry cut conditions cannot be defined. Checks have been of the effect of the $Ecal > 0$ requirement and its possible link to the target in place. No systematic bias is introduced since the calorimeter readout failures that yielded $Ecal = 0$ have been found not to be correlated to the target in place or to the conditions of the event.

Next, events are required to lie outside of the region in the *coplanarity* versus $Ecal/(\nu\ Nclus)$ plane that is occupied by bremsstrahlung and mu-e scattering. This region is defined by two conditions listed as B and C in Table 4.15 on page 103.

Table 4.16: $Ecal/\nu$ calorimetry cut

Description	Condition
Calorimeter Decoder	$A = (Ecal > 0)$
Energy Transfer	$B = (Ecal/\nu < 0.25)$
Energy Flow Topology	$C = (Coplanarity < 4.5)$
Combination	$D = (Coplanarity < 6.73 - 3.71 Ecal/\nu)$
Final Requirement	A .AND. (B .OR. C .OR. D)

$Ecal/\nu$ Cut

This calorimetry cut also requires events to have non-zero calorimeter energy. Events are required to lie outside of the region in the *coplanarity* versus $Ecal/\nu$ plane that is occupied by bremsstrahlung and mu-e scattering. This region is defined by three conditions listed as B, C, and D in Table 4.16 on page 104.

Effect of Calorimetry Cuts

Figure 4.12 on page 105 shows the $Ecal/(\nu\ Nclus)$ and $Ecal/\nu$ versus *coplanarity* distributions with the region eliminated by each of the calorimetry cuts shown. Figure 4.13 on page 106 shows the effect of each calorimetry cut on the x_{bj} distribution of SAT events, and Figure 4.14 on page 107 shows the same for LAT events. These figures show the almost complete rejection of the muon-electron elastic scattering events by the cuts.

Radiative Corrections

A separate effort at extraction of the cross section ratio was made using a simplified, non-iterative, application of radiative corrections [131]. The calculated ratio of the one-photon-exchange cross section and the total cross section was assigned to each events as an event weight. The dependence of this weight η on y_{bj} and x_{bj} is illustrated in Figure 4.15 on page 108. This weight was then summed to give the radiative corrected event count which was then used to calculate the cross section ratio.

This method is only used as a check of the calorimetry cut methods because the radiative corrections program has not been properly extended to cover the E665 range of kinematics. FERRAD version 35 has only been verified to operate properly

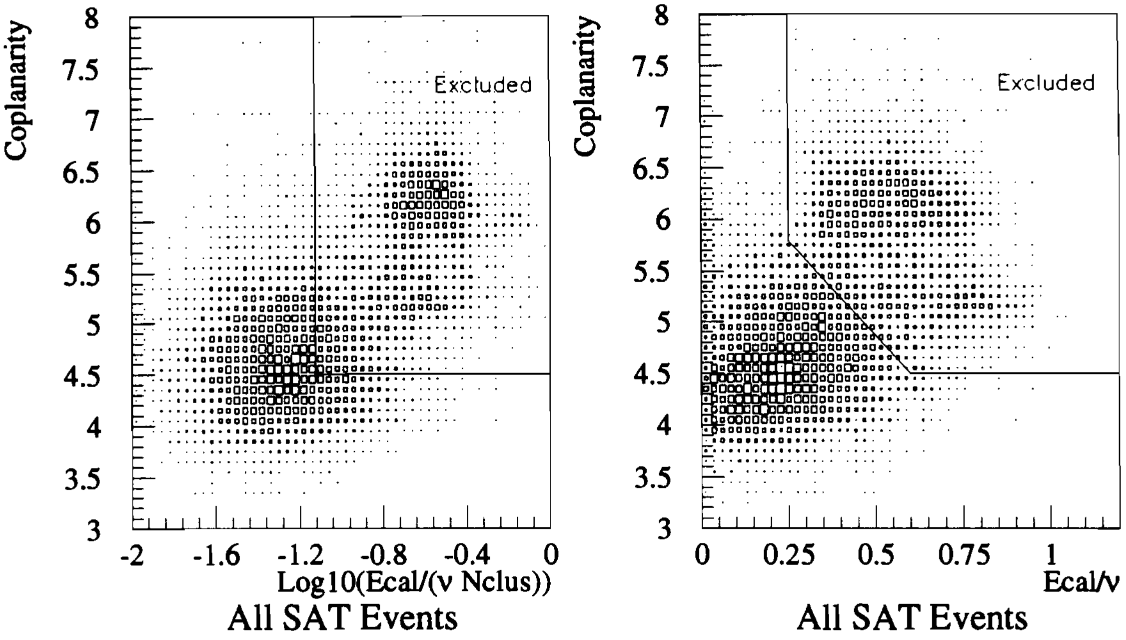

Figure 4.12: *Ecal*/(ν *Nclus*) and *Ecal*/ν versus *coplanarity* for all SAT events with the cut regions shown

for roughly $x_{bj} > 1 \times 10^{-3}$. Although several items used by FERRAD, such as the calculation grid, F_2, and R inputs, have been extended to cover the E665 low x_{bj} region, the calculation of the other cross sections has not been checked in detail. In fact, their calculation appears to break down at the smallest x_{bj} and largest y_{bj} values used (Note the unusual η ratio point for $x_{bj} = 0.0001$, $y_{bj} = 0.9$ in Figure 4.15). The radiative corrections method is used to verify that the calorimetry methods are sensible above $x_{bj} = 1 \times 10^{-3}$, and only the calorimetry methods are used below this point.

4.6.6 Iterative Correction

In order to understand in detail what is seen by the detector, we must have an idea how what the detector reports is related to the events of interest. Specifically, we are interested in how finite resolution of the detector, losses or biases in the reconstruction software, and subtle target-related differences in the trigger acceptance affect the measurement. Due to the size of the current statistical error on the raw cross section ratio and iterative correction measurements, it does not make sense to actually apply this iterative correction in an iterative procedure. Rather, the iterative correction is estimated and quoted as a systematic error.

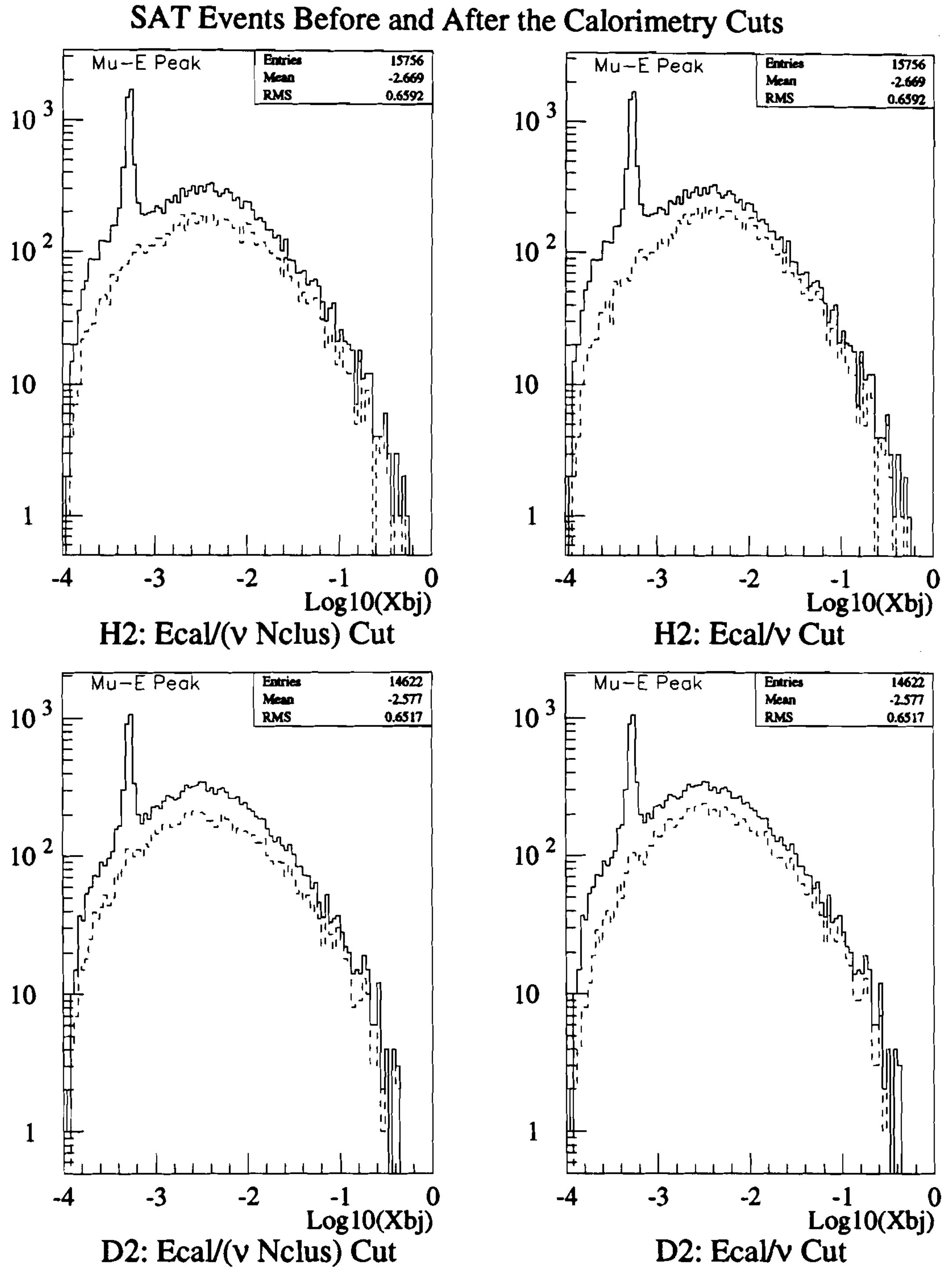

H2: Ecal/(ν Nclus) Cut

H2: Ecal/ν Cut

D2: Ecal/(ν Nclus) Cut

D2: Ecal/ν Cut

Figure 4.13: SAT: x_{bj} distributions of events before (solid) and after (dashed) $Ecal/(\nu\ Nclus)$ cut and $Ecal/\nu$ cut

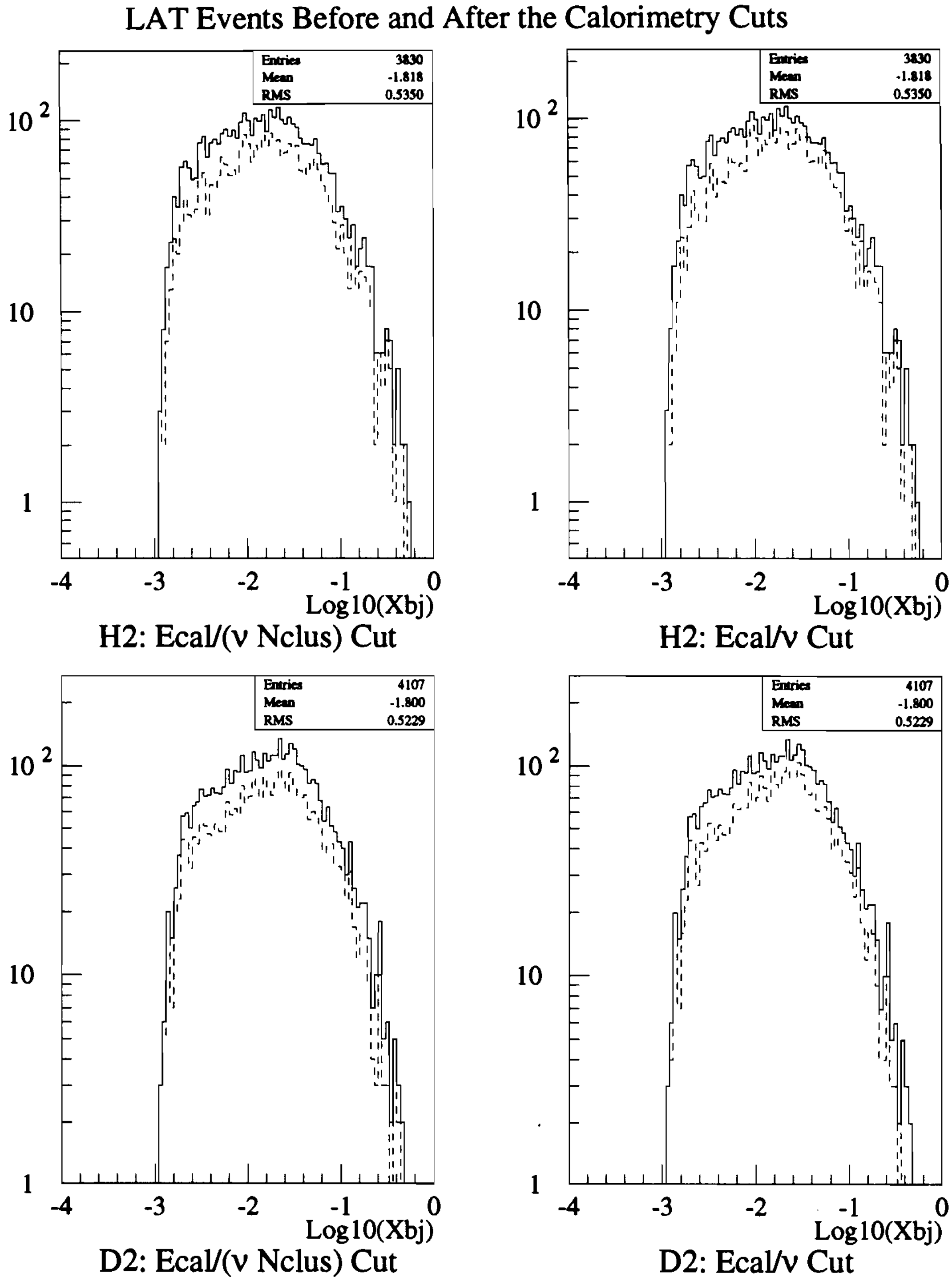

Figure 4.14: LAT: x_{bj} distributions of events before (solid) and after (dashed) $Ecal/(\nu\ Nclus)$ cut and $Ecal/\nu$ cut

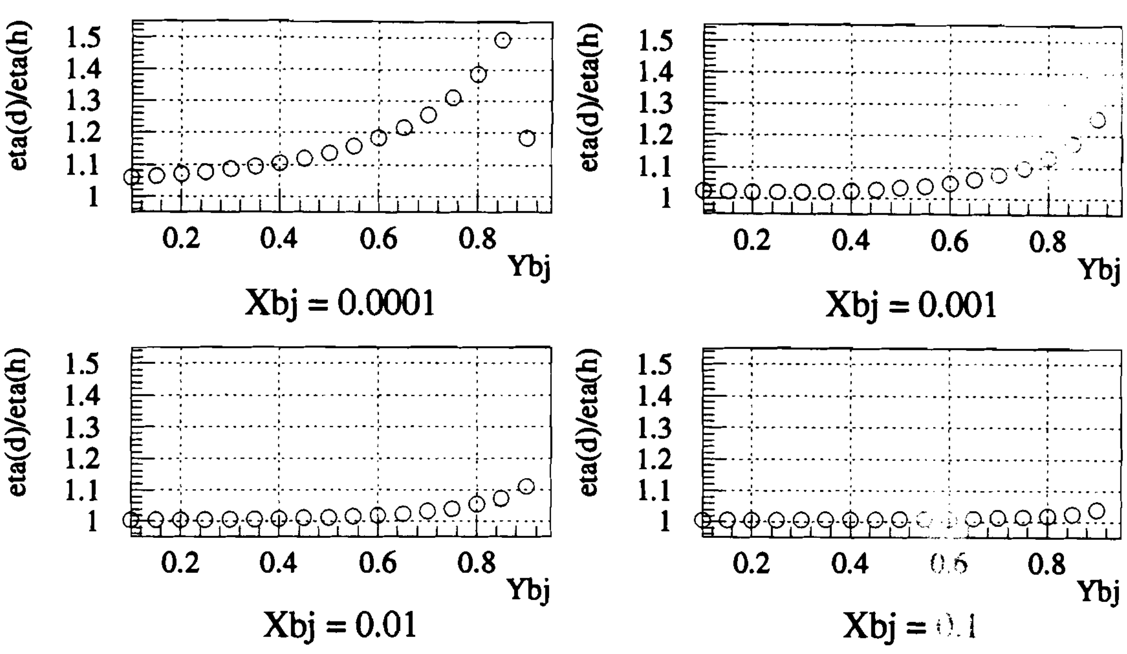

Figure 4.15: Radiative corrections weight ratio η^{D_2}/η^{H_2} versus y_{bj} for four values of x_{bj}

Simulation of the Beam Distribution

The beam distribution B used to account for beam position-dependent effects was implicitly measured from a sample of Rbeam events [109]. Other than requiring that a beam be reconstructed in the event, no other cuts were imposed on the Rbeam events used for input. The beam distribution was implemented in the Monte Carlo event simulation by starting each event simulation with a beam muon selected from the Rbeam event sample. No simulation was made of the beam or the muon beamline. Whatever the event reconstruction program reports from the Beam Spectrometer in the Rbeam sample was taken as an absolute. The SATB and LATB beam trigger logic requirements were imposed on the Monte Carlo events accepted for study so that the accepted beam phase peculiar to each trigger was regenerated from the mixed sample of RSATB and RLATB events used as input. The real beam distribution was found to be identical (for the same beam trigger definition) between the different target samples, aside from the overall number of beams, as required for the iterative correction to be small. The Monte Carlo beam distribution used for each target was identically the same, although some differences were introduced at random by the occasional failure of the Monte Carlo to generate an acceptable event. A comparison of the beam distributions is shown in Figure 4.16 on page 109. This comparison scales the D_2 beam information by a factor of two to match the H_2 statistics.

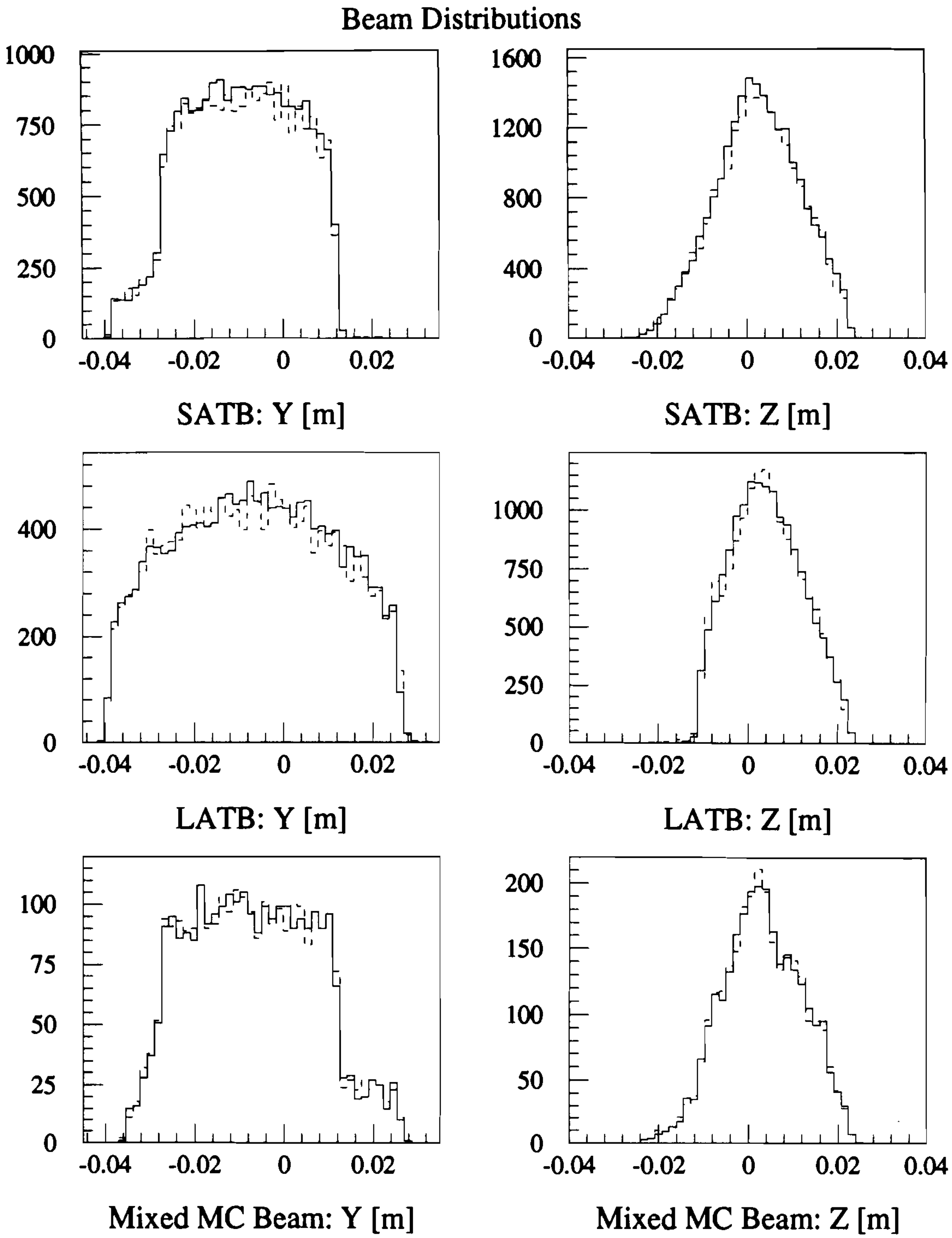

Figure 4.16: Comparison of Y intercept at mid-target between H_2 (solid) and D_2 (dashed)

Acceptance and Efficiency

The acceptance of the experiment used in the Monte Carlo was largely defined by the aperture of the tracking and triggering detectors as determined by alignment studies. Since hadrons, electrons, and photons were simulated, their effect on the trigger acceptance was included. Detector efficiencies were measured with real data and the E665 EFF program. Trigger efficiencies were modelled solely on the efficiency of the trigger detectors. The effects of hardware electronics inefficiencies, for instance due to signal coincidence mistimings, are not modelled. Software reconstruction efficiency was an output of the use of the Monte Carlo and is not included in the simulation.

Smearing

Smearing of the reported kinematics from event reconstruction relative to the 'true' kinematics of the muon-nucleon interaction came from several different sources, such as the finite resolution of the apparatus, event reconstruction biases, and radiation by the muon. Each of these sources is modelled in the Monte Carlo. In addition to simple random smearing of the kinematics, systematic errors in the kinematics were considered a part of smearing as well. The relative value of the kinematics reported by PTMV and that used as to generate an event by MC12 (the "truth"), separated by target, are shown in Figure 4.17, Figure 4.18, and Figure 4.19. The events used were restricted to those in which a simulated trigger fired and the PTMV kinematics passed the kinematic cuts applied to the real reconstructed data. The areas in the kinematic plane affected the most by smearing were small Q^2 (large relative error in θ_{scat} due to detector resolution), small y_{bj} (large relative error in incoming and scattered muon energy difference), and large y_{bj} (radiation by the muon). The smearing of x_{bj} is mixed, with small x_{bj} region affected by the small Q^2 and large y_{bj} effects and the large x_{bj} region affected by the small y_{bj} effects. The MC12 Monte Carlo predicts that there is no significant difference in the smearing between the targets nor any large systematic bias in the kinematics which may affect the results.

4.6.7 Target Impurity Correction

As described in Appendix E, there was a small correction to the cross section ratio related to the contamination of the D_2 material with a small amount of HD. The contamination causes the smaller cross section of the proton of HD to be averaged in with the larger cross section of the deuteron in D_2. Since the per-nucleon cross sections of the proton and deuteron differ, the correction for this effect has a weak x_{bj} dependence. The correction increases the cross section ratio by about 1.0% at

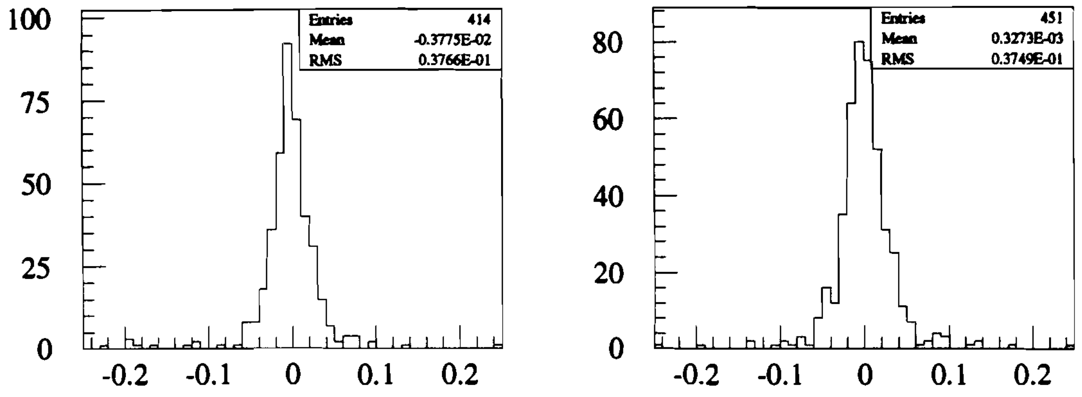

0.1 <= Q2 < 1   0.1 <= Q2 < 1

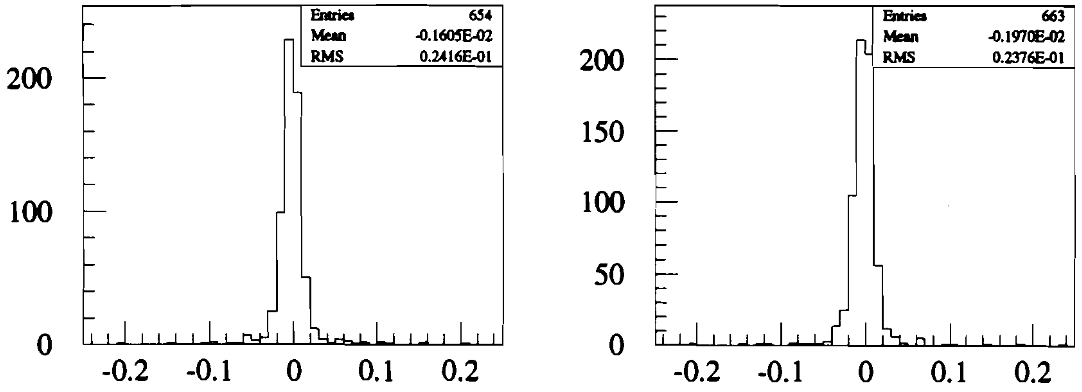

1 <= Q2 < 10   1 <= Q2 < 10

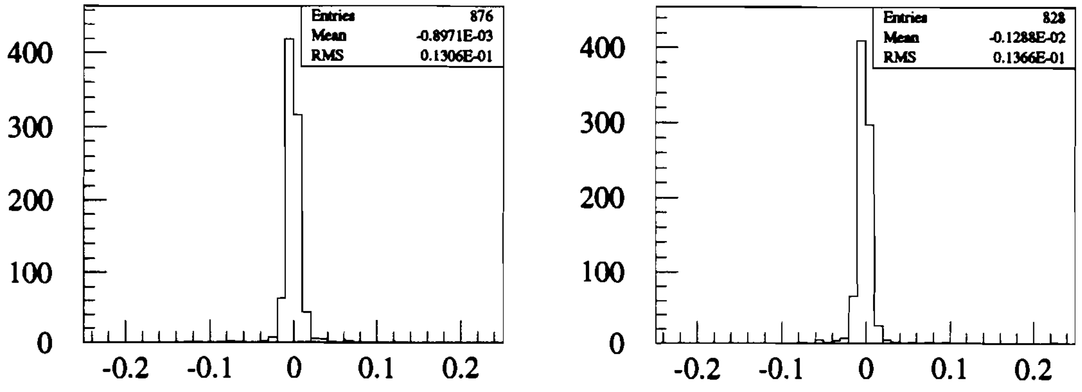

10 <= Q2   10 <= Q2

Figure 4.17: Log10(Q^2_{PTMV}/Q^2_{true}) for H_2 (left) and D_2 (right)

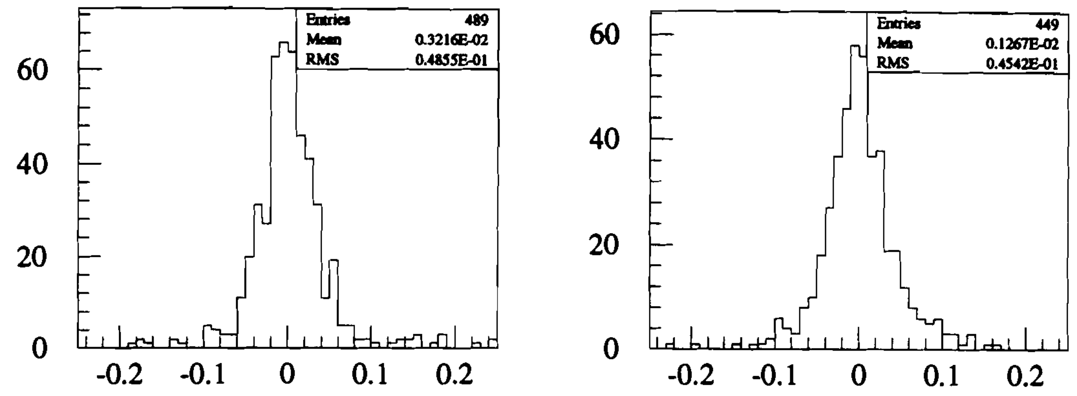

0.10 <= Ybj < 0.30

0.10 <= Ybj < 0.30

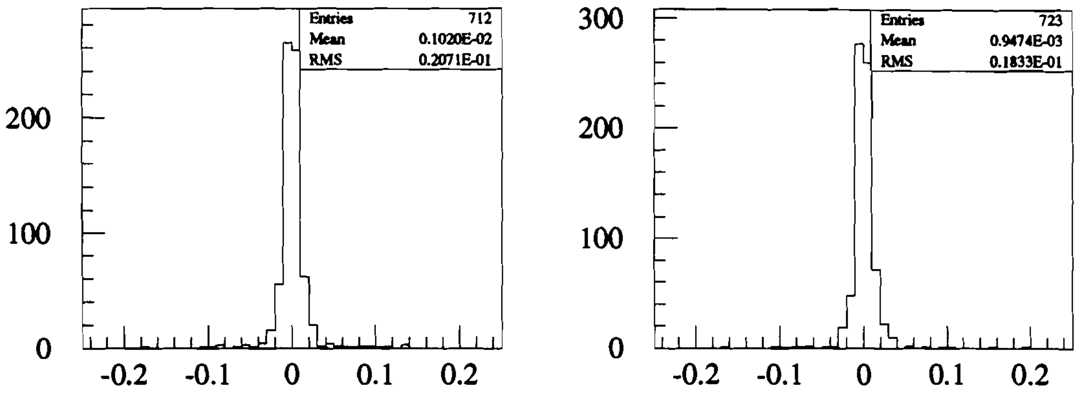

0.30 <= Ybj < 0.60

0.30 <= Ybj < 0.60

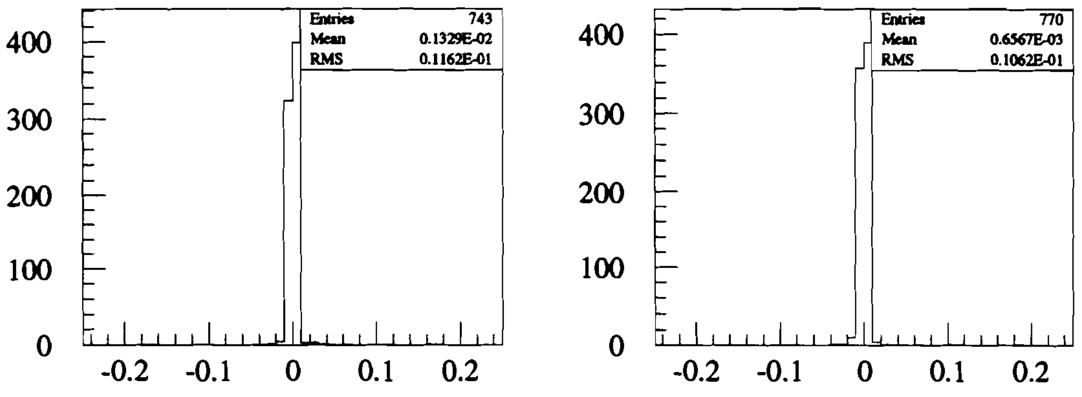

0.60 <= Ybj <= 0.90

0.60 <= Ybj <= 0.90

Figure 4.18: Log10(y_{PTMV}/y_{true}) for H_2 (left) and D_2 (right)

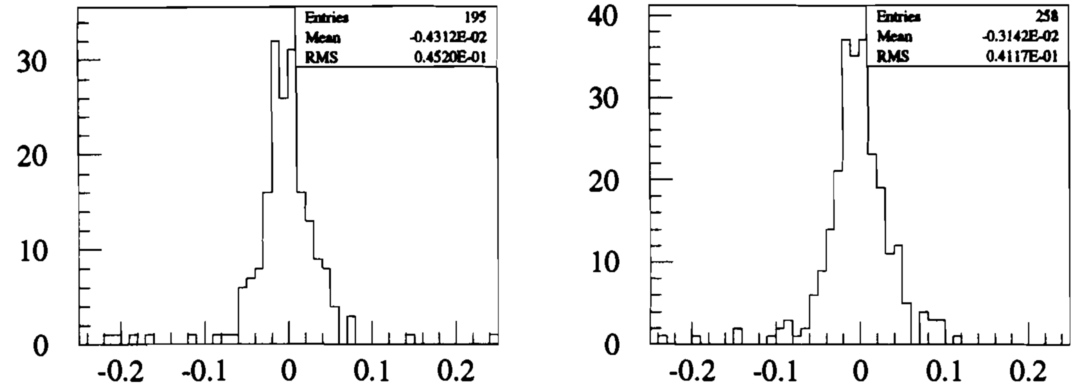

1.0E-4 <= Xbj < 1.0E-3 1.0E-4 <= Xbj < 1.0E-3

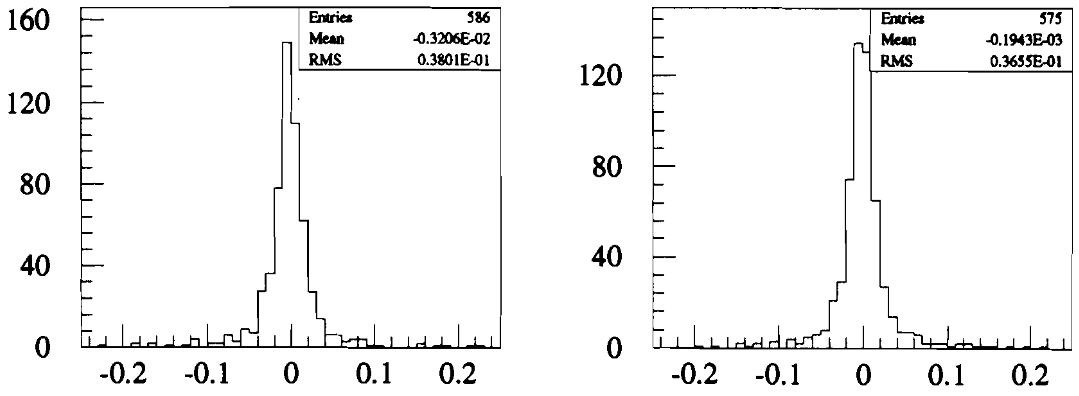

1.0E-3 <= Xbj < 1.0E-2 1.0E-3 <= Xbj < 1.0E-2

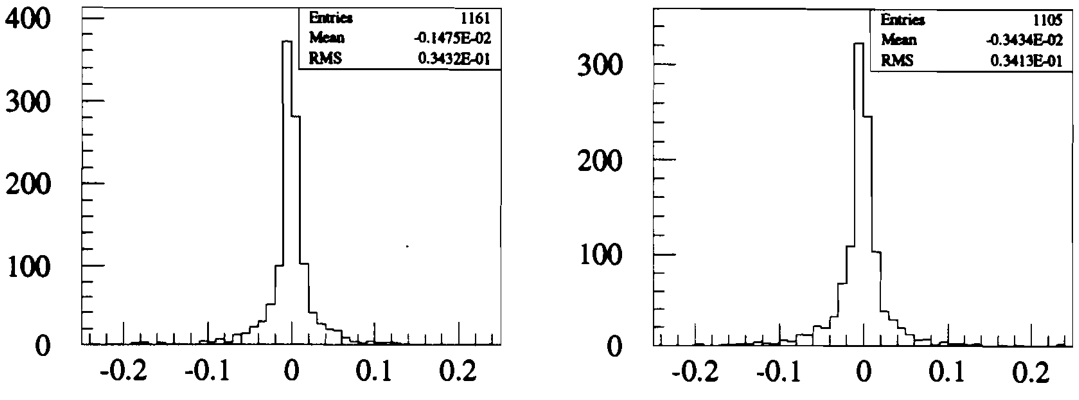

1.0E-2 <= Xbj < 0.9 1.0E-2 <= Xbj < 0.9

Figure 4.19: Log10(x_{PTMV}/x_{true}) for H_2 (left) and D_2 (right)

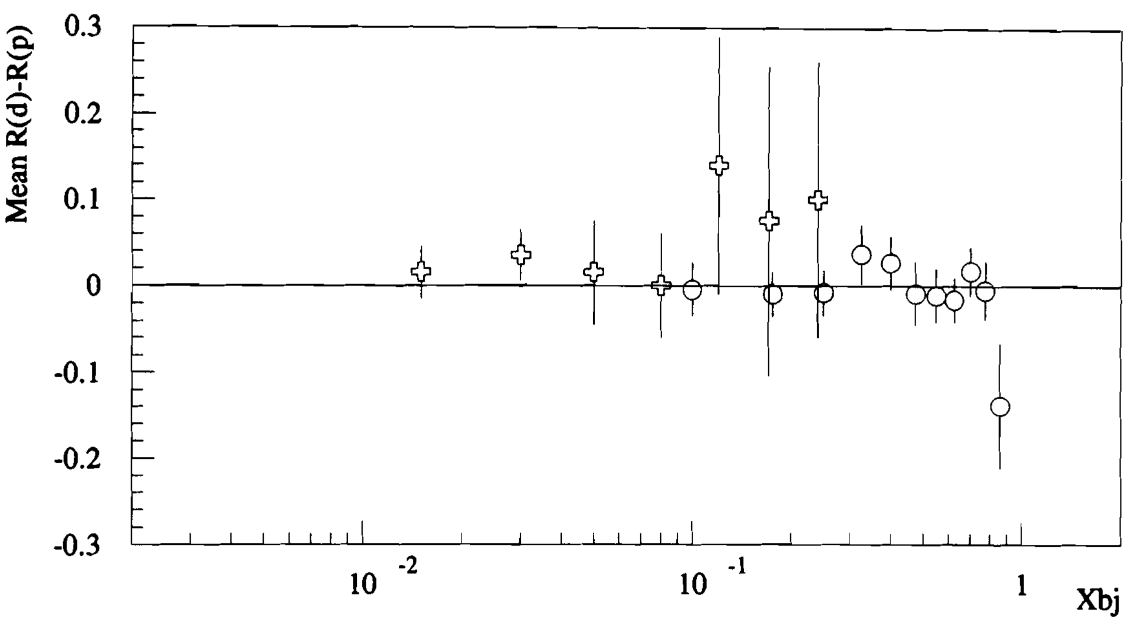

Figure 4.20: Mean difference between function R for D_2 and for H_2: SLAC results (circles) and preliminary NMC results (crosses)

smallest x_{bj} and about 0.8% at largest x_{bj}.

4.7 Structure Function Ratio Extraction

The cross section ratio is related to the structure function ratio through Equation 4.1. It is common practice to assume that the difference in the value of R measured for deuterium and hydrogen is identically zero. Figure 4.20 on page 114 shows $R^{\mathrm{D}_2} - R^{\mathrm{H}_2}$ as a function of x_{bj} [202, 153]. The difference measured has small errors and appears to be consistent with 0. It is also assumed that the neutron cross section is given by the difference in the deuteron cross section and the proton cross section since the deuteron is a very weakly bound proton and neutron. Given this, the structure function ratio is very simply related to the cross section ratio by

$$\frac{F_2^{\mathrm{n}}(x,Q^2)}{F_2^{\mathrm{p}}(x,Q^2)} = \frac{\frac{d\sigma^{1\gamma}}{dxdQ^2}(x,Q^2;D_2)}{\frac{d\sigma^{1\gamma}}{dxdQ^2}(x,Q^2;H_2)} - 1 \tag{4.17}$$

Chapter 5

Results

> *Sorcerers say that we are inside a bubble. It is a bubble into which we are placed at the moment of our birth. At first the bubble is open, but then it begins to close until it has sealed us in. That bubble is our perception. We live inside that bubble all our lives. And what we witness on its round walls is our own reflection.... The thing reflected is our view of the world. That view is first a description, which is given us from the moment of our birth until all our attention is caught by it and the description becomes a view.*
>
> — Don Juan Matus

Carlos Castañeda, *Tales of Power* (1974)

5.1 A Peek at the F_2^n/F_2^p Results

The chapter begins with the presentation of the results of this thesis, $F_2^n/F_2^p(x_{bj})$ without systematic errors. The systematic errors assigned to the results are then discussed, and the final results are presented. These results are compared to similar contemporary measurements and to the predictions of a phenomenological model of F_2. The chapter closes with a critique and conclusion.

To measure $F_2^n/F_2^p(x_{bj})$, the binned event count was summed over Q^2 and the ratio was extracted. The *Ecal/(ν Nclus)* method of removing electromagnetic background was selected over the *Ecal/ν* method since it uses an added piece of information about the event. The raw results (no calorimetry cuts) and the final results for the SAT and LAT triggers are presented in Figure 5.1 on page 117. Only the statistical errors after the empty target subtraction are shown. Note that the SAT data sample for $x_{bj} \geq 0.001$ largely, but not completely, overlaps the LAT data sample.

5.2 Systematic Errors

5.2.1 ν Offset

The ν Offset correction is an attempt to correct for a known momentum miscalibration of the Beam and Forward Spectrometers. The *ad hoc* model used corrects the kinematics of each event by assuming that the only two sources of the error are an error in the $p_\perp$ kick of the Beam Spectrometer magnet and an internal alignment error in the Beam Spectrometer which leads to an angle offset. To measure the possible systematic error in the results from this correction, the structure funciton ratio is remeasured with a data set to which the ν Offset correction has not been applied. The calorimeter energy was corrected for gas gain calibration and overall energy calibration as was the ν Offset corrected data set. The measurement with the sample lacking a ν Offset correction used a slightly different calorimeter cut value, listed in Table 5.1 on page 118, to make up for the shift in ν.

I quote a systematic error which is roughly half the difference between the measurements with and without this correction, shown in Figure 5.2 on page 119. This choice is influenced by early tests of event reconstruction with improved alignment and calibration data which seem to yield similar, though not identical, results as my *ad hoc* ν Offset correction model. The systematic error is smoothed to vary reasonably in x_{bj}. Since the largest relative shift in the kinematics is at small ν, the systematic

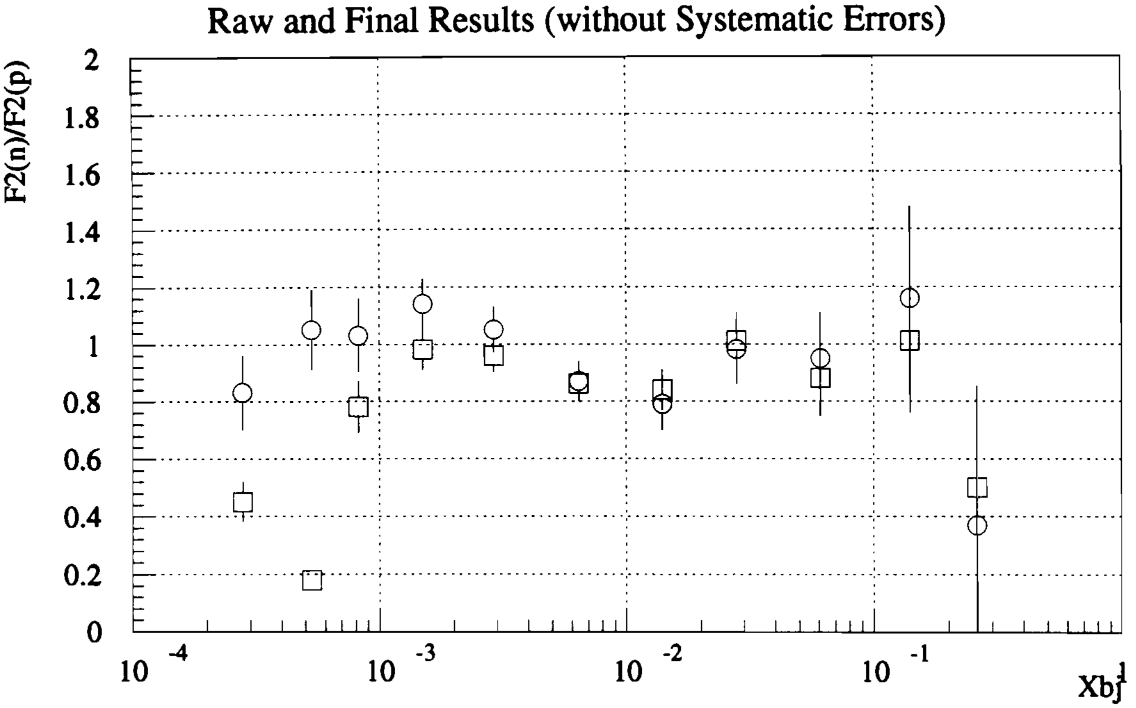

SAT Trigger

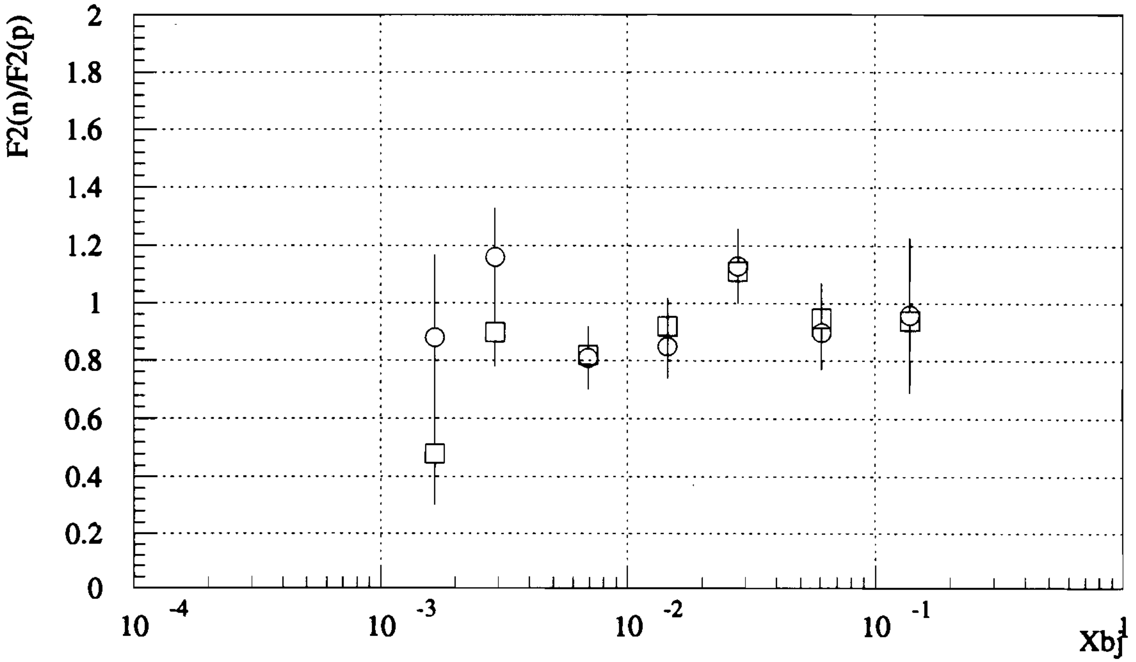

LAT Triggers

Figure 5.1: $F_2^n/F_2^p(x_{bj})$ raw results (without calorimetry cuts, squares) and final results (with calorimetry cuts, circles) ignoring systematic errors

Table 5.1: *Ecal*/(ν *Nclus*) calorimetry cut applied to data not corrected for the ν Offset

Description	Condition
Calorimeter Decoder	$A = (Ecal > 0)$
Energy Transfer	$B = (Ecal/(\nu\ Nclus) < 0.090)$
Energy Flow Topology	$C = (Coplanarity < 4.5)$
Final Requirement	A .AND. (B .OR. C)

error is at large x_{bj} where the small ν acceptance is located. Although the SAT and LAT triggers sample a slightly different Q^2 range in each x_{bj} bin, the change to Q^2 due to the ν Offset correction is relatively smaller than that to x_{bj}. Hence the error quoted is essentially the same for the both triggers.

5.2.2 Calorimetry Cut

There are several potential errors related to the calorimetry cut. The events sample passing the cut could be contaminated by bremsstrahlung or muon-electron elastic scattering events. The results could be affected by the loss of good muon-nucleon inelastic scatters due to the cut. Finally, the selection of the calorimetry cut method could bias the results. Each such potential problem is explored below.

Bremsstrahlung and Mu-E Contamination

In order to estimate the bremsstrahlung and muon-electron scatter contamination, I define two loose candidate sub-samples to test the effect of the calorimetry cut applied. The bremsstrahlung candidate sub-sample contains events in which no hadrons were fitterd or close to the vertex, some calorimeter energy was reported, and $x_{bj} < 1 \times 10^{-3}$. The muon-electron candidates were events with one negatively-charged fit or close hadron, no positively-charged hadrons, some calorimeter energy reported, and $3 \times 10^{-3} < x_{bj} < 8 \times 10^{-3}$. Figure 5.3 on page 121 shows the x_{bj} distribution of these samples before and after the *Ecal*/(ν *Nclus*) calorimeter cut is applied. Note that there appears to be small number of muon-electron events in the bremsstrahlung sub-sample (peak at $x_{bj} \approx 5 \times 10^{-3}$). The largest concentration of the apparent bremsstrahlung events is in the lowest x_{bj} bin and practically all the muon-electron events are in the next-to-lowest x_{bj} bin.

Figure 5.3 shows that only a small number of bremsstrahlung events appear

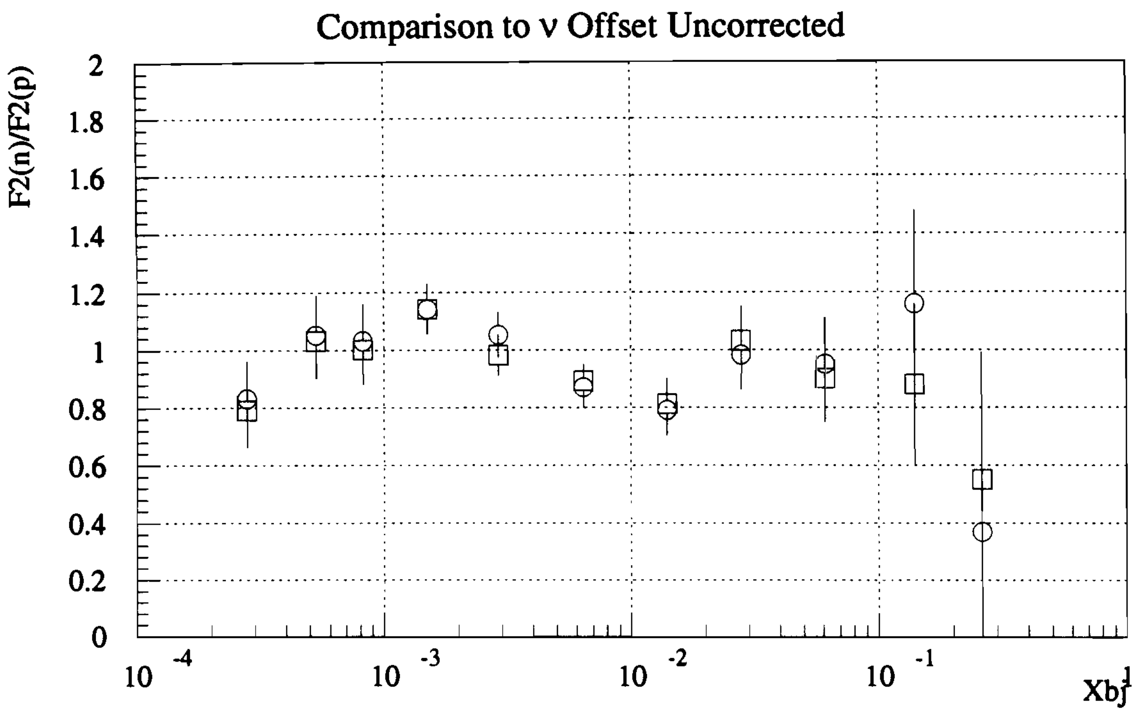

SAT Trigger

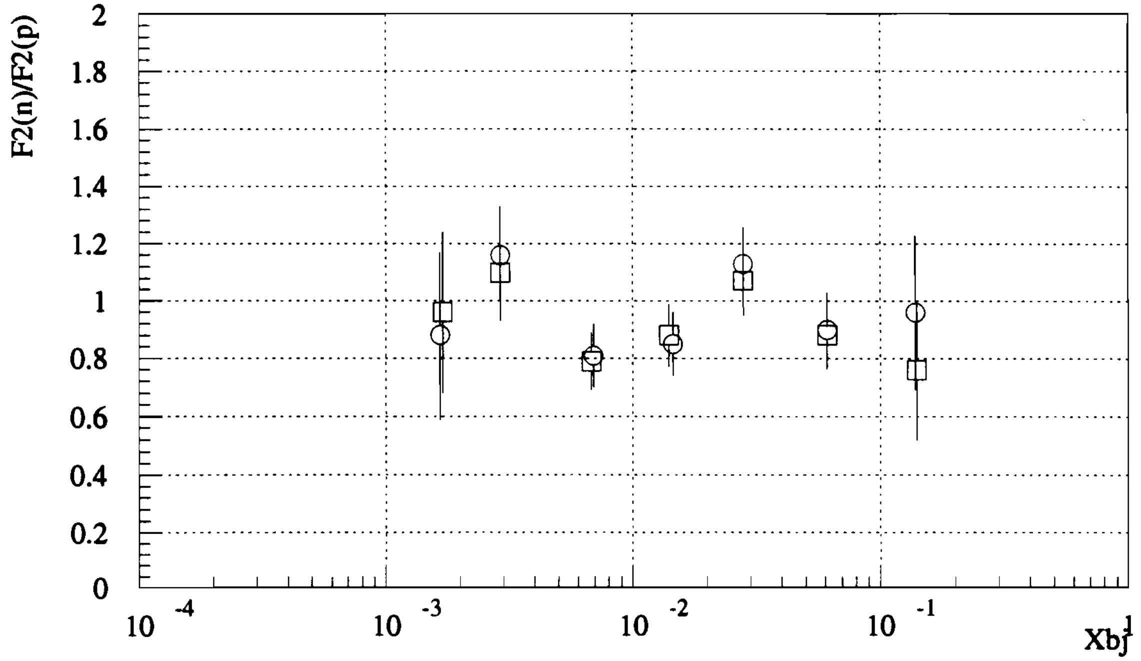

LAT Triggers

Figure 5.2: $F_2^n/F_2^p(x_{bj})$ with ν Offset correction applied (circles) and without the correction (squares)

to pass the calorimetry cut and contaminate. Two events from the bremsstrahlung candidate sample in the lowest x_{bj} bin pass the cut, compared to 838.4 total events (empty target subtracted) in that bin. The bremsstrahlung contamination is negligible and no systematic error is assigned.

Figure 5.3 shows 10 events (6 H_2 and 4 D_2) between the two bremsstrahlung and mu-e candidate sub-samples that are consistent with being muon-electron elastic scatters in the range $4.5 \times 10^{-3} \leq x_{bj} \leq 6.0 \times 10^{-3}$ and which pass the calorimeter cuts. In this next-to-lowest x_{bj} bin, 951 total events (empty target subtracted) pass this cut. Assuming all of these candidates are in fact muon-electron scattering, the correction for this contamination would lead to a less than 1% change in the measured structure function ratio for this bin. Because of this, I quote a 1% systematic error in this bin due to muon-electron elastic scattering event contamination in the data sample after the calorimetry cuts.

Muon-Nucleon Losses

The loss of good events only affects the structure function ratio result if the fraction of good events lost is correlated to the target. A sample of muon-nucleon candidate events with at least three hadrons fitted to the vertex, some calorimeter energy, with $0.3 < y_{bj} < 0.7$, and yet failing the calorimeter cut was used to test this. A crude structure function ratio, integrated over all x_{bj}, was measured with these events and found to be 0.98 ± 0.11 [127]. Practically all events used in this test were at $x_{bj} < 1 \times 10^{-2}$ where the measured structure function ratio using the calorimeter cut is consistent with this value. The recent E665 RUN87 F_2^n/F_2^p analysis effort has also shown that the loss of muon-nucleon inelastic scattering events by the calorimetry cuts is unbiased by target [171]. I assign no systematic error for biases in the loss of muon-nucleon inelastic scattering events.

Sensitivity to Cut Values

Variations of the calorimeter cut have been tried to determine the sensitivity of the results to the method or cut value chosen. The $Ecal/\nu$ method and the $Ecal/(\nu\ Nclus)$ method with a stricter cut value are contrasted with the results with the $Ecal/(\nu\ Nclus)$ method, as is shown in Figure 5.4 on page 122. All results agree within error, although the result in the lowest x_{bj} bin varies widely. A systematic error is assigned for sensitivity to the details of the calorimeter cut in the lowest x_{bj} bin. The cause of this difference is under investigation.

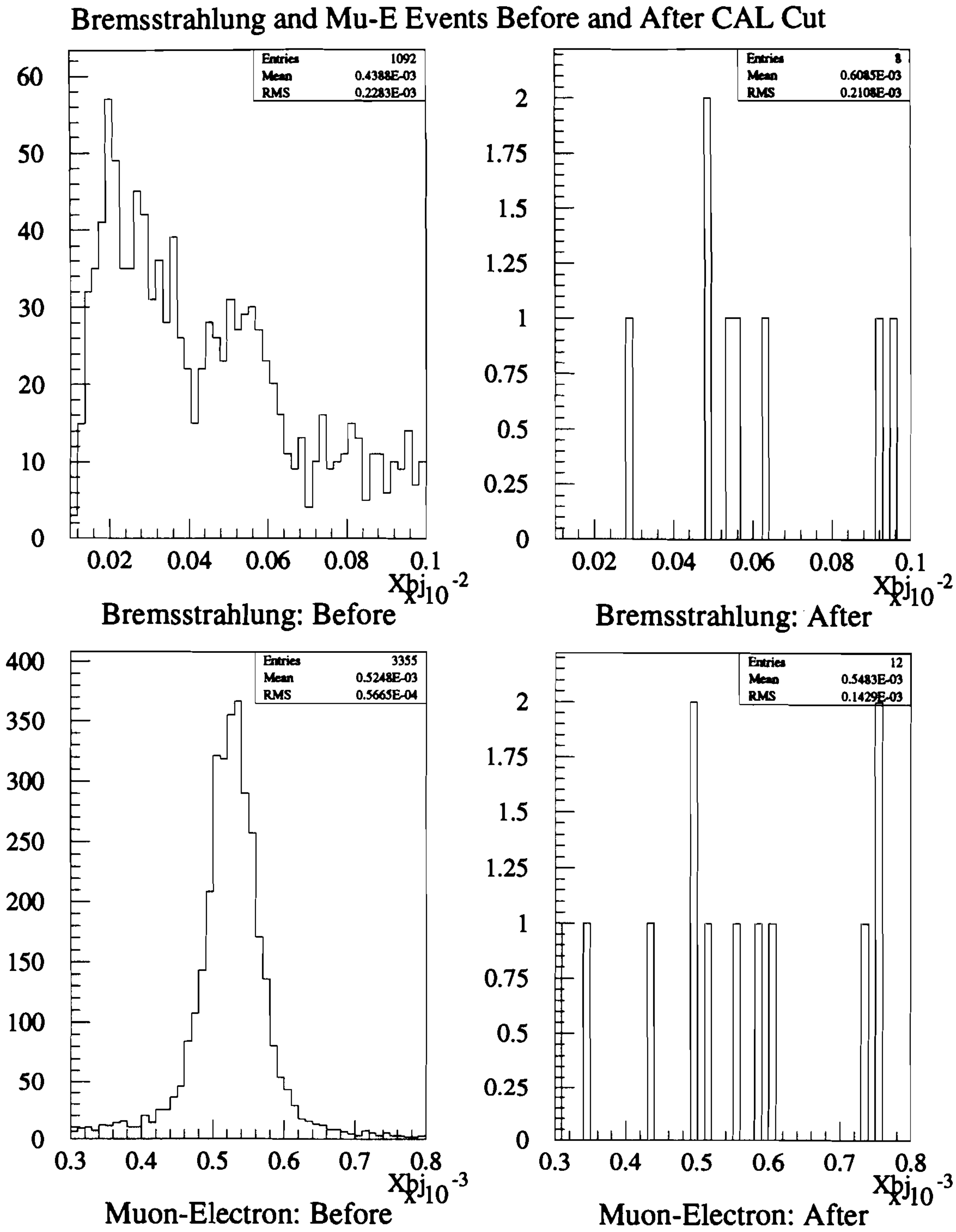

Figure 5.3: Effect of calorimetry cut on the bremsstrahlung and mu-e event candidates

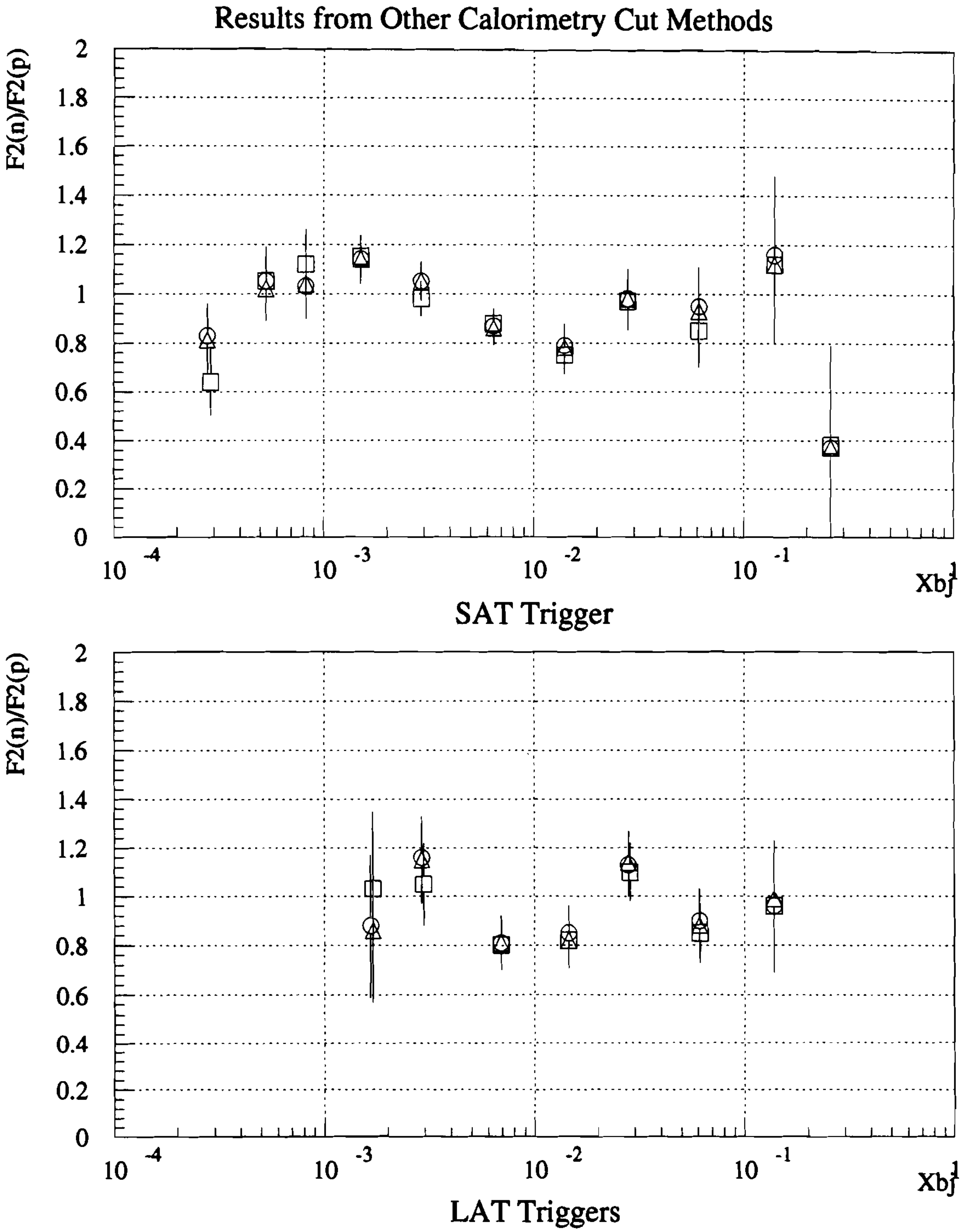

Figure 5.4: $F_2^n/F_2^p(x_{bj})$ with the final $Ecal/(\nu\ Nclus)$ cut (circles), a tighter $Ecal/(\nu\ Nclus)$ cut (triangles), and an $Ecal/\nu$ cut (squares)

5.2.3 Radiative Corrections

F_2 is interpreted in terms of the one-photon-exchange process. I have not, however, removed all the other radiative processes represented in the data set. Only bremsstrahlung for which the real photo strikes the electromagnetic calorimeter has been treated. While the bremsstrahlung rate classified as the inelastic tail is essentially the same for the two targets, the rates classified as the quasi-elastic tail and the coherent nucleus scattering are quite different between the targets. The sum of the two rates is greater in H_2 than in D_2 according to FERRAD version 35C, though this results is not fully tested. The specific concern is that these processes, which with the inelastic tail bremsstrahlung increasingly dominate the data at high y_{bj}, are not properly removed from the data sets. As shown in Section 5.2.2, however, all bremsstrahlung appears, within statistical errors, to be removed from the data set.

An estimate of the effect that higher-order processes have on the F_2 ratio measurement is made with a simplified use of radiative corrections as an alternative means to extract the ratio, as is shown in Figure 5.5. The effect at small x_{bj}, for instance, would be to lower the ratio reported when the nuclear coherent scattering in D_2 is corrected out. No significant difference between the results of the two methods is seen, although the kinematic region of greatest concern, small x_{bj} cannot be checked in this manner. I assign no systematic error for the failure to remove all radiative processes except one-photon-exchange from the data set.

5.2.4 Iterative Correction

Smearing Effects

Given the size of the smearing effects predicted by the Monte Carlo and the errors on the kinematics reported by the event reconstruction program, smearing does not appear to result in any significant change in the results.

Trigger Acceptance

H_2 and D_2 not only have different radiation lengths (865 cm and 757 cm), but they also have very different nuclear interaction lengths (718 cm and 338 cm). The materials appear to the scattered muon, for instance, to be somewhat similar, but relatively dissimilar to the hadrons produced in inelastic muon-nucleon interactions. These differences in activity in the targets can lead to target dependencies in the trigger acceptances. The SAT trigger, with its unshielded SSA veto element, could

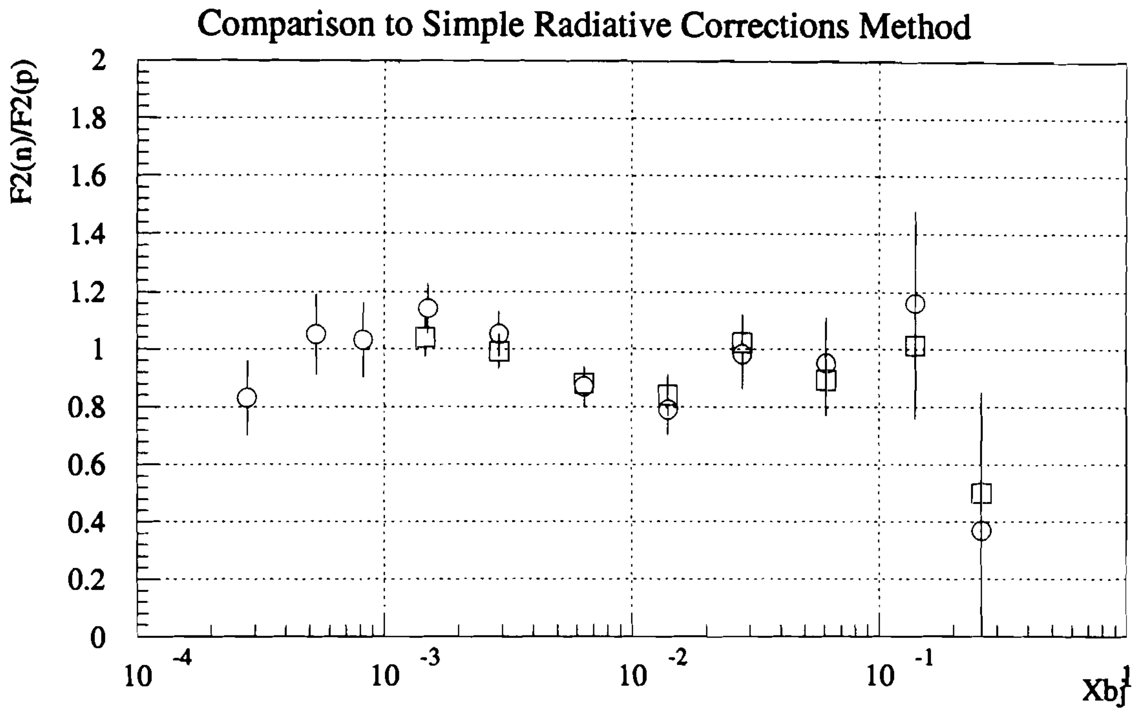

SAT Trigger

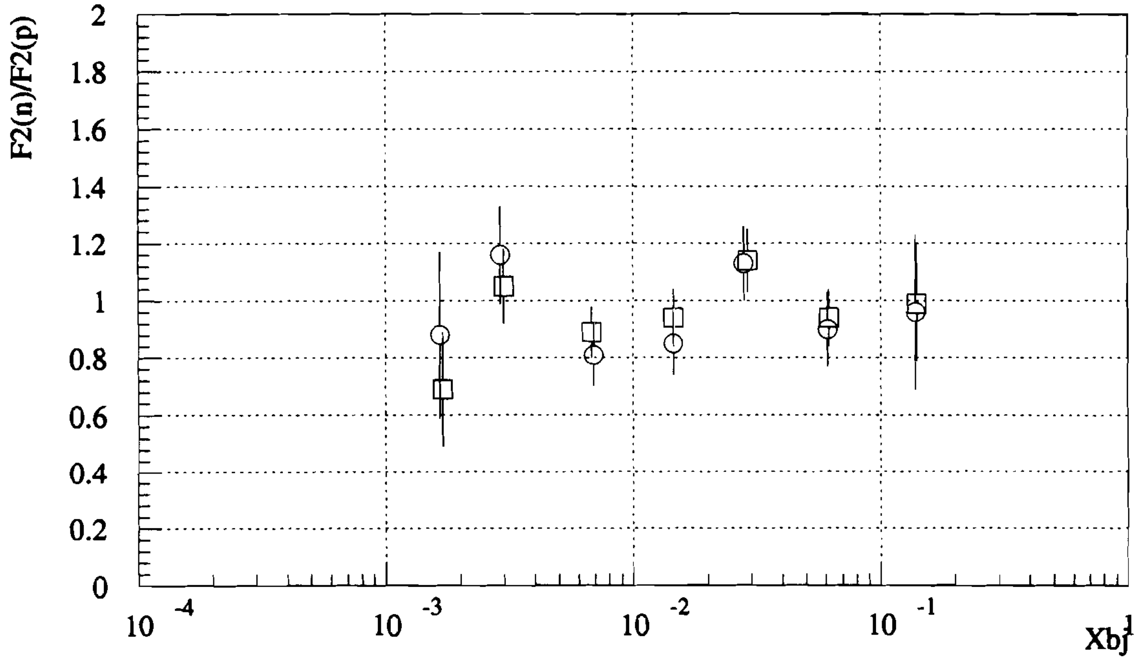

LAT Triggers

Figure 5.5: $F_2^n/F_2^p(x_{bj})$ from calorimeter cut method (circles) and simple radiative corrections method (squares)

have a larger fraction of good inelastic scatters vetoed in D_2 than H_2 by a hadron striking the SSA at the projected unscattered muon intercept. Both the SAT and LAT triggers could have the same "suicide" effect in the SMS and SVS veto elements respectively due to relatively small difference in electromagnetic activity in D_2 and H_2. Of the two, the SSA suicide effect is expected to be the larger, since it is related to the relatively larger difference in nuclear interation lengths. To date, a Monte Carlo simulation of this effect in RUN90 data for H_2 and D_2 has not included sufficent statistics to reliably estimate the size of these effects.

Vertex Location Comparison

The most direct check of how differences in target activity might influence the structure function ratio measurement is to compare measurements made with vertices in the upstream half of the target with those made with vertices in the downstream half of the target. The products of interactions in the upstream target half will on average see 0.5 m more target material than the products of interations in the downstream target half. Figure 5.6 on page 126 shows the two measurements for comparison.

Statistically significant differences are seen at large x_{bj} for both triggers and at moderate to small x_{bj} for the SAT trigger only. At large x_{bj}, the downstream target half results are larger, and at small x_{bj} the upstream target half results are larger. The differences seen only in the SAT trigger are assumed to be due to the difference in the radiation lengths of the targets and the one element in the SAT trigger definition that has no equivalent in the LAT triggers, the SSA veto. That the SAT-only differences are at small x_{bj} is consistent with the concern over electromagnetic or hadron suicides, but the upstream/downstream ratios are not as expected. For suicides to affect the structure function ratio as described, the upstream ratio should be depressed relative to the downstream ratio. The reverse is seen. The cause of these differences at small and at large x_{bj} are still under investigation. A systematic error is assigned based on the size of the difference, smoothed in x_{bj}.

5.2.5 Integrated Luminosity

Two sources of systematic error are related to the measurement of the relative integrated luminosity. I assign a 0.1% relative error to the cross section ratio due to the measurement of the relative target density and a 0.1% relative error due to the treatment of the HD contamination. Normalization contributes a relative error of 1.1% to the cross section ratio measured with the SAT trigger and 1.4% to that measured with the LAT trigger. These errors are added linearly to give a relative

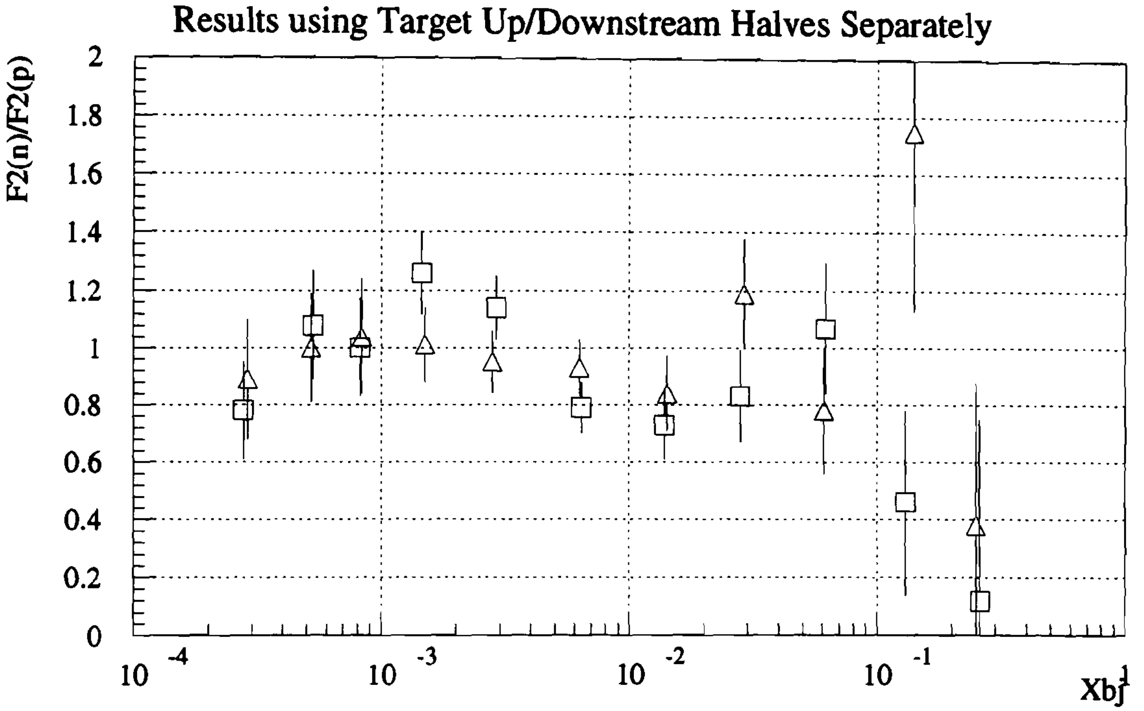

SAT Trigger

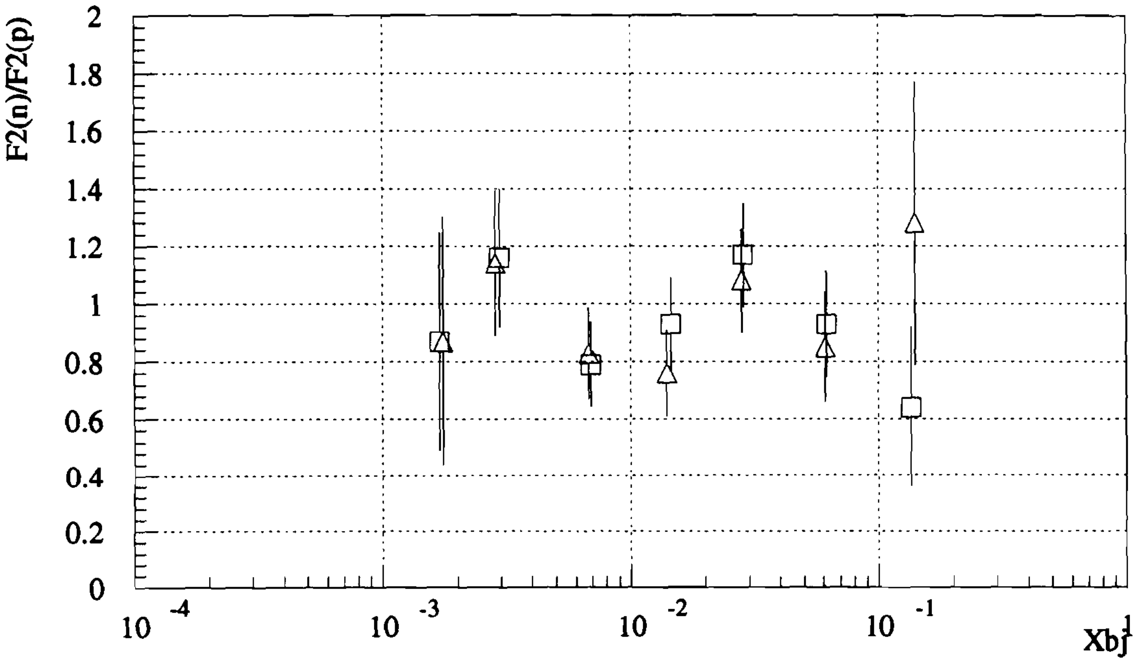

LAT Triggers

Figure 5.6: $F_2^n/F_2^p(x_{bj})$ in upstream target half (squares) and in downstream target half (triangles)

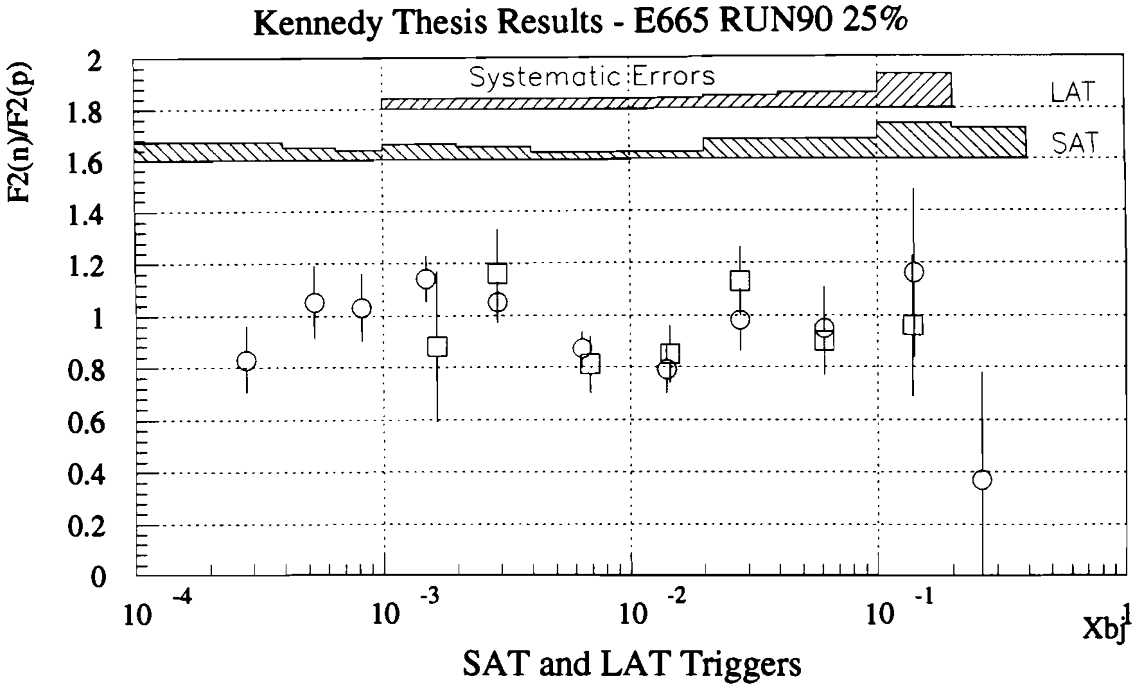

Figure 5.7: Final results for $F_2^n/F_2^p(x_{bj})$ from the SAT trigger (circles) and the LAT trigger (squares)

error on the relative luminosity measurement.

5.3 F_2^n/F_2^p Final Results

Table 5.2 and Table 5.3 give the values measured with the statistical and systematic errors.

Table 5.4 and Table 5.5 give the breakdown of the systematic errors assigned.

5.4 Comparison

5.4.1 E665 RUN87

Initial measurements of F_2^n/F_2^p at E665 using the RUN87 data set [7, 46] were restricted to $x_{bj} > 0.001$. Data from the H_2 and D_2 targets were taken at very

Table 5.2: $F_2^n/F_2^p(x_{bj})$ - $Ecal/(\nu\ Nclus)$ cut method - SAT trigger

Bin	Mean		Results		
x_{bj}	x_{bj}	Q^2	F_2^n/F_2^p	Stat Err	Sys Err
0.0001	0.00028	0.17	0.83	0.13	0.07
0.0004	0.00053	0.28	1.05	0.13	0.05
0.00065	0.00082	0.38	1.03	0.13	0.04
0.0010	0.00147	0.56	1.14	0.09	0.06
0.0020	0.0029	0.89	1.05	0.08	0.05
0.0040	0.0064	1.7	0.87	0.07	0.03
0.0100	0.0139	3.4	0.79	0.09	0.03
0.0200	0.028	6.7	0.98	0.12	0.08
0.0400	0.061	15	0.95	0.16	0.08
0.1000	0.138	30	1.16	0.32	0.14
0.2000	0.26	75	0.37	0.41	0.12

Table 5.3: $F_2^n/F_2^p(x_{bj})$ - $Ecal/(\nu\ Nclus)$ cut method - LAT trigger

Bin	Mean		Results		
x_{bj}	x_{bj}	Q^2	F_2^n/F_2^p	Stat Err	Sys Err
0.001	0.0017	1.2	0.88	0.29	0.04
0.002	0.0029	1.8	1.16	0.17	0.04
0.004	0.0068	3.2	0.81	0.12	0.04
0.010	0.0145	5.0	0.85	0.12	0.04
0.020	0.029	7.9	1.13	0.13	0.05
0.040	0.061	15	0.90	0.13	0.06
0.100	0.138	29	0.96	0.27	0.13

Table 5.4: Breakdown of systematic errors - SAT trigger

Bin x_{bj}	Total	ν Offset	Calorimeter Cut Method	Iterative Correction	Luminosity
0.0001	0.07	0.02	0.03	0.00	0.02
0.0004	0.05	0.01	0.01	0.00	0.03
0.00065	0.04	0.01	0.00	0.00	0.03
0.0010	0.06	0.01	0.00	0.02	0.03
0.0020	0.05	0.01	0.00	0.01	0.03
0.0040	0.03	0.01	0.00	0.00	0.02
0.0100	0.03	0.01	0.00	0.00	0.02
0.0200	0.08	0.02	0.00	0.03	0.03
0.0400	0.08	0.03	0.00	0.02	0.03
0.1000	0.14	0.06	0.00	0.05	0.03
0.2000	0.12	0.10	0.00	0.00	0.02

Table 5.5: Breakdown of systematic errors - LAT trigger

Bin x_{bj}	Total	ν Offset	Calorimeter Cut Method	Iterative Correction	Luminosity
0.0010	0.04	0.01	0.00	0.00	0.03
0.0020	0.04	0.01	0.00	0.00	0.03
0.0040	0.04	0.01	0.00	0.00	0.03
0.0100	0.04	0.01	0.00	0.00	0.03
0.0200	0.05	0.02	0.00	0.00	0.03
0.0400	0.06	0.03	0.00	0.00	0.03
0.1000	0.12	0.06	0.00	0.03	0.03

differents times. This introduced large systematic errors in the measurement, due to differences in detector efficiency, for instance. A more recent effort to use the SAT data from RUN87 does go to small x_{bj}, in fact down to $x_{bj} = 2 \times 10^{-5}$, a smaller value of x_{bj} than is kinematically possible in the RUN90 data set [170]. A comparison of all of these results is shown in Figure 5.8 on page 131. Within errors, the measurements appear to agree where there is overlap. The disagreement in the one point just above $x_{bj} = 0.1$ is partly due to the lack of a ν Offset correction to the preliminary RUN87 results.

5.4.2 NMC, BCDMS, and SLAC

A comparison of my results to those of NMC [13], BCDMS [40], and SLAC [204] is presented in Figure 5.9 on page 132. Note that the statistical errors on the other results are smaller than the points. Where there is overlap, my results appear to agree with these experiments.

5.4.3 Badełek and Kwieciński F_2 Model

A comparison of my results to the predictions of the Badełek and Kwieciński F_2 model [31] shows agreement.

5.5 Discussion

The challenges behind measurements of F_2^n/F_2^p at any x_{bj} are normalization, momentum calibration, acceptance, efficiency, and smearing. Changing targets one at a time practically eliminates detector acceptance and efficiency-related systematic errors. Clearly more work is required to better understand target-related differences in trigger acceptance near the small angle limit of acceptance. Normalization has been performed well with a relative error of less than 1.5% on the cross section ratio. Our momentum calibration is not completely understood, but understanding it has become one of E665's highest priorities. The *ad hoc* model applied as a correction in this study appears to be justified by recent attempts to remove this miscalibration from our event reconstruction program. Smearing effects from detector and software resolution appear to be reduced in magnitude from the RUN87 event reconstruction efforts.

The new challenges at very small x_{bj} are the treatment of radiative processes and muon-electron elastic scattering which overwhelm the inelastic scattering cross

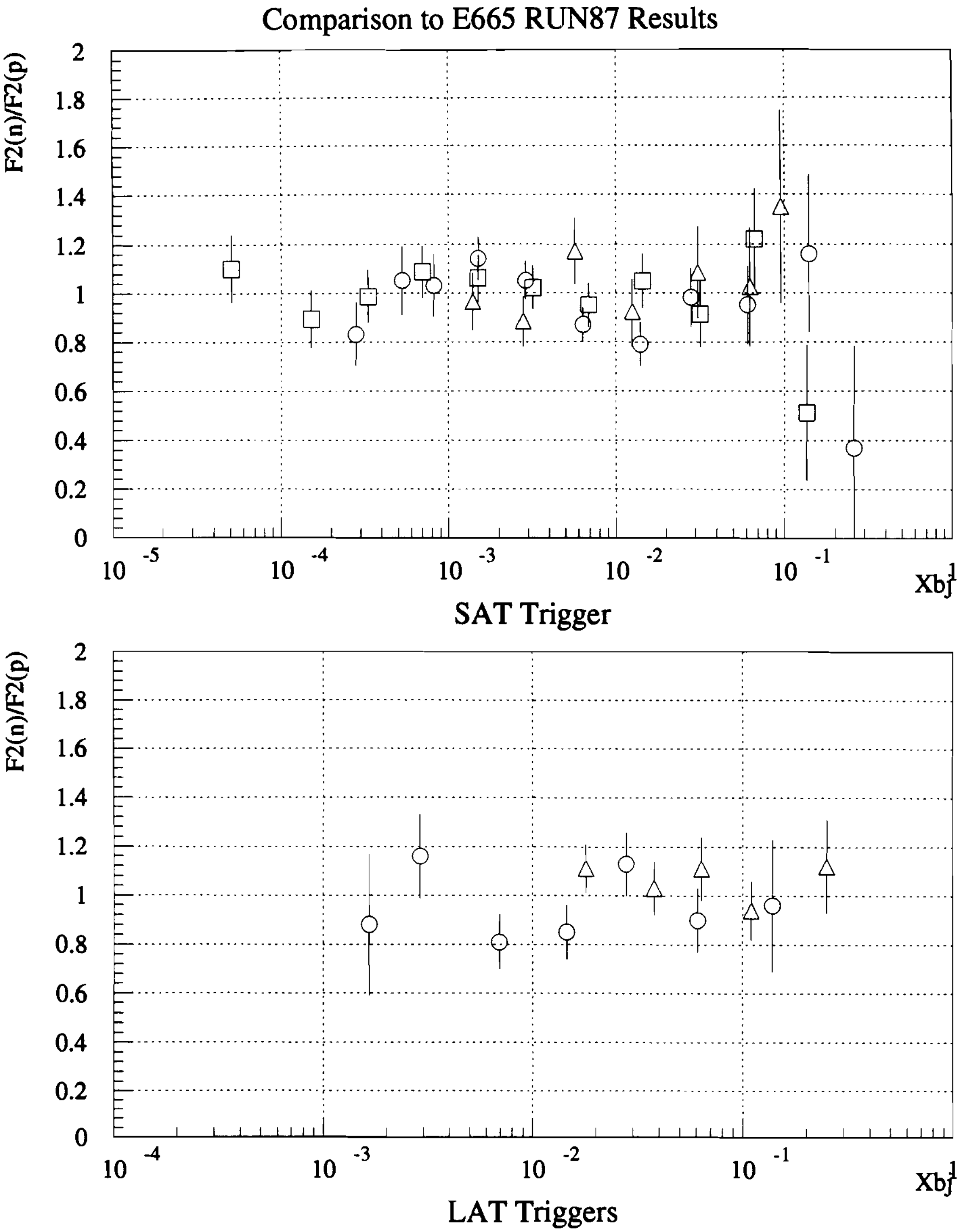

Figure 5.8: Results of this thesis (circles), recent preliminary RUN87 SAT results (squares), and early RUN87 results (triangles)

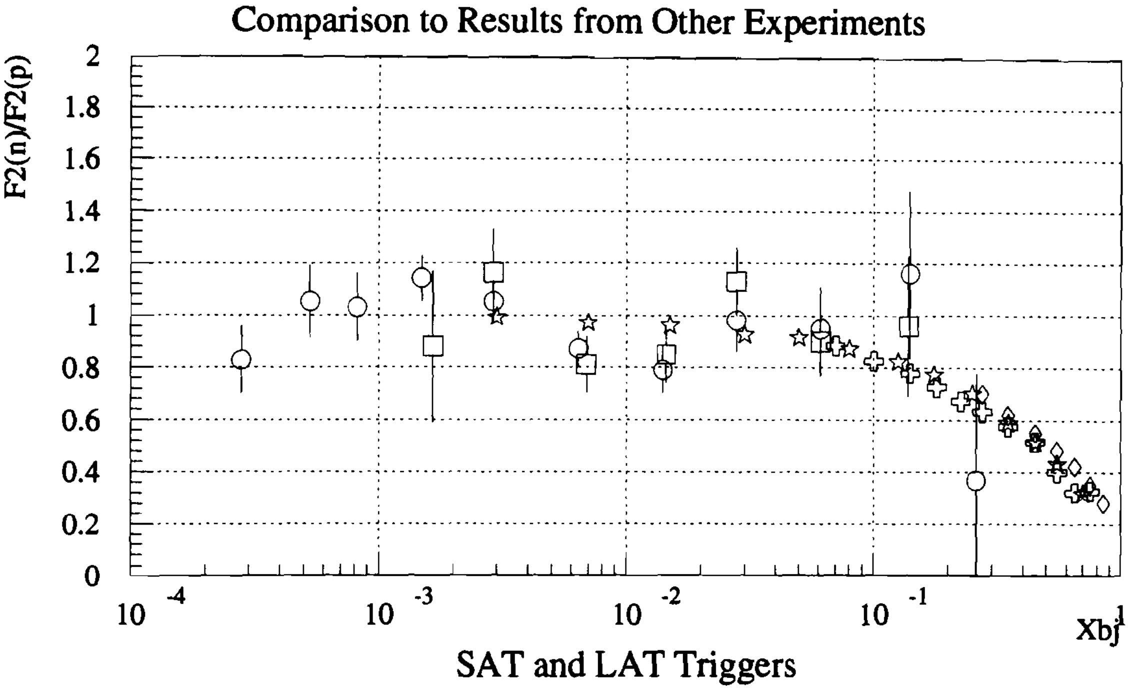

Figure 5.9: Results of this thesis for SAT (circles) and LAT (squares) compared to recent results from NMC (stars), BCDMS (crosses), and SLAC (diamonds)

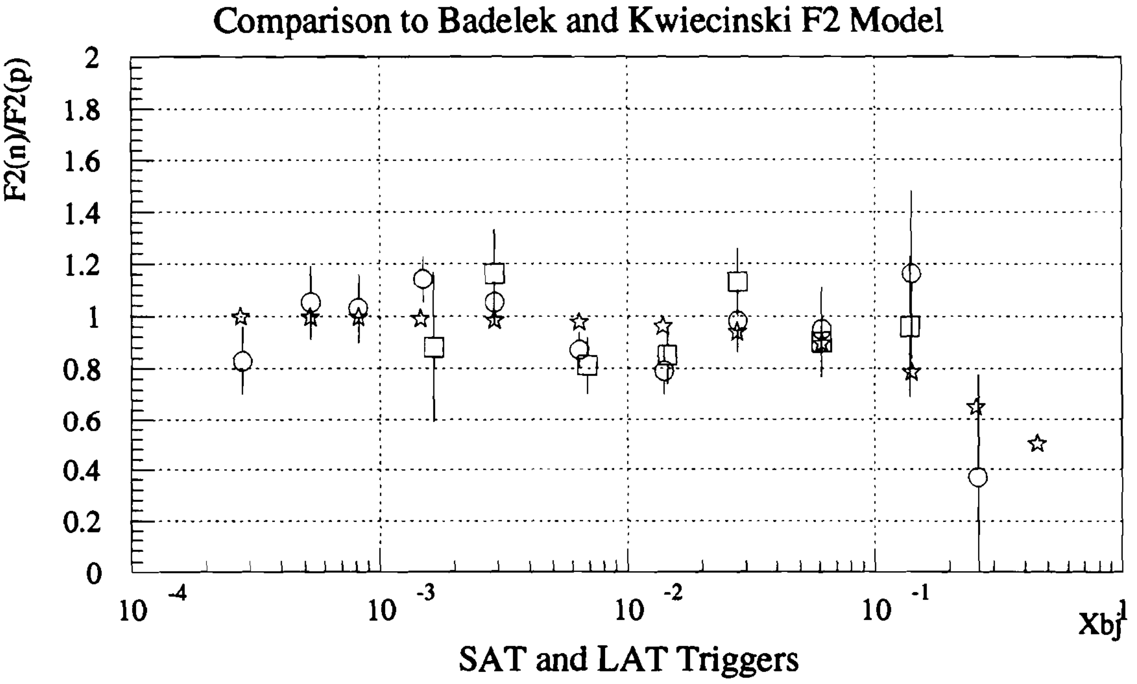

Figure 5.10: Results of this thesis for SAT (circles) and LAT (squares) compared to the Badelek and Kwiecinski F_2 model prediction (stars)

section. Nevertheless, these events tend to have distinct characteristics that enable them to be identified and removed on an event-by-event basis. There is an intimate connection between differences in the radiation and nuclear interaction lengths of the targets and trigger suicides in small angle scattering that has not been adequately explored. This is likely affect only the results in the lowest x_{bj} bin. An improved detector simulation and large-scale generation and reconstruction of Monte Carlo data are required to address this issue.

The utility of this measurement of the approach of F_2^n/F_2^p to unity is reduced by the relatively large statistical errors. Efforts are now underway to complete the analysis of the RUN90 data set. RUN90 is estimated to contain four times more statistics total than this thesis data set. RUN91, which was dedicated to H_2 and D_2 targets only, has an estimated ten times the event statistics of all of RUN90. This could yield a statistical precision in the structure function ratio as small as 1.5%, a much smaller relative error on the relative luminosity, and a practically eliminated ν Offset. If this holds up after eliminating data from questionable run periods, then we should be able to test for deuteron shadowing effects at the 5% level in the next year. Absolute structure function measurements are also possible, but only with a better understanding of detector and trigger behavior. The measurement of structure function ratios for heavy targets is also being pursued using the RUN90 data set.

5.6 Conclusion

The ratio of the neutron and proton structure functions F_2 has been found to be consistent with unity to very low x_{bj}. The data used in this measurement were taken in 1990 using 475 GeV muons incident on hydrogen and deuterium targets. Several different methods have been used to remove radiative backgrounds and muon-electron elastic scattering. The kinematic region covered by the data used is $0.0001 \leq x_{bj} \leq 0.40$ and $0.1\ \mathrm{GeV}^2/c^2 \leq Q^2 \leq 100.0\ \mathrm{GeV}^2/c^2$.

Appendices

Curiously enough, the dolphins had long known of the impending destruction of the planet Earth and had made many attempts to alert mankind to the danger; but most of their communications were misinterpreted as amusing attempts to punch footballs, or whistle for tidbits, so they eventually gave up and left the Earth by their own means shortly before the Vogons arrived.

The last dolphin message was misinterpreted as a surprisingly sophisticated attempt to do a double-backward somersault through a hoop while whistling the "Star-Spangled Banner," but in fact the message was this: So long and thanks for all the fish.

Douglas Adams, *The Hitchhiker's Guide to the Galaxy* (1979)

Appendix A

The Fermilab E665 Collaboration

A.1 E665 NIM Paper Author List

M. R. Adams(7), S. Aïd(8), P. L. Anthony(9), M. D. Baker(9), J. Bartlett(4), A. A. Bhatti(11), H. M. Braun(12), T. Burnett(11), W. Busza(9), J. M. Conrad(6), G. B. Coutrakon(4a), R. Davisson(11), S. K. Dhawan(13), W. Dougherty(11), T. Dreyer(5), V. Eckardt(10), U. Ecker(12), M. Erdmann(5), A. Eskreys(3,14), K. Eskreys(3,14), H. J. Gebauer(10), D. F. Geesaman(1), R. Gilman(1), M. C. Green(1b), J. Haas(5), C. Halliwell(7), J. Hanlon(4), V. W. Hughes(13), H. E. Jackson(1), G. Jancso(10), D. M. Jansen(11), S. Kaufman(1), R. D. Kennedy(2), T. Kirk(4d), H. G. E. Kobrak(2), S. Krzywdzinski(11c), S. Kunori(8), J. J. Lord(11), H. J. Lubatti(11), T. Lyons(9), D. McLeod(7), S. Magill(7), P. Malecki(3,14), A. Manz(10), H. Melanson(4), D. G. Michael(6), W. Mohr(5), H. E. Montgomery(4), J. G. Morfín(4), R. B. Nickerson(6), S. O'Day(8), A. M. Osborne(2,4,6f), L. Osborne(9), B. Pawlik(3,14), F. M. Pipkin(6), E. J. Ramberg(8), A. Röser(12), J. J. Ryan(9), A. Salvarani(2), M. Schmitt(6), K. P. Schüler(13), E. Sexton(2,7c), H. J. Seyerlein(10), A. Skuja(8), S. Söldner-Rembold(10), P. H. Steinberg(8h), H. E. Stier(5), P. Stopa(10g), P. Stube(10), R. A. Swanson(2), R. L. Talaga(8d), S. Tentindo-Repond(1e), H.-J. Trost(10d), H. Venkataramania(13), M. Vidal(10), M. Wilhelm(5), J. Wilkes(11), Richard Wilson(6), S. A. Wolbers(4), and T. Zhao(11)

(1) Argonne National Laboratory, Argonne, IL 60439, USA
(2) University of California, San Diego, La Jolla, CA 92093,USA
(3) Institute of Nuclear Physics, PL-31 342 Krakow, Poland
(4) Fermi National Accelerator Laboratory, Batavia,IL 60510,USA
(5) Albert-Ludwigs-Universität im Breisgau, W-7800 Freiburg, Germany
(6) Harvard University, Cambridge, MA 02138, USA
(7) University of Illinois, Chicago, IL 60680, USA
(8) University of Maryland, College Park, MD 20742, USA
(9) Massachusetts Institute of Technology, Cambridge, MA 02139, USA
(10) Max-Planck-Institut für Physik und Astrophysik, 8000 Münich 40, Germany
(11) University of Washington, Seattle, WA 98195, USA
(12) Universität-Gesamthochschule Wuppertal, 5600 Wuppertal 1, Germany
(13) Yale University, New Haven, CT 06520, USA
(14) Institute of Nuclear Physics and Technology, Krakow,Poland

[a] Current address: Loma Linda University Medical Center, Loma Linda, CA 92350, USA.
[b] Current address: LeCroy Research Systems, Spring Valley, NY 10977, USA.
[c] Current address: Fermi National Accelerator Laboratory, Batavia, IL 60510, USA.
[d] Current address: Argonne National Laboratory, Argonne, IL 60439, USA.
[e] Current address: Northern Illinois University, DeKalb, IL 60115, USA.
[f] Permanent address: CERN, 23 Genève 1211, Switzerland.
[g] Permanent address: Institute of Nuclear Physics, Krakow, Poland.
[h] Deceased.

A.2 E665 RUN87 Author List

M. R. Adams(6), S. Aïd(9), P. L. Anthony(10a), M. D. Baker(10), J. Bartlett(4), A. A. Bhatti(13b), H. M. Braun(14), W. Busza(10), T. J. Carroll(6), J. M. Conrad(5), G. B. Coutrakon(4c), R. Davisson(13), I. Derado(11), S. K. Dhawan(15), W. Dougherty(13), T. Dreyer(1), K. Dziunikowska(8), V. Eckardt(11), U. Ecker(14q), M. Erdmann(1e), A. Eskreys(7), J. Figiel(7), H. J. Gebauer(11), D. F. Geesaman(2), R. Gilman(2d), M. C. Green(2f), J. Haas(1), C. Halliwell(6), J. Hanlon(4), D. Hantke(11), V. W. Hughes(15), H. E. Jackson(2), D. E. Jaffe(6g), G. Jancso(11), D. M. Jansen(13h), S. Kaufman(2), R. D. Kennedy(3), T. Kirk(4i), H. G. E. Kobrak(3), S. Krzywdzinski(4), S. Kunori(9), J. J. Lord(13), H. J. Lubatti(13), D. McLeod(6), S. Magill(6i), P. Malecki(7), A. Manz(11), H. Melanson(4), D. G. Michael(5j), W. Mohr(1), H. E. Montgomery(4), J. G. Morfín(4), R. B. Nickerson(5k), S. O'Day(9l), K. Olkiewicz(7), L. Osborne(10), V. Papavassiliou(15i), B. Pawlik(7), F. M. Pipkin(5o), E. J. Ramberg(9l), A. Röser(14r), J. J. Ryan(10), A. Salvarani(3m), H. Schellman(12), M. Schmitt(5n), N. Schmitz(11), K. P. Schüler(15), H. J. Seyerlein(11), A. Skuja(9), G. Snow(9), S. Söldner-Rembold(11), P. H. Steinberg(9o), H. E. Stier(1o), P. Stopa(7), R. A. Swanson(3), R. L. Talaga(9i), S. Tentindo-Repond(2p), H.-J. Trost(2), H. Venkataramania(15), M. Vidal(11), M. Wilhelm(1), J. Wilkes(13), Richard Wilson(5), W. Wittek(11), S. A. Wolbers(4), and T. Zhao(13)

(1) Albert-Ludwigs-Universität im Breisgau, W-7800 Freiburg, Germany
(2) Argonne National Laboratory, Argonne, IL 60439, USA
(3) University of California, San Diego, La Jolla, CA 92093,USA
(4) Fermi National Accelerator Laboratory, Batavia,IL 60510,USA
(5) Harvard University, Cambridge, MA 02138, USA
(6) University of Illinois, Chicago, IL 60680, USA
(7) Institute of Nuclear Physics, PL-31 342 Krakow, Poland
(8) Institute of Nuclear Physics, Academy of Mining and Metallurgy, Krakow, Poland
(9) University of Maryland, College Park, MD 20742, USA
(10) Massachusetts Institute of Technology, Cambridge, MA 02139, USA
(11) Max-Planck-Institut für Physik und Astrophysik, 8000 Münich 40, Germany
(12) Northwestern University, Evanston, IL 60208, USA
(13) University of Washington, Seattle, WA 98195, USA
(14) Universität-Gesamthochschule Wuppertal, 5600 Wuppertal 1, Germany
(15) Yale University, New Haven, CT 06520, USA

(a) Current address: Lawrence Livermore National Laboratory, Livermore, CA 94550, USA.
(b) Current address: Rockefeller University, New York, NY 10021, USA.
(c) Current address: Loma Linda University Medical Center, Loma Linda, CA 92350, USA.
(d) Current address: Rutgers University, Piscataway, NJ 08855, USA.
(e) Current address: DESY, Notkestraße 85, W-2000 Hamburg, Germany.
(f) Current address: LeCroy Research Systems, Spring Valley, NY 10977, USA.
(g) Current address: Laboratoire de l'Accélérateur Linéaire, 91405 Orsay, France.
(h) Current address: Los Alamos National Laboratory, Los Alamos, NM 87545, USA.
(i) Current address: Argonne National Laboratory, Argonne, IL 60439, USA.
(j) Current address: California Institute of Technology, Pasadena, CA 91125, USA.
(k) Current address: Oxford University, Oxford OX1 3RH, United Kingdom.
(l) Current address: Fermi National Accelerator Laboratory, Batavia, IL 60510, USA.
(m) Current address: A. T. & T., Bell Laboratories, 2000 North Naperville Road, Naperville, IL, USA.
(n) Current address: University of Wisconsin, Madison, WI 53706, USA.
(o) Deceased.
(p) Current address: Northern Illinois University, DeKalb, IL 60115, USA.
(q) Current address: Büro Schellmann, Rabenhorst 29, Hamburg 65, Germany.
(r) Current address: Ruhruniversität Bochum, D-4630 Bochum 1, Germany.

A.3 E665 RUN90/91 Author List

M. R. Adams(7), S. Aïd(10), P. L. Anthony(9), D. A. Averill(7), M. D. Baker(11), B. R. Baller(5), A. Banerjee(15), A. A. Bhatti(16), U. Bratzler(16), H. M. Braun(17), H. Breidung(17), W. Busza(11), T. J. Carroll(7), H. Clark(14), J. M. Conrad(6), R. Davisson(16), I. Derado(12), S. K. Dhawan(18), F. S. Dietrich(9), W. Dougherty(16), T. Dreyer(1), V. Eckardt(12), U. Ecker(17), M. Erdmann(1), A. Eskreys(8), G. Y. Fang(6), J. Figiel(8), R. Finlay(14), H. J. Gebauer(12), D. F. Geesaman(2), K. Griffioen(15), R. S. Guo(7), J. Haas(1), C. Halliwell(7), J. Hanlon(5), D. Hantke(12), K. H. Hicks(14), V. W. Hughes(18), H. E. Jackson(2), D. E. Jaffe(7), G. Jancso(12), D. M. Jansen(16), Z. Jin(16), S. Kaufman(2), R. D. Kennedy(3), E. Kinney(4), T. Kirk(2), H. G. E. Kobrak(3), A. Kotwal(6), S. Kunori(10), M. Lenski(1), J. J. Lord(16), H. J. Lubatti(16), T. McKibben(7), D. McLeod(7), P. Madden(3), S. Magill(7), A. Manz(12), H. Melanson(5), D. G. Michael(6), W. Mohr(1), H. E. Montgomery(5), J. G. Morfín(5), R. B. Nickerson(6), S. O'Day(10), K. Olkiewicz(8), L. Osborne(11), R. Otten(17), V. Papavassiliou(2), B. Pawlik(8), R. S. Perry(16), F. M. Pipkin(6), D. Potterveld(2), E. J. Ramberg(10), A. Röser(17), J. J. Ryan(11), C. Salgado(5), A. Salvarani(3), H. Schellman(13), M. Schmitt(6), N. Schmitz(12), K. P. Schüler(18), G. Siegert(1), A. Skuja(10), G. Snow(10), S. Söldner-Rembold(12), P. Spentzouris(13), H. E. Stier(1), P. Stopa(8), R. A. Swanson(3), H. Venkataramania(18), M. Vidal(12), M. Wilhelm(1), J. Wilkes(16), Richard Wilson(6), W. Wittek(12), S. A. Wolbers(5), A. Zgiche(2), and T. Zhao(16)

(1) Albert-Ludwigs-Universität im Breisgau, W-7800 Freiburg, Germany
(2) Argonne National Laboratory, Argonne, IL 60439, USA
(3) University of California, San Diego, La Jolla, CA 92093, USA
(4) University of Colorado, Boulder, CO, USA
(5) Fermi National Accelerator Laboratory, Batavia, IL 60510, USA
(6) Harvard University, Cambridge, MA 02138, USA
(7) University of Illinois, Chicago, IL 60680, USA
(8) Institute of Nuclear Physics, PL-31 342 Krakow, Poland
(9) Lawrence-Livermore Laboratory, Livermore, CA 94550, USA
(10) University of Maryland, College Park, MD 20742, USA
(11) Massachusetts Institute of Technology, Cambridge, MA 02139, USA
(12) Max-Planck-Institut für Physik und Astrophysik, 8000 Münich 40, Germany
(13) Northwestern University, Evanston, IL 60208, USA
(14) Ohio University, Athens, OH, USA
(15) University of Pennsylvania, Philadelphia, PA, USA
(16) University of Washington, Seattle, WA 98195, USA
(17) Universität-Gesamthochschule Wuppertal, 5600 Wuppertal 1, Germany
(18) Yale University, New Haven, CT 06520, USA

Appendix B

Review of Inelastic Scattering

B.1 The Naïve Quark-Parton Model

The QCD-enhanced Quark-Parton model describes a free nucleon under a set of assumptions, many of which are not realistic from the point of view of the experimenter. In order to show where certain approximations are made in the model, this appendix presents a review of the QCD-enhanced Quark-Parton Model. This description is certainly incomplete, and the reader is referred to a number of texts [62, 97, 104, 173, 209] and review articles [15, 43, 73, 75, 91, 168, 26] for more detailed information. First, a description of the non-relativistic "naïve" Quark-Parton Model is given. This is followed by a brief outline of some of the features of the relativistic QCD-enhanced Quark-Parton Model. Finally, a number of experimental issues beyond the QCD-enhanced Quark-Parton Model are discussed.

B.1.1 Isospin

The striking similarities between the proton and the neutron led to the idea that the two particles may represent two different states of the same particle, called the nucleon. The property distinguishing the two states came to be known as isospin. The original statement of isospin symmetry was that the properties of hadronic interactions were unchanged under the exchange of a proton with a neutron. The symmetry is broken by the differences in mass, electromagnetic interactions, and weak interactions between the proton and the neutron. While this model is not in common use today as a description of nucleon-nucleon interactions, a variant of it is used today to motivate models of the effect of sea quarks on nucleon structure. This variant is stated as a symmetry under the interchange of down and up quarks. This interchange can be considered a symmetry because the differences in mass, electromagnetic interactions, and weak interactions between the down and up quark flavors are small compared to the strong interactions each undergoes. Again, the symmetry is only approximate since these differences do exist and are important for sufficiently small energy phenomena.

B.1.2 The Quark-Parton Model

In the Quark-Parton Model, the nucleon is composed of three valence quarks and an indefinite number of sea quarks and gluons. All of these quarks and gluons are collectively referred to as partons. The connection to Inelastic Muon Scattering is made by considering the one-photon-exchange interaction under the assumption that the muon mass, nucleon mass, and all transverse momenta of the partons are negligible. Furthermore, the partons are considered to be essentially non-interacting during the one-photon-exchange interaction. This is realized in the limit that $Q^2 \rightarrow \infty$ (in other words, $Q^2 \gg M^2$) or by assuming the time scale of the intra-nucleon interactions is much longer than that of the Inelastic Muon Scatter interaction. In this limit, scattering is referred to as being "deep", meaning that individual partons are distinguished (the nucleon is "deeply" penetrated by the virtual photon). At E665, given the scale of Q^2 observed (0.1 GeV^2/c^2 to 100 GeV^2/c^2), these approximations hold in some, but not all, of the data set. Target mass and other corrections are applied to the model to maintain its validity for $Q^2 \sim M^2$.

B.1.3 Deep-Inelastic Scattering Cross Section

A cross section for the one-photon-exchange process can be constructed, even though the details of the nucleon-photon vertex are not known, by assuming that it takes on a form similar to that describing lepton-lepton scattering:

$$d\sigma \sim \frac{L_{\mu\nu}W^{\mu\nu}}{(\alpha\hbar c)^2} \tag{B.1}$$

The muon-photon vertex contribution to the scattering amplitude $L_{\mu\nu}$ is completely described by Quantum Electrodynamics and is thus calculable. The nucleon-photon vertex cannot yet be calculated from first principles. Its contribution $W^{\mu\nu}$ to the scattering amplitude is parameterized by "structure functions". By requiring Lorentz invariance, charge conservation, and averaging over spins of incoming particles and summing over spins of outgoing particles, only two structure functions are required to construct the most general parameterization of the contribution in terms of the independent momenta in the interaction.

$$\begin{aligned} W^{\mu\nu}(Q^2,\nu) &= \left(-g^{\mu\nu} + \frac{q^\mu q^\nu}{q^2}\right) W_1(Q^2,\nu) & \text{(B.2)} \\ &\quad + \frac{1}{M^2}\left(P^\mu - \frac{P\cdot q}{q^2}q^\mu\right)\left(P^\nu - \frac{P\cdot q}{q^2}q^\nu\right) W_2(Q^2,\nu) & \text{(B.3)} \end{aligned}$$

The structure functions W_1 and W_2 describe the electric and magnetic interactions of the hadron current through the nucleon-photon vertex. In inelastic scattering, the structure functions are dependent on two of the Lorentz scalars listed above. W_1 and W_2 are traditionally stated as functions of Q^2 and ν since Q^2 describes the length scale probed by the virtual photon and ν is related to the degree of inelasticity of the interaction.

It is useful to define R, the ratio of the total absorption cross sections for longitudinally (σ_L) and transversely (σ_T) polarized virtual photons.

$$R(Q^2,\nu) \equiv \frac{\sigma_L(Q^2,\nu)}{\sigma_T(Q^2,\nu)} \tag{B.4}$$

This ratio can be related to the structure functions[1] using the following expressions:

$$W_1(Q^2,\nu) = \frac{\alpha}{\pi}\left(\frac{\nu - Q^2/2M}{4\pi(\alpha\hbar c)^2}\right)\sigma_T(Q^2,\nu) \tag{B.5}$$

$$W_2(Q^2,\nu) = \frac{\alpha}{\pi}\left(\frac{\nu - Q^2/2M}{4\pi(\alpha\hbar c)^2}\right)\left(\frac{Q^2}{\nu^2+Q^2}\right)\left(\sigma_T(Q^2,\nu)+\sigma_L(Q^2,\nu)\right) \tag{B.6}$$

B.1.4 Bjorken Scaling

The kinematic region in which $Q^2 \gg M^2$ and $\nu \gg M$, but Q^2/ν remains finite, is referred to as the deep-inelastic region[2]. If the nucleon is made up of constituent particles, then in this region the structure functions are dependent only on a fixed combination of Q^2 and ν described by the variable $x_{bj} \equiv Q^2/2M\nu$. This property is known as Bjorken scaling. The kinematic variable x_{bj} can be interpreted in the Quark-Parton model as the fraction of the nucleon momentum carried by the quark struck by the virtual photon. To codify the expectation of scaling, the structure functions F_1 and F_2 are introduced in the deep-inelastic region:

$$MW_1(Q^2,\nu) \rightarrow F_1(x_{bj}) \tag{B.7}$$

$$\nu W_2(Q^2,\nu) \rightarrow F_2(x_{bj}) \tag{B.8}$$

---

[1] There is some discrepancy in the presentation of the definition of the W_2 structure function amongst authors. Some include ϵ, the polarization parameter, as a coefficient of the σ_L term.

[2] "Deep" is related to the Q^2 and ν large limit and "inelastic" is related to $Q^2/2M\nu \neq 1$.

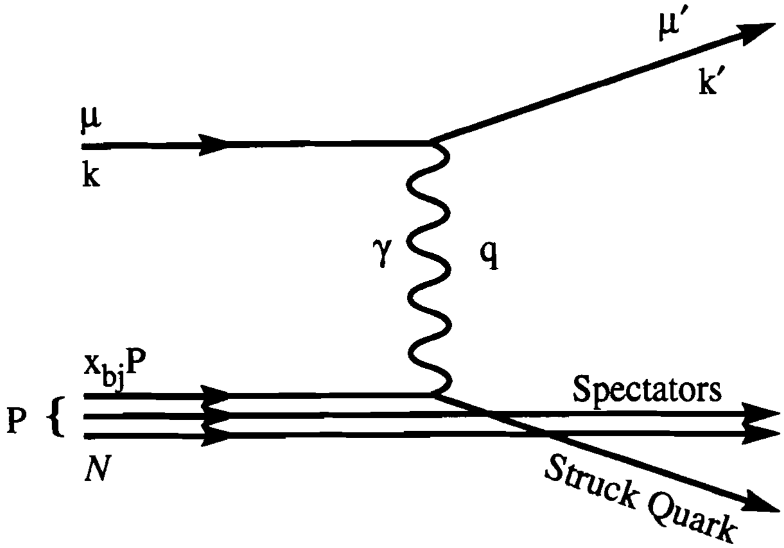

Figure B.1: Inelastic Muon Scattering as elastic scattering off a quark

The interaction is no longer viewed as inelastic scattering on the nucleon as a whole, but is now seen as elastic scattering on a single nucleon constituent as is shown in Figure B.1 on page 145. The virtual photon is often called the exchange photon, the quark absorbing the photon is called the struck quark, and all other partons in the nucleon are called the spectator partons.

The function R is often expressed as the ratio of the longitudinal and transverse components of F_1 and F_2 structure functions in a manner similar to Equations B.4, B.5, and B.6. This anticipates that the longitudinal component will pick up significant corrections as QCD and target mass effects are considered.

$$R(x_{bj}) = \frac{F_L(x_{bj})}{F_T(x_{bj})} \tag{B.9}$$

where, to this approximation

$$F_L(x_{bj}) = 2x_{bj}F_1(x_{bj}) - F_2(x_{bj}) \tag{B.10}$$
$$F_T(x_{bj}) = 2x_{bj}F_1(x_{bj}) \tag{B.11}$$

giving

$$R(x_{bj}) = \frac{2x_{bj}F_1(x_{bj}) - F_2(x_{bj})}{2x_{bj}F_1(x_{bj})} \qquad \text{(B.12)}$$

B.1.5 Callan-Gross Relation

The exchange photon is absorbed by the only electrically charged constituents of the nucleon, the quarks. In this approximation, only transversely polarized photons can be absorbed since the quarks are spin 1/2 particles, helicity is conserved in electromagnetic interactions, and the transverse momentum of the quarks has been neglected in the model. Hence,

$$\sigma_L = 0 \qquad \text{(B.13)}$$

$$F_L(x_{bj}) = 0 \qquad \text{(B.14)}$$

This results in the Callan-Gross relation:

$$2x_{bj}F_1(x_{bj}) = F_2(x_{bj}) \qquad \text{(B.15)}$$

which means that

$$R(x_{bj}) = 0 \qquad \text{(B.16)}$$

The Callan-Gross relation states that the cross section depends on only one structure function, usually taken to be $F_2(x_{bj})$.

B.1.6 Structure Function F_2

The cross section for Inelastic Muon Scattering is described in the Quark-Parton Model by the incoherent sum of elastic scattering from the charged point-like quarks inside the nucleon. In this approximation, the structure function F_2 can be written as x_{bj} times the sum over the quark flavors of the quark and anti-quark probability distributions, $q(x_{bj})$ and $\overline{q}(x_{bj})$, weighted by the quark charges squared, e_i^2:

$$F_2(x_{bj}) = x_{bj} \sum_{i=u,d,s,c,b,t} e_i^2 \left(q_i(x_{bj}) + \overline{q_i}(x_{bj})\right) \tag{B.17}$$

where the various values of q represent the up quark flavor, down quark flavor, and so on. Note that while the sum over quark flavors involves all quark flavors, only the lighter quark flavors actually contribute given the energy scale of the inelastic muon-nucleon interactions at E665. Quarks other than u and d quarks exist only in the sea as virtual quark-anti-quark pairs.

The quark distributions can be separated into valence and sea quark components by defining q_v and q_s, respectively.

$$q \equiv q_v + q_s \tag{B.18}$$

Since the nucleons of interest are made up of three valence quarks, all anti-quarks are in the sea. Using this leads to a number of relations,

$$q_s = \overline{q} \tag{B.19}$$
$$q_v = q - \overline{q} \tag{B.20}$$
$$q_s = \overline{q_s} \tag{B.21}$$

Since the proton consists of two up valence quarks and one down valence quark, the quark distributions in the proton must obey the following sum rules, derived from Equation B.20:

$$\int_0^1 dx \left(u^{\text{proton}}(x) - \overline{u}^{\text{proton}}(x)\right) = \int_0^1 dx u_v^{\text{proton}}(x) \equiv 2 \tag{B.22}$$
$$\int_0^1 dx \left(d^{\text{proton}}(x) - \overline{d}^{\text{proton}}(x)\right) = \int_0^1 dx d_v^{\text{proton}}(x) \equiv 1 \tag{B.23}$$

Similarly, for the neutron, we have

$$\int_0^1 dx \left(u^{\text{neutron}}(x) - \overline{u}^{\text{neutron}}(x)\right) \equiv 1 \tag{B.24}$$

$$\int_0^1 dx \left(d^{\text{neutron}}(x) - \overline{d}^{\text{neutron}}(x)\right) \equiv 2 \tag{B.25}$$

B.1.7 Gottfried Sum Rule

A number of simple integral relations involving structure functions, called sum rules, were predicted even before the Quark-Parton Model was formulated. Several are measurable only with neutrino scattering experiments, such as the Adler Sum Rule [6] and the Gross-Llewellyn-Smith Sum Rule [99]. Others are appropriate only for interactions between polarized beams and targets, such as the Ellis-Jaffe Sum Rule [78]. An integral relation measurable in unpolarized Inelastic Muon Scattering is the Gottfried Sum Rule [98]. This predicts the integrated difference, S_G, between the proton and neutron structure functions F_2.

$$S_G \equiv \int_0^1 \frac{dx}{x}(F_2^{\text{p}}(x) - F_2^{\text{n}}(x)) \tag{B.26}$$

Note that the measure dx/x of the integral emphasizes the contribution of the integrand in the small x_{bj} region. Using the notation developed above, this can be simplified by substituting the quark distributions for the F_2.

$$S_G = \int_0^1 dx \sum_{i=u,d,s,c,b,t} e_i^2\,(q_i^{\text{p}}(x) + \overline{q_i}^{\text{p}}(x) - q_i^{\text{n}}(x) - \overline{q_i}^{\text{n}}(x)) \tag{B.27}$$

Separating out the valence part from the sea part using Equations B.19 and B.20 yields

$$\begin{aligned} S_G = & \int_0^1 dx \sum_{i=u,d,s,c,b,t} e_i^2\,(q_v^{\text{p}}(x) + q_v^{\text{n}}(x)) \\ & +2\int_0^1 dx \sum_{i=u,d,s,c,b,t} e_i^2\,(\overline{q}^{\text{p}}(x) - \overline{q}^{\text{n}}(x)) \end{aligned} \tag{B.28}$$

The integral over the valence part can be done immediately using Equations B.22 and B.23 and the corresponding formulae for the neutron.

$$S_G = \frac{1}{3} + 2\int_0^1 dx \sum_{i=u,d,s,c,b,t} e_i^2 \left(\overline{q}^{\mathrm{p}}(x) - \overline{q}^{\mathrm{n}}(x)\right) \tag{B.29}$$

Using a form of isospin symmetry, the sea part can be simplified by assuming that

$$d_s^{\mathrm{n}} = \overline{d}^{\mathrm{n}} = \overline{u}^{\mathrm{p}} \equiv \overline{u} \tag{B.30}$$

$$u_s^{\mathrm{n}} = \overline{u}^{\mathrm{n}} = \overline{d}^{\mathrm{p}} \equiv \overline{d} \tag{B.31}$$

To simplify matters, the heavier quarks in the sea are ignored. This leads to

$$S_G = \frac{1}{3} + \frac{2}{3}\int_0^1 dx \left(\overline{u}(x) - \overline{d}(x)\right) \tag{B.32}$$

Assuming that the quark sea is flavor symmetric, the integral over the sea part is zero and we arrive at the Gottfried Sum Rule.

$$S_G \equiv \int_0^1 \frac{dx}{x}\left(F_2^{\mathrm{p}}(x) - F_2^{\mathrm{n}}(x)\right) = \frac{1}{3} \tag{B.33}$$

B.1.8 Momentum Integral

Another example of an integral relation that is applicable to unpolarized Inelastic Muon Scattering is the Momentum Integral, whose value is not predicted. This measures the fraction, I_M, of the nucleon momentum carried by all quarks, valence and sea:

$$I_M = \int_0^1 dx F_2(x) \tag{B.34}$$

Muon beam experiments [28, 29, 30] have measured I_M to be about 0.50. This means that the valence and sea quarks carry only about 50% of the nucleon momentum. The constituents carrying the remaining nucleon momentum are identified as the gluons of the QCD-enhanced Quark-Parton Model.

B.2 The QCD-Enhanced Quark-Parton Model

In the naïve Quark-Parton Model, no specification of the dynamics of the quarks and gluons is made. In the QCD-enhanced Quark-Parton Model, Quantum Chromodynamics is used as the theory of quark and gluon interactions. QCD is a relativistic field theory based on the gauge symmetry group SU_3^{color}. QCD interactions are mediated by massless gluons. The gluons themselves are charged; QCD gauge fields are self-interacting. The quarks are labelled by the "color" quantum number. Color interactions do not affect the flavor of particles as do weak interactions. No mechanism exists in QCD for generating quark masses, unlike electroweak theory. QCD is renormalizable, as was first demonstrated by 't Hooft [198]. No free colored states have been directly observed. This observation has not been proven to be a consequence of QCD dynamics, though it is expected that eventual improvements in the performance of QCD calculations without perturbation theory will lead to such a proof. In the meantime, QCD is augmented with the confinement hypothesis to cover this observation. The confinement hypothesis states that all observable fields and particles are net colorless states.

B.2.1 Asymptotic Freedom

In Quantum Electrodynamics, processes such as vacuum polarization lead to a screening of the electric charge. The effective charge depends on the Q^2 of the scatter interaction. Charge screening leads to an effective QED coupling constant that decreases with decreasing Q^2. The net effect for static charges is that the electric force decreases with increasing separation. While QCD has the equivalent of QED bremsstrahlung and pair production processes, it also has a field self-interaction process which leads to an anti-screening of color charge. In leading order in the perturbative expansion, the (QCD) strong coupling constant is described by:

$$\alpha_s(Q^2) = \frac{1}{\beta_0 \ln(Q^2/\Lambda^2)} \tag{B.35}$$

The constant β_0 is to this order

$$\beta_0 = \frac{1}{4\pi}\left(11 - \frac{2}{3}N_f\right) \tag{B.36}$$

N_f is the number of quark flavors. Λ is the scale parameter of QCD. Its value is not predicted by the theory. Experimental evidence seems to indicate that $\Lambda \sim 200$ MeV [41, 38]. The variation of the coupling constant with Q^2 is often referred to as the running of the coupling constant.

One of the interesting features of QCD is that, for $Q^2 \gg \Lambda^2$, the strong coupling constant becomes negligible. The quarks can be considered as free particles inside the nucleon in the asymptotic limit of infinite Q^2, just as Bjorken scaling predicts and the naïve Quark-Parton Model assumes. This property, called asymptotic freedom, is a feature of an entire class of relativistic field theories to which QCD belongs [101, 174].

B.2.2 Confinement

The strong force increases between color charges with increasing distance due to the anti-screening of the field self-interactions. The anti-screening of color charge can be related directly to the confinement hypothesis in the following manner. As the separation between color charges grows, the energy stored in the color field between the charges becomes so great that the QCD vacuum becomes unstable. While the energy density is sufficently large, particles are created out of the vacuum from the stored energy. Net colorless states are eventually achieved by local collections of color charges. This leads to an effect, called infrared slavery, that prevents the existence of free, bare quarks or gluons. Perturbative methods, however, are helpless to substantiate this scenario since the growing coupling constant forces perturbative expansions to diverge. To date, infrared slavery has not been proven by non-perturbative means to be generated by the theory.

In terms of the study of nucleon structure, the increase in the coupling constant with decreasing Q^2 has serious consequences. Sensible values for QCD-related quantities can be calculated in a perturbative expansion in the coupling constant α_s for interactions involving distance scales smaller than the radius of the nucleon (large Q^2). However, at distance scales on the order of the size of the nucleon or larger, the perturbative expansion breaks down as the expansion coefficient, α_s/π becomes greater than unity. Unlike Quantum Electrodynamics which is relatively simple to use to calculate the structure of the simplest electric charge bound state, the hydrogen atom, QCD generally requires the use of complicated, computationally expensive, non-perturbative approaches to describe the details of the nucleon.

B.2.3 Scaling Violations

QCD can make some useful predictions about the dependence of structure functions on Q^2. In the naïve Quark-Parton Model, the structure functions can be used to describe the probability that the exchanged photon interacts with a parton with $x_{bj} = x_0$. This probability is independent of the $Q^2 = Q_0^2$ of the photon (Bjorken scaling). QCD, however, adds some dynamics to this picture that breaks this independence. At some $Q^2 \gg Q_0^2$, the photon can resolve any strong interactions that the parton may have undergone just before absorption. The parton may have lost energy due to gluon bremsstrahlung causing the scatter to occur at some $x_{bj} < x_0$. At this higher Q^2, the probability decreased to find a parton at a larger value of x_{bj} and increased to find a parton at a smaller value of x_{bj}. The added dynamics of QCD introduces a Q^2 dependence to the structure functions. The breaking of the Bjorken scaling behavior is referred to as scaling violations. The photon is also sensitive to the gluon distribution, even though it cannot interact directly with gluons, through the influence the gluon distribution has on the sea quark distributions.

A quantitative description for the Q^2 evolution of structure functions at high Q^2 was first given by Altarelli and Parisi [17]. They predicted that the structure functions have a weak logarithm dependence on Q^2 in a leading order perturbative expansion. Analysis of measured absolute structure functions appears to verify this prediction [41, 38].

B.2.4 The x_{bj} Behavior of F_2

QCD does not explicitly predict the x_{bj} behavior of F_2. Nevertheless, a simple heuristic model can be used to make a guess at the behavior. In the limit that the valence quarks are alone and barely interacting, they would tend to share the available momentum roughly equally. Their momentum distribution would peak in x_{bj} at about 1/3. As interactions and other particles are added, some of the valence quark momentum would be carried instead by the sea quarks and gluons. This would cause the valence quark peak to move to a lower value of x_{bj}. Color field self-interaction should lead to a gluon distribution increasing quickly at small x_{bj}. Since sea quarks are derived from the gluons, their distribution should rise as well.

Measurements of F_2 on hydrogen and deuterium have established that F_2 increases with decreasing x_{bj}. Assuming isospin symmetry and a negligibly bound deuteron, one can look at the F_2 due to the valence quarks alone with $F_2^p(x) - F_2^n(x)$ [40]. This tends to peak in x_{bj} at a value of 0.2 to 0.3 and decreases as x_{bj} decreases. The implication is that the structure functions for $x_{bj} \geq 0.2$ are dominated by the valence quark distributions. Extraction of the gluon structure function alone [38] shows that it increases rapidly as x_{bj} decreases. In the region $x_{bj} \leq 0.1$, the structure functions are dominated by the sea quark and gluon distributions.

Recent data for $F_2^{H_2}$ and $F_2^{D_2}$ exist from NMC [19], BCDMS [39, 41], and SLAC [204]. A comparison of these data sets can be found in Reference [49, 201].

B.2.5 Function R

QCD Corrections

As described above, the function R in the naïve Quark-Parton Model is identically zero since longitudinally polarized photons cannot be absorbed by the transverse momentum-less quarks. With the addition of QCD to the model, however, a mechanism is introduced that leads to a non-zero R. Next-to-leading order QCD analysis of structure functions by Altarelli and Martinelli [16] shows that there is a contribution[3] to F_L, and therefore R, that is of order α_s labelled $R^{\mathrm{QCD}}(Q^2)$. This is caused by the development of non-negligible transverse momentum by the quarks due to gluon emission. This introduces to R a weak Q^2 dependence through the running of α_s. Higher order calculations have been performed as well [72, 71].

Target Mass Corrections

Since QCD predicts that R is non-zero, it is of interest to see what other significant contributions there might be to R as the assumptions of the QCD-enhanced Quark-Parton Model are relaxed. If we no longer assume that $Q^2 \gg M^2$, which in fact it is not in most of our data set, then F_L picks up a target mass correction, a correction for non-negligible target mass M.

$$F_L(x_{bj}, Q^2) = 2x_{bj}\left(1 + \frac{4M^2x^2}{Q^2}\right) F_1(x_{bj}, Q^2) - F_2(x_{bj}, Q^2) \qquad \text{(B.37)}$$

which looks an additional R contribution of the form:

---

[3] Care should be exercised in using the expression given for R^{QCD} given in Reference [16]. F_2 is defined there in terms of quarks distributions, with a dependence on R that is missing in other definitions.

$$R(x_{bj}, Q^2) = \frac{4M^2x^2}{Q^2} \tag{B.38}$$

Primordial k_t

If we also consider non-negligible tranverse momentum of the quarks, then a contribution to R comes from the mean transverse momentum of the quarks[89]. This term assumes the limit of non-interacting quarks and so does not include the $R^{\mathrm{QCD}}(Q^2)$ contribution generated by gluon emission in QCD.

$$R(x, Q^2) = \frac{4\langle k_t^2\rangle + \delta}{Q^2} \tag{B.39}$$

where k_t, called the "primordial k-t", is the transverse momentum of the quarks, and δ represents the effect of individual parton masses.

R Measurements

Recent data for R^{H_2} and R^{D_2} exist from a re-analysis of several SLAC experiments [202, 203] and from BCDMS [39, 41]. A comparison of these data sets can be found in Reference [203]. Preliminary results from NMC are also just now becoming available as well [153]. From these measurements, R is seen to increase beyond 0.1 as x_{bj} decreases below 0.2. At larger values of xbj, however, R is essentially 0.

A crucial point in this analysis is that the difference in the value of R measured for deuterium and hydrogen is assumed to be identically zero. Figure 4.20 on page 114 shows $R^{\mathrm{D}_2} - R^{\mathrm{H}_2}$ as a function of x_{bj} [202, 153]. The difference measured has small errors and appears to be consistent with 0.

B.2.6 Deep-Inelastic Scattering Cross Section

Extending the QPM deep-inelastic cross section to account for the effects of QCD leads to an expression of the cross section that is dependent on two structure functions F_1 and F_2. These structure functions are strongly dependent on x_{bj} and weakly dependent on Q^2. In order to capture the expectation that the Callan-Gross relation is still approximately true, though, the function R is used in place of F_1. Looking ahead, there is also evidence that these functions depend on the atomic weight A_W of the nucleus under study (the EMC effect), but this dependence is not shown explicitly in the following expressions. In terms of F_2 and R, the differential cross section for the one-photon-exchange process is given by:

$$\frac{d\sigma^{1\gamma}}{dxdQ^2}(x,Q^2) = \frac{4\pi(\alpha\hbar c)^2}{Q^4}\left\{1 - y - \frac{Q^2}{4E^2} - \frac{y^2 + Q^2/E^2}{2(1+R(x,Q^2))}\right\}\frac{F_2(x,Q^2)}{x} \tag{B.40}$$

where y_{bj} is treated as a function of x_{bj} and Q^2 via Equations 1.3 and 1.4. The measured differential cross section is used to calculate the functions F_2 and R. The same kinematic regions must be sampled with different beam energies in order to extract both F_2 and R. Since E665 has insufficient event statistics to do this, I extract the F_2 ratio for deuterium and hydrogen by relying upon the experimental result that R is essentially identical for these target materials [202, 153]. This result, however, only does not cover the small x_{bj} range of E665 data.

B.3 The Realistic Nucleon

The QCD-enhanced Quark-Parton Model picture of Inelastic Muon Scattering is limited by a number of assumptions that the experimentalist must consider when interpreted the data set. For instance, the QCD-enhanced Quark-Parton Model interpretation using structure functions only considers the single-photon-exchange process in the limit that $Q^2 \rightarrow \infty$. The experiment, however, is sensitive to a number of processes that must be removed from the data set directly or indirectly in order to measure a one-photon-exchange cross section. Some of these processes involve exchanges other than one photon. Some involve the one exchange photon having finite Q^2, in other words $Q^2 \sim M^2$, and thus being unable to resolve just one parton in the nucleon. Yet more processes involve higher-order QCD interactions between nucleons. A more mundane problem is that muons interact not only with the nucleons in the experiment target, but also with the electrons in the target. These muon-electron scatters are removed from the data set.

B.3.1 Electroweak Radiative Processes

The one-photon-exchange process, while dominant, is not the only process seen in inelastic scattering experiments. Various higher order electromagnetic processes

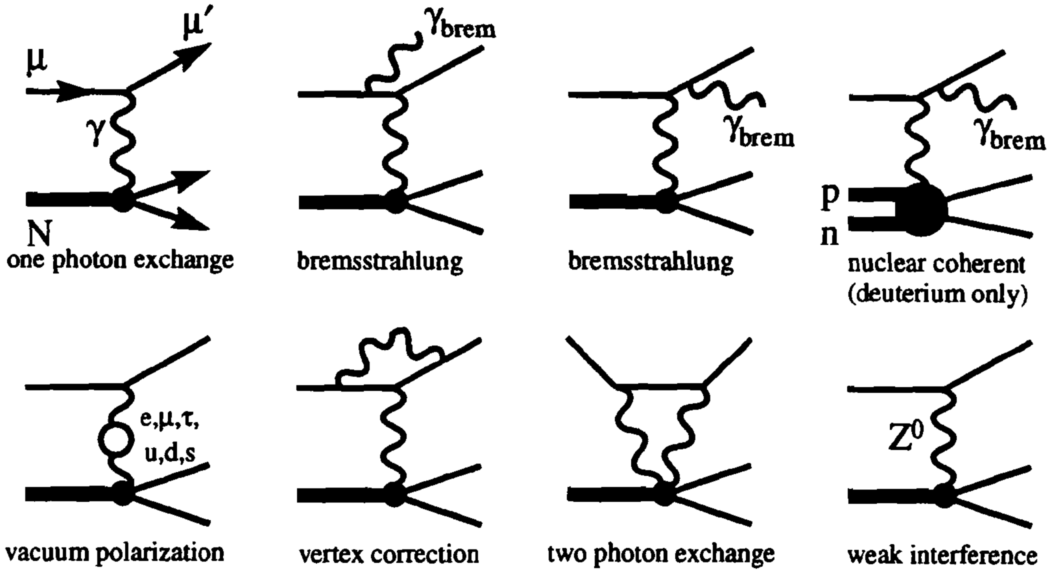

Figure B.2: Electroweak processes contributing to the observed cross section

can occur which affect the measured kinematics of the event. Examples of such processes are illustrated in Figure B.2 on page 156. In order to calculate the structure functions for the one-photon-exchange process, these processes must be considered.

These processes can be removed from the data set directly by rejecting events believed to contain non-one-photon-exchange processes or indirectly by applying a calculated correction to the data set that estimates the probability that each event involved only a one-photon-exchange. The latter method is referred to as applying radiative corrections.

B.3.2 Finite Q^2

Amongst the approximations that are made in the QPM is that $Q^2 \gg M^2$, and thus that the nucleon mass is negligible. At the Q^2 range of the E665 data set, however, Q^2 is comparable to or smaller than the nucleon mass-squared. For finite Q^2, various effects give rise to corrections to F_2 and R. These effects can be classified into two categories. Kinematic corrections are due to the consideration of non-zero nucleon mass (and constituent quark masses) and are handled by "target mass corrections". Dynamic corrections are generated by interactions between the struck quark and the other quarks in the target nucleon. These are collected under the term "higher twist effects".

Target Mass Corrections

Target mass corrections are handled by a formalism described by Nachtmann [161] that extends the infinite Q^2 Quark-Parton Model formalism to finite Q^2 by using the Nachtmann scaling variable ξ as an alternative to the Bjorken scaling variable x_{bj}.

$$\begin{aligned}\xi &= \frac{(Q^2+\nu^2)^{1/2}-\nu}{M} \\ &= \frac{2x_{bj}}{1+\left(1+4M^2x_{bj}^2/Q^2\right)^{1/2}} \\ &= \frac{2x_{bj}}{1+(1+Q^2/\nu^2)^{1/2}} \qquad \text{(B.41)}\end{aligned}$$

This leads to corrections of order $(M^2/Q^2)^n$. A revised structure function $F_2(\xi, Q^2)$ can be calculated from the measured $F_2(x_{bj}, Q^2)$ by direct application of target mass corrections [35, 36]. The predictions of Quantum Chromodynamics hold for this altered structure function [96].

The leading order target mass corrections have already been included in the expression for R in Equation B.38 and the double-differential cross section in Equation B.40 (the $4M^2x_{bj}^2/Q^2$ terms). Higher order target mass effects are ignored. The Nachtmann scaling variable differs from the Bjorken scaling variable by only a small amount throughout the E665 acceptance, even at small Q^2 where the E665 acceptance is limited to large ν. There is some concern, however, that at sufficently small Q^2, the primordial k_t contribution to R can become significant.

Higher Twists

The treatment of higher twist effects is far more difficult that target mass corrections. The term "twist" refers to the classification of terms in the operator product expansion in the treatment of asymptotic freedom [205, 100]. Twist is defined as the dimension of a term in the expansion minus its spin. The generating processes involve higher order QCD interactions and in principle can only be exactly calculated by non-perturbative means, although some perturbative calculations have been made

[79, 80]. Leading higher twist corrections are of order $(\Lambda^2/Q^2)^n$. Higher twist effects on structure functions are often parameterized as follows:

$$F_2(x, Q^2) = F_2^{\mathrm{LT}}(x, Q^2)\left(1 + \frac{C(x)}{Q^2}\right) \tag{B.42}$$

$F_2(x, Q^2)$ is the measured structure function, $F_2^{\mathrm{LT}}(x, Q^2)$ is the desired "leading twist" structure function for which QCD-enhanced Quark-Parton Model predictions hold, and $C(x)$ parameterizes the x_{bj} dependence of the next-to-leading twist, known as twist-4, effects. It is expected that higher twist effects are greatest at small Q^2 and high x_{bj}, but there is not yet a conclusive calculation of their magnitude.

B.3.3 QCD Processes

The muon only scatters directly off the electrically-charged partons, the quarks. It can also be considered to scatter indirectly off gluons. The photon can fluctuate into a superposition of vector meson states, allowing the photon to interact via the strong force with the partons in the nucleon [89]. This process is described by the Generalized Vector-Meson Dominance model[4]. This coupling of photons to gluons is important at small x_{bj} due to gluon distribution growing rapidly as $x_{bj} \rightarrow 0$. This process is considered as part of the observed structure of the nucleon since it cannot be removed from the data set and is very difficult to calculate and correct for in the analysis.

B.3.4 Bound State Effects

The binding energy of the deuteron, defined as the difference between the deuteron mass and the free constituents mass sum, is only about 2.23 MeV. This is generally assumed to be small enough to treat the proton and neutron in a deuteron as quasi-free for the sake of experiment analysis. Nevertheless, explanations of apparent deviations of measured values from the predictions of the QCD-enhanced Quark-Parton Model often consider the influence that various bound state effects might have on the deuteron.

At different values of x_{bj}, different bound state effects dominate the behavior of:

---

[4] A review of the GVMD model with a comparison to current results can be found in Reference [26]

$$R_{\rm EMC} \equiv F_2^{\rm Heavy\ Nucleus}/F_2^{\rm Deuterium} \tag{B.43}$$

where the F_2 shown are the per-nucleon structure functions. While this is not a quantity I report in this thesis, the description of the behavior of $R_{\rm EMC}$ in different kinematic regions provides a convenient context for a describing the bound state effects that may be noticeable in the deuteron.

Fermi Motion

As described in Equation B.17, the structure function F_2 is proportional to the sum of the weighted momentum distributions of the quarks inside the free nucleon. Bound nucleons, however, are not stationary with respect to the nucleus center-of-momentum. The kinematic variable x_{bj} is nevertheless calculated as if the nucleon were at rest. The actual F_2 measured is a convolution of the true (nucleon at rest) structure function with the momentum distribution function $f(z)$ of the nucleon inside a nucleus with atomic weight A_W.

$$F_2^{\rm measured}(x) = \int_x^{A_W} dz f_N(z) F_2^{\rm true}(x/z) \tag{B.44}$$

where z is the fraction of the nucleus momentum carried by the nucleon. Many calculations of the size and A_W dependence of Fermi motion effects have been performed, for example [52, 160, 195]. The rise in $R_{\rm EMC}$ above one at large x_{bj} is explained by the Heisenberg Uncertainty Principle. As x_{bj} approaches one, the struck quark is essentially unbound in the nucleon, but is still bound in the nucleus by the confinement hypothesis. The larger the target nucleus, the less localized the struck quark is. With a larger uncertainty in position, there is a smaller uncertainty in the momentum of the struck quark. Thus, the quark momentum distribution in larger nuclei is narrower than that in smaller nuclei as $x_{bj} \to 1$. Since high x_{bj} quarks are rare, the narrower momentum distribution enhances the chance of finding an energetic quark in larger nuclei. This effect is noticeable for $x_{bj} > 0.7$ when comparing helium to deuterium [25]. The smearing effect is calculated to be completely negligible for deuterium for $x_{bj} < 0.7$ [92, 25]. In any case, E665 has no data in this region.

The region of $0.3 < x_{bj} < 0.7$ is referred to as the depletion region. $R_{\rm EMC}$ falls below one. This is interpreted as meaning that in larger nuclei, the momentum distribution of the valence quarks is "depleted" relative to that in smaller nuclei. This is partly caused by the large effect of Fermi motion smearing of high x_{bj} quarks to lower x_{bj} in smaller nuclei. E665 has only a small amount of data in this region.

Shadowing and Anti-Shadowing

In the region $x_{bj} < 0.3$, the color dipole structure of the photon begins to become apparent, as is described by the Generalized Vector-Meson Dominance model [26]. The cross section for interactions assumed to be entirely electromagnetic in nature now acquires a strong force component. In the range $0.1 < x_{bj} < 0.3$, the per-nucleon cross section for larger nuclei is greater than that for smaller nuclei. This effect is referred to as anti-shadowing.

In the region of $x_{bj} < 0.1$, the sea quarks and gluons dominate the nucleon interactions. While the cross section for interactions increases as the photon's color-charge structure becomes apparent, eventually this cross section becomes so great that only the partons on the exterior surface of the nucleon have a chance to interact with the photon [167]. The cross section is predicted to scale with the surface area of the nucleus, while the number of nucleons scales with the volume of the nucleus. Since larger nuclei have a smaller area to volume ratio, this heuristic model of shadowing predicts that the cross section per nucleon decreases as the atomic number increases.

In the region of $x_{bj} < 0.001$, saturation of the shadowing effect has been observed by E665 [4]. The saturation refers to R_{EMC} becoming independent of x_{bj}. Extrapolation of real photon ($Q^2 = 0$) experiments to the energy range of E665 seems to confirm the saturation effect seen.

B.3.5 Muon-Electron Elastic Scattering

E665 is also sensitive to muon-electron elastic scattering. In the context of the Quark-Parton Model, muon-electron scattering occurs at a single value of x_{bj} since the scattering is elastic. While elastic scattering off a nucleon occurs at $x_{bj} = 1$, elastic scattering off an electron occurs at $x'_{bj} = 1$, where x'_{bj} is x_{bj} with the electron mass substituted for the nucleon mass.

$$\begin{aligned} x_{bj}^{\mu-e} &= m_{\text{electron}}/M_{\text{proton}} x'_{bj} \\ &= m_{\text{electron}}/M_{\text{proton}} \\ &= 5.446 \times 10^{-4} \end{aligned} \tag{B.45}$$

In practice, however, the muon-electron scattering is seen as a sharply-peaked distribution in the x_{bj} spectrum centered at a value close to, but lower than, $x_{bj}^{\mu-e}$. The width of the distribution is due to experiment resolution and radiative processes smearing the measured kinematics. The offset of the peak to lower x_{bj} is caused by the muon energy loss in radiative processes always reducing the observed Q^2 from the true value. The muon-electron elastic scatters are removed from the data set on an event by event basis. The events are identified by their event topology, energy deposition, and hadron multiplicity characteristics.

B.4 Comparing the Neutron to the Proton

While the measurement presented in this thesis is that of the ratio of the differential cross section for deuterium to that for hydrogen, the intended connection to the QCD-enhanced Quark-Parton Model is a comparison of the neutron to the proton.

B.4.1 $F_2^{\mathrm{n}}/F_2^{\mathrm{p}}$

The neutron is expected to be quite similar to the proton. The most straightforward approach to comparing them is to measure the small difference in their structure functions. This requires the use of absolute structure functions which are difficult to measure well. An alternative is to measure their ratio [204, 40, 13].

As $x_{bj} \rightarrow 0$, the gluon distribution dominates over that of the sea quark distributions and the valence quark distribution should be negligible. Since the gluon distribution and sea quark distribution are expected to be very nearly the same for the neutron and the proton, the expectation is that the ratio $F_2^{\mathrm{n}}/F_2^{\mathrm{p}} \rightarrow 1$ as $x_{bj} \rightarrow 0$.

At the opposite limit, as $x_{bj} \rightarrow 1$, the valence quark distributions dominate over that of the sea quarks and the gluons. Expanding F_2 in terms of the valence quark distributions and assuming isospin symmetry $(u^{\mathrm{n}} = d^{\mathrm{p}})$, one gets

$$\frac{F_2^{\mathrm{n}}}{F_2^{\mathrm{p}}} = \frac{\sum_{i=u,d,s,c,b,t} e_i^2\,(q^{\mathrm{n}}(x_{bj}) + \overline{q}^{\mathrm{n}}(x_{bj}))}{\sum_{i=u,d,s,c,b,t} e_i^2\,(q^{\mathrm{p}}(x_{bj}) + \overline{q}^{\mathrm{p}}(x_{bj}))} \tag{B.46}$$

$$\rightarrow \frac{\frac{4}{9}u_v^{\mathrm{n}} + \frac{1}{9}d_v^{\mathrm{n}}}{\frac{4}{9}u_v^{\mathrm{p}} + \frac{1}{9}d_v^{\mathrm{p}}} \tag{B.47}$$

$$\frac{F_2^{\mathrm{n}}}{F_2^{\mathrm{p}}} \rightarrow \frac{\frac{1}{9}u_v^{\mathrm{p}} + \frac{4}{9}d_v^{\mathrm{p}}}{\frac{4}{9}u_v^{\mathrm{p}} + \frac{1}{9}d_v^{\mathrm{p}}} \tag{B.48}$$

Since the quark distributions are always positive, the ratio $F_2^{\mathrm{n}}/F_2^{\mathrm{p}}$ is bounded between

1/4 and 4 as $x_{bj} \to 1$. The ratio is expected to fall below 1 since the d quark is slightly more massive than the u quark. The fact that there are two u quarks and only one d quark is a statement about the integral of the quark distributions and does not necessarily influence the limiting value of the integrands.

Recent data for the ratio F_2^n/F_2^p as a function of x_{bj} exist from NMC [20, 19], BCDMS [40], and SLAC [204]. As expected, the ratio goes to 1 at small x_{bj} and appears to go the limiting value of 1/4 at large x_{bj}.

Measurements made by real photon experiments ($Q^2 = 0$) can be used to evaluate the ratio exactly at $x_{bj} = 0$. The result is dependent on the real photon energy. Unfortunately, the current world data set [105] only covers the photon energy range 3.0 to 183 GeV for hydrogen and 2.0 to 18 GeV for deuterium. To get a result at the energy range of our experiment, where ν is in the range of 50 to 500 GeV, requires a large extrapolation of the real photon on deuterium cross section measurement results.

B.4.2 Gottfried Integral

The Gottfried Sum Rule is tested by measuring the value of the Gottfried Integral.

$$I_{\mathrm{G}}(x_0) = \int_{x_0}^{1} \frac{dx}{x} (F_2^p(x) - F_2^n(x)) \tag{B.49}$$

For this discussion, I ignore the uncertainties in the extrapolation of experimental results to $x_{bj} = 1$, hence the integral is from x_0 to 1. The evaluation of I_{G} is complicated by a number of issues. In addition to the difficulties in the absolute measurement of F_2, the structure functions in the integrand cannot be measured to arbitrarily small values of x_{bj}. An extrapolation to $x_{bj} = 0$ must be performed even though there may be large, poorly understood, contributions at small x_{bj}. Measurements of the value of the Gottfried Integral have been made using Inelastic Electron Scattering by E140 at SLAC [202] and using Inelastic Muon Scattering by the BCDMS [40] and NMC [18, 20] collaborations.

The NMC measurement is currently the "best" measurement of the Gottfried Integral. NMC ignores binding effects in the deuteron, representing the proton and neutron structure functions as

$$F_2^p \propto \sigma^{\mathrm{H}_2}$$

$$
\begin{aligned}
&= F_2^{\mathrm{H_2}} \qquad \text{(B.50)}\\
F_2^{\mathrm{n}} &\propto \sigma^{\mathrm{D_2}} - \sigma^{\mathrm{H_2}}\\
&\approx F_2^{\mathrm{D_2}}/2 - F_2^{\mathrm{H_2}} \qquad \text{(B.51)}
\end{aligned}
$$

This leads to a useful expression from the extraction of the Gottfried Integral.

$$
I_{\mathrm{G}}(x_0) \approx 2\int_{x_0}^{1} \frac{dx}{x}\left(\left(\frac{F_2^{\mathrm{H_2}}(x)}{F_2^{\mathrm{D_2}}(x)} - 1\right) F_2^{\mathrm{D_2}}(x)\right) \qquad \text{(B.52)}
$$

The NMC result [18] for the Gottfried Integral of 0.240 ± 0.016 contradicts the Gottfried Sum Rule. Since it has been shown to be plausible that this integral involves non-perturbative behavior not calculable from the QCD-enhanced Quark-Parton Model [77], this may not be as surprising as first thought. Various non-perturbative effects have been suggested to explain this result, such as binding effects, shadowing, and flavor asymmetry in the quark sea. A measurement of the contribution to the integral by the structure functions at smaller x_{bj} is crucial to deciding the error associated with the extrapolation of the integral to $x_{bj} = 0$.

The measurement of the $F_2^{\mathrm{n}}/F_2^{\mathrm{p}}$ ratio I present extends to over an order of magnitude smaller x_{bj} than available absolute $F_2^{\mathrm{D_2}}$ measurements. Any statement of the systematic error on the calculation from the extrapolation $F_2^{\mathrm{D_2}}$ to such small values of x_{bj} would be difficult to defend. As such, I consider it inappropriate to attempt to use the ratio I present in an evaluation of the Gottfried Integral. The measurement I present, however, can be related to the Gottfried Integral measurement by noting that it is consistent with the extrapolation of the ratio used by NMC to arrive at their result.

Appendix C

SPM and SMS Detector - Implementation and Monitoring

C.1 The Detectors

This chapter describes the implementation and monitoring of the SPM and SMS detectors for the RUN90 data-taking. The central feature of the monitoring of these detectors was a PC-based workstation running a user-friendly control program which was used to set-up and monitor many aspects of these detectors. The design, implementation, and use of this monitoring station was one of my responsibilities as a UCSD graduate student.

C.1.1 SPM Detector

Since the SPM detector was last described in detail [179], significant changes have been made to some of the counters and to all of the data paths associated with the detector. The SPM counters were constructed in two different varieties. The central six counters in each plane, called the "inner counters", were made of NE110[1]. Inner counters in the upper bank were coupled to Hamamatsu[2] R329 phototubes by an acrylic light guide. Inner counters in the lower bank were coupled to Hamamatsu R329 phototubes by an air guide, since their guides were in or very near the beam. All other SPM counters, collectively referred to as the "outer counters", were made of ROHM[3] GS2030 acrylic scintillator with ROHM GS1919 wavelength shifter bars on each side edge.

The phototube signals in most counters were discriminated by custom circuitry mounted on the counter. Many of the counters furthest from the trigger electronics had their custom discriminators replaced by LeCroy[4] 4413 or 4416 discriminators. A low voltage power system delivered power to and set the threshold level for the custom discriminator electronics. The discriminated signals were reshaped by Fermilab ECL Repeaters before arriving at LeCroy 4418 fanout modules. One copy of the counter signals was sent to the Large Angle Trigger electronics and one copy, after significant cable delay, was reshaped by Fermilab ECL Repeaters and sent to LeCroy 4448 latches. Phototube signals were also sent to LeCroy 2249A ADCs for digitization. A small LED was installed next to each scintillator in order to test the operation of that counter's signal paths.

---

[1] NE: Nuclear Enterprises Ltd.
[2] Hamamatsu: Hamamatsu Photonics K.K.
[3] ROHM: Rohm GmbH, Chemische Fabrik
[4] LeCroy: LeCroy Research Systems Corp.

C.1.2 SMS Detector

The SMS detector itself was largely unchanged from the last description [179]. Each of the four detector packages consisted of 16 counters in the Y view and 16 counters in the Z view. The inner 14 counters in a view were 1.32 cm wide by 21.6 cm long. The outer counter on each side in a view was 1.96 cm wide by 21.6 cm long.

One Hamamatsu R1166 phototube was used to detect light from each counter. Signals from the phototubes were sent to LeCroy 4413 discriminators. Output from the discriminators was sent to the SAT trigger logic. Also, after a significant delay in cables, the signals were reshaped by Fermilab ECL Repeaters (design DFG 5-8-89) and sent to LeCroy 4448 latches. The phototube signals were also sent to LeCroy 2249 ADCs. The effective time resolution of the SMS latches was one RF bucket due to the careful timing of the latches and the large amount of light transferred from the small counters to the phototube. A small LED was installed next to each scintillator in order to test the operation of that counter's signal paths.

C.2 Detector Monitoring Station

After the experience gained in RUN87 working with the SPM and SMS detectors, it was decided to implement a dedicated local monitoring workstation in order to reduce the manpower required for and improve the reliability of the testing and maintenance of these detectors. This workstation was built around a a PC/AT compatible personal computer, a complete local data acquisition system, and custom menu-driven software. The high voltage monitoring, for instance, was previously performed from the over-burdened PDPs used in data acquisition and took up to an hour or longer to respond to a simple high voltage check request from the shift personnel. This led to occasional gaps in the high voltage monitoring of the SPM trigger detectors and occasional loss of data due to undetected high voltage failures. The new system provided practically instantaneous response, and permitted the shift personnel themselves to reset the high voltages without fear of setting incorrect or damaging levels.

C.2.1 Computer and Interface

The detector monitoring workstation was based on an AST[5] Model 20 PC/AT compatible, equipped with an Intel 80286 CPU running at 10 MHz. It ran under the

---

[5] AST: AST Research

MS-DOS operating system. Using a PC-based CAMAC interface card, the AST was able to communicate with up to four DSP 6002 CAMAC crate controllers. Three were dedicated to the system described here and the fourth was installed later to be used in a separate electronics test station. The controllers were installed as auxiliary controllers to Jorway 71B type A-2 CAMAC master crate controllers used by the experiment DAQ system to prevent conflicts with DAQ activities. The first crate contained input/output registers, latches, and ADCs. The second contained ADCs. The third crate contained a high voltage supply interface, an output register, prescalers, scalers, TDCs, and ADCs for low voltage monitoring. While the PC was not directly connected to the experiment data acquisition system, a method to pass information between the two was developed using a "mailbox" register in the master CAMAC crate controller.

C.2.2 S1S2 Trigger

The S1S2 trigger was the coincidence of the discriminated output of two 0.5 m × 0.5 m scintillator paddles and the sum of the SUM counters. These paddles were mounted to a wooden board with hooks for placement at various locations downstream of the Scattered Muon Detector. The trigger was used to look at SPM detector response to halo muons in a specific region.

C.2.3 Gating Logic

The gating logic shown in Figure C.1 on page 168 used by the workstation integrated logic for several different activities. Included in it was a private data acquisition system using the S1S2 trigger, safeguards to prevent conflicts with the experiment DAQ system, and controls for latches, ADCs, and TDCs. A number of control levels from a Jorway 41 were used by the workstation to control the mode in which the gating logic operated.

A separate element of the gating logic was an Addressable Fan-Out (AFO) module used to control the enables on the SPM and SMS LED flashers. The module was a custom-built output and input register which I had designed and built. Communications with the AFO module was accomplished with one of two channels of a PR612 output register and one of two channels of a PR604 input register. The routines used for this purpose are in the AFUTIL software package.

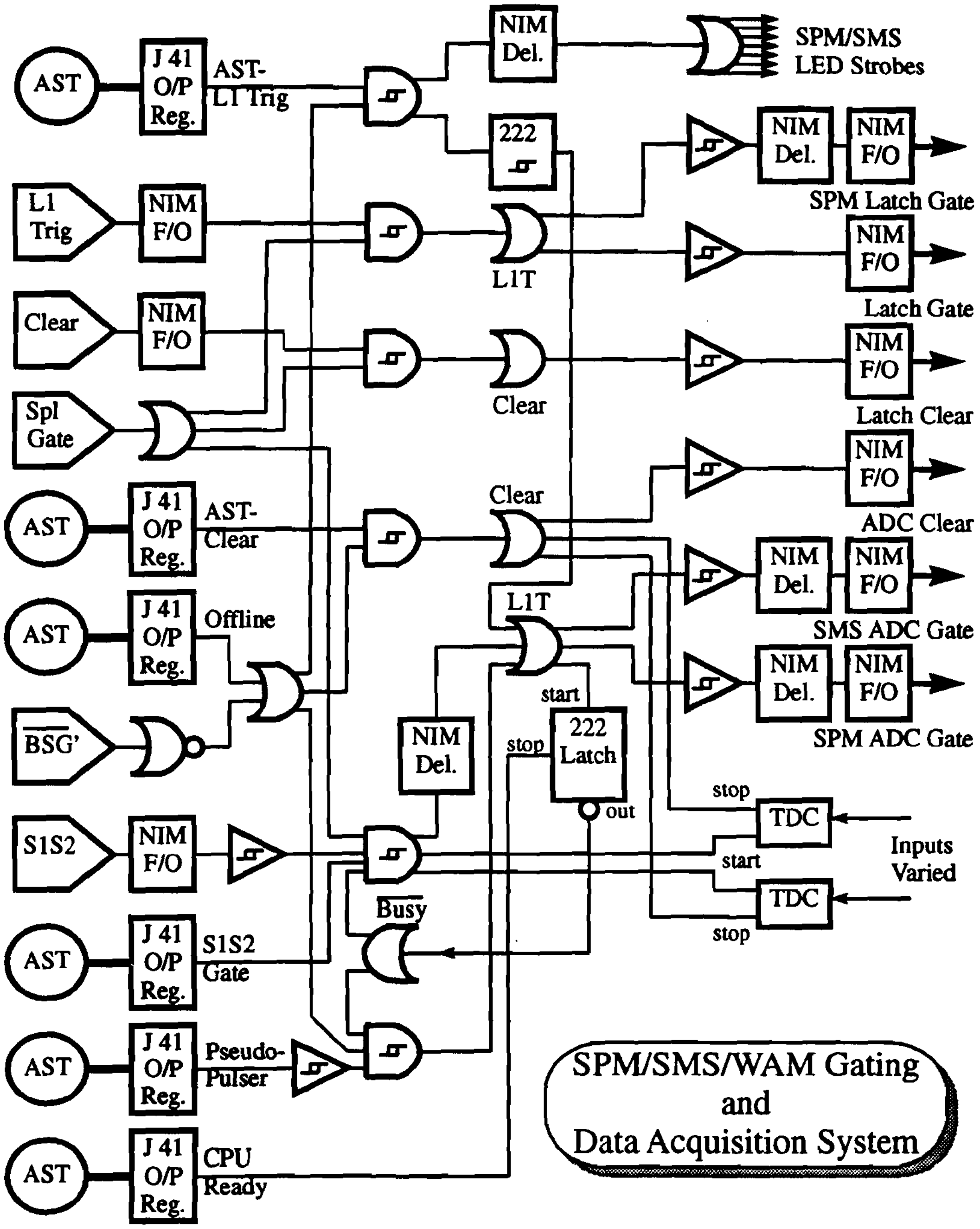

Figure C.1: SPM/SMS detector monitoring gating logic

C.2.4 Software

Software for the system was developed in Microsoft FORTRAN. This imposed certain constraints on the code development since MS FORTRAN under MS-DOS only supports object sizes up to 64 kBytes. All of the software I developed for the workstation is therefore in one of several source code "packages" whose compiled object size is less than 64 kBytes.

The software to control the detector monitoring workstation resided in one central program, W1CTRL. The W1CTRL program source was stored in the W1UTIL package. The program operated as a text-based, scrolling, menu-driven directory of the various functions available to shift personnel and to expert users. Groups of function existed for low level CAMAC crate operations (CMUTIL package), AFO module communications (AFUTIL package), RF prescaler utilities (PSUTIL package), detector interface and gating logic utilities (FHUTIL and SLUTIL packages), high voltage monitoring (VMUTIL package), WAM-L1 trigger control (TRUTIL package), and local data acquisition control (DAUTIL package). In addition to these user-visible functions, a custom-built package was developed (QHUTIL package) to collect, save, read, and view histograms. The locations of all the CAMAC modules and the high voltage settings was stored in a block data sub-program (BDUTIL package).

C.3 Applications

C.3.1 High Voltage

The high voltage system for the SPM, SMS, and PHI detectors consisted of a total of 9 LeCroy 4032 High Voltage Power Supplies attached to a serial bus to a single LeCroy 2132 Serial Interface module. Four supplies each were dedicated to the SPM and SMS, and one supply was allocated to the PHI detector. The LeCroy 2132 was used by the workstation to zero, check, read out in detail, or restore the high voltage settings in the LeCroy 4032 power supply pods.

Software for the high voltage monitoring was constructed in two layers. HVUTIL contained jackets for the low-level LeCroy 2132 operations. VMUTIL provided specific functions for use by shift personnel or expert. This separation of powers was non-trivial. Interaction with the 2132 required considerable knowledge of the details of the operation of the module and the cantankerous serial bus. The exact form of the interactions with the module were modified, without changing the functions seen by the user, to insure that any error detected by the software could be reproduced.

The standard high voltage set values were defined in the block data subprogram BDUTIL. This removed unnecessary flexibility which could have led to the setting incorrect values due to the use of an incorrect data file.

C.3.2 ADCs

After the ADC input signals and gates were timed, the ADCs were set for optimal operation using the detector monitoring workstation. A utility within W1CTRL called SLFH gathered automated the process of gathering ADC spectra. Pedestals were first measured without the S1S2 trigger, and the ADCs adjusted to reduce this response to noise and dark current. Then the S1S2 counters were placed behind each counter in SPM station 4 to look at halo muons in a particular location. ADC spectra were gathered with the S1S2 trigger and the data acquisition system. If the response of a counter was abnormal in its mean level or in its distribution, then the phototube high voltage was adjusted or the phototube replaced.

Figure C.2 on page 171 shows an early example of the ADC spectra taken before all the ADC channels had been adjusted. The figure on the left indicates that the pedestal (huge spike) should be moved lower in the ADC spectra in order to use all of the available ADC range. The figure on the right shows a counter whose high voltage might be raised to move the muon peak higher in the ADC spectra to improve counter response, if other conditions permit. Note also the difference in the muon peaks in the two spectra. The counter on the left is an GS2030/GS1919 outer counter which gave far less light for a muon passage (far wider muon peak) than the NE110 inner counter on the left.

C.3.3 Latches

After the SPM and SMS latch input signals and gates were timed, the latches were maintained in optimal condition in a number ways. TDCs were implemented in the gating logic for fine-timing. The ECL repeaters used to regenerate the signals after long cable delays generated an OR output which made scanning for bad counter signals much faster and did not require the counter latch signals be disturbed. The experiment data acquisition system maintained a standard set of latch histograms for perusal by the shift crew.

A generally more useful check of the latch integrity, however, was provided by the LED flashers under the control of the detector monitoring workstation. The SLIF utility inside the W1CTRL program allowed the user to define a pattern of LED flashes for a set of SPM and SMS counters. In single flash operation, the latches

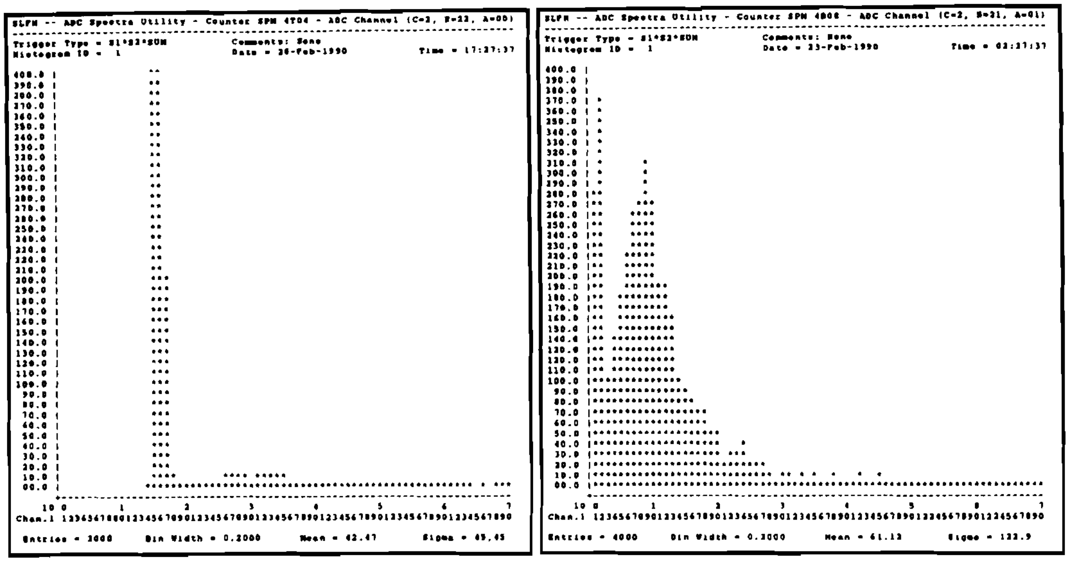

```
SLFM -- ADC Spectra Utility - Counter SPM 4T04 - ADC Channel (C=2, B=22, A=00)
Trigger Type = S1*S2*SUM            Comments: None
Histogram ID =  1                   Date = 26-Feb-1990          Time = 17:27:37
Entries = 2000     Bin Width = 0.2000     Mean = 42.47     Sigma = 45.45
```

```
SLFM -- ADC Spectra Utility - Counter SPM 4B08 - ADC Channel (C=2, B=21, A=01)
Trigger Type = S1*S2*SUM            Comments: None
Histogram ID =  1                   Date = 23-Feb-1990          Time = 02:27:37
Entries = 4000     Bin Width = 0.2000     Mean = 61.12     Sigma = 122.9
```

Figure C.2: SPM ADC spectra for an outer counter (left) and an inner counter (right)

of both detectors were subsequently read out. Since the LED flashers produced an enormous amount of light, this provided a simple, quick test of the latch operational status. Because of the amount of light, however, this did not actually simulate the passage of a muon though the detectors. This same set-up, when used in pseudo-pulser mode, was invaluable to generate combinations of firing counters to test data paths and the WAM Level One Trigger.

Appendix D

The WAM-L1 Trigger

D.1 Introduction

One of my early responsibilities as a UCSD graduate student was to build, test, and implement the WAM Level One Trigger Processor, a scattered muon trigger without a beam veto element [115]. The WAM Level One trigger was essentially a large electronic coincidence circuit. It detected the presence of an interesting scattering event by forming a coincidence between the beam signal, the RF signal (which set the timing of the leading edge of the output signal), and any one of many acceptable combinations of SPM and SUM counters which indicated that a muon was present outside of the nominal unscattered beam location in the Scattered Muon Detector. These acceptable combinations of counters were called "roads".

D.1.1 RUN87 WAM Level One Trigger

The original RUN87 design of the processor used the LAT beam signal, the experiment RF signal, and the signals from 120 SPM counters and 128 SMS counters to determine whether a scattered muon was present in under 50 ns from input to output. After over a year of design, construction, and testing, the trigger processor was operational shortly after the beginning of RUN87. Unfortunately, the trigger was unable to reject a sufficiently large fraction of the beam to keep the deadtime due to false triggers down to an acceptable level. These false triggers were due primarily to electromagnetic activity generated by the passage of unscattered muons through the hadron absorber. Halo muons and large angle scattering events in the absorber also contributed to the false trigger rate. No physics data were used from the WAM trigger in RUN87.

D.1.2 RUN90 WAM Level One Trigger

For RUN90, the trigger was redesigned and re-implemented to use the 96 new SUM counters placed in front of the absorber in order to help reject the interactions in the absorber. The WAM trigger no longer used the SMS counters for small angle triggering. The trigger achieved the goal of < 0.01 trigger per beam muon at the beginning of RUN90. Unfortunately, the undetected and untimely failure of an SVW counter near the beam caused the trigger rate to rise to an unacceptable 0.015 trigger per beam muon. The unrejected halo muons appeared to the trigger to be scattered muons. The WAM Level One trigger was then used as part of the new CVT trigger which used the SMS counters and a separate processor to add a beam veto to the scattered muon definition. The WAM Level One trigger itself was prescaled and used only as a monitor trigger. Only sparse physics data from early in RUN90 were taken with the WAM trigger before it was prescaled. This appendix describes the RUN90 incarnation of the WAM Level One trigger.

D.2 Design Goals

There were four basic design goals of the WAM-L1 trigger. It had to produce a trigger signal within 50 ns after the arrival of the SPM inputs. It was required to have wide acceptance for scattered muons. The avoidance of an unscattered beam veto element was a central part of the trigger specification. Finally, the fraction of the beam on which the WAM-L1 triggered was required to be less than 1 part in 100.

The 50 ns propagation delay limit for the trigger was based on the demands of several detectors, notably the PC, to have the Level One trigger arrive by a certain time to accommodate the fixed-length delay cables used for signals from the chambers. Having the trigger arrive any later would have required that these lines be lengthened at great cost in manpower and materials. This requirement was one of the most difficult of the design goals to meet. It required that the trigger logic be implemeted in ECL logic which is expensive and power-hungry, in addition to being fast. A large amount of work went in to minimizing the length of PC board to PC board cables to reduce the overall propagation delay time.

The WAM Level One trigger was designed not to limit the geometric acceptance of the experiment unneccessarily. In order to have wide acceptance for muons originating from somewhere in the general vicinity of the target, the trigger roads were required to be three counters wide in all but the upstream-most SPM plane. Given the focussing condition established with the CVM and CCM magnets, the location of the muons in the first SPM plane was related, to first order, only the scattering angle. Hence, the width of the roads defined the maximium scattering angle accepted by the trigger.

The scattered muon triggers at E665 were intended to operate in concert; the shortcomings of any one being addressed by the others. The niche that the WAM trigger was designed to fill was to detect large angle muon scattering without using a beam veto element. This was to be used as a check of the E665 Small Angle Trigger which used a floating beam veto and later the RUN87 Large Angle Trigger which used a fixed beam veto. These veto elements can lead to incomprehensible trigger acceptance for scattering in which the muon travels near the veto element. The muon can undergo some interaction in the absorber and be deflected into the veto element, killing the trigger for the event (a suicide). Alternatively, the passage of the muon through the absorber could have generated a hard electromagnetic shower, a knock-on electron, or soft electromagnetic activity which then strikes the veto element, again suiciding the event. In any case, legitimate inelastic scattering events at a given scattering angle are lost even though there should acceptance for that angle. The WAM trigger was intended to gather a sufficiently large sample of such events in order to measure the effect of suicides in the SAT and LAT triggers.

Finally, the Level One trigger rate generated by the WAM-L1 was required to be sufficiently low that the experiment did not suffer excessive deadtime. Each Level One trigger caused the apparatus to go dead for at least 600 ns while a Level Two trigger decision was made. If the Level Two decision was affirmative, then the detectors were read out. If the decision was not made within that 600 ns deadtime, though, the experiment automatically reset. Excessive Level One trigger rate kept the experiment in the Level Two decision deadtime, unable to accept any more beam. The real problem is, of course, that the excessive Level One rate is due to uninteresting events fooling the Level One trigger processors into thinking it may be an interesting event. Only about 1×10^{-6} of incoming muons actually generate interesting events. The goal rate of the WAM-L1 trigger to keep the deadtime to 10% was less than 1×10^{-2}.

D.3 Trigger Processor Sub-Systems

The WAM Level One Trigger Processor consists of several distinct sub-systems. The Beam Logic sub-system handles the beam signal and RF signal coincidence. The Road Logic system handles the SPM and SUM road signal definitions and subsequent road and beam coincidences. The Level One Trigger sub-system handles the sum of the roads and the RF signal to form the final WAM Level One trigger. This sub-system is also used by all other Level One triggers in the experiment to form the common Level One trigger and to perform the Level One - Level Two gating. Selection of the WAM Level One trigger configuration was performed by Control Levels sub-system. The flow of data amongst the elements of these sub-systems is illustrated in Figure D.1 on page 176.

D.3.1 Beam Logic

The beam logic sub-system provided a beam signal for each road that was synchronized to a prescaled experiment RF. The LAT beam signal was transmitted from the general experiment beam electronics located near the downstream-most beam station to the beam logic sub-system located above the hadron absorber. There the signal was reshaped and sent to the Beam-RF coincidence logic (B*RF board

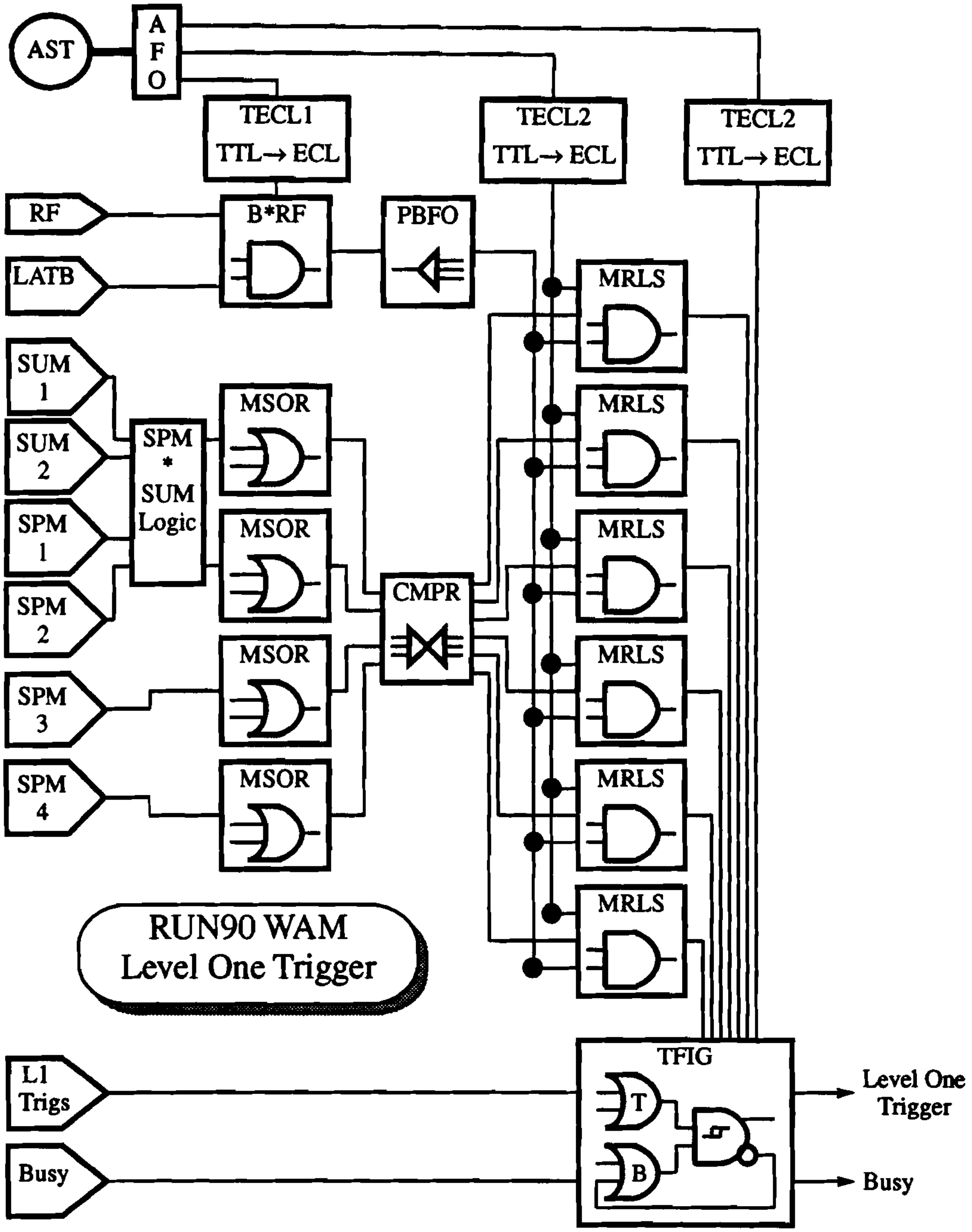

Figure D.1: Data Flow in the WAM-L1 Trigger design). Experiment RF was prescaled by a software selectable modulus from 1 to $2^24 - 1$ with the relative output-input phase insensitive to the modulus choice (RFPS board design). The prescaled RF output could also be forced DC on for testing purposes. The Beam-RF coincidence logic was an eight channel, software selectable, coincidence circuit with any of eight beams and any of eight prescaled RF inputs used in any one output channel. The eight synchronized beam outputs were next fanned out to each road (PBFO board design).

D.3.2 Road Logic

While the road logic inside in the WAM-L1 trigger processor remained the same for RUN90, the signals used were changed from just the SPM counters to a preprocessed combination of the SUM and SPM counters [166]. Corresponding top and bottom bank, plane 1 and plane 2 counters, SUM counters were summed into "towers". Combinations of three SUM towers and each SPM counter at a similar Y-coordinate were made for SPM planes 1 and 2.

The combined signals from the SPM and SUM counters were then organized (in the WAM-L1 trigger) within each SPM plane (MSOR board design). Corresponding top and bottom bank counters were summed to form "towers". In all but the upstream-most SPM plane, the towers were summed in overlapping combinations three across to form road sections. The towers themselves were the road sections in SPM plane 1. These road sections were then re-shuffled from an SPM plane organization to a trigger road organization (CMPR board design). The road sections were then combined in software-selectable majority logic to form roads (MRLS board design). Depending on the logic configuration selected, a coincidence of either two of the four planes, three of the four planes, or four of the four planes were required for a road to fire. Physics data-taking only used three out of four logic only to insure some means of monitoring the trigger and detector efficiency. The effect of combining the old RUN87 WAM-L1 trigger processor logic and the SUM-SPM preprocessing logic was to require that within a road, if one of two SUM layers detects a muon and three of four SPM planes detects a muon, then that road will fire. A coincidence of the SUM-SPM road and a software-selectable sum of synchronized, prescaled beams was then made.

D.3.3 Level One Trigger

All synchronized roads were sent to the Level One Trigger board to be summed (TFIG board design). This trigger board not only handled the WAM-L1 trigger, but also implemented the gating functions for all the level one triggers in the experiment. This board was redesigned for RUN90 and only the new design is described.

The Level One Trigger board summed all the WAM-L1 roads, as well as all the other Level One triggers in the experiment. This sum was synchronized to the experiment RF to insure that the timing of the output trigger was independent of which input trigger fired. The trigger was shaped with a one-shot whose output was fanned out to all the detectors in the experiment. In addition, this Level One trigger signal started the Level One Busy. External busy inputs were available so that the general data acquisition system could hold the trigger offline if an event was to be recorded. A latch strobed by the experiment RF was used to synchronize the disabling of the Level One Busy to prevent the trigger from coming live in the middle of an RF bucket. This would have disturbed the timing of the leading edge of triggers occurring in that same bucket. The Busy was also fanned out to the detectors.

D.3.4 Control

One of the design goals of the WAM Level One Trigger was to maintain flexibilty in the hardware-implemented logic by permitting a selection of paths through the logic to be enabled or disabled by 1024 DC levels. The control of these levels, and therefore the logic configuration, was performed by the detector monitoring workstation described in Appendix C and four Addressable Fan-Out (AFO) modules. The W1CTRL program, running on the monitoring PC, read a trigger configuration file (the TRUTIL package) and loaded the corresponding WAM-L1 control levels into the AFO modules (the AFUTIL package). The AFO modules latched and output the TTL levels and performed simple cable continuity checks with current loops built into the cabling. The levels were then shifted by a large number of TTL to ECL converters (TECL1 and TECL2 designs) for use in the trigger logic.

D.3.5 Miscellaneous

The PC boards used to implement the logic were suspended from a G-10 framework in a set of electronics racks on the hadron absorber. Each of the PC boards received low voltage power distributed in the back of these racks on copper bus bar. As described in Appendix C, the low voltage power was monitored at the supplies by the detector monitoring workstation.

In order to simplify the maintenance of the trigger, nearly all important signals from the WAM-L1 trigger, as well as the general experiment Level One Trigger, were buffered and made available at a set of testing points. Also, most signals used to form the WAM-L1 trigger were sent to latches for read-out in DAQ.

D.4 Construction

After laying out the electronics schematics of each board, I laid out the PC board design with McCad PCB Design[1]. Both processes were done by hand on a personal computer without automation. The PC board layers were then sent to a graphics company to be rendered on transparencies with a laser plotter[2]. The PC boards were manufactured at a local board house. After receiving the boards, I verified that they reflected the original design. I then stuffed each board and performed some low level testing to insure no shorts existed in the power distribution traces.

D.5 Implementation

After each PC board was constructed, it was checked with an automated test program running on an LSI IS-11 CAMAC module micro-computer. A test program was designed for each PC board design. These programs generally involved looping through all possible control level configurations for a board. For each configuration, fake inputs were generated and fed into a board. Latches were then used to insure that the proper logical combination of outputs was generated by the PC board. Given the combinatorics involved, a well-chosen subset of all possible inputs was used to reduce the test time to less than a day per board. The timing characteristics were checked by hand with an oscilloscope. Once an individual board was certified to work properly, it was installed in the trigger racks.

The next challenge of implementing the trigger was to set the timing of all the paths through the logic. This was done on paper initially, and was no simple or menial task. A timing imperfection in the RUN87 LAT trigger led to severe trigger ineffiencies after the experiment RF and the LAT trigger relative timing changed by three nanoseconds [7]. The timing of the trigger inputs, for instance, had to include allowances for the time variations in the output time of the counter signals as a function of the altitude of the muon intercept[3], as well as for the large jitter in the

---

[1] VAMP, Inc.

[2] Originally, the designs were pen plotted at Fermilab and transferred to transparency at a local photographic service. This was very manpower intensive since the pen plotter often failed to operate consistently and took many hours to complete a design when it did not fail.

[3] Note that the top bank SUM and SPM counters had their phototube at the same end of the counters, but the bottom bank counters had their phototubes at opposite ends of the counters. This

SPM signals. Inter-board cable lengths were set and then the relative timing of signals was spot-checked at various points in the logic. Once confidence was established in the correspondence of the timing diagrams to the actual properties of the circuitry, the laborious task of checking every path began. After this was done, the optimal relative timing of the beam and the roads was determined. This was done by delaying the beam by a increasing amounts to look for changes in the resulting trigger rate.

D.6 WAM-L1 Trigger Rate

The trigger rate for the WAM-L1 trigger at the beginning of data-taking in RUN87 was 0.08, much too high to be used in the experiment data acquisition system. During that run, counter combinations in the beam region roads which not considered necessary to maintain angular acceptance were removed. This led to the trigger rate dropping to 0.06, still far larger than the goal rate of less than 0.01 for Level One triggers.

The source of the false triggers was obvious. The primary problem was soft electromagnetic activity associated with the muon passage through the hadron absorber or shielding walls. The thresholds on the SPM counters next to the beam in RUN87 were set to fire on the presence of 1 to 3 photons. With thresholds set so low, the SPM counters had a tendency to refire long after the passage of a scattered muon or the passage of an unscattered muon with some soft electromagnetic activity around it. The wavelength shifter bar material used in the outer counters has two re-transmission decay half-lifes, one of 20 ns and one of about 600 ns. The latter also contributed to the high trigger rate. Of secondary importance were halo muons that evaded the SVW veto wall, and hard electromagnetic showers associated with the beam muon, and hard scatters in the hadron absorber.

Between RUN87 and RUN90, a considerable effort was made to upgrade the large angle triggers, in part to help reduce the WAM Level One trigger rate. Many of these changes are described in Chapter 2. Also of interest is the fact that the central counters were all replaced by NE110 counters mounted in steel boxes with lead shielding on the upstream face. These NE110 counters generated far more light than the previous counters. With this SPM upgrade, the WAM-L1 trigger rate fell to 0.045. Once the SUM wall was implemented in the WAM logic, the rate dropped to 0.015. This still was not quite acceptable.

I undertook a systematic study to optimize the trigger rate by raising the SPM thresholds. As the thresholds were raised, the efficiency of the SPM counters

---

made the task of properly timing the SUM-SPM coincidence somwhat more complicated.

was checked to insure that counters, and therefeore the trigger, did not become inefficient. Some counters, for instance, had their high voltage adjusted higher to improve response and permit a higher threshold to be used. Once the SPM thresholds were raised as high as possible without creating inefficient counters, the WAM Level One trigger rate stood at just below 0.008, an acceptable level.

Shortly after data-taking began, however, a veto wall counter failed. Unfortunately, this was not detected. The WAM-L1 trigger rate rose to 0.015 as halo muons, accompanying unscattered incoming muons, began to generate triggers. Other triggers were not seriously affected since they contained beam veto elements that rejected the unscattered beam. The WAM-L1 trigger was subsequently prescaled and used only as a monitoring trigger.

D.7 Critique

After having dedicated so much effort over several years to implementing the WAM-L1 trigger, I learned some hard lessons. The effort to bring up the beam veto-less WAM trigger was constantly challenged by the overwhelming presence of triggers on unscattered beam travelling down the center of the nominal unscattered beam path. This problem was never adequately solved. Raising the SPM thresholds did help reject some triggers due to the random coincidences related to the softest electromagnetic activity. However, the SPM counters were never fully understood in their role as trigger counters. Each counter should have been considered as a trigger unto itself, able to reject all activity except the passage of highly energetic charged particles. Yet they were originally implemented as highly efficient tracking counters, able to avoid *not* firing at the presence of any noticeable activity. The high noise rate, correlated from plane to plane, related to the presence of beam 10 cm away was never fully explored. Also challenging the trigger implementation effort was the presence of hard electromagnetic showers behind the absorber. Much of this was removed by the use of the SUM counters in front of the shower generating calorimeter and hadron absorber. The Level One trigger was also troubled by halo evading the SVW veto wall, but the Level Two trigger was able to reject most of these events for which the halo muon did not point back to the target. The summary lesson is that a simple beam veto-less trigger either requires a hole in the apparatus through which the unscattered beam might travel without generating a cloud of photons and knock-on electrons around it, or that the trigger counters must be designed smaller, generate more light, have adequate shielding, and thus be made more efficient individually at rejecting soft activity.

Another constant challenge was to implement and then maintain the WAM-L1 trigger electronics through the many design changes made over the years to attack the rate problems. The choice made early on to use a large number of different PC board designs with cable runs between them was far from ideal. The use of a motherboard to carry the signals would have eliminated the linguine of precisely timed cables carrying signals from one PC board to the next. Spending time and money to move the detector signals earlier rather than the trigger propagation delay shorter could have permitted the use of standard off-the-shelf electronics for much of the trigger, freeing up tremendous manpower for other projects. Its no wonder that software-based triggers, made feasible for many experiments with the coming of cheap, reliable, and powerful UNIX workstations, are generally considered superior in their construction and flexibility. These points are finally being taken seriously in making decisions about the economics of supporting a trigger over its life cycle in the experiment, rather than simply considering the cost of getting "something" installed and working.

Appendix E

Extraction of the Structure Function Ratio

E.1 Introduction

This appendix is a detailed description of the extraction of the ratio of the one-photon-exchange differential cross section for hydrogen to that for deuterium using a subset of the produced data set. This extraction method is somewhat idealized; it assumes that there are sufficient event statistics to make the corrections described. The ratio is then used to calculate the structure function ratio $F_2(\mathrm{n})/F_2(\mathrm{p})$. The extraction is based on the relation between the differential number of scatters and the differential cross section for all scattering processes. The criteria for selecting the subset used in this analysis come from the assumptions made in the derivation of the formula governing the extraction of the cross section ratio.

$$\frac{dN}{d\xi}(\xi) = L \int_{all\ \xi^*} d\xi^*\, A(\xi^*)\, E(\xi^*)\, S(\xi^*;\xi)\, \frac{d\sigma^{total}}{d\xi^*}(\xi^*) \tag{E.1}$$

where ξ represents the set of true kinematic variables (x_{bj}, Q^2) describing the event, ξ^* represents the measured (x^*_{bj}, Q^{2*}) associated with the event, L is the integrated luminosity, A is the experiment acceptance, E is the experiment efficiency, S is the experiment smearing function, and $\frac{d\sigma^{total}}{d\xi^*}$ is the differential cross section for scattering by all processes. This relation ignores the dependence of the quantities involved on the beam phase space. Including these dependencies, using μ^* to represent the measured phase space of the accepted beam muon, one arrives at:

$$\frac{dN}{d\xi}(\xi) = \int_{all\ \xi^*} d\xi^* \int_{accepted\ \mu^*} d\mu^*\, \frac{dL}{d\mu^*}(\mu^*)\, A(\xi^*,\mu^*)\, E(\xi^*,\mu^*)\, S(\xi^*,\mu^*;\xi)\, \frac{d\sigma^{total}}{d\xi^*}(\xi^*) \tag{E.2}$$

The smearing function now describes, for a given measured beam phase space region, how the measured kinematics are smeared from the true kinematics. The ratio of cross sections for different nuclear targets is then extracted from ratios of this relation for different targets.

E.2 Integrated Luminosity

The integrated luminosity can be broken down into components describing the accepted beam and components describing the target. Since a range of beam phase space is accepted for study, the dependence of the luminosity on the beam phase space is explicitly shown.

$$\frac{dL}{d\mu^*}(\mu^*) = TN_\mu B(\mu^*) \tag{E.3}$$

where T is the number of target particles per unit area normal to the beam axis, N_μ is the total number of accepted beam muons in the study, and $B(\mu^*)$ is the normalized beam phase space density. $B(\mu^*)$ is used to take into account effects that are strongly dependent on the beam energy (energy transfer resolution) and beam position (strongly position dependent tracking efficiencies). The number of target particles per unit cross sectional area is given by:

$$T = N_A M\, l_f \tag{E.4}$$

where N_A is Avogadro's number, M is the molar density of nuclein in the target material, l_f is the defined fiducial length of the target. The molar density of nuclei M is given by:

$$M = \frac{\rho}{A_W} \tag{E.5}$$

where A_W is the atomic weight of the target material, and ρ is the mass density of target material. This gives, for the luminosity:

$$\frac{dL}{d\mu^*}(\mu^*) = N_A \frac{\rho}{A_W} l_f N_\mu B(\mu^*) \tag{E.6}$$

The atomic weight and mass density are determined by a study of the isotopic composition and state conditions (pressure and temperature) of the target material. The fiducial length of the target is the length of target material in which events are accepted. It is determined by an analysis of the position resolution of the interaction vertex along the beam axis and is smaller than the physical target length. The number of muons accepted for study is calculated by several means which fall under the general title of normalization. The beam phase space density is determined by a study of a randomly selected sample of beam muons in the experiment.

The relative luminosity between the H_2 target and the target D_2 is, using Equations E.3 and E.4 and assuming that the fiducial target lengths are defined to be identical:

$$\begin{aligned} \frac{\frac{dL}{d\mu^*}(\mu^*;H_2)}{\frac{dL}{d\mu^*}(\mu^*;D_2)} &= \frac{N_\mu^{H_2}}{N_\mu^{D_2}}\frac{T^{H_2}}{T^{D_2}}\frac{B^{H_2}(\mu)}{B^{D_2}(\mu)} \\ &= \frac{N_\mu^{H_2}}{N_\mu^{D_2}}\frac{M^{H_2}}{M^{D_2}}\frac{B^{H_2}(\mu^*)}{B^{D_2}(\mu^*)} \end{aligned} \tag{E.7}$$

By substituting Equation E.3 into Equation E.2 can be expressed as:

$$\frac{dN}{d\xi}(\xi) = TN_\mu \int_{all\ \xi^*} d\xi^*\ B\ A(\xi^*)\ E(\xi^*)\ S(\xi^*;\xi)\ \frac{d\sigma^{total}}{d\xi^*}(\xi^*) \tag{E.8}$$

Here I have dropped references to the beam phase space. There is still an implied integration over all beam phase space and implied dependencies in B, A, E, and S on the beam phase space. As a reminder of this, I hold the B term inside the integration in ξ^*.

E.3 Acceptance

The experiment acceptance is the probability that the experiment is capable of detecting an interaction described by (ξ^*, μ^*). The primary contributions to the overall acceptance are the geometric acceptance of the tracking equipment, the acceptance of the triggering equipment, and the acceptance of the event analysis software. Other miscellaneous effects, such as the limit on the maximum event size accepted by the data acquisition system, also contribute to the acceptance.

E.4 Efficiency

The experiment efficiency is the probability that the experiment actually detects an interaction described by (ξ^*, μ^*) which it is capable of detecting. The overall efficiency can be broken down into several major factors: apparatus efficiency, trigger efficiency, and software efficiency. Especially worrisome are systematic problems in the triggering system, such as the self-vetoing of events.

E.5 Smearing Function

The experiment smearing function is the probability that the experiment detects an interaction described by (ξ^*, μ^*) which is in fact described by (ξ, μ). There are many important components to the smearing function. For instance, since detectors have finite spatial and/or temporal resolutions, they can provide only a finite resolution in the measured values of the kinematic variables. A general class of processes, collectively referred to as radiative processes, can lead to a change in the phase space of the muon between the last detection of the beam muon and the first detection of the scattered muon. Corrections for the radiation of energy by the muon are implemented through the smearing function, while corrections for other processes occurring at the interaction vertex are handled by a weighting process described in Section E.8. Effects which are not included in the smearing function are, for instance, miscalibration of the beam and forward spectrometer momentum measurements and detector misalignment. These are treated as systematic errors since they introduce correlated errors on the kinematics of the event.

E.6 Binning

In practice, measurements are made of the number of scattering events occurring in the interval described by $\Delta\xi$. To denote this, the following notation is used:

$$f(\Delta\xi) \equiv \int_{\Delta\xi} d\xi \, \frac{df}{d\xi}(\xi) \tag{E.9}$$

The 'binned' number of scattering events refers to the number of events found in the interval $\Delta\xi$, and is given by:

$$N(\Delta\xi) = TN_\mu \int_{\Delta\xi} d\xi \int_{all\ \xi^*} d\xi^*\, B\, A(\xi^*)\, E(\xi^*)\, S(\xi^*;\xi)\, \frac{d\sigma^{total}}{d\xi^*}(\xi^*) \qquad \text{(E.10)}$$

E.7 Background Corrections

The $N(\Delta\xi)$ count is the count of the number of muon-nucleon scatters occurring inside the fiducial target vessel and falling in the kinematic bin $\Delta\xi$. The actual count made on a target, referred to as $N^{actual}(\Delta\xi)$, includes events containing a number of processes, collectively referred to as background, which must be removed from the actual event count to get the desired count.

$$N(\Delta\xi) = N^{actual}(\Delta\xi) - N^{background}(\Delta\xi) \qquad \text{(E.11)}$$

This background can be broken down into several identifiable contributions:

$$N^{background}(\Delta\xi) = N^{\mu-e} + N^{\mu-\gamma} + N^{vessel} \qquad \text{(E.12)}$$

where $N^{\mu-e}$ represents the count from muon-electron scattering. An effort is made to identify muon-electron scattering events from their event topology. $N^{\mu-\gamma}$ represents the count from coherent bremsstrahlung (no interaction with target nucleons). This contribution is removed from the data sample implicitly by applying the calculated radiative corrections weight η and so is dropped from this breakdown of the background event count. N^{vessel} represents the count from target vessel and exterior interactions. This number is measured by considering the number of events from an empty target vessel that is essentially identical in construction and position to the full target vessel. This particular correction is referred to as the 'empty target subtraction'. This can then by implemented in the ratio measurement via:

$$\begin{aligned} W(\Delta\xi) &= \int_{\Delta\xi} d\xi\, \eta(\xi)\, (N^{actual}(\xi) - N^{\mu-e}(\xi) - N^{vessel}(\xi) - N^{other}(\xi)) \\ &= W^{actual} - W^{\mu-e} - W^{vessel} - W^{other} \qquad \text{(E.13)} \end{aligned}$$

Note that the radiative corrections weight applied is that for the muon-nucleon scattering process, since it is that process to which the count total refers.

The empty target contribution to the background correction can be measured to first approximation by using Equation E.25. Since the empty target vessel is essentially identical in construction and position to the filled target vessel, the ratio of the number of events on a filled target (here, H_2) to that on an empty target is approximately:

$$W^{vessel}(\Delta\xi) = W^{empty}(\Delta\xi)\frac{N_\mu^{H_2}}{N_\mu^{empty}} \tag{E.14}$$

where $W^{empty}(\Delta\xi)$ is the weighted count on the empty target, $N_\mu^{H_2}$ is the number of beam muons accepted on the filled target 1, and N_μ^{empty} is the number of beam muons on the empty target. The correction to this due to the empty target not really being empty is small. The weighted event count ratio is then given by:

$$\frac{W^{D_2}(\Delta\xi)}{W^{H_2}(\Delta\xi)} = \frac{W^{actual}(D_2) - W^{\mu-e}(D_2) - W^{other}(D_2) - W^{empty}\frac{N_\mu^{D_2}}{N_\mu^{empty}}}{W^{actual}(H_2) - W^{\mu-e}(H_2) - W^{other}(H_2) - W^{empty}\frac{N_\mu^{H_2}}{N_\mu^{empty}}} \tag{E.15}$$

E.8 Radiative Corrections

Radiative corrections handle two problems with the measurement of the event kinematics. The first is that the physical scattering process can involve interactions other than, or in addition to, one-photon-exchange. A set of reconstructed deep inelastic scattering events can thus be used only to evaluate directly the differential cross section for all scattering processes, not just that for the one-photon-exchange process. A procedure, referred to as internal radiative corrections, has been applied to derive the desired one-photon-exchange differential cross section ratio for the deep inelastic scattering process by modifying the counting of $N(\Delta\xi)$. The ratio of the one-photon-exchange cross section to the cross section for all processes is used to weight the count of each event. Define:

$$\eta(\xi) \equiv \frac{\frac{d\sigma^{1\gamma}}{d\xi}(\xi)}{\frac{d\sigma^{total}}{d\xi}(\xi)} \tag{E.16}$$

This ratio is calculated using the NMC radiative corrections computer program FERRAD [191]. The weighted count, represented by W, is defined by:

$$W(\xi) \equiv \eta(\xi) N(\xi) \tag{E.17}$$

The weighted differential count is then given by:

$$\begin{aligned} \frac{dW}{d\xi}(\xi) &\equiv \eta(\xi)\, \frac{dN}{d\xi}(\xi) \\ &= T N_\mu\, \eta(\xi) \int\limits_{all\ \xi^*} d\xi^*\, B\, A(\xi^*)\, E(\xi^*)\, S(\xi^*;\xi)\, \frac{d\sigma^{total}}{d\xi^*}(\xi^*) \end{aligned} \tag{E.18}$$

and the binned weighted count is given by:

$$W(\Delta\xi) = T N_\mu \int\limits_{\Delta\xi} d\xi\, \eta(\xi) \int\limits_{all\ \xi^*} d\xi^*\, B\, A(\xi^*)\, E(\xi^*)\, S(\xi^*;\xi)\, \frac{d\sigma^{total}}{d\xi^*}(\xi^*) \tag{E.19}$$

The second effect is due to the muon radiating energy after it is last detected as a beam muon and before it is first detected as a scattered muon. These radiative processes can cause the measured event kinematics to differ from the true kinematics at the muon-photon vertex. The corrections for this effect, referred to as external radiative corrections, are implemented by way of the experiment smearing function.

E.9 Extraction of the Ratio

The ratio of the binned weighted number of scatters in the bin $\Delta\xi$ on the D_2 target to that on the H_2 target, using Equation E.4, can be expressed as:

$$\frac{W^{D_2}(\Delta\xi)}{W^{H_2}(\Delta\xi)} = \frac{M^{D_2}}{M^{H_2}}\, \frac{N_\mu^{D_2}}{N_\mu^{H_2}}\, \frac{\int\limits_{\Delta\xi} d\xi\, \eta^{D_2} \int\limits_{all\ \xi^*} d\xi^*\, B^{D_2}\, A^{D_2}\, E^{D_2}\, S^{D_2}\, \frac{d\sigma^{total}}{d\xi^*}(D_2)}{\int\limits_{\Delta\xi} d\xi\, \eta^{H_2} \int\limits_{all\ \xi^*} d\xi^*\, B^{H_2}\, A^{H_2}\, E^{H_2}\, S^{H_2}\, \frac{d\sigma^{total}}{d\xi^*}(H_2)} \tag{E.20}$$

Each differential cross section is, unfortunately, buried in a complicated convolution. If one knew of an appropriate basis set for representation of the differetial cross section, then one can solve this equation for the coefficients of the basis vectors. However, the choice of a basis set would necessarily restrict the solution found to the space representable by that basis set, thus hiding behavior not anticipated by the choice of basis set.

To extract the cross section ratio from this formula several convenient facts are exploited. Essentially identical target vessels were used for hydrogen, deuterium, and liquid empty. Systematic effects are also essentially identical since the targets were alternated every few minutes. Thus the beam phase spaces, acceptances, and efficiencies on the different liquid targets are, for all practical purposes, identical. The smearing functions and weighting functions are nearly identical, with some small differences being introduced by differences in radiative corrections for the target materials. Further, the ratio of the cross sections is expected to be approximately a constant within the chosen bins, provided the bins are chosen to be sufficiently small in size. These facts are combined with the mean value theorem [56, p. 178], which states:

Theorem 1 (Mean Value Theorem) Let D be a compact, connected, bound set with positive area. Let f and g be continuous and bounded on D, with $g(p) \geq 0$ for all $p \in D$. Then there exists a point $p_0 \in D$ such that

$$\int\!\!\int_D fg = f(p_0)\int\!\!\int_D g \tag{E.21}$$

applied separately to the denominator and numerator to yield:

$$\frac{\int_{\Delta\xi} d\xi\ \eta^{D_2} \int_{all\ \xi^*} d\xi^*\ B^{D_2}\ A^{D_2}\ E^{D_2}\ S^{D_2}\ \frac{d\sigma^{total}}{d\xi^*}(D_2)}{\int_{\Delta\xi} d\xi\ \eta^{H_2} \int_{all\ \xi^*} d\xi^*\ B^{H_2}\ A^{H_2}\ E^{H_2}\ S^{H_2}\ \frac{d\sigma^{total}}{d\xi^*}(H_2)} = \frac{\frac{d\sigma^{1\gamma}}{d\xi}(\xi = \xi_2)}{\frac{d\sigma^{1\gamma}}{d\xi}(\xi = \xi_1)} \tag{E.22}$$

where ξ_1 and ξ_2 are independent points in the bin $\Delta\xi$. The location of these points in the bin depends on the as yet unknown shape of the cross section. While this simplifies the problem of extraction somewhat, the method of determining the exact location of these points is not defined. Further, the goal of the extraction is the ratio evaluated at a single point, not the ratio of items evaluated at different points.

An alternative is to consider an approximate relation, similar to the exact result in Equation E.22, at a single known point:

$$\frac{\int_{\Delta\xi} d\xi\ \eta^{D_2} \int_{all\ \xi^*} d\xi^*\ B^{D_2}\ A^{D_2}\ E^{D_2}\ S^{D_2}\ \frac{d\sigma^{total}}{d\xi^*}(D_2)}{\int_{\Delta\xi} d\xi\ \eta^{H_2} \int_{all\ \xi^*} d\xi^*\ B^{H_2}\ A^{H_2}\ E^{H_2}\ S^{H_2}\ \frac{d\sigma^{total}}{d\xi^*}(H_2)} \approx \frac{\frac{d\sigma^{1\gamma}}{d\xi}(\xi = \bar{\xi}; D_2)}{\frac{d\sigma^{1\gamma}}{d\xi}(\xi = \bar{\xi}; H_2)} \tag{E.23}$$

where $\bar{\xi}$ is the mean value of the kinematic variables of the events falling into the bin $\Delta\xi$. This relation is approximate for a number of reasons, including the fact that the radiative correction weights do differ somewhat between targets and that the relation has been forced away from the mean value theorem result for easier calculation. Since the degree to which this approximation holds will determine the validity of the process to extract the cross section ratio, some means of quantifying this assumption is required, such as defining:

$$I(\Delta\xi) \equiv \frac{\int_{\Delta\xi} d\xi\ \eta \int_{all\ \xi^*} d\xi^*\ B\ A\ E\ S\ \frac{d\sigma^{total}}{d\xi^*}}{\Delta\xi\ \frac{d\sigma^{1\gamma}}{d\xi}(\xi = \bar{\xi})} \tag{E.24}$$

where the term $\Delta\xi$ represents the area of the bin. Note that some descriptions state that the binned I functions themselves are expected to be close in value to unity [25]. This is not the case where the cross section changes rapidly across a bin, such as where the acceptance is turning off. The ratio, however, is close to 1 provided the cross sections in the ratio change across the bin in approximately the same manner.

The weighted count ratio becomes:

$$\frac{W^{D_2}(\Delta\xi)}{W^{H_2}(\Delta\xi)} = \frac{M^{D_2}}{M^{H_2}}\ \frac{N_\mu^{D_2}}{N_\mu^{H_2}}\ \frac{I^{D_2}(\Delta\xi)}{I^{H_2}(\Delta\xi)}\ \frac{\frac{d\sigma^{1\gamma}}{d\xi}(\xi = \bar{\xi}; D_2)}{\frac{d\sigma^{1\gamma}}{d\xi}(\xi = \bar{\xi}; H_2)} \tag{E.25}$$

It is now possible to extract the cross section ratio from

$$\frac{\frac{d\sigma^{1\gamma}}{d\xi}(\xi = \bar{\xi}; D_2)}{\frac{d\sigma^{1\gamma}}{d\xi}(\xi = \bar{\xi}; H_2)} = \frac{M^{H_2}}{M^{D_2}}\ \frac{N_\mu^{H_2}}{N_\mu^{D_2}}\ \frac{W^{D_2}(\Delta\xi)}{W^{H_2}(\Delta\xi)}\ \frac{I^{H_2}(\Delta\xi)}{I^{D_2}(\Delta\xi)} \tag{E.26}$$

Using, as a first approximation,

$$\left.\frac{I^{H_2}(\Delta\xi)}{I^{D_2}(\Delta\xi)}\right|^{0} \equiv 1 \tag{E.27}$$

yields the raw measurement of the cross section ratio:

$$\left.\frac{\frac{d\sigma^{1\gamma}}{d\xi}(\xi=\bar{\xi};D_2)}{\frac{d\sigma^{1\gamma}}{d\xi}(\xi=\bar{\xi};H_2)}\right|^{0} = \frac{M^{H_2}}{M^{D_2}}\,\frac{N_\mu^{H_2}}{N_\mu^{D_2}}\,\frac{W^{D_2}(\Delta\xi)}{W^{H_2}(\Delta\xi)} \tag{E.28}$$

E.10 Iterative Improvement in Ratio Measurement

The approximation used to extract the cross section ratio can be tested by evaluating the binned I ratio. If, as expected, this ratio is close to 1, then any deviation from 1 can be seen as a simple correction to the cross section ratio in Equation E.26. A more exact extraction, as is used to measure absolute cross sections, continues this scheme iteratively by using the corrected cross section in the next evaluation of the binned I ratio, then re-evaluating the cross section with the updated binned I ratio, and so on. The bin size is chosen to be sufficiently small to insure that the I ratio is close to 1. For iteration n, $(n > 0)$, the I ratio and cross section ratio are given by:

$$\begin{aligned}\left.\frac{I^{H_2}(\Delta\xi)}{I^{D_2}(\Delta\xi)}\right|^{n} \equiv\ & \left.\frac{\frac{d\sigma^{1\gamma}}{d\xi}(\xi=\bar{\xi};D_2)}{\frac{d\sigma^{1\gamma}}{d\xi}(\xi=\bar{\xi};H_2)}\right|^{n-1} \times \\ & \frac{\int_{\Delta\xi} d\xi\,\eta^{H_2} \int_{all\ \xi^*} d\xi^*\, B^{H_2}\,A^{H_2}\,E^{H_2}\,S^{H_2}\,\left.\frac{d\sigma^{total}}{d\xi^*}(H_2)\right|^{world}}{\int_{\Delta\xi} d\xi\,\eta^{D_2} \int_{all\ \xi^*} d\xi^*\, B^{D_2}\,A^{D_2}\,E^{D_2}\,S^{D_2}\,\left.\frac{d\sigma^{total}}{d\xi^*}(D_2)\right|^{world}}\end{aligned} \tag{E.29}$$

where $\left.\frac{d\sigma^{total}}{d\xi^*}\right|^{world}$ is derived from a fit to the world data set extrapolated to the values of ξ included in the measurement.

$$\left.\frac{\frac{d\sigma^{1\gamma}}{d\xi}(\xi=\bar{\xi};D_2)}{\frac{d\sigma^{1\gamma}}{d\xi}(\xi=\bar{\xi};H_2)}\right|^{n} = \left.\frac{I^{H_2}(\Delta\xi)}{I^{D_2}(\Delta\xi)}\right|^{n}\frac{M^{H_2}}{M^{D_2}}\,\frac{N_\mu^{H_2}}{N_\mu^{D_2}}\,\frac{W^{D_2}(\Delta\xi)}{W^{H_2}(\Delta\xi)} \tag{E.30}$$

The iterative process is ended when the change in the extracted cross section ratio is small compared to its errors. Cross sections derived from fits to the data sets of other experiments are used in this extraction since the ξ-dependence of the absolute cross section is not measured in this analysis. The extracted cross section ratio is largely insensitive, within error, to the absolute cross sections used, provided these cross sections are reasonable.

E.11 Target Impurities

The material used in the experiment targets is not chemically pure. Some 4.4% of the deuterium target material volume consisted of HD molecules, as is shown in Table 4.5 on page 84. This impurity affects several items, including the number of target nucleons, the target molar density, and the observed cross section itself. The quantities used to describe the effect of the contamination are the molar densities of D_2 and HD, labelled M^{D_2} and M^{HD}, determined from the measured pressure of the contaminated deuterium target material and the volume fraction of the target material that is HD, labelled f_V^{HD}.

In order to avoid introducing the error associated with these contamination-related measurements more than once, I limit the application of the contamination corrections to the final values presented. Thus, I do not correct the luminosity, use that luminosity to calculate a cross section, and then correct the cross section. In such a process, when done analytically, many of the corrections cancel.

The basic goal of this correction is to eliminate the effect of the H nuclei contamination in the deuterium target. The measured values describing the contamination, however, are in terms of the HD molecules. One could apply corrections that eliminate the HD molecules altogether. Rather than do that and lose the small amount of data from those deuterons in HD, I apply a correction to explicitly eliminate only the H contributions.

To evaluate the effect on muon-nucleon scattering, I exploit the fact that the observed scatter events on the contaminated target involve a nucleon in either a D_2 molecule or a HD molecule.

$$N^{target} = N^{D_2} + N^{HD} \tag{E.31}$$

Using Equation E.4, Equation E.5, and the definition:

$$\sigma^{target} \equiv \int_{\Delta\xi} d\xi\ \eta(\xi) \int_{all\ \xi^*} d\xi^*\ B\ A(\xi^*)\ E(\xi^*)\ S(\xi^*;\xi)\ \frac{d\sigma^{total}}{d\xi^*}(\xi^*) \qquad \text{(E.32)}$$

Equation E.19, ignoring radiative corrections, can be re-arranged to give:

$$N^{target} = N_A l_f^{target} N_\mu M^{target} \sigma^{target} \qquad \text{(E.33)}$$

This describes the number of scatters on the actual contaminated target. Using Equation E.33 in Equation E.31 yields:

$$l_f^{target} M^{target} \sigma^{target} = l_f^{D_2} M^{D_2} \sigma^{D_2} + l_f^{HD} M^{HD} \sigma^{HD} \qquad \text{(E.34)}$$

The number of muons N_μ on each substance is the same in the limit of small interaction probabilities. The fiducial length can be related to the volume occupied by either the D_2 or HD molecules by assuming each substance is uniformly spread across the area normal to the beam.

$$V^{target} M^{target} \sigma^{target} = V^{D_2} M^{D_2} \sigma^{D_2} + V^{HD} M^{HD} \sigma^{HD} \qquad \text{(E.35)}$$

Using

$$\begin{aligned} V &\equiv V^{target} && \text{(E.36)} \\ V^{D_2} &= (1 - f_V^{HD})V && \text{(E.37)} \\ V^{HD} &= f_V^{HD} V && \text{(E.38)} \end{aligned}$$

this can be written as

$$M^{target} \sigma^{target} = (1 - f_V^{HD}) M^{D_2} \sigma^{D_2} + f_V^{HD} M^{HD} \sigma^{HD} \qquad \text{(E.39)}$$

Since scatters on a deuteron in a HD molecule are still of interest, I break up the HD cross section with:

$$\sigma^{HD} = \frac{1}{2}\left(\sigma^{D_2} + \sigma^{H_2}\right) \tag{E.40}$$

To simplify this further, I define two quantities, δM and $\delta\sigma$, that are expected to be small.

$$\begin{aligned} \delta M &\equiv 4\frac{M^{HD}}{M^{D_2}} - 3 && \text{(E.41)} \\ &\approx 0.6 && \text{(E.42)} \end{aligned}$$

$$\begin{aligned} \delta\sigma &\equiv 2\frac{\sigma^{H_2}}{\sigma^{D_2}} - 1 && \text{(E.43)} \\ &\approx 0.0; \quad x_{bj} \rightarrow 0 && \text{(E.44)} \\ &\approx 0.6; \quad x_{bj} \rightarrow 1 && \text{(E.45)} \end{aligned}$$

Using the fact the number of moles of the substances are additive, the ratio of the molar densities of the contaminated and pure target can be written as:

$$\frac{M^{target}}{M^{D_2}} = 1 - \frac{1}{4} f_V^{HD}(1 - \delta M) \tag{E.46}$$

After some algebra, the cross section of all deuterons in the target, including those in D_2 and those in HD, can be related to the measured cross section. I prefer to express this as the effective D_2 cross section to avoid extraneous factors of two relating the nuclei per molecule:

$$\frac{\sigma^{D_2}}{\sigma^{target}} = \frac{1 - \frac{1}{4} f_V^{HD}(1 - \delta M)}{1 - \frac{7}{16} f_V^{HD}\left(1 - \frac{3}{7}\delta M - \frac{3}{14}\delta\sigma\left(1 + \frac{1}{3}\delta M\right)\right)} \tag{E.47}$$

Given that $f_V^{HD} \approx 4.4\%$, the deuterium cross section is increased 1% by this correction at small X_{bj} and less than 1% at large x_{bj}. Note that the actual number of events in a bin depends on the ratio of the proton cross section to the deuteron cross section through $\delta\sigma$. This is the source of the small x_{bj} dependence on the correction. Fortunately, the dependence of the correction on the $\delta\sigma$ term is rather weak. The F_2 model of Badełek and Kwieciński [31] is used to evaluate this term.

E.12 Structure Function Ratio

The differential cross section is parameterized by two functions F_2 and R as follows:

$$\frac{d\sigma^{1\gamma}}{dxdQ^2}(x,Q^2) = \frac{4\pi(\alpha\hbar c)^2}{Q^4}\left\{1 - y - \frac{Q^2}{4E^2} - \frac{(y^2 + Q^2/E^2)}{2(1+R(x,Q^2))}\right\}\frac{F_2(x,Q^2)}{x} \tag{E.48}$$

In order to extract both structure functions from the differential cross section, one requires data taken at a wide range of beam energies. The data set at E665, although spread over a wide range of energies, is concentrated at the beam energy for which the beamline magnets were tuned. Fortunately, a re-analysis of SLAC deep-inelastic electron scattering data and preliminary results from NMC seem to indicate that

$$R^{D_2} = R^{H_2} \tag{E.49}$$

within experimental error, although at higher x_{bj} and Q^2 than some of the E665 data set [202, 153]. Assuming this relation to be exact, the measured ratio of differential cross sections can then be related directly to the ratio of structure functions F_2.

$$\frac{F_2^{D_2}(x,Q^2)}{F_2^{H_2}(x,Q^2)} = \frac{1}{2}\frac{\frac{d\sigma^{1\gamma}}{dxdQ^2}(x,Q^2;D_2)}{\frac{d\sigma^{1\gamma}}{dxdQ^2}(x,Q^2;H_2)} \tag{E.50}$$

where the factor of 1/2 comes from the conversion of the deuterium structure function to a per-nucleon structure function.

Since the deuteron is weakly bound, it is common practice to consider the constituent neutron and proton to be quasi-free. Under this assumption, the deuteron and hydrogen cross sections can be broken down as follows:

$$\frac{d\sigma^{1\gamma}}{dxdQ^2}(D_2) = \frac{d\sigma^{1\gamma}}{dxdQ^2}(\mathrm{n}) + \frac{d\sigma^{1\gamma}}{dxdQ^2}(\mathrm{p}) \tag{E.51}$$

$$\frac{d\sigma^{1\gamma}}{dxdQ^2}(H_2) = \frac{d\sigma^{1\gamma}}{dxdQ^2}(\mathrm{p}) \tag{E.52}$$

Then, the so-called "n over p ratio" $F_2^{\mathrm{n}}/F_2^{\mathrm{p}}$ is given by:

$$\frac{F_2^{\mathrm{n}}(x,Q^2)}{F_2^{\mathrm{p}}(x,Q^2)} = \frac{\frac{d\sigma^{1\gamma}}{dxdQ^2}(x,Q^2;D_2)}{\frac{d\sigma^{1\gamma}}{dxdQ^2}(x,Q^2;H_2)} - 1 \tag{E.53}$$

Bibliography

[1] M. R. Adams, "SAT MWPC's", E665 Internal Report BT020, July 1986.

[2] M. R. Adams and T. J. Carroll, "SAT Trigger Processor Users Guide", E665 Internal Report SW192, August 1992.

[3] M. R. Adams *et al.* (E665 Collaboration), "A Spectrometer for Muon Scattering at the Tevatron", *Nucl. Instrum. Meth.* **A291**, 533 (1990).

[4] M. R. Adams *et al.* (E665 Collaboration), "Saturation of Shadowing at Very Low Bjorken x", *Phys. Rev. Lett.* **68**, 3266 (1992).

[5] M. R. Adams *et al.* (E665 Collaboration), "Shadowing in the Muon-Xenon Inelastic Scattering Cross-Section at 490 GeV/c", *Phys. Lett.* **B287**, 375 (1992).

[6] S. Adler, "Sum Rules Giving Tests of Local Current Commutation Relations in High-Energy Neutrino Reactions", *Phys. Rev.* **143**, 1144 (1966).

[7] S. Aïd, *Measurement of the Ratio of Neutron Cross-Section to Proton Cross-Section in Muon Deep Inelastic Scattering at 490 GeV/c*, Ph.D. thesis, University of Maryland (USA), 1991.

[8] S. Aïd and M. Schmitt, "Inefficiencies of the Muon Match, Muon Projection Reconstruction, and LAT Filter", E665 Internal Report AN090, March 1991.

[9] S. Aïd and M. Schmitt, "Muon Match Inefficiency – An Update", E665 Internal Report AN091, April 1991.

[10] A. A. Akhundov, D. Yu. Bardin, and N. M. Shumeĭko, "Electromagnetic Corrections to Deep Inelastic μp Scattering at High Energies", *Sov. J. Nuc. Phys.* **26**, 660 (1977).

[11] A. A. Akhundov, D. Yu. Bardin, and N. M. Shumeĭko, "Electromagnetic Corrections to the Elastic Radiative Tail in Deep Inelastic Lepton-Nucleon Scattering", *Sov. J. Nuc. Phys.* **44**, 988 (1986).

[12] J. P. Albanese *et al.* (EMC Collaboration), "The Vertex and Large Angle Detectors of a Spectrometer for High Energy Muon Physics", *Nucl. Instrum. Meth.* **212**, 111 (1983).

[13] D. Allasia *et al.* (NMC Collaboration), "Measurement of the Neutron and the Proton F_2 Structure Function Ratio", *Phys. Lett.* **B249**, 366 (1990).

[14] D. Allspach *et al.*, "Calibration of E665 Liquid Target Readouts", E665 Internal Report AN102, May 1991.

[15] G. Altarelli, "Partons in Quantum Chromodynamics", *Phys. Rep.* **81**, 1 (1982).

[16] G. Altarelli and G. Martinelli, "Transverse Momentum of Jets in Electroproduction from Quantum Chromodynamics", *Phys. Lett.* **B76**, 89 (1978).

[17] G. Altarelli and G. Parisi, "Asymptotic Freedom in Parton Language", *Nucl. Phys.* **B126**, 298 (1977).

[18] P. Amaudruz *et al.* (NMC Collaboration), "Gottfried Sum from the Ratio F_2^n/F_2^p", *Phys. Rev. Lett.* **66**, 2712 (1991).

[19] P. Amaudruz *et al.*, "Proton and Deuteron F_2^n Structure Functions in Deep Inelastic Muon Scattering", CERN Preprint No. CERN-PPE/92-124, 1992, (unpublished).

[20] P. Amaudruz *et al.* (NMC Collaboration), "The Ratio F_2^n/F_2^p in Deep Inelastic Muon Scattering", *Nucl. Phys.* **B371**, 3 (1992).

[21] P. L. Anthony, "X Coordinates of PTM Planes, SMS Planes, and SPM Planes", E665 Internal Report GN033, October 1988.

[22] P. L. Anthony, "PTM/PTA Commissioning: Initial Report", E665 Internal Report FS028, May 1989.

[23] P. L. Anthony, "The Utility Match Pam (UMPAM)", E665 Internal Report SW082, April 1989.

[24] P. L. Anthony, *Bose-Einstein Correlations in Deep-Inelastic Muon Scattering*, Ph.D. thesis, Massachusetts Institute of Technology (USA), 1990.

[25] M. Arneodo, *Measurement of the Structure Function Ratio F_2^{He}/F_2^D and a Comparison with Existing Models on the Nuclear Effects in Deep Inelastic Scattering*, Ph.D. thesis, Princeton University (USA), 1992.

[26] M. Arneodo, "Nuclear Effects in Structure Functions", CERN Preprint No. CERN-PPE/92-113, 1992, (unpublished).

[27] J. J. Aubert *et al.* (EMC Collaboration), "The Ratio of the Nucleon Structure Functions F_2^N for Iron and Deuterium", *Phys. Lett.* **B123**, 275 (1983).

[28] J. J. Aubert *et al.* (EMC Collaboration), "A Detailed Study of the Proton Structure Functions in Deep Inelastic Muon-Proton Scattering", *Nucl. Phys.* **B259**, 189 (1985).

[29] J. J. Aubert *et al.* (EMC Collaboration), "A Detailed Study of the Nucleon Structure Functions in Deep Inelastic Muon Scattering in Iron", *Nucl. Phys.* **B278**, 158 (1986).

[30] J. J. Aubert *et al.* (EMC Collaboration), "Measurements of the Nucleon Structure Functions F_2^N in Deep Inelastic Muon Scattering from Deuterium and Comparison with Those from Hydrogen and Iron", *Nucl. Phys.* **B293**, 740 (1987).

[31] B. Badełek and J. Kwieciński, "Electroproduction Structure Function F_2 in the Low Q^2, Low x Region", University of Warsaw Preprint No. IFD-3-92, 1992, (unpublished).

[32] B. Badełek and J. Kwieciński, "Shadowing in Inelastic Lepton-Deuteron Scattering", *Nucl. Phys.* **B370**, 278 (1992).

[33] M. D. Baker, "Charged Particle Trajectories in the "Non-Bend" View", E665 Internal Report SW109, November 1989.

[34] B. Baller and H. G. E. Kobrak, "Field in the E665 Beam Spectrometer Magnet (NMRE) when the Current is Zero", E665 Internal Report AN099, May 1991.

[35] R. Barbieri, J. Ellis, M. K. Gaillard, and G. G. Ross, "A Quest for a Wholly Scaling Variable", *Phys. Lett.* **B64**, 171 (1976).

[36] R. Barbieri, J. Ellis, M. K. Gaillard, and G. G. Ross, "Mass Corrections to Scaling in Deep Inelastic Processes", *Nucl. Phys.* **B117**, 50 (1976).

[37] D. Yu. Bardin and N. M. Shumeĭko, "Theoretical Estimate of Systematic Effects in Experiments on Deep Inelastic $1^{\pm}N$ Scattering", *Sov. J. Nuc. Phys.* **29**, 499 (1979).

[38] K. Bazizi and S. J. Wimpenny, "A QCD Analysis of the Proton Structure Function $F_2(x,Q^2)$", University of California, Riverside Preprint No. UCR/DIS/91-03, 1991, (unpublished).

[39] A. C. Benvenuti *et al.* (BCDMS Collaboration), "A High Statistics Measurment of the Proton Structure Functions $F_2(x,Q^2)$ and R from Deep Inelastic Muon Scattering at High Q^2", *Phys. Lett.* **B223**, 485 (1989).

[40] A. C. Benvenuti *et al.* (BCDMS Collaboration), "A Comparison of the Structure Functions F_2 of the Proton and the Neutron from Deep Inelastic Muon Scattering at High Q^2", *Phys. Lett.* **B237**, 599 (1990).

[41] A. C. Benvenuti *et al.* (BCDMS Collaboration), "A High Statistics Measurment of the Deuteron Structure Functions $F_2(x, Q^2)$ and R from Deep Inelastic Muon Scattering at High Q^2", *Phys. Lett.* **B237**, 592 (1990).

[42] D. M. Berg *et al.*, "A High-Speed CAMAC Data Acquisition System for PDP-11", *IEEE Trans. Nucl. Sci.* **32**, 1368 (1985).

[43] E. L. Berger and F. Coester, "Nuclear Effects in Deep Inelastic Lepton Scattering", *Ann. Rev. Nucl. Part. Sci.* **37**, 463 (1987).

[44] E. Berman *et al.*, "The VAXONLINE Software System at Fermilab", *IEEE Trans. Nucl. Sci.* **34**, 763 (1987).

[45] Philip R. Bevington, *Data Reduction and Error Analysis for the Physical Sciences*, (McGraw-Hill, New York, 1969).

[46] A. A. Bhatti, *The Ratio of the Proton and Neutron Structure Functions in 490 GeV/c Deep Inelastic Scattering*, Ph.D. thesis, University of Washington (USA), 1991.

[47] A. A. Bhatti *et al.*, "Seattle MWPC System (PCF Detector)", E665 Internal Report FS011, 1985, (Estimated date).

[48] Joe Biel *et al.*, *ACP Cooperative Processes User's Manual*, Fermi National Accelerator Laboratory, Batavia, IL (1990), FNAL Computing Publication GA0006.

[49] I. G. Bird, *Measurement of the Nucleon Structure Functions in Deep Inelastic Muon Scattering*, Ph.D. thesis, Vrije Universiteit te Amsterdam (Netherlands), 1991.

[50] J. D. Bjorken, "Asymptotic Sum Rules at Infinite Momentum", *Phys. Rev.* **179**, 1547 (1969).

[51] E. D. Bloom *et al.* (SLAC-MIT Collaboration), "High-Energy Inelastic $e - p$ Scattering at 6° and 10°", *Phys. Rev. Lett.* **23**, 930 (1969).

[52] A. Bodek and J. L. Ritchie, "Fermi-Motion Effects in Deep-Inelastic Lepton Scattering from Nuclear Targets", *Phys. Rev.* **D23**, 1070 (1981).

[53] Uwe Bratzler, *Design, Fabrication and Testing of a Low-Mass, High Resolution, Multiwire Proportional Chamber System for Experiment 665 at FERMILAB*, Ph.D. thesis, University of Washington (USA), 1991.

[54] H. M. Braun, "C0 in E665", E665 Internal Report VS010, April 1985.

[55] M. Breidenbach *et al.* (SLAC-MIT Collaboration), "Observed Behavior of Highly Inelastic Electron-Proton Scattering", *Phys. Rev. Lett.* **23**, 935 (1969).

[56] R. Creighton Buck, *Advanced Calculus*, third ed., International Series in Pure and Applied Mathematics (McGraw-Hill, New York, 1978).

[57] T. J. Carroll, "A Comparison of Event Scalers and Spill Scalers in RUN91", E665 Internal Report AN114, August 1991.

[58] T. J. Carroll, "Status of the Event Scalers for RUN90", E665 Internal Report AN107, May 1991.

[59] T. J. Carroll (private communication), August 1992.

[60] T. J. Carroll, "Implementation of Event Scaler Normalization in RUN90/91", E665 Internal Report AN147, April 1992.

[61] T. J. Carroll, "Using TRASTF to Improve the Muon Matching Efficiency", E665 Internal Report SW185, February 1992.

[62] M. Chaichian and N. F. Nelipa, *Introduction to Gauge Field Theories*, Texts and Monographs in Physics (Springer-Verlag, Berlin, 1984).

[63] D. B. Chelton and D. B. Mann, "Cryogenic Data Book", University of California Radiation Laboratory Report No. UCRL-3421, May 1956.

[64] J. M. Conrad, "Level-II Trigger Roads", E665 Internal Report BT064, September 1988.

[65] J. M. Conrad, "A Study of the SMS Road Veto", E665 Internal Report BT073, January 1989.

[66] J. M. Conrad, "Description of Physics Triggers in RUN90 and What's Fixed/Improved for RUN91", E665 Internal Report AN108, June 1991.

[67] J. M. Conrad, "Method Used for the Software Alignment", E665 Internal Report SW160, March 1991.

[68] J. M. Conrad, "Quality of Alignment for 8 Data Periods", E665 Internal Report AN145, March 1992.

[69] J. M. Conrad, H. G. E. Kobrak, and R. B. Nickerson, "The E665 Level-II Trigger Logic", E665 Internal Report BT053, February 1988.

[70] G. Coutrakon, S. K. Dhawan, and K. P. Schüler, "The Ring Imaging Cerenkov Detector for Fermilab Experiment 665", E665 Internal Report RC010, October 1987.

[71] A. Devoto, D. W. Duke, J. D. Kimel, and G. A. Sowell, "A New Calculation of the Order-g^4 QCD Corrections to the Longitudinal Structure Function", *Phys. Lett.* **B138**, 418 (1984).

[72] A. Devoto, D. W. Duke, J. D. Kimel, and G. A. Sowell, "Analytic Calculation of the Fourth-Order Quantum Chromodynamic Contribution to the Nonsinglet Quark Longitudinal Structure Function", *Phys. Rev.* **D30**, 541 (1984).

[73] M. Diemoz, F. Ferroni, and E. Longo, "Nucleon Structure Functions from Neutrino Scattering", *Phys. Rep.* **130**, 293 (1986).

[74] W. Dougherty, "E665 Production Monitor Ntuple", E665 Internal Report AN162, June 1992.

[75] J. Drees and H. E. Montgomery, "Muon Scattering", *Ann. Rev. Nucl. Part. Sci.* **33**, 383 (1983).

[76] T. Dreyer *et al.*, "Calibration and Validation of a Time of Flight Detector", E665 Internal Report PB016, April 1991, Published at Freiburg, Germany.

[77] E. Eichten, I. Hincliffe, and C. Quigg, "Flavor Asymmetry in the Light-Quark Sea of the Nucleon", FNAL Preprint No. Fermilab-PUB-91/272-T, 1991, (unpublished).

[78] J. Ellis and R. Jaffe, "Sum Rule for Deep-Inelastic Electroproduction from Polarized Protons", *Phys. Rev.* **D9**, 1444 (1974), Erratum in *Phys. Rev.* **D10**, 1669 (1974).

[79] R. K. Ellis, W. Furmański, and R. Petronzio, "Power Corrections to the Parton Model in QCD", *Nucl. Phys.* **B207**, 1 (1982).

[80] R. K. Ellis, W. Furmański, and R. Petronzio, "Unravelling Higher Twists", *Nucl. Phys.* **B212**, 29 (1982).

[81] A. Engelkemeir, "Report of Analytical Results", The Analytic Chemistry Laboratory (of Argonne National Laboratory) Report No. 90-0574-01, September 1990, (see E665 Experiment Logbook Volume 19, p. 106).

[82] M. Erdmann, "Brief Documentation for E665 about Freiburg's Time of Flight Detector", E665 Internal Report VS015, August 1986.

[83] G. Y. Fang, "Some Results on the SVS Studies", E665 Internal Report AN072, September 1990.

[84] G. Y. Fang, "SUM and SVS Counter Status", E665 Internal Report TR139, July 1990, presentation at E665 July 1990 Collaboration Meeting.

[85] G. Y. Fang (private communication), August 1992.

[86] Matt Fausey *et al.*, *CPS & CPS Batch Reference Guide: Version 2.7.0*, Fermi National Accelerator Laboratory, Batavia, IL (1992), FNAL Computing Publication GA0008.

[87] H. Fenker, "Standard Beam MWPC for Fermilab", Fermilab Technical Report TM 1179 2557.0, February 1983.

[88] R. P. Feynman, "Very High-Energy Collisions of Hadrons", *Phys. Rev. Lett.* **23**, 1415 (1969).

[89] R .P. Feynman, *Photon-Hadron Interactions*, Frontiers in Physics Lecture Note Series (W. A. Benjamin, Reading, Mass., 1972).

[90] W .R. Francis *et al.*, "Muon Scattering with Hadron Detection at the Tevatron", Fermilab Experiment Proposal 665, August 1983.

[91] W. R. Francis and T. Kirk, "Muon Scattering at Fermilab", *Phys. Rep.* **54**, 307 (1979).

[92] L. L. Frankfurt and M. I. Strikman, "On the Problem of Extracting the Neutron Structure Function from eD Scattering", *Phys. Lett.* **B76**, 333 (1978).

[93] H. J.. Gebauer, "The Vertex Proportional Chamber", E665 Internal Report VS012, October 1985.

[94] D. F. Geesaman *et al.*, "Data Acquisition for FNAL E665", *IEEE Trans. Nucl. Sci.* **36**, 1528 (1989).

[95] M. Gell-Mann, "A Schematic Model of Baryons and Mesons", *Phys. Lett.* **8**, 214 (1964).

[96] H. Georgi and H. D. Politzer, "Freedom at Moderate Energies: Masses in Color Dynamics", *Phys. Rev.* **D14**, 1829 (1976).

[97] Howard Georgi, *Weak Interactions and Modern Particle Theory*, (Benjamin/Cummings, Menlo Park, CA, 1984).

[98] K. Gottfried, "Sum Rule for High-Energy Electron-Proton Scattering", *Phys. Rev. Lett.* **18**, 1174 (1967).

[99] D. J. Gross and C. H. Llewellyn-Smith, "High-Energy Neutrino-Nucleon Scattering, Current Algebra, and Partons", *Nucl. Phys.* **B14**, 337 (1969).

[100] D. J. Gross and S. B. Treiman, "Light-Cone Structure of Current Commutators in the Gluon-Quark Model", *Phys. Rev.* **D4**, 1059 (1971).

[101] D. J. Gross and F. Wilczek, "Ultraviolet Behavior of Non-Abelian Gauge Theories", *Phys. Rev. Lett.* **30**, 1343 (1973).

[102] R. Guo, "PSA Time Line data", E665 Internal Report AN074, September 1990.

[103] R. Guo (private communication), August 1992.

[104] Francis Halzen and Alan D. Martin, *Quarks and Leptons: An Introductory Course in Modern Particle Physics*, (John Wiley & Sons, New York, 1984).

[105] J. J. Hernández *et al.* (Particle Data Group), "Review of Particle Properties", *Phys. Lett.* **B239**, 1 (1990), Erratum in *Phys. Lett.* **253B**, 525 (1991).

[106] K. H. Hicks, "Measurements of Large-Angle Neutron Spectra as E665", E665 Internal Report PB018, May 1991, Submitted to the 4th Conference on the Intersection between Particle and Nuclear Physics.

[107] Paul Horowitz and Winfield Hill, *The Art of Electronics*, (Cambridge University Press, Cambridge, 1980).

[108] E. Iarocci, "Plastic Streamer Tubes and Their Application in High-Energy Physics", *Nucl. Instrum. Meth.* **A217**, 30 (1984).

[109] D. E. Jaffe, "Real Beam in Monte-Carlo", E665 Internal Report ST0116, December 1988.

[110] D. E. Jaffe, "The 1990 Small Angle Trigger", E665 Internal Report BT057, September 1989.

[111] D. E. Jaffe, "The Small Angle Scintillator (SSA)", E665 Internal Report FS033, January 1990.

[112] D. E. Jaffe, "The Bremsstrahlung Monte-Carlo", E665 Internal Report MC043, June 1991.

[113] J. E. Jensen *et al.*, "Selected Cryogenic Data Notebook", Brookhaven National Laboratory Report No. BNL-10200-R, August 1980.

[114] S. Kaufman and S. A. Wolbers, "CPS, the Farms, and E665", E665 Internal Report SW184, January 1992.

[115] R. D. Kennedy, "Level One Trigger Processor", E665 Internal Report BT031, April 1987.

[116] R. D. Kennedy, "SPM Alignment/Efficiency Results", E665 Internal Report SW0108, November 1988.

[117] R. D. Kennedy, "E665 New User Primer: UNIX Version 2.3", E665 Internal Report SW136, November 1990.

[118] R. D. Kennedy, "E665 Spill Number Decoder Revision for RUN90", E665 Internal Report SW133, November 1990.

[119] R. D. Kennedy, "E665 Use of UNIX AWK: UNIX Version 1.0", E665 Internal Report SW139, November 1990.

[120] R. D. Kennedy, "E665 newver Program: UNIX Version 3.6", E665 Internal Report SW175, August 1991.

[121] R. D. Kennedy, "E665 shell Program: UNIX Version 3.6", E665 Internal Report SW174, August 1991.

[122] R. D. Kennedy, "Porting Code to IBM Risc-based AIX", E665 Internal Report SW172, July 1991.

[123] R. D. Kennedy, "RUN90 Spill Scaler Normalization: Inputs and Results to Date", E665 Internal Report AN100, May 1991.

[124] R. D. Kennedy, "RUN90 Spill Scaler Normalization Production Code", E665 Internal Report SW166, May 1991.

[125] R. D. Kennedy, "E665 Production N-tuples for Physics and Rbeam Analysis", E665 Internal Report SW189, June 1992.

[126] R. D. Kennedy, "F2(n)/F2(p) Event Statistics: A Comparison between RUN90 10% and RUN87", E665 Internal Report AN157, July 1992.

[127] R. D. Kennedy, "F_2^n/F_2^p in RUN90", E665 Internal Report 0, December 1992, in preparation.

[128] R. D. Kennedy, "Liquid Target Densities in RUN90", E665 Internal Report 0, December 1992, in preparation.

[129] R. D. Kennedy, "Normalization in RUN90", E665 Internal Report 0, December 1992, in preparation.

[130] R. D. Kennedy, "Nu Offset in RUN90 10%-B Production", E665 Internal Report 0, December 1992, in preparation.

[131] R. D. Kennedy, "Radiative Corrections for RUN90", E665 Internal Report 0, December 1992, in preparation.

[132] E. R. Kinney, "E665 Target Control Software User's Guide, Version 2.1", E665 Internal Report OL031, June 1990.

[133] E. R. Kinney, "Results of August 1990 Survey of E665 Targets (Revised)", E665 Internal Report AN088, April 1991.

[134] T. Kirk, "A Multihit Time Encoder System (MUTES)", E665 Internal Report FS017, December 1978.

[135] T. Kirk, "CCM Magnetic Field", E665 Internal Report FS001, May 1982.

[136] H. G. E. Kobrak and M. Schmitt, "CCM Field Strength", E665 Internal Report AN112, June 1991.

[137] A. V. Kotwal (private communication), August 1992.

[138] S. Kunori, "CVM and CCM Field Maps", E665 Internal Report SW038, March 1986.

[139] J. Kuti and V. Weisskopf, "Inelastic Lepton-Nucleon Scattering and Lepton Pair Production in the Relativistic Quark-Parton Model", *Phys. Rev.* **D4**, 3418 (1971).

[140] Fermi National Accelerator Laboratory, "The Fermilab Upgrade - An Overview", Fermilab Proposal (unnumbered), January 1989, Fermilab Library Item QA787.P7F46.

[141] D. R. Lide, editor, *CRC Handbook of Chemistry and Physics*, 72 ed., (CRC Press, Boca Raton, FL, 1991).

[142] P. B. Madden (private communication), August 1992.

[143] A. Malensek and J. G. Morfín, "The Tevatron Muon Beam: A High Intensity Beam with Well-Defined Polarization", Fermilab Technical Report TM 1193 2966.0, July 1983.

[144] A. Manz, "2M x 2M Proportional Chamber (PC 1-3)", E665 Internal Report VS012, October 1985.

[145] A. D. Martin, R. G. Roberts, and W. J. Stirling, "New Information on Parton Distributions", Rutherford Appleton Laboratory Preprint No. RAL-92-021, 1992, (unpublished).

[146] H. Melanson, "E665 DC Calibration, Pass 1", E665 Internal Report FS027, December 1988.

[147] H. Melanson, "E665 DC Calibration, Pass 2", E665 Internal Report AN059, December 1989.

[148] H. Melanson, "Cross-calibration of the Beam and Forward Spectrometers using RBEAM Run through PTMV", E665 Internal Report AN062, January 1990.

[149] H. Melanson (private communication), August 1992.

[150] H. Melanson, T. Kirk, and S. A. Wolbers, "Fermilab Drift Chamber System", E665 Internal Report FS010, October 1985.

[151] D. G. Michael, "The FASTBUS Data Acquisition System for E665", E665 Internal Report OL026, February 1989, Fermilab Computing Note PN378.

[152] D. G. Michael, *A Study of the Transverse Momentum and Jets using Forward Hadrons and Photons in Deep Inelastic Muon Scattering at 490 GeV/c*, Ph.D. thesis, Harvard University (USA), 1990.

[153] A. Milsztajn, "Target Dependence of R Measured in Deep Inelastic Muon Scattering", DAPNIA Preprint No. SPP-92-15, 1992, (presented at the 27th Recontres de Moriond, Les Arcs, France, March 22-28, 1992).

[154] L. W. Mo and Y. S. Tsai, "Radiative Corrections to Elastic and Inelastic ep and νp Scattering", *Rev. Mod. Phys.* **41**, 205 (1969).

[155] H. E. Montgomery, "Beam Tagging for E665", E665 Internal Report BT007, July 1984.

[156] H. E. Montgomery, "Test of Counters for Halo Veto Wall for E665", E665 Internal Report BT008, July 1984.

[157] H. E. Montgomery *et al.*, "E665 Target Specification for the 1989-90 Run II", E665 Internal Report BT074, February 1989.

[158] J. G. Morfín, "A SWIC Oriented Guide to Muon Beamline Tuning", E665 Internal Report BT039, June 1987.

[159] J. G. Morfín and W.-K.Tung, "Parton Distributions from a Global Analysis of Deep Inelastic Scattering and Lepton-Pair Production", FNAL Preprint No. Fermilab-PUB/90-74, 1990, (unpublished).

[160] P. D. Morley and I. Schmidt, "Relativistic Fermi Motion and Nuclear Structure Functions", *Phys. Rev.* **D34**, 1305 (1986).

[161] O. Nachtmann, "Positivity Constraints for Anomalous Dimensions", *Nucl. Phys.* **B63**, 237 (1973).

[162] O. Nachtmann and H. J. Pirner, "Color-Conductivity in Nuclei and the EMC-Effect", *Z. Phys.* **C21**, 277 (1984).

[163] R. B. Nickerson, "Brief Documentation of the E665 EM Calorimeter", E665 Internal Report EM012, October 1985.

[164] R. B. Nickerson, "Halo Veto Wall", E665 Internal Report BT061, May 1988.

[165] R. B. Nickerson, "Light Guide Design for the SVS Veto Counter", E665 Internal Report BT083, April 1989.

[166] R. B. Nickerson, F. M. Pipkin, and Richard Wilson, "Upstream Trigger Wall and Trigger Timing for the 1989 Run", E665 Internal Report BT062, August 1988.

[167] N. N. Nicolaev and V. I. Zakharov, "Parton Model and Deep Inelastic Scattering on Nuclei", *Phys. Lett.* **B55**, 397 (1975).

[168] W.-D. Nowak, "Review of Deep Inelastic Charged Lepton Scattering", *Fortschr. Phys.* **34**, 57 (1986).

[169] M. De Palma *et al.*, "A System of Large Multiwire Proportional Chambers for a High Intensity Experiment", *Nucl. Instrum. Meth.* **A217**, 135 (1983).

[170] V. Papavassiliou (for the E665 Collaboration), "Measurement of the Cross-Section Ratio σ_n/σ_p in Inelastic Muon-Nucleon Scattering at Very Low x and Q^2", Submitted to the *Proceedings of the XXVI International Conference on High Energy Physics*, Dallas, Texas, August 6–12, 1992.

[171] V. Papavassiliou (private communication), October 1992.

[172] B. Pawlik (private communication), August 1992.

[173] Donald H. Perkins, *Introduction to High Energy Physics*, third ed., (Addison-Wesley, Menlo Park, CA, 1983).

[174] H. D. Politzer, "Reliable Perturbative Results for String Interactions", *Phys. Rev. Lett.* **30**, 1346 (1973).

[175] E. J. Ramberg, "Data Correction, Calibration, and Resolution of the Calorimeter", E665 Internal Report AN061, February 1990.

[176] J. J. Ryan, *Particle Production in Deep Inelastic Muon Scattering*, Ph.D. thesis, Massachusetts Institute of Technology (USA), 1991.

[177] C. Salgado, "E665 Run 1990-91 Monte-Carlo", E665 Internal Report MC034, September 1990.

[178] C. Salgado, "Run 1990 Alignment", E665 Internal Report AN077, September 1990.

[179] A. Salvarani, *Forward Hadron Production in Muon Deep Inelastic Scattering at 490 GeV from Deuterium and Xenon*, Ph.D. thesis, University of California, San Diego (USA), 1991.

[180] H. Schellman, "Preliminary Final Design for Vertex Tracking System", E665 Internal Report VS023, March 1989.

[181] H. Schellman, "Effects of HD Contamination in the D_2 Target", E665 Internal Report AN118, October 1991.

[182] H. Schellman, "The E665 Proton Calibration Run - Part I", E665 Internal Report AN152, December 1991.

[183] H. Schellman (private communication), August 1992.

[184] H. Schellman, "The Vertex Drift Chamber System", E665 Internal Report 0, December 1992, in preparation.

[185] M. Schmitt, "Using the Calorimeter to Remove Electromagnetic Background", E665 Internal Report AN058, November 1989.

[186] M. Schmitt, "Something Odd in the PSRF", E665 Internal Report BT091, July 1990.

[187] M. Schmitt, "A Modification to Nickerson's Pad Clustering Routine", E665 Internal Report EM017, July 1991.

[188] M. Schmitt, "A Study of the Momentum Discrepancy between the Beam and Forward Spectrometers", E665 Internal Report AN098, May 1991.

[189] M. Schmitt, *Deep Inelastic Exclusive* ρ^0 *Production using 485 GeV Muons*, Ph.D. thesis, Harvard University (USA), 1991.

[190] M. Schmitt, "The Nu-Offset and Z", E665 Internal Report AN101, May 1991.

[191] Ch. Scholz, computer program FERRAD, Version 35, (NMC Collaboration, October 1992).

[192] R. B. Scott, editor, *Technology and Uses of Liquid Hydrogen*, (Pergamon Press, New York, 1964).

[193] G. Siegert, "RUN90 Interspill Split", E665 Internal Report SW129, October 1990.

[194] G. Siegert *et al.*, "Mapping NMRE for E665 RUN90", E665 Internal Report AN087, February 1990.

[195] R. D. Smith, "Effect of Nuclear Binding and Fermi Motion on the Ratio $R_A = \sigma_L/\sigma_T$ in Deep-Inelastic Electron Scattering", *Phys. Lett.* **B182**, 283 (1986).

[196] P. Spentzouris and H. Schellman, "The E665 Proton Calibration Run – Part II", E665 Internal Report AN153, June 1992.

[197] R. A. Swanson (private communication), September 1992.

[198] G. 't Hooft, "Renormalization of Massless Yang-Mills Fields", *Nucl. Phys.* **B61**, 455 (1973).

[199] S. Tentindo-Repond, "C1 Status Report", E665 Internal Report TR056, December 1987.

[200] Y. S. Tsai, SLAC Report No. PUB-848, 1971, (unpublished).

[201] M. van der Heijden, *The Structure of Nucleons Studied in Deep Inelastic Muon Scattering*, Ph.D. thesis, Universiteit van Amsterdam (Netherlands), 1991.

[202] L. W. Whitlow, *Deep Inelastic Structure Functions from Electron Scattering on Hydrogen, Deuterium, and Iron at* 0.6 $\mathrm{GeV}^2 \leq Q^2 \leq 30.0\ \mathrm{GeV}^2$, Ph.D. thesis, Stanford University (USA), 1990, also published as SLAC Report No. 357.

[203] L. W. Whitlow *et al.*, "A Precise Extraction of $R = \sigma_L/\sigma_T$ from a Global Analysis of the SLAC Deep Inelastic e-p and e-d Scattering Cross Sections", *Phys. Lett.* **B250**, 193 (1990).

[204] L. W. Whitlow *et al.*, "Precise Measurements of the Proton and Deuteron Structure Functions from a Global Analysis of the SLAC Deep Inelastic Electron Scattering Cross Sections", *Phys. Lett.* **B282**, 475 (1992).

[205] K. Wilson, "Non-Lagrangian Models of Current Algebra", *Phys. Rev.* **179**, 1499 (1969).

[206] S. A. Wolbers *et al.*, "E665 Code Conversion to UNIX on Silicon Graphics", E665 Internal Report SW135, December 1990.

[207] H. W. Woolley, R. B. Scott, and F. G. Brickwedde, "Compilation of Thermal Properties of Hydrogen in Its Various Isotopic and Ortho-Para Modifications", *J. Res. U.S. Natl. Bur. Stand.* **41**, 379 (1948).

[208] R. Yamada, "Magnet Measurement on Neutrino Wide Gap Magnet: (WGNT-4)", E665 Internal Report BT052, September 1974.

[209] F. J. Yndurâin, *Quantum Chromodynamics: An Introduction to the Theory of Quarks and Gluons*, Texts and Monographs in Physics (Springer-Verlag, Berlin, 1983).

[210] G. Zweig, CERN Report No. TH401, 1964, (unpublished).

[211] G. Zweig, CERN Report No. TH412, 1964, (unpublished).